IN-PLANE RESPONSE AND MODE II FRACTURE RESPONSE OF Z-PIN WOVEN LAMINATES

by

Hseng-Ji Huang

A dissertation submitted in partial fulfillment
of the requirements for the degree of
Doctor of Philosophy
(Aerospace Engineering)
in The University of Michigan
2008

Doctoral Committee:

Professor Anthony M. Waas, Chair
Professor Victor C. Li
Assistant Professor Veera Sundararaghavan
Senior Scientist Chian-Fong Yen, Army Research Office

To my family.

ACKNOWLEDGEMENTS

Firstly and most importantly, I would like to express my greatest appreciation to my advisor, Professor Anthony M. Waas, for his support in my life and instruction of the research for the past couple years. Professor Waas gave me not only the freedom to decide the research direction but also the valuable opinions when I was stuck. I would also like to thank Dr. Chian-Fong Yen for his continuing suggestions from the beginning this research project. Professor Victor Li's useful comments on this thesis about fracture mechanics and Professor Veera Sundararaghavan's useful recommendations with respect to this thesis are also appreciated.

I would like to express my gratitude to ARL (Army Research Lab) for the financial support received during my research. Additionally, during the manufacture of Z-pin woven laminates, the preparation of the weave S2 glass fibers by Dr. Seth Ghiorse in ARL, the binder process by Dr. Bazle Gama in University of Delaware, Z-pinning process by Tom Fusco in Aztec, and final resin infusion by Dr. Seth Ghiorse in ARL are greatly appreciated. I would also like to thank Dr. Bruce LaMattina and Dr. Christopher Hoppel from the ARL for their suggestion.

I would like to thanks the faculties in the department of aerospace engineering, from which I have learnt invaluable knowledge of solid mechanisms. Especially, I would like to express my gratitude to Professor Nicolas Triantafyllidis, from which I could enjoy the whole pictures of the continuum mechanics and the methods of determining the post buckling behavior of a structure by use of the asymptotic method.

I am glad to know so many good friends here in Ann Arbor for the past couple years. Those good friends include, Dr. Fuyuan Hsiao, Dr. Joseph Rakow, Dr. Basu Shiladitya, Amit Salvi, Mark Pankow, Dr. Wei Heok Ng, Evan Pineda, Dr. Peter Gustafson, Wooseok Ji, Dr. Ce Sun, Smith Thepvongs, Dr. Youshifumi Suzuki, Ken Salas, Dr. Farzad Ismail, Dr. Jesse David Thomas, Dr. Bryan Glaz, and Kah Mun Wong, Dr. Xie De, Dr. Shunjun Song.

Finally, I would like to thank the unconditional support and generous understanding from my family.

This work was funded by the Army Research Office through grant W911NF-05-1-02S9 to the University of Michigan. Any opinions and findings of this thesis are solely that of the author.

TABLE OF CONTENTS

DEDICATION ii

ACKNOWLEDGEMENTS iii

LIST OF FIGURES vii

LIST OF TABLES xiv

LIST OF APPENDICES xv

CHAPTER

I. Introduction 1

II. Compressive Response and Failure of Z-pin Composites . . 18

III. Compression Strength Limiting Mechanism in Woven Fiber Z-pinned Composites 68

IV. Prediction of Compressive Strength in Multilayered Woven Z-pin Textile Composites 116

V. Compressive Response and Failure of Z-Pin Textile Composites: 3D Numerical Simulation 140

VI. Static and Dynamic Fracture Mode II Tests 175

VII. Conclusions and Recommendations for Future Research . . 225

APPENDICES **229**

BIBLIOGRAPHY **272**

LIST OF FIGURES

Figure

1.1 The Side View of a Representative Unit Cell of a Laminated Multi-layer Woven Composite 14
1.2 Schematic of the Z-pin Process (2D Side View) 15
1.3 Different Hierarchy in a Multi-layered Woven Composite 16
1.4 Scanning Electron Microscope (SEM) Image of a Fiber Tow Cross Section 17

2.1 MTS Machine and Speckle Setup 38
2.2 Fixture Used in the Compressive Tests 39
2.3 Front View of the Tested Specimen 40
2.4 Back View of the Tested Specimen 41
2.5 Typical Stress-Strain Curve for Compression(1%Z-pin $[45/-45/0/90]_{2s}$ Composite) 42
2.6 Comparison of Young's Modulus in Group A 43
2.7 Comparison of Young's Modulus in group B 44
2.8 Comparison of Young's Modulus in Group C 45
2.9 Comparison of Young's Modulus in Group D 46
2.10 Illustration of d=0.5080 mm (0.02 in.) Z-pin and d=0.2794 mm (0.011 in.) Z-pins 47
2.11 (a) SEM Image of d=0.5080 mm (0.02 in.) Z-pin (b)SEM Image of d=0.2794 mm (0.011 in.) Z-pin 48
2.12 Comparison of the Strength in Group A 49
2.13 Comparison of the Strength in Group B 50
2.14 Comparison of the Strength in Group C 51
2.15 Comparison of the Strength in Group D 52
2.16 Macroscopic Compression Failure Mechanism for Group A and B . 53
2.17 Macroscopic Compression Failure Mechanism for Group C and D . 54
2.18 Macroscopic Compression Failure Mechanism for Group E 55

2.19 Crack Path in Group A3 56
2.20 Kink Band in Fiber Tow at the Fiber/Matrix Scale in Group C1 . 57
2.21 (a) Crack near the Z-pin of Specimen in Group A2 (b) Crack near the Z-pin of Specimen in Group A3 58
2.22 Comparison of the Young's Modulus 59
2.23 Illustration of Line Average 60
2.24 Illustration of Area Average 61
2.25 Speckle Pattern in 2% Z-pin Composites 62
2.26 Speckle Pattern in 3% Z-pin Composites 63
2.27 ε_{yy} when Load=1824.58N 64
2.28 ε_{yy} when Load=1576.17N 64
2.29 ε_{yy} when Load=3897.60N 64
2.30 ε_{yy} when Load=3400.75N 64
2.31 ε_{yy} when Load=5988.04N 64
2.32 ε_{yy} when Load=5105.36N 64
2.33 SEM Image of the Composites 65
2.34 SEM Image of Fiber Tow 66
2.35 The Movement of the Monitored Window in this Algorithm 67

3.1 Model of a [45/-45] Lamina 83
3.2 Longitudinal and Transverse Fiber Tows 84
3.3 Schematics of Compression Test of [± 45] Composite Specimen . . 85
3.4 Matrix Mesh (FE) 86
3.5 Final Axial Stress-Axial Strain Response Curve of In-Situ Matrix 87
3.6 SEM Image of a Typical Fiber Tow 88
3.7 Illustration of the Representative Unit Cell of a Fiber Tow 89
3.8 Failure Pattern of 1 RUC 90
3.9 Damage Zone near the Z-pin 91
3.10 Illustration of 2D Model Unit Cell Constituents 92
3.11 2D Buckling Mode Used as the Initial Geometric Imperfection . . 93
3.12 Results of Different Imperfection 94
3.13 Effect of Imperfection on Compression Strength of Z-pin Composite (Z-pin Diameter=0.508 mm (0.02 in), 1% Density), and Global Initial Imperfection 95
3.14 Local Buckling Mode 96
3.15 Comparison of Stress-Strain Curves for Global and Local Imperfection 97
3.16 Finite Element Model of a Damaged Composite, where the Z-pin is Replaced by a Hole 98

3.17 2D Response Curve for Damage and no Damage Curve of a Composite with Z-pin Diameter of d=0.508 mm (0.02 in) and 1% Density 99
3.18 Finite Element Models of the 9 Unit Cell and 16 Unit Cell Representation of the 2D Problem Studied 100
3.19 Stress-Strain Response of 9 Unit Cell Simulation. Note the Breaking of Symmetry at the Onset of Kink Banding 101
3.20 Stress-Strain Response of a 16 Unit Cell Simulation 102
3.21 Comparison of Stress-Strain Curve for Different Density 103
3.22 Comparison of Stress-Strain Curve for Different Diameter 104
3.23 Kind Band in a Two Dimensional Model 105
3.24 Kink Band in a SEM Image. Arrow Indicates Global Loading Direction 106
3.25 Z-pin Touches Fiber Tow Directly 107
3.26 Models of Composites with d=0.0508 cm (0.02 in), 9 Z-pins, , and 1% Density 108
3.27 Models of Composites with d=0.0279 cm (0.011 in), 36 Z-pins, and 1% Density 109
3.28 Comparison of the Composite with d=0.0508 cm (0.02 in) Z-pin Diameter and the Composite with d=0.0279 cm (0.011 in) Z-pin Diameter 110
3.29 Kink Band of the Composite with d=0.0279 cm (0.011 in) Corresponding to point A 111
3.30 Kink Band of the Composite with d=0.0508 cm (0.02 in)corresponding to point B 112
3.31 1% Z-pin Composite with d=0.0508 cm (0.02 in) with Larger Matrix Surrounding Matrix. Note the Z-pin is Touching the Fiber Tow . . 113
3.32 1% Z-pin Composite with d=0.0508 cm (0.02 in) with Small Matrix Surrounding Matrix. Note the Z-pin is touching the Fiber Tow . . 114
3.33 Comparison of Axial Stress and Axial Strain Curve for two 1% Z-pin Composites with Different Matrix Area 115

4.1 Side Image of a Cross Section. Notice that Phase Shifts between Axial Tows (Lighter Shade) of Different Laminae 123
4.2 Schematic of a Failed Specimen Viewed in the 1-2 Plane and the 1-3 Plane (Commonly Observed for All Types of Specimens Studied in this Thesis) 124
4.3 Images of a Failed Z-pin Specimen ($[45/-45/0/90]_{2s}$, 1% Z-pin) under Uniaxial Compression in the “1” Direction 125
4.4 3D Model with 9 Unit Cells in One Lamina 126
4.5 Model without Axial Fiber Tows, Cross-Section AA in Figure 4.4 127

4.6 Idealized Model with 13 Axial Fiber Tows 128
4.7 Schematic of Boundary Condition 129
4.8 Comparison of Model AA, Model BB, and Model CC against the Experimental Results 130
4.9 Idealized Model with No Phase Difference 131
4.10 Idealized Model with Phase Difference $\frac{\pi}{2}$ between Neighboring Laminae 132
4.11 Axial Stress- Axial Strain Response with Phase Difference and without Phase Difference 133
4.12 Model without Z-Pins 134
4.13 Model with Z-Pins 135
4.14 Comparison of Simulations of Z-pin Composites and no Z-pin Composites against Experiment 136
4.15 Deformed Shape Corresponding to Point A, Marked in Figure 4.14 for the 1% Z-pin Composite 137
4.16 Deformed Shape Corresponding to Point B, Marked in Figure 4.14 for the 1% Z-pin Composite 138
4.17 Deformed Shape Corresponding to Point C, Marked in Figure 4.14 for the 1% Z-pin Composite 139

5.1 Schematics of Fiber Tow and Matrix 147
5.2 Image of Cross Section 148
5.3 SEM Image of Fiber Tow and Matrix 149
5.4 Fiber Parameters for RUC 150
5.5 Longitudinal and Transverse Fiber Tows 151
5.6 Matrix 152
5.7 Schematic of RUC that is Used to Explain the Boundary Condition 153
5.8 Failure Pattern of 1 RUC 154
5.9 Numerical Model of 1 RUC 155
5.10 Numerical Model of 9 RUCs 156
5.11 Numerical Model of 16 RUCs 157
5.12 Numerical Model of 25 RUCs 158
5.13 Stress-Strain Curve for Different Number of RUCs 159
5.14 1 RUC Model at B 160
5.15 9 RUC Model at $B^{'}$ 161
5.16 16 RUC Model at $B^{''}$ 162
5.17 Stress-Strain Curve for Different Layers of Composites 163
5.18 comparison of Stress-Strain Curve with and without Phase Difference 164
5.19 Failure Mode of Composites without Phase Difference 165

5.20 Failure Mode of Composites with Phase Difference 166
5.21 Models with Phase Difference 167
5.22 Models without Phase Difference 168
5.23 Comparison of Simulations between Models with Phase Difference and without Phase Difference 169
5.24 Deformed Shape at A 170
5.25 Deformed Shape at B 171
5.26 Deformed Shape at C 172
5.27 Kind Band Viewed from X-Y Plane. Note that the Comparison between the Experimentally Observed Kink Band Failure and that of the 3D Numerical Prediction 173
5.28 Comparison of Axial Stress-Axial Strain Response of Z-pin Composites and no Z-pin Composites 174

6.1 Specimen and Spacer (Only Half of the Specimen is Shown, as a Side View) 191
6.2 Setup of Camera 192
6.3 Schematic of a ENF Test Specimen 193
6.4 Load Deflection Plot for Group A. ‘E’ Denotes the Case with no Z-pins. 194
6.5 Load Deflection Plot for Group B. ‘F’ Denotes the Case with no Z-pins. 195
6.6 Load Deflection Plot for Group C. ‘E’ Denotes the Case with no Z-pins. 196
6.7 Load Deflection Plot for Group D. ‘F’ Denotes the Case with no Z-pins. 197
6.8 Tested Specimen of C1 after Experiments 198
6.9 Tested Specimen of C2 after Experiments 199
6.10 Tested Specimen of C3 after Experiments 200
6.11 F1 Specimen Deflection=3.27 mm 201
6.12 F1 Specimen Deflection =3.29 mm 202
6.13 D3 Specimen Deflection=4.14 mm 203
6.14 D3 Specimen Deflection=5.12 mm 204
6.15 Crack Length vs Deflection for Group B 205
6.16 Crack Length vs Deflection for Group D 206
6.17 Cohesive Element 207
6.18 Cohesive Law 208
6.19 Numerical Model for Mode II Simulation 209
6.20 Comparison of Numerical Simulation and Experiment 210

6.21 Fracture Toughness of $[45/-45/0/90]_{2s}$ Composites 211
6.22 Fracture Toughness of $[0]_{16}$ Composites 212
6.23 Set-up of Drop Tower 213
6.24 Crack Advanced Gage 214
6.25 Load Versus Time of B3-1 Specimen 215
6.26 Load Versus Time of the Load Cell Transient Response, due to a "Hammer" Strike 216
6.27 Load Versus Time of B3-1 Specimen Before and After Filtering, Using the FFT 217
6.28 Dynamic Fracture Toughness for $[0]_{16}$ Composites 218
6.29 Dynamic Fracture Toughness for $[45/-45/0/90]_{2s}$ Composites . . 219
6.30 Crack Propagation Information of B3-1 Specimen 220
6.31 Image Taken When Time is 0 Second 221
6.32 Image Taken When Time is 100 μ Second 221
6.33 Image Taken When Time is 550 μ Second 222
6.34 Image Taken When Time is 1050 μ Second 222
6.35 Crack Propagation Information of B3-2 Specimen 223
6.36 Crack Propagation Information of B2-1 Specimen 224

A.1 Experimental Setup 242
A.2 Schematic Drawing of the Experimental Setup 243
A.3 The Movement of the Monitored Window in this Algorithm 244
A.4 Peak before Bi-Cubic Interpolation 245
A.5 Peak after Bi-Cubic Spline Interpolation 245
A.6 Speckle Pattern 246
A.7 Horizontal Displacement Field after Stretching 247
A.8 Horizontal Displacement Field after Compression 248
A.9 Horizontal Displacement Field after Rigid Body Translation . . . 249
A.10 Speckle before Rotation 250
A.11 Speckle after Rotation 250
A.12 Displacement Field of Rigid Body Rotation 251
A.13 Aluminum Specimen 252
A.14 Speckle Image of the Monitored Area 252
A.15 Comparison of Stress-Strain Curve 253
A.16 Illustration of Monitored Area 254
A.17 ε_{xx} from State 1 to State 2 255
A.18 ε_{xx} from State 1 to State 3 255
A.19 $\varepsilon_{xx}$from State 1 to State 4 255

A.20 $\varepsilon_{xx}$from State 1 to State 5 255
A.21 ε_{xx} from State 1 to State 6 255
A.22 ε_{xx} from State 1 to State 7 255
A.23 ε_{yy} from State 1 to State 2 256
A.24 ε_{yy} from State 1 to State 3 256
A.25 ε_{yy} from State 1 to State 4 256
A.26 ε_{yy} from State 1 to State 5 256
A.27 ε_{yy} from State 1 to State 6 256
A.28 ε_{yy} from State 1 to State 7 256
A.29 γ_{xy} from State 1 to State 2 257
A.30 γ_{xy} from State 1 to State 3 257
A.31 γ_{xy} from State 1 to State 4 257
A.32 γ_{xy} from State 1 to State 5 257
A.33 γ_{xy} from State 1 to State 6 257
A.34 γ_{xy} from state 1 to state 7 257
A.35 Schematic Drawing of the Specimen 258

B.1 "Dog Bone" Shape Specimen for Tension Test 261
B.2 Stress-Strain Response for Group A and Group E 262
B.3 Stress-Strain Response for Group C and Group E 263
B.4 Comparison of Strength between Group A and Group E 264
B.5 Comparison of Strength between Group C and Group E 265
B.6 Comparison of Stiffness between Group A and Group E 266
B.7 Comparison of Stiffness between Group C and Group E 267
B.8 Failure Pattern in Group A and Group E (A1 is 1% Z-pin Density, A2 is 2% Z-pin Density, A3 is 3% Z-pin Density). Notice How the Smaller Spacing between Z-pins (Larger Density) Leads to a Small Zone of Intense Damage 268
B.9 Failure Pattern in Group C and Group E (C1 is 1% Z-pin Density, C2 is 2% Z-pin Density, C3 is 3% Z-pin Density). Notice How the Smaller Spacing between Z-pins (Larger Density) Leads to a Small One of Intense Damage 269
B.10 Delamination between Fiber Tows,as Seen in a Failed A Specimen, after Tension Load 270
B.11 Fiber Tow Breakage near Z-pin Imaged through a SEM 271

LIST OF TABLES

Table

1.1 Details of the 6 Groups of Composites Investigated 13

2.1 Comparison of the Young's Modulus between Experiments and Analysis for Group A, Group C, and Group E 34
2.2 Comparison of the Young's Modulus between Experiments and Analysis for Group B, Group D, and Group F 35
2.3 Comparison of Kink Band Angle for Group A, Group C, and Group E 36
2.4 Comparison of Kink Band Angle for Group B Group D, and Group F 37

6.1 Crack Speed of the Composite 190

LIST OF APPENDICES

Appendix

A. Improved Speckle Method for Measuring In-Plane Displacement and Strain Fields 230

B. In-Plane Tensile Properties of Z-pin Composites 259

CHAPTER I

Introduction

1.1 Why 3D Textile Composites?

Polymer composite materials are synthetic man-made materials that contain two or more materials to make a third material, specifically tailored to achieve some function that is (hopefully) better than that which could be performed by the individual constituents. There are many types of composite material in use today.

Composite materials have been in existence in nature for a long time. After second World War II, as technology advanced, fiber reinforced polymer composites emerged as a substitute for traditional materials, such as aluminum and steel. For the past four decades, composites have been widely used in the aerospace and automobile industry for various reasons, such as ease of production, reduced-weight, high-strength, high resistance to fatigue and so on. Pre-preg based continuous fiber composites were first widely used as structural components in the aerospace industry. A serious disadvantage of using pre-preg composites is that the manufacturing process is expensive. The manufacturing processes, such as wet hand lay-up and autoclave curing require high skilled labor for production. In manufacturing some components of aircraft structures, more than 50 plies of carbon/epoxy pre-peg tape must be processed individually. Amongst the many types of composites, polymer matrix based textile fiber composites (TFC) prove to be the most attractive and cost effective due to ease of manufacturing as compared to pre-preg based continuous fiber tape composites or laminates. A detailed introduction to TFCs can be found in [14]. Even though the cost is reduced by use of TFCs, 2D textile composites still suffer from disadvantages that pre-peg composites have, such as sensitivity to impact loads which can lower the performance of composite structures due to lack of through-the-thickness strength. The low through-the-thickness strength is dictated by the interfacial strength between the polymer matrix and the fiber tows. One effective way to improve through-the-thickness strength is to use special resins, such as rubber toughened resins. However, the manufacturing process of these resin may be expensive. Another way to improve through-the-thickness properties is by inserting reinforcement in the through-the-thickness direction, such as by stitching, Z-pin insertion, or by using 3D textile composites. Previous investigations have showed that stitched joint performance is superior to traditional joints such as by adhesive bonding and co-curing in [55] and [60].

The commonly used TFCs are woven composites, knitted composites, stitched composites, and braided composites depending upon the application. These textile composites can be used as a structural unit (2D) to assemble a large structure or they can be manufactured directly as a 3D structure by changing the equipment for manufacturing 2D structural units. For example, woven composites can be produced as one lamina and then stacked together as a composite laminate as show in Figure 1.1 and Figure 1.3.

Whether composite units are assembled to a large structure or used as a stack of composite laminates, lack of strength of the interface between the different laminae is always an issue and challenge that affects the performance of the entire structure.

Adhesives are used to assemble different parts of a composite structure, unlike welding which is used to assemble different parts of a metal. There have been many researchers [57], [33], and [3] that have discussed the performance of structures that have been bonded using different adhesives. Even though improving the adhesives can increase the strength of the interface, interface failure is still a dominant failure mode that limits the performance of a structure. Thus, 3D composites are produced in order to improve through-the-thickness properties to provide more toughness and strength against impact and fracture.

3D composites were originally developed in 1970s, but it has only been in the last 15-20 years that major progress has been made to develop these materials to a commercial level. The factors propelling mankind to develop advanced “3D materials” include lower manufacturing costs, improved material quality, high through-thickness properties, superior delamination resistance, better impact damage resistance, and better post-impact mechanical properties compared to conventional laminated composites. Almost all engineering load bearing applications require high stiffness, high strength, and improved fatigue resistance.

3D woven composites, 3D knitted composites, 3D braided composites, 3D stitched composites, and 3D Z-pin composites are the commonly seen composites. Among these 3D composites, stitched composites have been developed for almost two decades and Z-pin composite are a relatively new type of 3D composite. The potential of 3D Z-pinned composites is still being evaluated. A comprehensive overview of 3D composites is provided in [56]

Z-pinning technology was developed by Aztex Inc. in 1990s. The technology involves embedding small pins, known as Z-fibers, into composites to produce reinforcement to a 3D stack of lamina, as schematically shown in Figure 1.2. The pins are inserted with a method known as Ultrasonically Assisted Z-fiber process. Undoubtedly, some damage might arise during the Z-pinning process. Whether the damage due to Z-pinning would affect the performance of the structural unit is of great concerns. Researches in [21] indicated that the Young's modulus decreases 7% to 10% by adding 2% density of Z-pins. In other work described in [19], [18], and [17], it is shown that the Young's modulus has a trend to degrade with the increase of Z-pin density and the value of Young's modulus doesn't change appreciably when the density of Z-pins is less than 1.5%. However, the Young's modulus can degrade by as much as 30% when the density of Z-pins is up to 10%, [53]. In [39], pure compression and combination of compression with shear deformation is considered. It is concluded that adding the shear dramatically decreases the strength of the Z-pin composites. The flexural properties of Z-pin carbon/epoxy laminates are investigated in [9]. It is pointed out that flexural strength decreases as Z-pin density increases but flexural stiffness doesn't change when Z-pin density changes. Both fiber distortion and damage are found in the specimens used in the tests. A beam model for dynamic delamination of through-the-thickness reinforced laminates is proposed in [52], the through-the-thickness reinforcement considerably enhances the delamination resistance for small crack velocities. At higher velocities, the kinetic energy term dominates the overall response and the effect of the reinforcement on the delamination resistance is insignificant. A one dimensional model is derived in [15] to account the bridging friction effect for through-the-thickness composites

1.2 Motivation for the Thesis Research

This research project is concerned with in-plane response and failure of Z-pin plain weave textile fiber composite panels. The motivation for this research stems from the recent increase in the use of cost efficient, injection molded textile composites in a wide range of industrial and military applications. In particular, the goal of the light weight armor program of the US army is to develop appropriate textile composites for the armor body. Z-pin composites have resulted in an increase in the interlaminar fracture toughness and impact resistance, and are regarded as potential structural materials for the armor body. However, a question remains as to whether Z-pinning can be detrimental to the in-plane properties of the composites.

The primary objective of this thesis is to systematically investigate the Z-pin effect on the in-plane stiffness and strength of woven composites in compression, tension, and transverse loading. While mode I interlaminar fracture of Z-pin composites have been studied extensively before [8], [64], and [16], the mode II interlaminar fracture of Z-pin laminates has only been explored by a few researchers. Therefore, the effect of Z-pins on both the static and dynamic mode II fracture toughness will also be investigated. This mode of failure is triggered by transverse loading.

Several aspects of Z-pinning will be studied. For a fixed diameter, the effect of Z-pin density on two types of laminates will be investigated. Table1.1 shows the types of laminates, the Z-pin size, and the Z-pin densities that are studied in this thesis, while Figure 1.3 provides an overview of the different length scales in the laminates that are investigated. This figures shows that a laminated, woven textile composite has many length scales, starting from the fiber/matrix scale within tows to the lamina scale and finally to the laminate as a collection of stacked laminae.

In order to apply composites to load bearing situations, reliable design methods and models have to be used during the initial and final design stages. Classical composite laminated theory treats composite structures as two-dimensional homogeneous and anisotropic laminates. In a laminated structure level, this is an effective way to predict the performance before failure occurs. Failure criteria, such as the Tsai-Wu failure criteria [29], are used to predict the onset of failure of pre-peg laminates. However, traditional design methods are not suitable for textile composites because fibers are clustered as tows and these tows undulate in the plane of the laminate. Thus, it is not valid to assume that the lamina is homogeneous unless the geometry is indirectly accounted for. It has been shown that many experimental results on simple coupon tests reveal that material failure mechanisms at the microstructural level, such as tow buckling, matrix cracking and matrix inelasticity are the initiating mechanisms of failure of textile composites [41]. Since the textile architecture is repeating, one can identify a representative unit cell, based on the repeating geometry to represent the composite structure. A necessity exists to develop a means of measuring the strength of textile structures at the representative unit cell (RUC) level. The first step for designing textile composites for structural application is to identify the stiffness of the structure. Two commonly used approaches are simplified analytical method [28], [36], [37], and [24] and the finite element method [59]. The microstructure in a textile composite can be idealized as consisting of fiber tows and matrix. When geometry and volume fraction of the fiber tows are identified, the effective stiffness provided by the fiber tows can be obtained.

In the literature, most of the researchers used one unit cell and periodic boundary conditions to perform simulations. This is an efficient way to do simulations if the mechanical behavior in each unit cell repeats itself. As shown in the scanning electron micrograph (SEM) images within a fiber tow, Figure 1.4 shows numerous similar RUC in a fiber tow. The RUC of a fiber tow is indicated in Figure 1.3. Therefore, it is reasonable to assume that each representative unit cell behaves similarly. However, this assumption is only valid to extract stiffness. When failure starts to occur, periodic boundary conditions at RUC boundaries will be violated, thus other means are needed to study failure mechanism and predict strength. It is therefore the goal of this thesis to investigate the difference between one RUC and multi RUC representations of the entire composite for studying stiffness and predicting strength.

Microstructures of one layer lamina are used extensively to perform simulations. Mosaic methods are used to homogenize the microstructure and the homogenized parameter are used to represent the whole layer of the lamina. In mosaic method, each lamina in woven composites is simplified as an asymmetric cross-ply laminate [27]. Mosaic method is good for predicting stiffness but is not good for predicting the strength and especially the post-peak behavior of the composites. Therefore, it is the goal of this thesis to develop an appropriate numerical model to predict the strength of a multi-layer woven, Z-pinned composite. As indicated in Figure 1.1 and Figure 1.3, when woven lamina are stacked together to create a multilayer laminate, consolidation of the layers within the mold leads to a shift in the position of the laminae with respect to each other. Thus, this leads to a phase shift in the undulation of the stacked layers. Therefore, the difference of phase angle between laminae when stacked together as laminates can also be investigated by use of multi-layer models.

Digital image correlation is an optical method that has received a lot of attention because of ease in application and its ability to extract inhomogeneous deformation which is commonly found in composites. By use of strain gages, only the deformation of some points at which the strain gages are attached can be measured. In the literature, there are many ways to process the data from the digital images. The first method is to process the data in the spatial domain and the second is to process the data in the frequency domain. An algorithm in the frequency domain of digital image correlation is developed to monitor the inhomogeneous deformation during loading. Results from this work showed that Z-pins can introduce local inhomogeneity in the deformation field. This aspect is discussed in Appendix A of the thesis.

1.3 Outline of Thesis

In chapter 2, the results obtained from numerous compression loading experiments are reported. Coupon level compressive tests based upon different Z-pin density and different Z-pin diameter were performed. Specimens used in this thesis are categorized into 6 groups. Group A, group C, and group E have a $[45/-45/0/90]_{2s}$ lay-up, with Z-pin diameters of 0.5080 mm (0.02 in.), 0.2794 mm (0.011 in.), and no Z-pin, respectively. Group B, group D, and group F are $[0]_{16}$ lay-ups with Z-pin diameter of 0.5080 mm (0.02 in.), 0.2794 mm (0.011 in.), and no Z-pin, respectively. It is to be noted that group A, group C, and group E are quasi-isotropic composites while group B, group D, and group F are cross-ply composites. From group A to group D, each group is further sub-divided into three subgroups based on the Z-pin density (1%, 2%, or 3%). Detailed descriptions of these 6 groups are summarized in Table 1.1. Before tests, the microstructural geometry of a RUC in a lamina is identified. From the geometry, the volume fraction of matrix and fiber tows can be captured, respectively. The SEM image of fiber tows similar to the one shown in Figure 1.4 can be observed to consist of numerous fibers and matrix. Therefore, volume fraction of matrix and fiber within fiber tow can be obtained. The information of volume fraction of matrix and fiber is used as input to a transversely isotropic representation of a fiber tow, as will be discussed in chapter 3. The failed specimens were examined under a SEM to identify corresponding failure mechanisms. Based on geometry and material properties, an analytical method is developed to predict the stiffness of Z-pin composites. In the analytical model, the fiber tow is assumed to undulate like a sinusoidal curve. Experimental results in chapter 2 show that initial cracks between the Z-pin and its surrounding matrix may have an effect on in-plane strength and stiffness.

In chapter 3, in-plane 2D models based upon Z-pin density and Z-pin diameter are established to perform a thorough investigation of the effect of a Z-pin on reducing the strength of tows. The effect of initial imperfections on the compressive strength will be studied first. These are followed by simulations based upon different Z-pin density and Z-pin diameter. These models successfully capture the failure mechanisms of Z-pin composites close to the Z-pin as observed in experiments.

In chapter 4, a 2D multi-layer model is presented to study the effect of phase difference on the response of the composites subjected to compression. This 16 layer model is proposed based on the experimental finding that the failure plane is independent of the transverse direction. This 16 layer numerical model is based upon a typical cross section as observed under a Nikon D2 Camera. The other ideal 16 layer numerical models with no phase difference are also studied.

A detailed study of a fully 3D, multi-layer and multi-unit cell representation of a

3D Z-pinned composite is presented in chapter 5. Multi-RUC models consisting of 4, 9, 16, and 25 cell representations are used to simulate compression response. In each of the cases, multi-layer representation of the composites are studied in order to determine the smallest number of layers that are needed to adequately capture the response observed in experiments. The results from these simulations suggest that a 3 layer representation of the Z-pinned composite, with 16 RUC, is capable of resolving all the important features of the compression response.

Results from mode II static and dynamic fracture experiments and associated numerical simulations are presented in chapter 6. A discrete cohesive zone element is used to simulate results from the experiments. A triangular cohesive law is adopted to account for the interlaminar traction-separation relation for the no Z-pin composites and a trapezoidal cohesive law is used to simulate Z-pin composites. The higher density of Z-pin composite greatly increases the fracture toughness compared to the unpinned composites. It is also concluded that the strength of $[45/-45/0/90]_{2s}$ composites and $[0]_{16}$ composites are similar, provided the Z-pin density and Z-pin diameter are fixed. Additionally, a novel crack advance gage (CAG) is introduced in order to detect the onset of fracture when the crack starts to propagate. In the dynamic fracture test, conductive silver paint is placed near the path of the crack and a strain gage is used to connect the silver paint line in series with the strain gage to a Wheatstone bridge circuit. Before the crack starts, the voltage of the crack advance gage (CAG) is zero. Upon cracking, the silver paint line gets torn apart suddenly and leads to an abrupt increase in the output voltage. When the line is completely broken, the voltages reaches a maximum of 12V. This sudden change in the output signal is used to trigger a high-speed camera at the initiation of crack advance. By placing crack advance gages (CAG) at different locations, the speed of the crack can be detected. The experiments show that the crack propagation speed scales with the Z-pin density, leading to slower speeds with increase in Z-pin density.

Chapter 7 summarizes the major contributions of the thesis and directions for future research.

Appendix A introduces the digital image correlation technique developed and used in the experiments primarily to investigate the post failure behavior. This technique is based on concepts of speckle photography. The intensity of the images taken are transformed by use of the discrete Fourier transform. The derived algorithm is then verified by use of numerical examples, including stretch, rigid body translation, and rigid body rotation. Results from strain gages are used to capture the predictions of the speckle method.

Appendix B includes experimental results from tensile tests. The results show a similar trend to that obtained in compressive tests. That is, the strength of Z-pin composites decreases as Z-pin density increases when the Z-pin diameter is fixed. In addition, the strength of Z-pin composites decreases as Z-pin diameter decreases for fixed Z-pin density.

1.4 Original Contribution of this Thesis

(1) A set of in-plane compression response experiments that examine the effect of Z-pin density and Z-pin size on compression strength and stiffness is an original contribution in this work.

(2) The development of a new model for kink band initiation and growth, which links the axial compression strength of fiber tows in Z-pin textile composites is novel.

(3) The effect of stacking and the resulting phase difference among layers and its effect on compression strength of Z-pin composites investigated through the implementation of 2D and 3D numerical simulations is a novel contribution.

(4) The increase in static and dynamic mode II fracture toughness, as a function of Z-pin density and Z-pin size of Z-pin composites obtained experimentally and explained through the use of a cohesive zone model (static) is an original contribution.

Table 1.1: Details of the 6 Groups of Composites Investigated

Type	Description	Size	Quantity
A	UAZ-T6B-0.02-1%	15"by15"	1
A	UAZ-T6B-0.02-2%	15"by15"	1
A	UAZ-T6B-0.02-3%	15"by15"	1
B	UAZ-T6B-0.02-1%	15"by15"	1
B	UAZ-T6B-0.02-2%	15"by15"	1
B	UAZ-T6B-0.02-3%	15"by15"	1
C	UAZ-T3B-0.011-1%	15"by15"	1
C	UAZ-T3B-0.011-2%	15"by15"	1
C	UAZ-T3B-0.011-3%	15"by15"	1
D	UAZ-T3B-0.011-1%	15"by15"	1
D	UAZ-T3B-0.011-2%	15"by15"	1
D	UAZ-T3B-0.011-3%	15"by15"	1
E	No-Zpins	15"by15"	1
F	No-Zpins	15"by15"	1

Type A:$[45/-45/0/90]_{2s}$
Type B:$[0]_{16}$
Type C:$[45/-45/0/90]_{2s}$
Type D:$[0]_{16}$
Type E:$[45/-45/0/90]_{2s}$
Type F:$[0]_{16}$

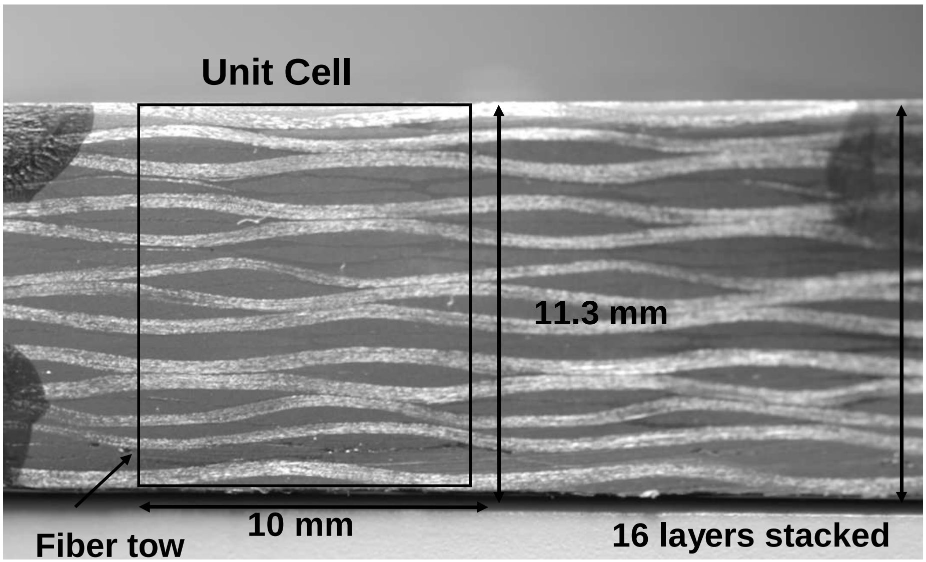

Figure 1.1: The Side View of a Representative Unit Cell of a Laminated Multi-layer Woven Composite

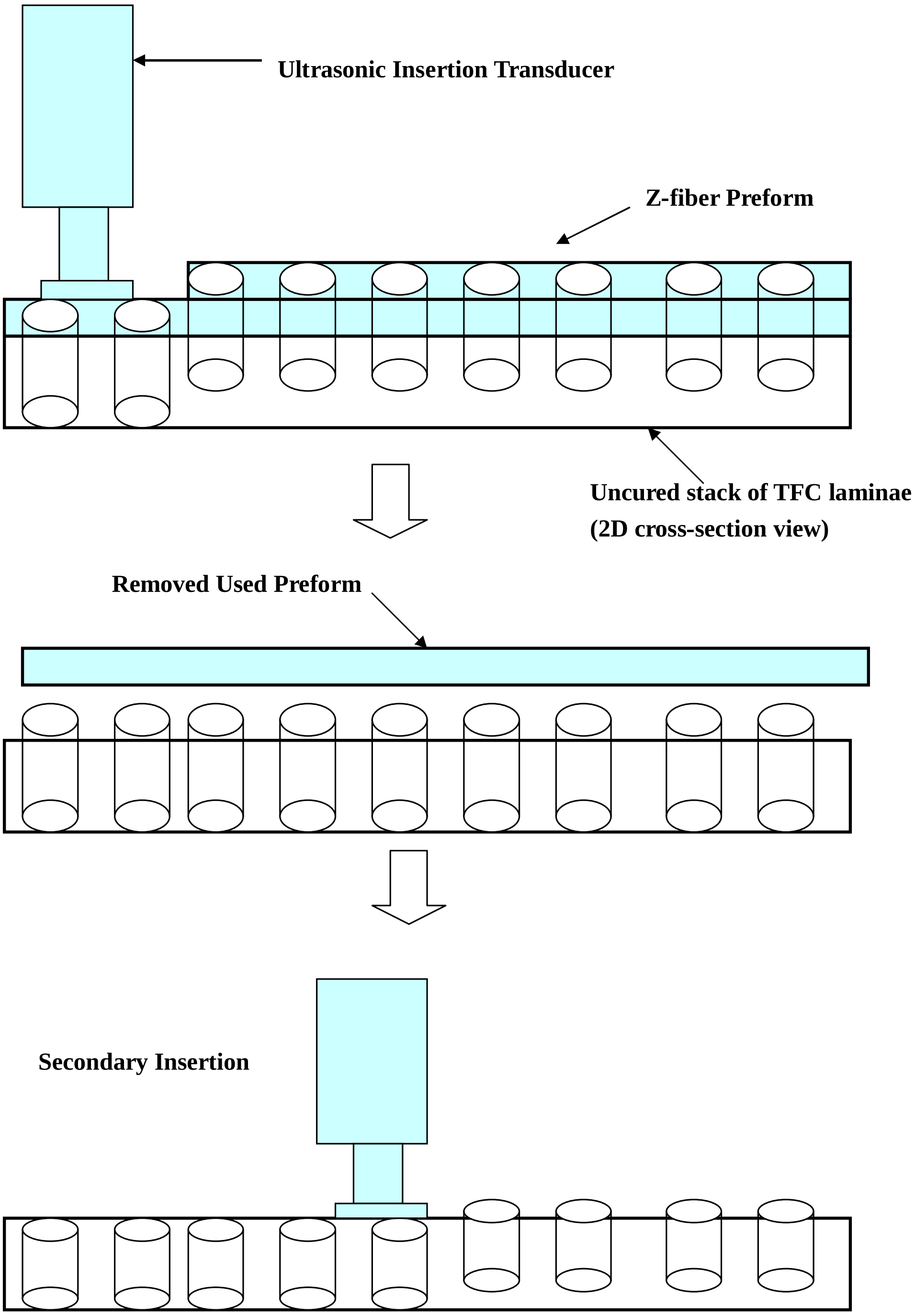

Figure 1.2: Schematic of the Z-pin Process (2D Side View)

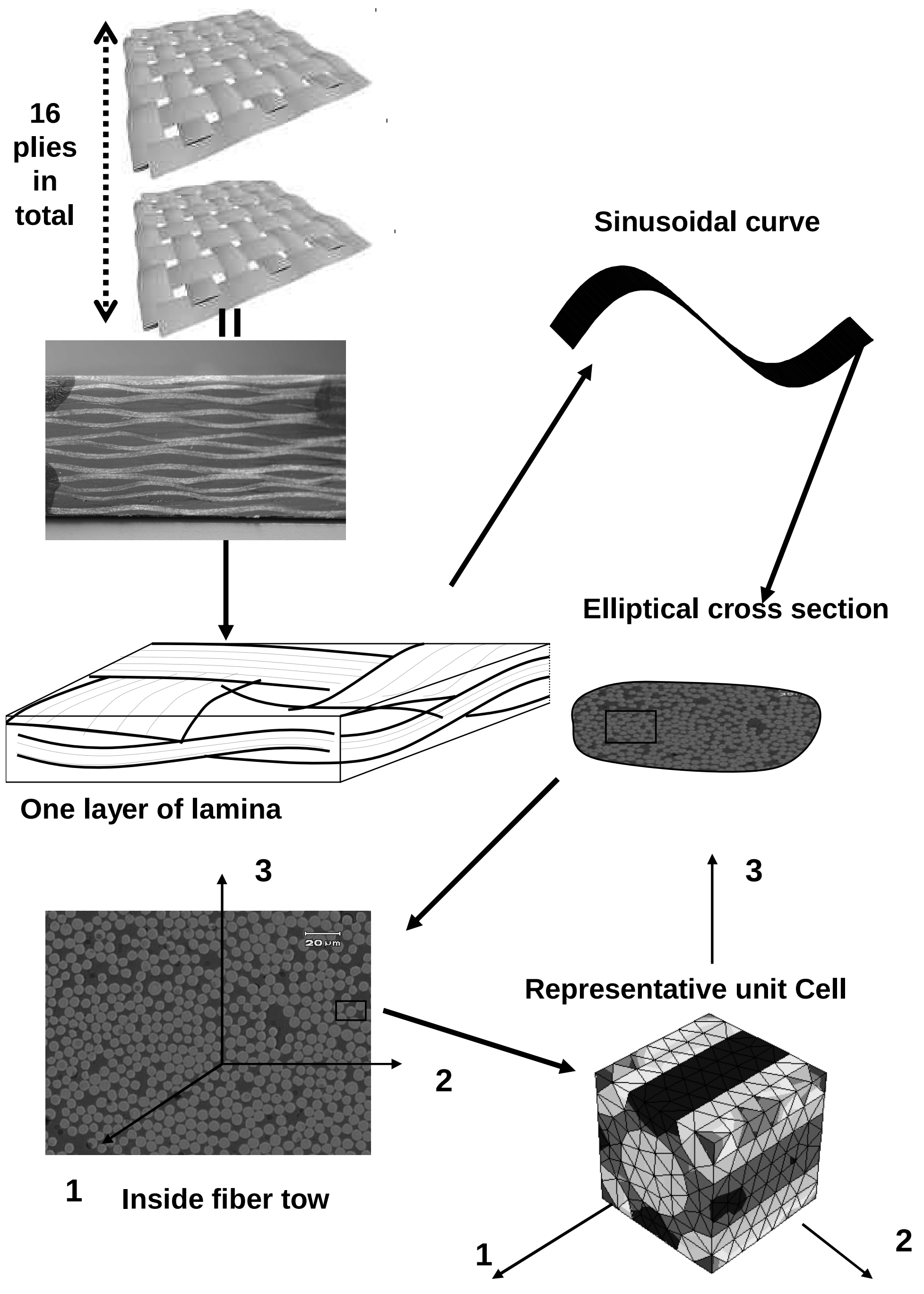

Figure 1.3: Different Hierarchy in a Multi-layered Woven Composite

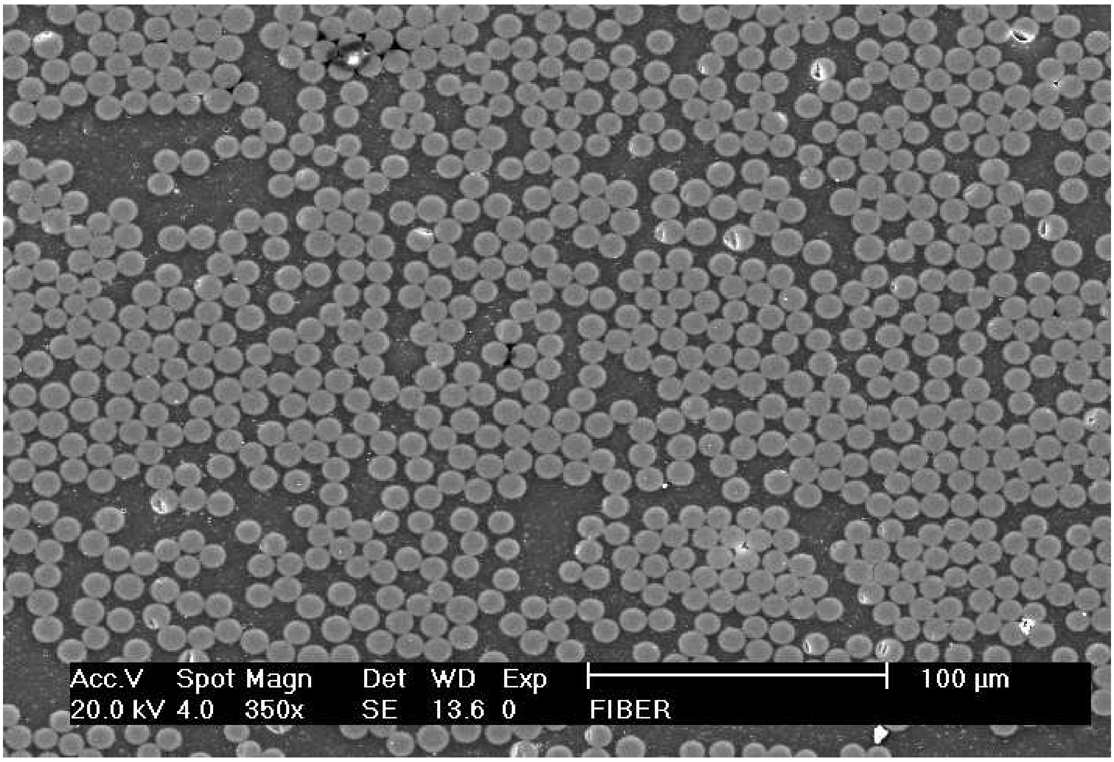

Figure 1.4: Scanning Electron Microscope (SEM) Image of a Fiber Tow Cross Section

CHAPTER II

Compressive Response and Failure of Z-pin Composites

In this chapter, experimental results pertaining to the compressive response and failure of Z-pin S-Glass fiber plain weave composites are presented. These experiments are motivated by a need to know the effect of Z-pinning on the strength and stiffness of these composites. A series of experiments are performed based upon density of the Z-pins and the diameter of the Z-pins. It is concluded that the fiber distortion and the damage zone around a Z-pin may play an important role in influencing the strength of the Z-pin composites. Before the experiments were performed, the geometry of the composite microstructure was probed using images from a scanning electron microscope (SEM). A representative unit cell (RUC) for these composites is also identified. This cell consists of matrix and fiber tows. The fiber tows are composed of fiber and matrix. The volume fraction of fiber and matrix in a fiber tow is obtained from SEM images of the fiber tow cross section. These data are then used for subsequent numerical simulations that are presented in later chapters. The failed specimens are also investigated under a SEM in order to accurately identify failure mechanisms.

2.1 Introduction

Delamination resistance of layered textile composites can be improved by Z-pinning. Evidence of such improvements are discussed in [46], [8], and [16]. While improvement in out of plane strength is desired, a simultaneous degradation (or improvement) in in-plane response remains to be systematically explored. In this chapter, results for the in-plane compression response of Z-pin S2-Glass fiber plain weave composites are presented. For a fixed Z-pin diameter, the effect of Z-pin density is examined for two different Z-pin diameters. Two types of stacking are examined. One is a quasi-isotropic lay-up, while the other is a cross-ply lay-up, from the terminology for laminated straight fiber reinforced composites. The failure mechanism in all cases is found to be kink banding within the axial tows, which can be found in all of the failed specimens. Initially, the composites shows a linear load-load point displacement response (P-Δ). The linear region is culminated at a maximum load that is associated with the loss of load carrying capacity of the axial fiber tows. When the specimens fail, the failure region appears as a localized band that runs across the specimens.

2.2 Details of Z-pin Composite Materials

Plain weave S2 Glass fabrics are sized, Z-pinned and infused with epoxy resin to make two types of laminated textile composites (see Figure 1.2 and Figure 1.3 for an overview). The glass fiber tows contain 9k fibers with a nominal fiber volume fraction of 52%. Measurements indicate a mean major tow diameter of (a)4.4 mm and a mean minor tow diameter of (b) 0.4 mm in the cured state. That is, the fiber tows are very close to being elliptical in shape. The standard deviation in (a) is 0.214 mm and in (b) is 0.0135 mm (based on 40 SEM images). The Z-pins are two types. The larger diameter Z-pin is a T650 carbon fiber in a BMI matrix, while the smaller diameter Z-pin is a T300 carbon fiber in a BMI matrix . The height of the stacked 16 layer laminates is from 11 mm to 13 mm thick. Specimens are categorized into 6 groups. Group A, group C, and group E are $[45/\text{-}45/0/90]_{2s}$ lay-ups, with Z-pin diameters of 0.5080 mm (0.02 in.), 0.2794 mm (0.011 in.), and no Z-pin, respectively. Group B, group D, and group F are $[0]_{16}$ lay-ups with Z-pin diameter of 0.5080 mm (0.02 in.), 0.2794 mm (0.011 in.), and no Z-pin, respectively. It is to be noted that group A, group C, and group E are quasi-isotropic composites while group B, group D, and group F are cross-ply composites. From group A to group D, each group is further sub-divided into three subgroups based on the Z-pin density (1%, 2%, or 3%). Detailed descriptions of these 6 groups were given in Table 1.1.

2.2.1 Compressive Loading Apparatus

Compressive tests were performed on a servo-hydraulic MTS machine. An image of the experimental setup is shown in Figure 2.1. The specimen support fixture is shown in Figure 2.2. In order to obtain the compressive strength of the material, the specimen is prevented from global buckling by using anti-buckling guides (knife edge supports that allow in-plane sliding and out-of-plane rotation, but constraints out-of-plane deflection) as indicated in a top-view image of the support fixture. The front view and back view of a typical specimen is as shown in Figure 2.3 and Figure 2.4. The width of the specimen is 63.5 mm (2.5 in.) and the height of the specimen is 50.8 mm (2 in.). The thickness of the specimens ranges from 11.0 mm (0.436 in.) to 13.0 mm (0.512 in.). For each experiment, two strain gages were attached to the specimen (back to back) aligned with the loading direction and one in the transverse direction on one side. The purpose of using two strain gages in the loading direction is to monitor any unwanted bending that may occur during the compression loading. In addition to these deformation diagnostics, one surface of the specimen was illuminated with a He-Ne laser red light with wavelength 632.9 nm that generated a speckle image. The speckle images were collected through a Nikon D2X digital camera for later analysis using a speckle photography method. Speckle maps were used to calculate incremental strain fields as a function of load and they were also used (averaging over a suitable area) to compare against the strain gage results.

2.2.2 Experimental Procedure

In a compressive test, the specimen is placed within the grip as shown in Figure 2.2. A small pre-load 1336 N (300 lbf.) is imposed on the specimen and all strain gages are zeroed at this state. A high resolution digital camera is positioned to capture speckle images from a pre-defined area on the specimen at a rate of one frame per four seconds. The strain gage readings and the load cell readings are acquired at 4Hz, while the axial cross-head movement rate imposed on the specimen is 0.010 mm/sec.

2.2.3 Compressive Stiffness

Figure 2.5 shows a typical load-strain curve obtained from a compression test. Here, the horizontal axis corresponds to average axial strain (the average of the back to back strain gages). Notice that the response is fairly linear up to the maximum load point (‘B’ in Figure 2.5), after which the load suddenly drops due to the “band of cells” that fail leading to a localization of the deformation. Here, note that at A, the response deviates from being strictly linear. This aspect will be discussed in the context of numerical results to be presented later.

Figure 2.6 shows a comparison of the slope of the axial stress (defined as load divided by nominal cross-sectional area) - axial strain (averaged between the two back to back axial strain gages) curves, between group A and group E. This measure corresponds to the axial Young's modulus of the specimen. Figure 2.7 shows a comparison of the Young's moduli between group B and group F. The horizontal axis represents density of the Z-pins and the vertical axis represents the corresponding Young's modulus. Figure 2.8 and Figure 2.9 show the comparison of group C and group D with the corresponding no Z-pin composites group. For group A and C, the Young's modulus decreases as the density of the Z-pins increases. However, the decrease of the Young's modulus is not significant. This is consistent with the conclusion in [21] that the Young's modulus decreases 7% to 10% by adding 2% density of Z-pins. In other work described in [19], [18], and [17], it is shown that the Young's modulus has a trend to degrade with the increase of Z-pin density and the value of Young's modulus doesn't change appreciably when the density of Z-pins is less than 1.5%. However, the Young's modulus can degrade by as much as 30% when the density of Z-pins is up to 10% [53]. Comparing Figure 2.6 with Figure 2.8 for the subgroup of the same density of Z-pins, say 1%, we can observe that the Young's modulus in group A is slightly higher than that in group C. This can be understood as follows: After insertion of the Z-pins, the Z-pins in subgroup C have a larger contacting area with the surrounding glass fiber tows in the composite than the corresponding contacting area in subgroup A. A larger contacting area leads to a larger probability of the presence of initial interfacial cracks as well as a larger probability of unintended tow undulations, thus inducing stress and strain concentration and resulting lowering of the axial stiffness.

Furthermore, the undulations lead to lowering of the compression strength caused by fiber tow kinking. A further explanation is as follows: for composites with the same Z-pin density, each Z-pin of diameter 0.508 mm (0.02 in.) inserted in the composites can be“replaced” by four Z-pins of diameter 0.254 mm (0.01 in.) Z-pins as shown in Figure 2.10. Suppose that the height of the composite is h. Then, the contacting area in the through-the thickness direction around one Z-pin of diameter d=0.508 mm (0.02 in.) is 0.508 πd. The contacting area around the four d=0.2540 mm (0.01 in.) in Z-pins is 0.2540πd$\times$4=1.016πd. This shows that the smaller diameter Z-pin has a larger “contacting area” than a Z-pin with d=0.5080 mm (0.02 in.) provided that the density of the Z-pins is the same. Under this circumstance, it is likely that, in the composites of d=0.254 mm (0.01 in.), more damage is probable during the insertion of the Z-pins. Figure 2.11 shows scanning electron microscope (SEM) images of a d=0.508 mm (0.02 in.) Z-pin composite and a d=0.2794 mm (0.011 in.) Z-pin composite, respectively. Both of these images were taken from as manufactured plaques prior to conducting compression experiments. The monitored image plane (xy) is cut at the center of the thickness as shown in Figure 2.11. These images show that Z-pin insertion and subsequent cure leads to interfacial damage and an interfacial crack can be seen at the circumferential boundary of the Z-pin, although such damage is not observed at every Z-pin location. Therefore, in a given area, as the number of Z-pins increases, the resulting “initial damage” is also larger. This can explain why a 3% Z-pin composite has slightly lower Young’s modulus than the 1% or 2% Z-pin composite.

Similar trends for the variation of the Young’s modulus in group B and group D are found (similar to group A and group C except that, initially, the Young’s modulus of the 1% composites is slightly larger than the composites without Z-pins). The Young's modulus in subgroup 2% and 3% degrades slightly for both group B and group D. Comparing Figure 2.7 corresponding to group B with Figure 2.9 corresponding to group D for the same density of Z-pins, we can observe that the Young's modulus in subgroup B is slightly higher than that in group D. This is true for the 1%, 2%, and 3% Z-pin composites. It is to be noted that the Young's modulus for group B and group D is higher than that corresponding to group A and group C. This is because group A and group C, belonging to the $[45/-45/0/90]_{2s}$, have a smaller percentage of "0 degree tows" in comparison to group B and D which have a $[0]_{16}$ lay-up.

2.2.4 Compressive Strength

Figure 2.12 shows the comparison of the compressive strength between group A and group E. The horizontal axis represents the density of the Z-pins and vertical axis represents the compressive strength. Figure 2.13 shows the comparison of the compressive strength between group B and group F. Figure 2.14 shows the comparison of the compressive strength between group C and group E. Finally, Figure 2.15 shows the comparison of the compressive strength between group D and group F. From Figure 2.12 to Figure 2.15, it is observed that the compressive strength for group A to group D decreases as the density of Z-pins increase. For the $[45/-45/0/90]_{2s}$ composites of group A and group C, the subgroups of the composites with the same Z-pin density are compared. It is found that the strength of the subgroup in group A is higher than that of the subgroup in group C. The same trend is also observed for the comparison of group B and group D, which shows that subgroups in group B are higher in compression strength than those in group D. The reason which the strength in group A is lager than that in group C and that the strength in group B is higher than that in group D is as follows: The Z-pins in subgroups C and D have more contacting area with the glass fiber tows than that in subgroups A and B. Therefore, these subgroups contain a larger population of initial “defects” leading to a lowering of the compression strength. Exactly how defects contribute to the observed lowering of strength is explained next.

2.2.5 Compression Failure Mechanisms

Figure 2.16 and Figure 2.17 show an image of the failure pattern that is typical for most of the Z-pin composites under compression. It is noticed that all failed specimens exhibit the same pattern. That is, an out of plane macroscopic kink band can be found in the axial load bearing tows. Further examination under SEM shows that individual fiber tow kinks due to unintended initial fiber misalignment caused by Z-pin insertion. Figure 2.19 shows the kink band passing through the area around Z-pins. In these images, the direction of loading is indicated with “arrows”. These sites are location of stress (strain) concentration. It is also observed, in Figure 2.20, that a kink band formed between the two Z-pins within one specimen of group C1. In this figure, notice that one of the kink bands has been initiated from a Z-pin/fiber tow boundary. Figure 2.21 shows existence of kind bands and cracks around the Z-pins of the specimen in group A2 and group A3, respectively. These failure mechanisms are repeatedly found in all of the specimens.

The typical failure pattern for composites without Z-pins is shown in Figure 2.18. As shown before with the Z-pin composites, an out of plane macroscopic kink band can also be found. This finding presents an important clue to the observed experimental trends. While it is true that insertion of Z-pin introduces unintended defects into the composites, all specimens (including the ones that have no Z-pins) show kink banding in the axial tows, signalling that the compressive strength of these composites is controlled by the compression failure mechanics of the axial tows. The initial defects around the Z-pins are sites where the kink band initiates. If we examine the side view of a failed specimens in Figure 2.18, slight lateral expansion is noticed as opposed to the side view in Figure 2.16. This is because the Z-pins provide constraint in the through the thickness direction. Previous work has found that this through the thickness constraint is responsible for an increase in the interlaminar fracture toughness. Table 2.3 and Table 2.4 provides the kink band angle observed for the specimens of quasi-isotropic composites and cross-ply composites under compression. As can be seen from the two tables, most of the angles of kink band range from 30 degree to 45 degree.

2.3. Speckle photography Analysis

2.3.1 Comparison of Strain Gages and Speckle Method

A newly developed speckle method that is outlined in details in Appendix A was used to extract strain fields within the imaged surface are of the specimens during compression loading. Further details of the speckle method are given appendix A or in [25]. Figure 2.22 shows a comparison of the stress-strain response deduced from strain gage measurements and speckle photography for specimen C1-3 (the third experiment performed in the subgroup C1). The horizontal axis represents the strain and the vertical axis represents the stress. Two approaches are adopted to obtain the average strain, which are line average method and the area average method, respectively. Line average method first gets relative displacement between the two lines AA and BB shown in Figure 2.23. The relative strain is thus obtained from dividing the relative displacement by the distance between AA and BB. The area average method computes the strain within each sub-element. The average strain of the monitored area is the average strain obtained from the different sub-elements within the area. It is observed that the curves obtained from both methods match quite well with curve obtained from the strain gage. However, the speckle method can further resolve the strain within the monitored area.

2.3.2 Analysis near the Z-pins

Figure 2.25 and Figure 2.26 show the speckle patterns of the 2% Z-pin composites and 3% Z-pin composites in group B, respectively, near Z-pin locations. For the two tests, four speckle images corresponding to similar load are chosen, thus three incremental strain fields are obtained.

Figure 2.27, Figure 2.29, and Figure 2.31 show the surface strain of 2 % composites at three different load stages. Figure 2.28, Figure 2.30, and Figure 2.32 show the surface strain of 3 % composites at three different load stage. The surface strain field is more uniform in the 2% composites than the 3% composites if we compare Figure 2.27 and Figure 2.28. This phenomenon can also be observed if we compare Figure 2.29 and Figure 2.30 as well as Figure 2.31 and Figure 2.32. The higher density of Z-pins have influence in causing a non-uniform surface strain field of the composites than the lower density one. A better illustration of this non-uniform field is shown in Figure 2.25 where a quiver plot of the displacement field is shown. Clearly, the deformation field is influenced by the presence of the Z-pins as indicated here. This shows that the Z-pins act as sites where strain non-uniformity (at the Z-pin diameter scale) is introduced, whereas when one uses a strain gage, it is the average strain over some representative area that is needed.

2.4 A Simplified Analytical Model for Z-pin Composites

Prior to undertaking a numerical model development of the Z-pin composites, a simplified analytical model was developed to quickly extract the stiffness of the composites. The Z-pin composites are assumed to consist of Z-pin, matrix, and undulating fiber tows as shown in Figure 2.33. 40 similar images are used to evaluate the volume fraction of each constituent and the geometry of the fiber tows (assumed as elliptical cross-section sinusoidally undulating solids). A typical image is shown in Figure 2.34. It is noted that fiber tows are composed of fibers and matrix. Consequently, the volume fractions of the fibers and matrix in a fiber tow are estimated by use of these images.

2.4.1 Computation of Stiffness for Fiber Tows

Locally, fiber tows and Z-pin fibers are regarded as transversely isotropic materials. The stiffness for a transversely isotropic material with respect to material coordinate axe x-y can be written as

$$\begin{bmatrix} \sigma_{11} \\ \sigma_{22} \\ \sigma_{33} \\ \sigma_{23} \\ \sigma_{13} \\ \sigma_{12} \end{bmatrix} = \begin{bmatrix} Q_{11} & Q_{12} & Q_{12} & 0 & 0 & 0 \\ Q_{12} & Q_{22} & Q_{23} & 0 & 0 & 0 \\ Q_{12} & Q_{23} & Q_{22} & 0 & 0 & 0 \\ 0 & 0 & 0 & \frac{1}{2}(Q_{22}-Q_{23}) & 0 & 0 \\ 0 & 0 & 0 & 0 & Q_{55} & 0 \\ 0 & 0 & 0 & 0 & 0 & Q_{55} \end{bmatrix} \begin{bmatrix} \varepsilon_{11} \\ \varepsilon_{22} \\ \varepsilon_{33} \\ \varepsilon_{23} \\ \varepsilon_{13} \\ \varepsilon_{12} \end{bmatrix} \tag{2.1}$$

The stress-strain curve for an isotropic matrix with respect to material coordinate x-y can be expressed in terms of Young's modulus E_{matrix} and its poission's ratio ν_{matrix}. It is to be noted that, in the global lamina coordinate, the stiffness of the fiber tow is not the same if moving along the fiber tow as shown in Figure 2.35. Transforming the local stiffness from the local coordinate x'-y' to the global lamina coordinate x-y is necessary. The detailed derivation is presented in [44].

After we obtain stiffness for fiber tows, we are ready to establish the stiffness for the whole laminate. The stiffness of the laminate is expressed in terms of a 6×6 matrix. The fiber direction of the Z-pins is along the global Z direction. Transformation matrices are used to convert the local stiffness of Z-pin fibers to the global direction. It is to be noted that the stiffness of fiber tows, Z-pins, and matrix are all expressed as three dimensional entities, ie 6×6 matrix. Therefore, the contribution of the stiffness of each constituent after converting to global coordinate can be put into one 6×6 matrix. For quasi-isotropic composites $[45/-45/0/90]_{2s}$, transformation matrices are also imposed to transform the local stiffness of the lamina to the corresponding global laminate coordinate. Finally, the stiffness of the laminate, provided that the volume fraction for matrix, Z-pins, and fiber tows are known, is obtained as,

$$\begin{bmatrix} Q_{Lamite} \end{bmatrix} = \begin{bmatrix} Q_{fibertows} \end{bmatrix} V_{fibertows} + \begin{bmatrix} Q_{Z-pins} \end{bmatrix} V_{Z-pins} + \begin{bmatrix} Q_{matrix} \end{bmatrix} V_{matrix} \tag{2.2}$$

where $V_{fibertows}$, V_{Z-pins}, and V_{matrix} represents the volume fraction of fiber tows, Z-pins, and matrix, respectively within a representative unit of the composites. Furthermore, $V_{fibertows} + V_{Z-pins} + V_{matrix}$=1.

The details of the calculation are as follows: For the non z-pin woven laminates, it is assumed that the undulation $z(x)$ in the through-the-thickness direction of the fiber tows undulating along x axis (loading direction) and along y axis are given by

$$z(x) = a\sin(\frac{2\pi x + \phi}{\lambda}) \tag{2.3}$$

$$z(y) = a\sin(\frac{2\pi y+\phi}{\lambda}) \tag{2.4}$$

where $\lambda = 0.5cm$, a=3.6 cm, and ϕ is equal to 0 and π for two fiber tows undulating either in x-axis or y-axis. The tows are transversely isotropic S-2 glass/epoxy with a fiber volume fraction of 52%. The expression of the stiffness matrix for a fiber tows is the following:

$$Q_{Fibertow} = \begin{bmatrix} 65 & 2.75 & 2.75 & 0 & 0 & 0 \\ 2.75 & 8.8 & 2.5 & 0 & 0 & 0 \\ 2.75 & 2.5 & 8.8 & 0 & 0 & 0 \\ 0 & 0 & 0 & 3.15 & 0 & 0 \\ 0 & 0 & 0 & 0 & 4 & 0 \\ 0 & 0 & 0 & 0 & 0 & 4 \end{bmatrix} 10^9 Pa \tag{2.5}$$

Within a unit cell of the woven RVE, the volume fraction of the fiber tow is $V_{fibertows} = 56\%$. The Z-pins are transversely isotropic materials composed of the carbon fiber and BMI matrix. The stiffness of the Z-pin is the following

$$Q_{Z-pin} = \begin{bmatrix} 51.7 & 2.07 & 2.07 & 0 & 0 & 0 \\ 2.07 & 6.6 & 2.6 & 0 & 0 & 0 \\ 2.07 & 2.6 & 6.6 & 0 & 0 & 0 \\ 0 & 0 & 0 & 2.46 & 0 & 0 \\ 0 & 0 & 0 & 0 & 2.26 & 0 \\ 0 & 0 & 0 & 0 & 0 & 2.26 \end{bmatrix} 10^9 Pa \tag{2.6}$$

The stiffness of the matrix is expressed as follows

$$Q_{matrix} = \begin{bmatrix} 37.2 & 2.29 & 2.29 & 0 & 0 & 0 \\ 22.9 & 37.2 & 22.9 & 0 & 0 & 0 \\ 22.9 & 22.9 & 37.2 & 0 & 0 & 0 \\ 0 & 0 & 0 & 7.15 & 0 & 0 \\ 0 & 0 & 0 & 0 & 7.15 & 0 \\ 0 & 0 & 0 & 0 & 0 & 7.15 \end{bmatrix} 10^8 Pa \tag{2.7}$$

If the Z-pin density is %1 (ie $V_{Z-pins} = 1\%$), the volume fraction of the matrix is computed by use $V_{matrix} = 1 - V_{fibertows} - 1\% = 43\%$. These numbers are used to calculated the stiffness summarized in Table 2.1

2.4.2 Comparison of Predicted Stiffness against Experiments

Table 2.1 shows the comparison of the Young's Modulus between experiments and analysis for the non-Z-pin $[0]_{16}$ composites. It is seen that the Young's modulus obtained from the analytical model is close to that obtained from experiments. However, for Z-pin composites the predictions are lower. This is because part of the volume of the fiber tows is replaced by the through-the-thickness Z-pins. These replaced Z-pins provide additional stiffness in the through-the-thickness direction but they don't contribute much to the in-plane stiffness. This trend is also observed from the experiments. However, as opposed to the slight decrease of the Young's modulus predicted from analysis as the density of the Z-pins increases, the Young's modulus obtained from the experiments show a larger decrease with increase in Z-pin density. It is believed that the initial damage induced during the insertion of the Z-pins causes this additional decrease which is unaccounted for in the analytical model at present.

A comparison of experimental results against analysis for Quasi-isotropic composites $[45/-45/0/90]_{2s}$ is shown Table 2.2. For the composites with no Z-pins, the analysis provides a reasonable prediction. The analytical results show that the Young's modulus exhibits a decreasing trend with increasing Z-pin density. Overall, the analytical method provides a quick tool for predicting the Young's modulus of composites with no Z-pins but further refinement is necessary for providing good results for composites with Z-pins.

2.4.3 Conclusion

Important aspects of the compression response have been identified in section 2.3.1. The influence of Z-pin diameter, Z-pin density, and lay-up were all examined. Initial defects between the Z-pin and the surrounding area and unintended fiber waviness caused by Z-pin insertion have been identified as causes responsible for lowering the compression strength which is limited by fiber tow kinking, leading to macroscopic kink banding. When the Z-pin diameter is set to be the same, the higher density Z-pin composites have lower strength than the lower density Z-pin composite. When the density is set to be the same, the small diameter Z-pin composites have lower strength than the larger diameter Z-pin composites. Since all the composite specimens exhibited a similar macroscopic failure mechanism, the kink band angle (defined as θ in Figure 2.18)

A simplified analytical method proves to be reliable in predicting the initial stiffness of the no Z-pin composite. The experimental finding are further examined by developing models for the compression strength of a fiber tow (chapter 3), and the compression strength of the entire composite (chapter 4 and chapter 5).

Table 2.1: Comparison of the Young's Modulus between Experiments and Analysis for Group A, Group C, and Group E

Group	Young's Modulus(GPa) (Experiment)	Young's Modulus(GPa) (Analysis)
A1-1	15.27	18.19
A1-2	15.78	
A1-3	14.35	
A2-1	16.38	18.06
A2-2	13.67	
A2-3	14.65	
A3-1	13.78	17.93
A3-2	13.89	
A3-3	13.02	
C1-1	13.57	18.19
C1-2	13.46	
C1-3	12.11	
C2-1	11.73	18.06
C2-2	12.72	
C2-3	11.14	
C3-1	12.82	17.93
C3-2	13.22	
C3-3	10.53	
E-1	17.02	18.32
E-2	17.85	
E-3	16.5	

Table 2.2: Comparison of the Young's Modulus between Experiments and Analysis for Group B, Group D, and Group F

Group	Young's Modulus(GPa) (Experiment)	Young's Modulus(GPa) (Analysis)
B1-1	22.24	21.70
B1-2	28.15	
B1-3	24.10	
B2-1	28.45	21.53
B2-2	27.5	
B2-3	26.53	
B3-1	22.51	21.37
B3-2	25.75	
B3-3	22.89	
D1-1	27.14	21.70
D1-2	25.66	
D1-3	25.51	
D2-1	23.19	21.53
D2-2	24.23	
D2-3	22.00	
D3-1	19.98	21.37
D3-2	21.82	
D3-3	19.51	
F-1	19.05	21.86
F-2	21.2	
F-3	22.37	

Table 2.3: Comparison of Kink Band Angle for Group A, Group C, and Group E

Group	Kink Band Angle(degree)
A1-1	39.61
A1-2	29.57
A1-3	*
A2-1	37.05
A2-2	*
A2-3	*
A3-1	35.08
A3-2	35.25
A3-3	*
C1-1	35.72
C1-2	42.65
C1-3	*
C2-1	43.56
C2-2	29.80
C2-3	*
C3-1	44.15
C3-2	*
C3-3	*
E-1	29.49
E-2	*
E-3	*

The specimen with “*” indicates that the specimen has been investigate under SEM before the angle of kink band is computed.

Table 2.4: Comparison of Kink Band Angle for Group B Group D, and Group F

Group	Kink Band Angle(degree)
B1-1	44.53
B1-2	36.29
B1-3	*
B2-1	44.26
B2-2	31.86
B2-3	*
B3-1	43.61
B3-2	44.75
B3-3	*
D1-1	31.22
D1-2	23.92
D1-3	36.48
D2-1	37.22
D2-2	26.04
D2-3	*
D3-1	35.38
D3-2	*
D3-3	*
F-1	43.74
F-2	34.26
F-3	42.49

The specimen with “*” indicates that the specimen has been investigate under SEM before the angle of kink band is computed.

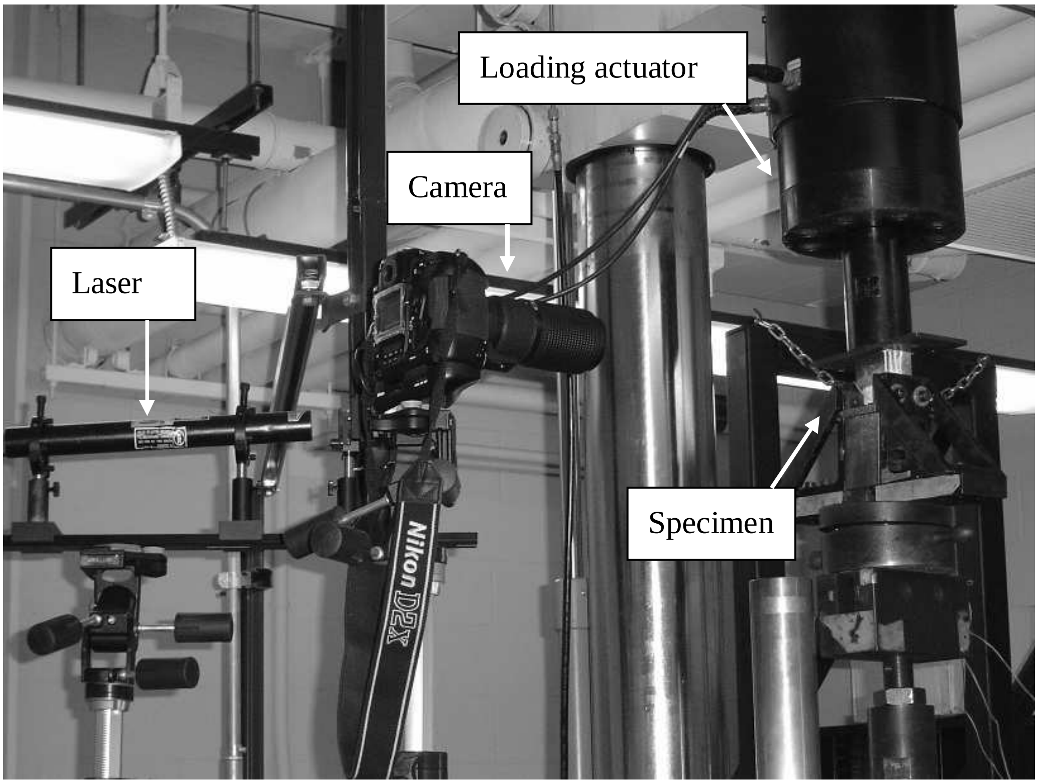

Figure 2.1: MTS Machine and Speckle Setup

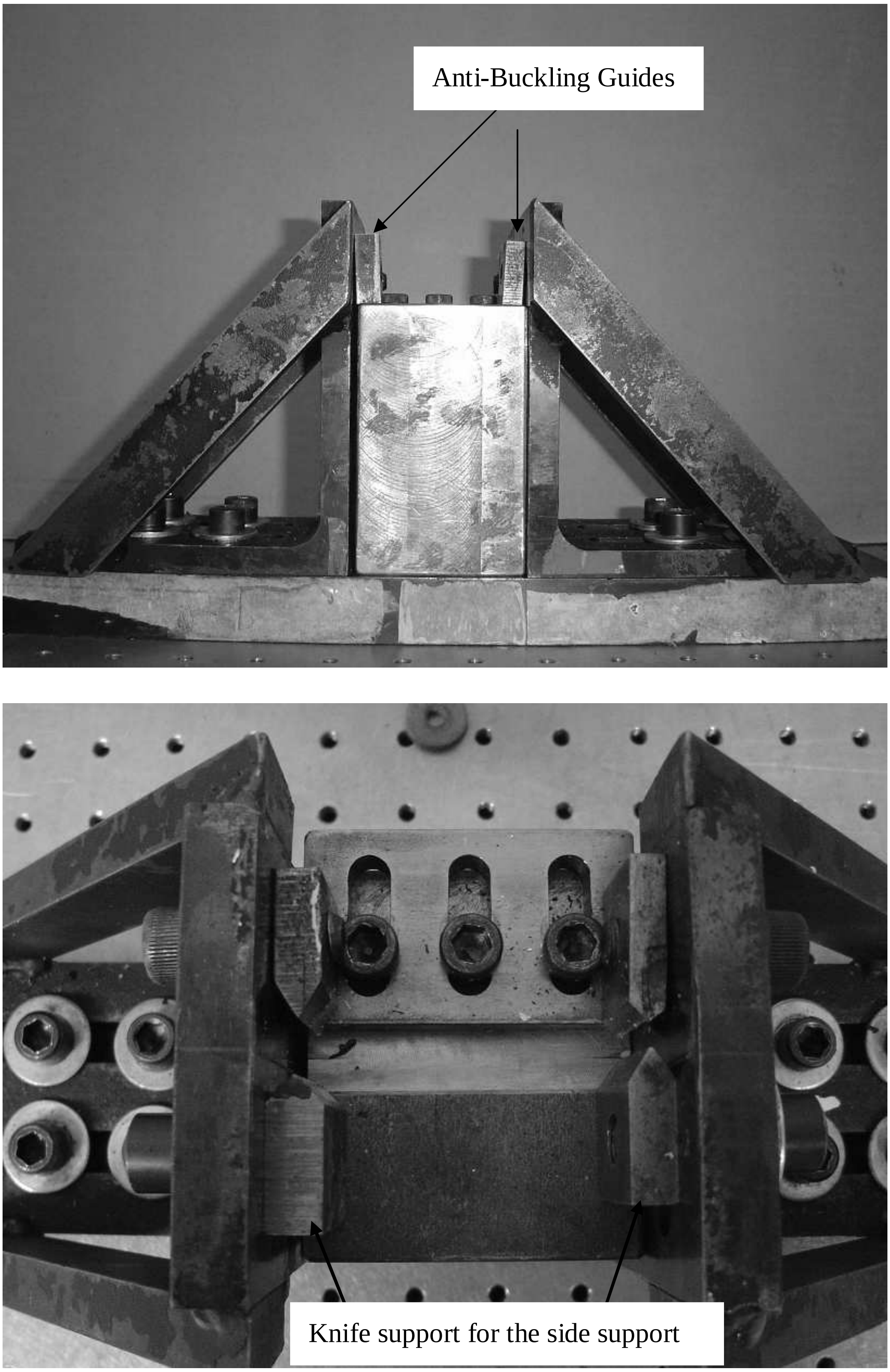

Figure 2.2: Fixture Used in the Compressive Tests

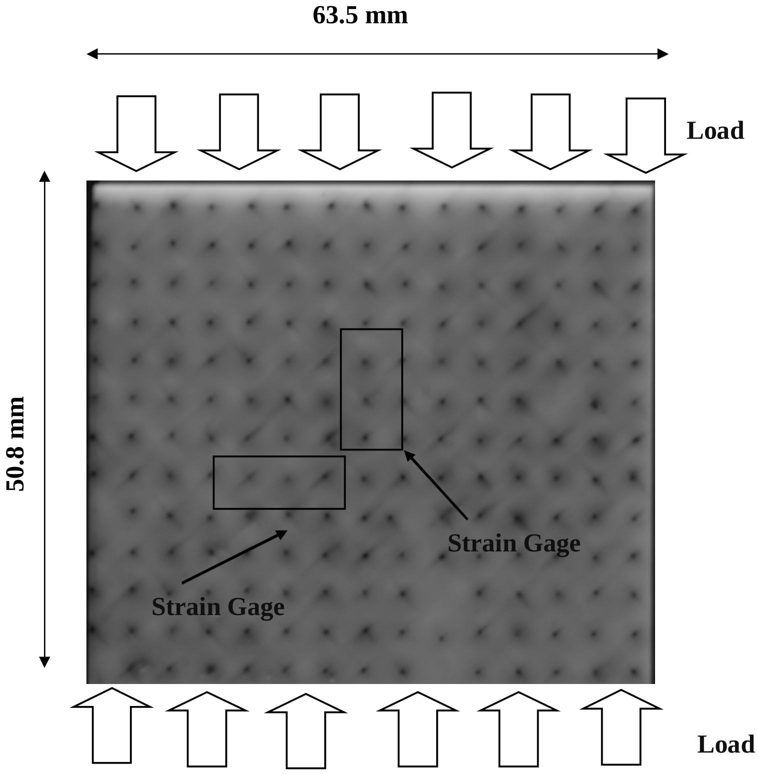

Figure 2.3: Front View of the Tested Specimen

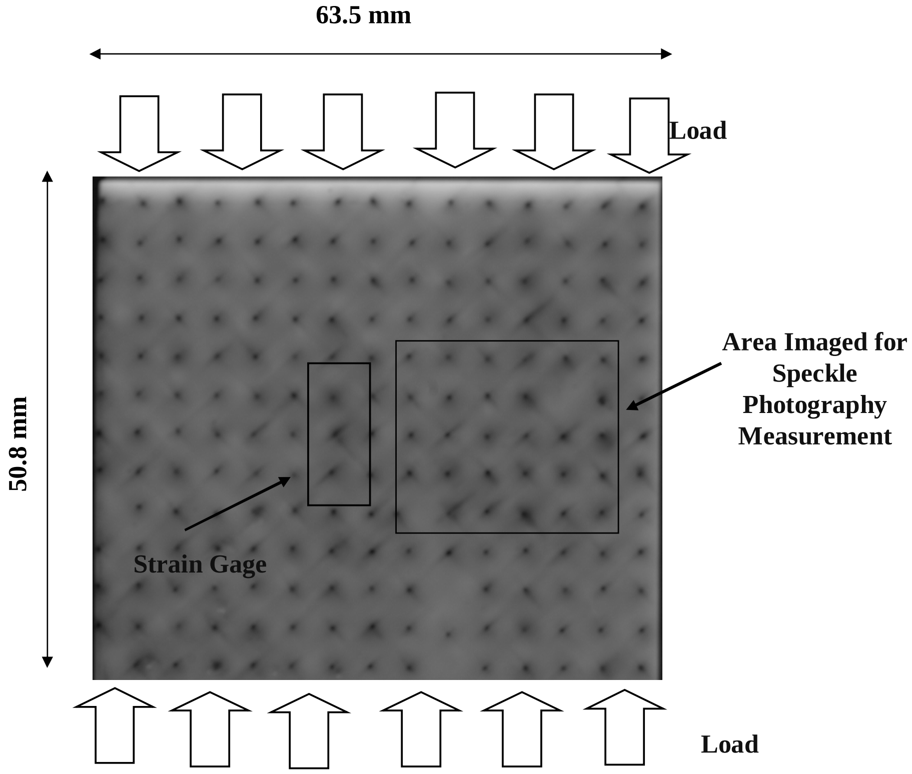

Figure 2.4: Back View of the Tested Specimen

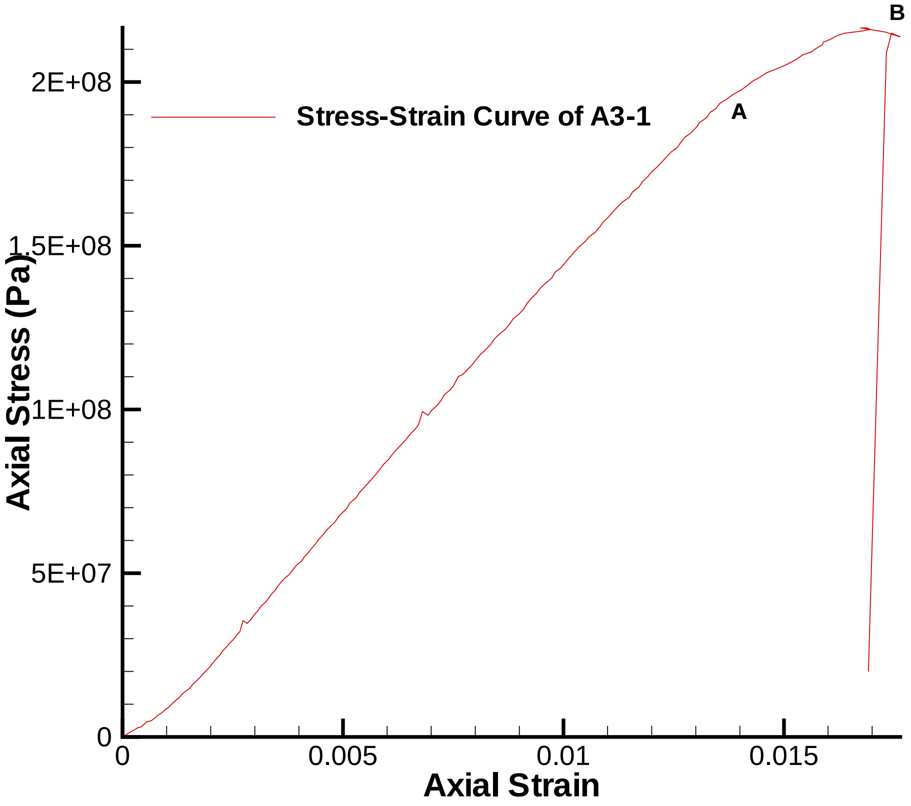

Figure 2.5: Typical Stress-Strain Curve for Compression(1%Z-pin $[45/-45/0/90]_{2s}$ Composite)

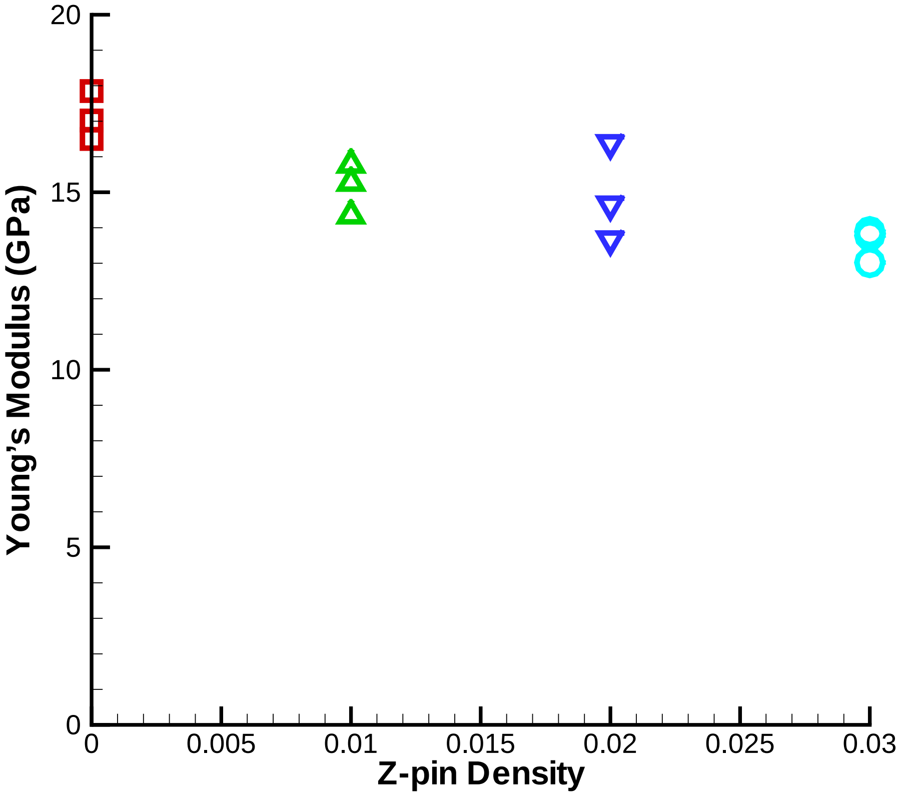

Figure 2.6: Comparison of Young's Modulus in Group A

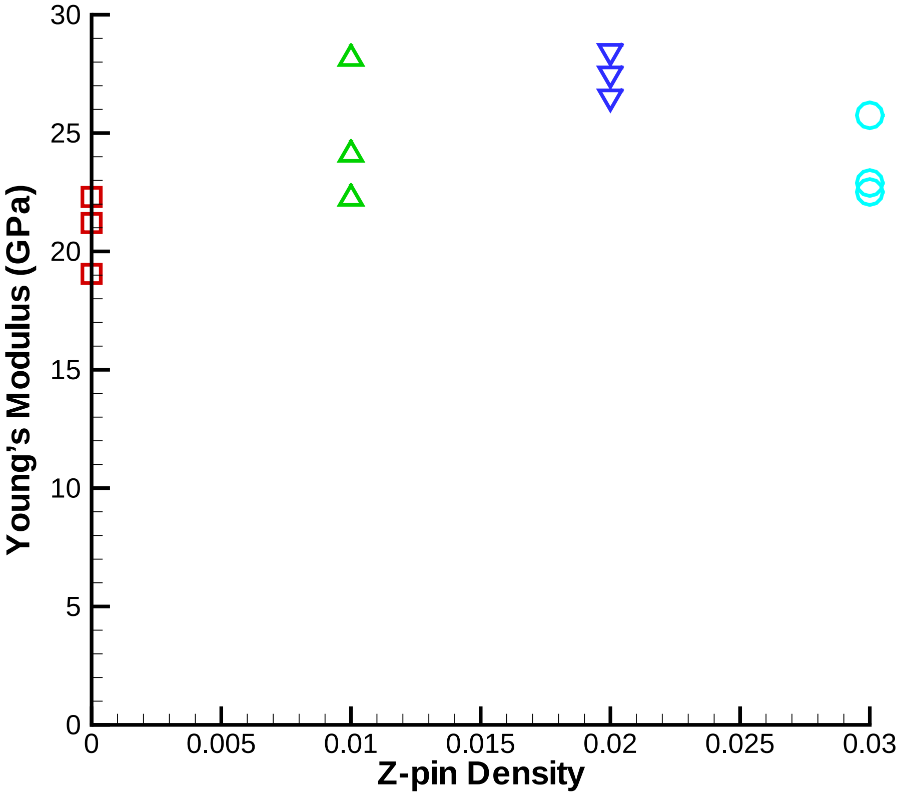

Figure 2.7: Comparison of Young's Modulus in group B

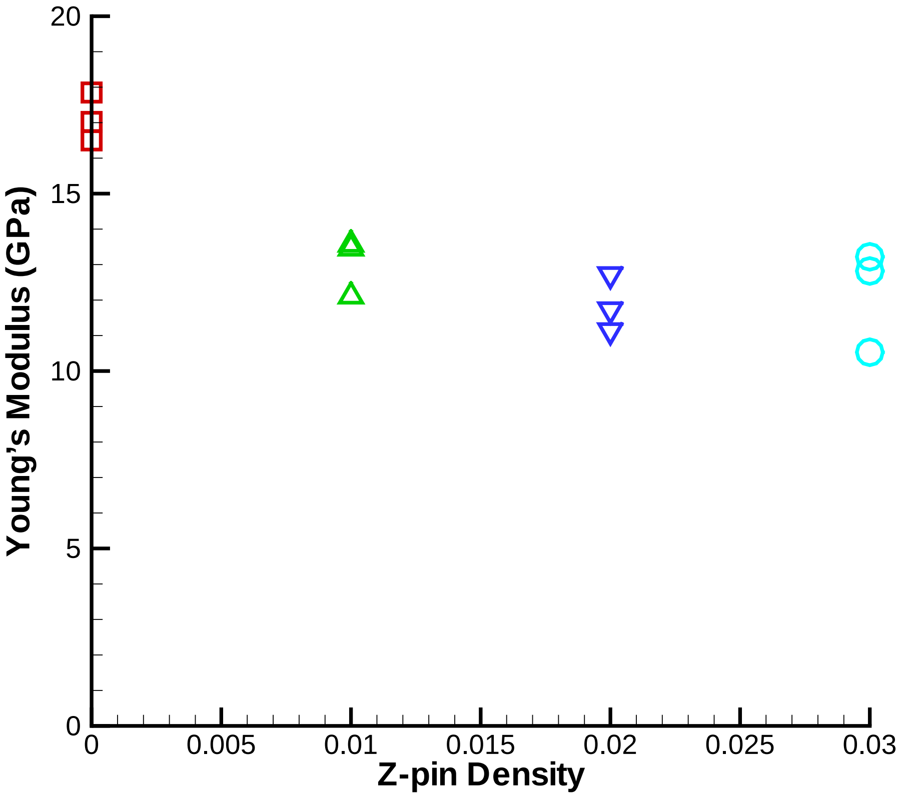

Figure 2.8: Comparison of Young's Modulus in Group C

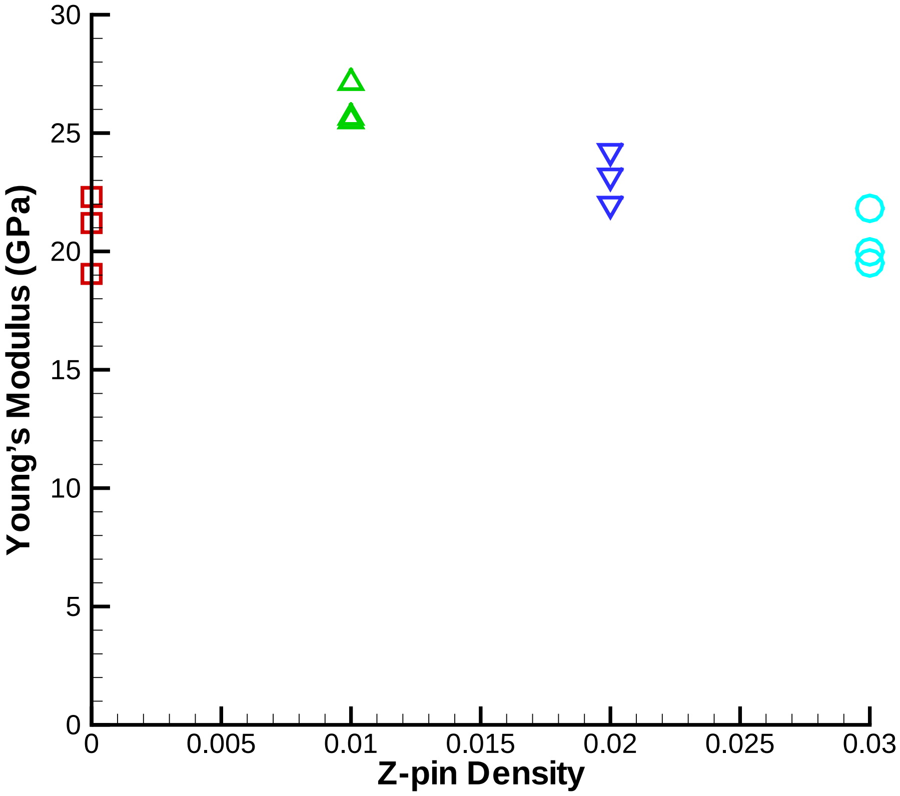

Figure 2.9: Comparison of Young's Modulus in Group D

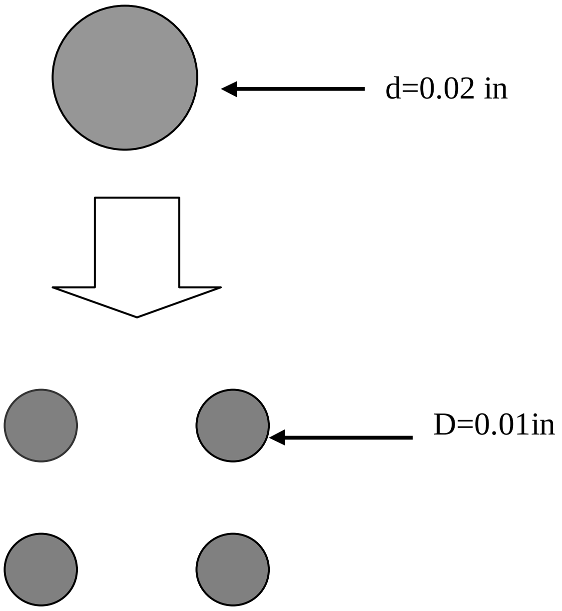

Figure 2.10: Illustration of d=0.5080 mm (0.02 in.) Z-pin and d=0.2794 mm (0.011 in.) Z-pins

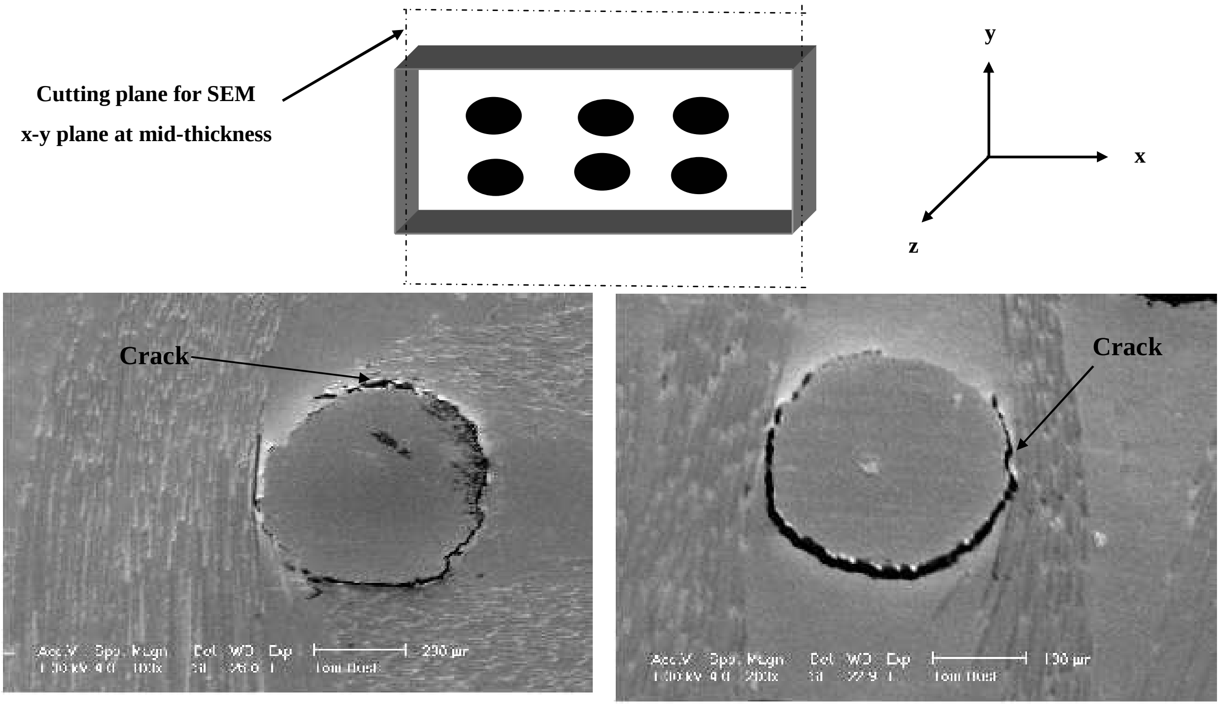

Figure 2.11: (a) SEM Image of d=0.5080 mm (0.02 in.) Z-pin (b)SEM Image of d=0.2794 mm (0.011 in.) Z-pin

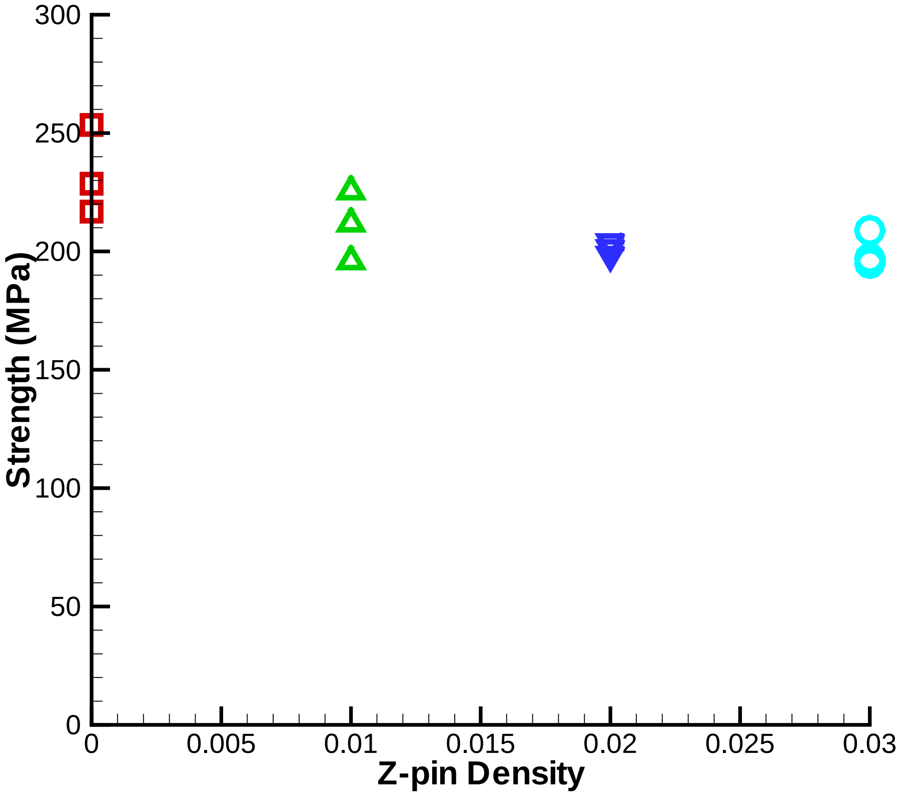

Figure 2.12: Comparison of the Strength in Group A

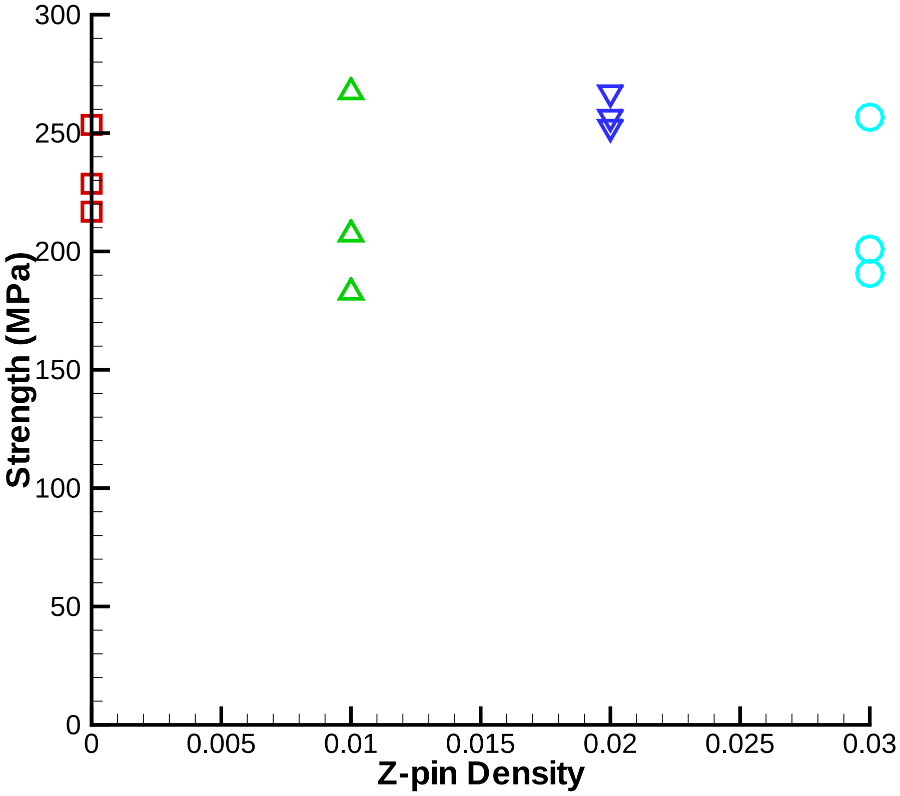

Figure 2.13: Comparison of the Strength in Group B

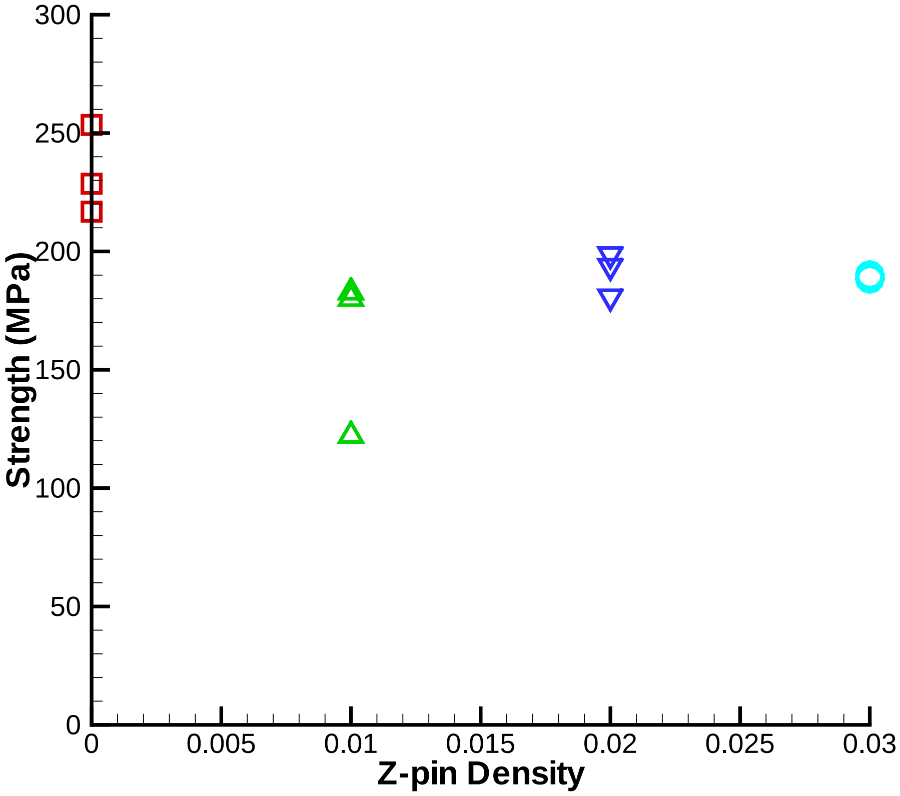

Figure 2.14: Comparison of the Strength in Group C

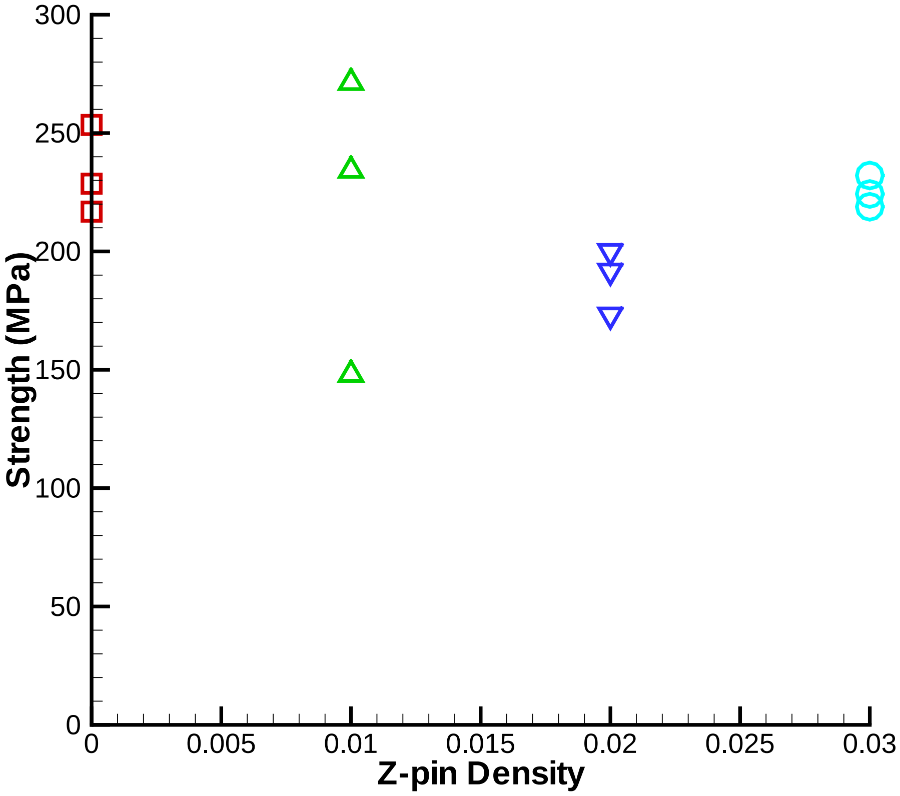

Figure 2.15: Comparison of the Strength in Group D

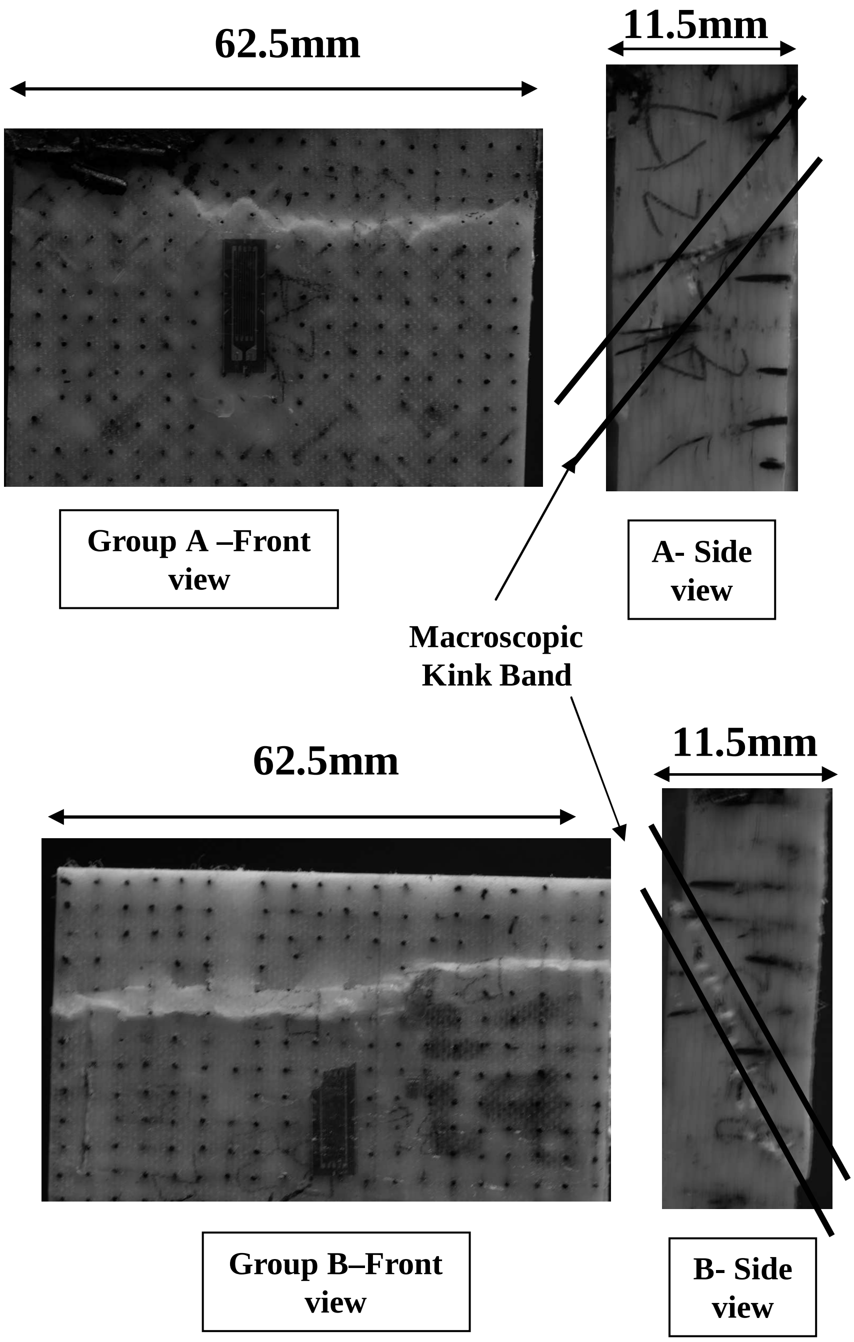

Figure 2.16: Macroscopic Compression Failure Mechanism for Group A and B

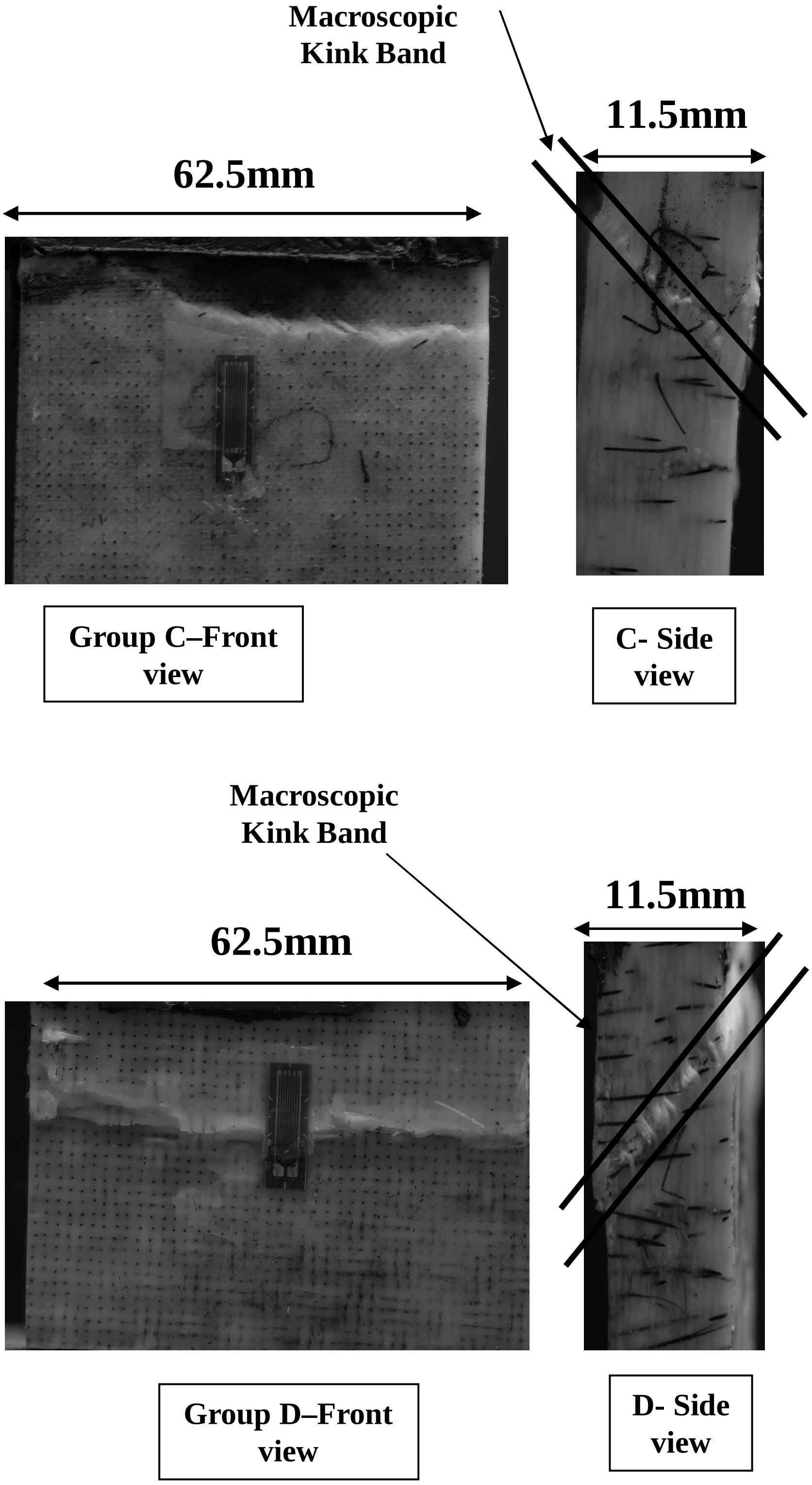

Figure 2.17: Macroscopic Compression Failure Mechanism for Group C and D

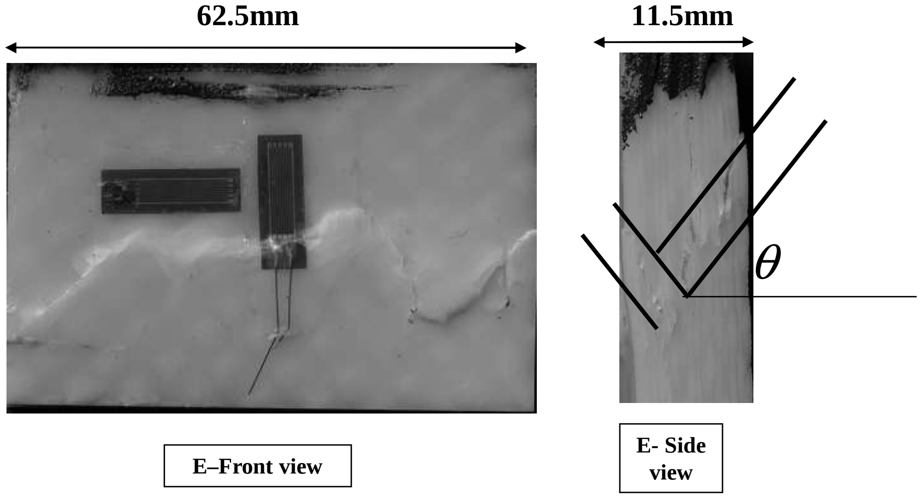

Figure 2.18: Macroscopic Compression Failure Mechanism for Group E

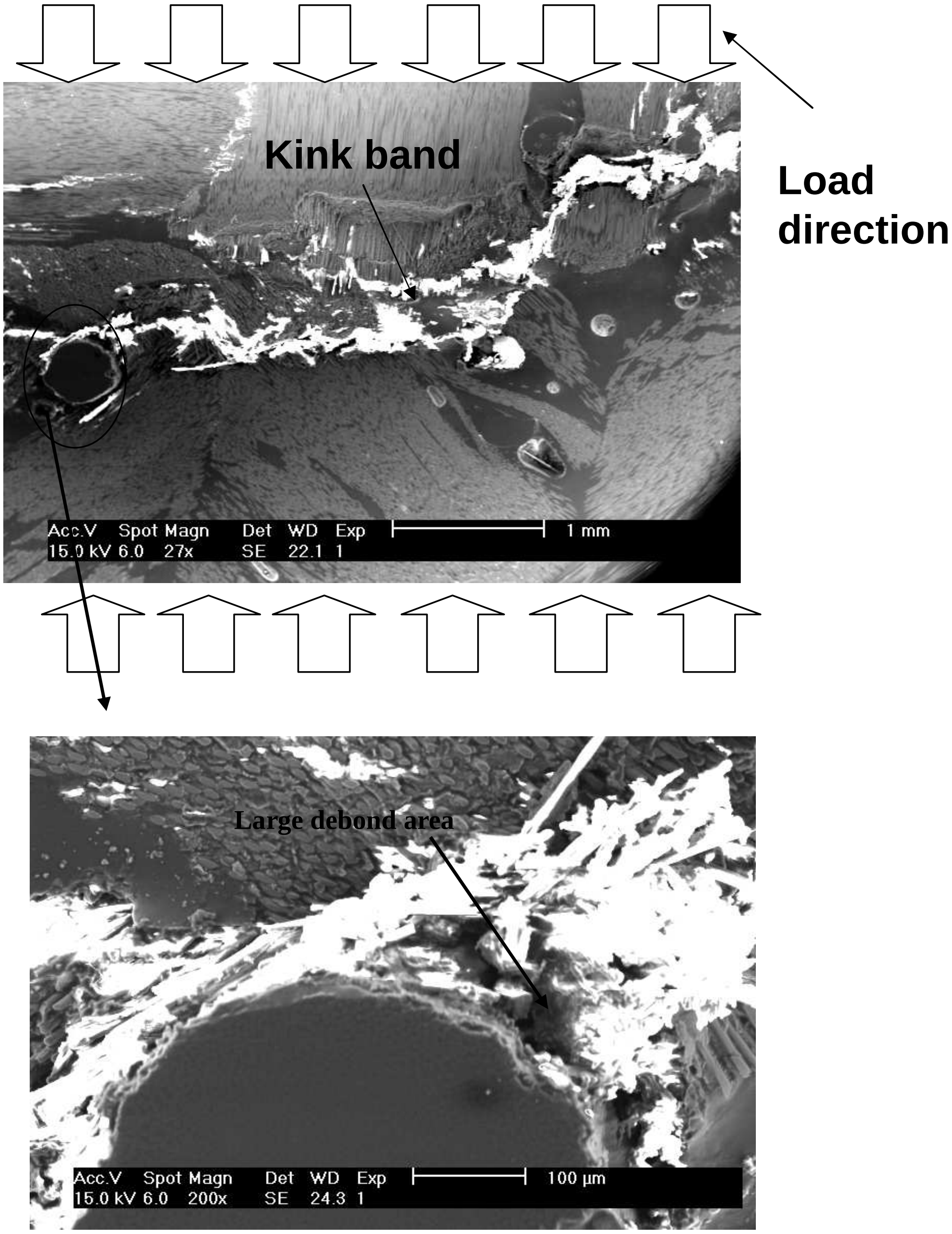

Figure 2.19: Crack Path in Group A3

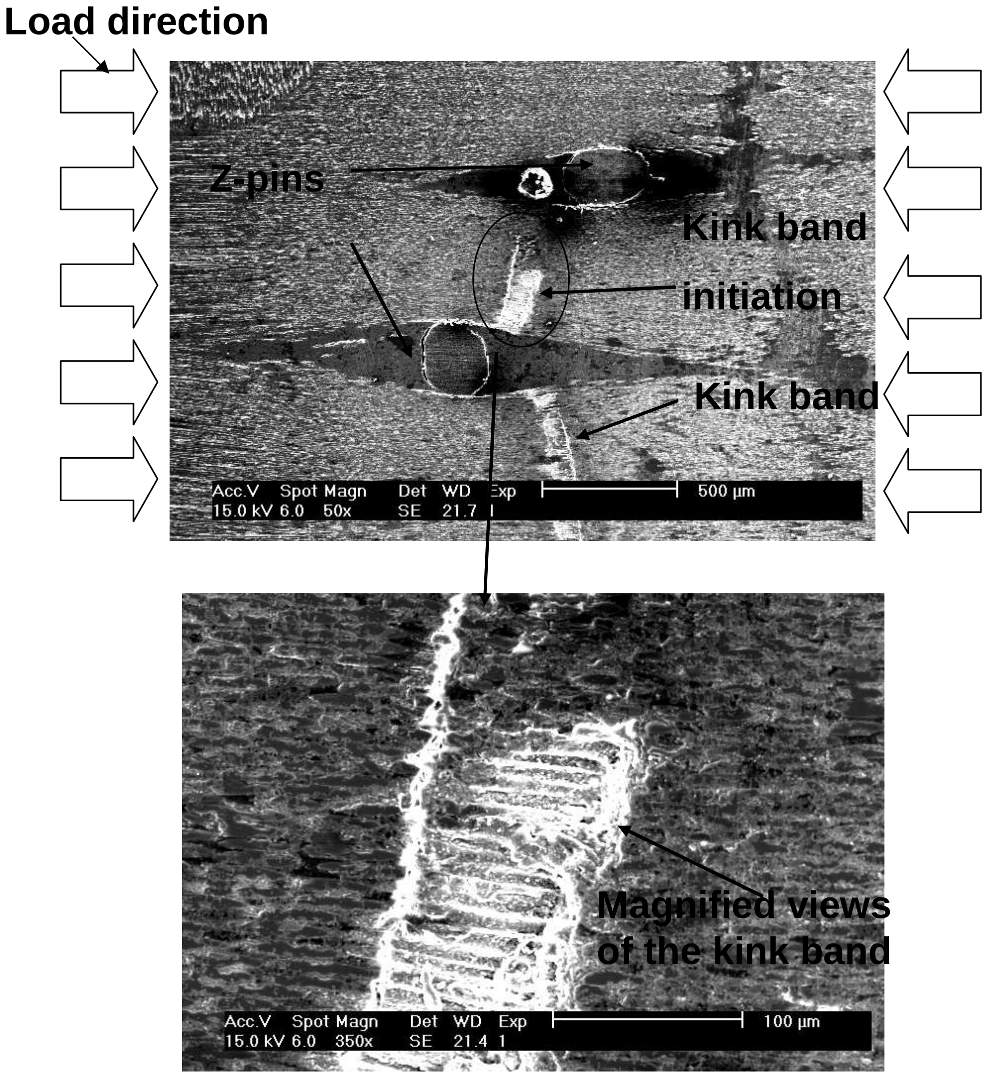

Figure 2.20: Kink Band in Fiber Tow at the Fiber/Matrix Scale in Group C1

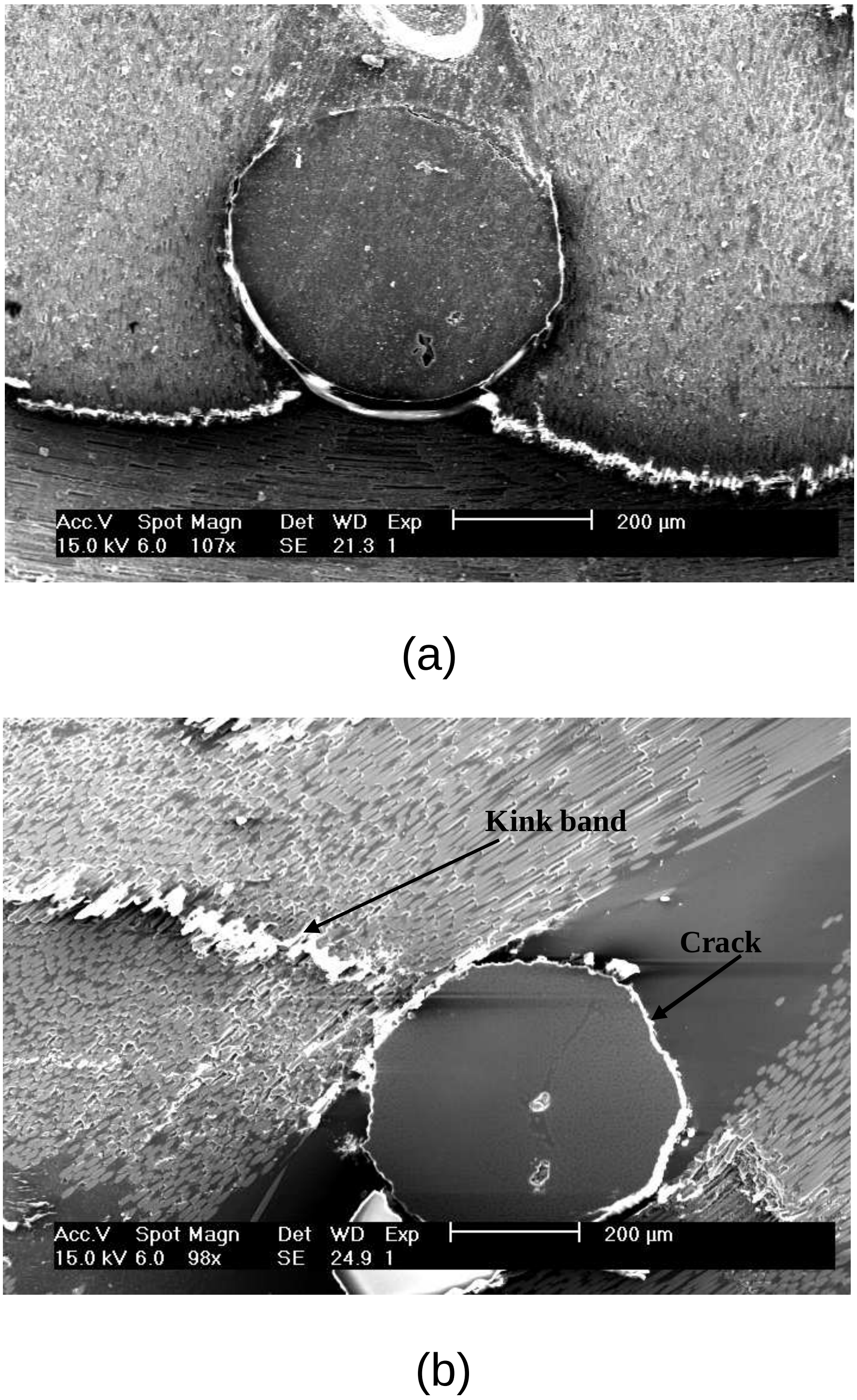

Figure 2.21: (a) Crack near the Z-pin of Specimen in Group A2 (b) Crack near the Z-pin of Specimen in Group A3

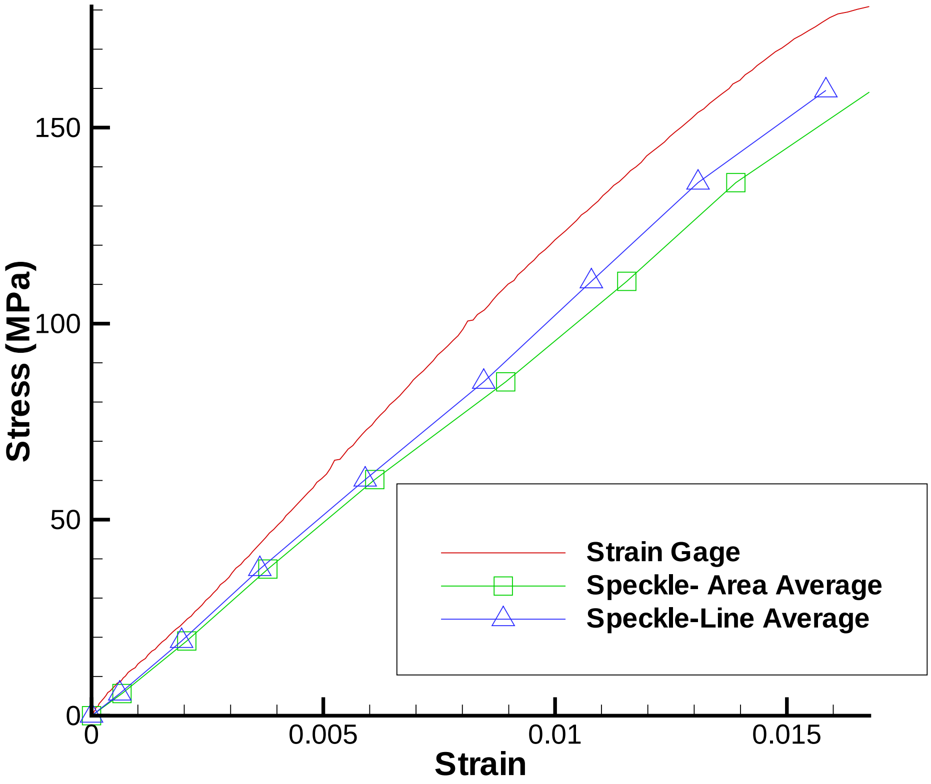

Figure 2.22: Comparison of the Young's Modulus

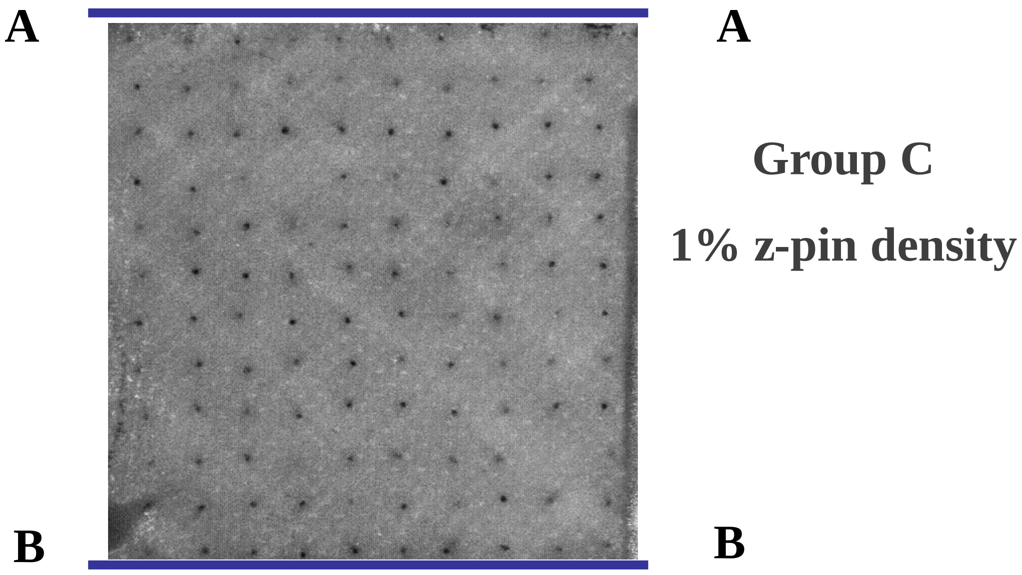

Line Average Method

$$\varepsilon_{line} = \frac{(\delta_{AA} - \delta_{BB})}{L}$$

Figure 2.23: Illustration of Line Average

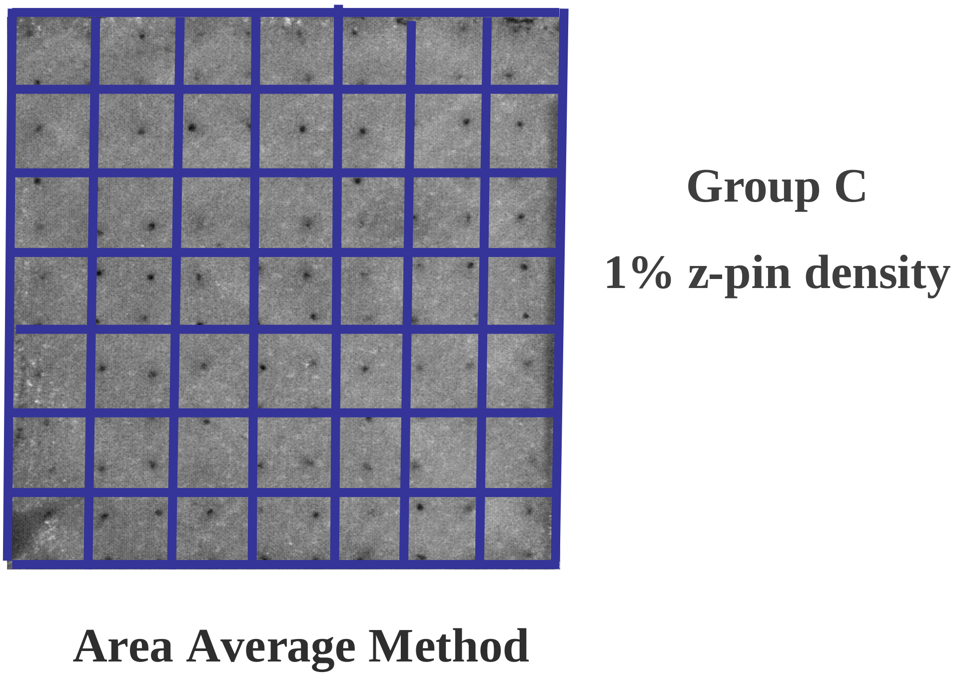

$$\varepsilon_{area} = \frac{\sum \varepsilon_i}{Area}$$

Figure 2.24: Illustration of Area Average

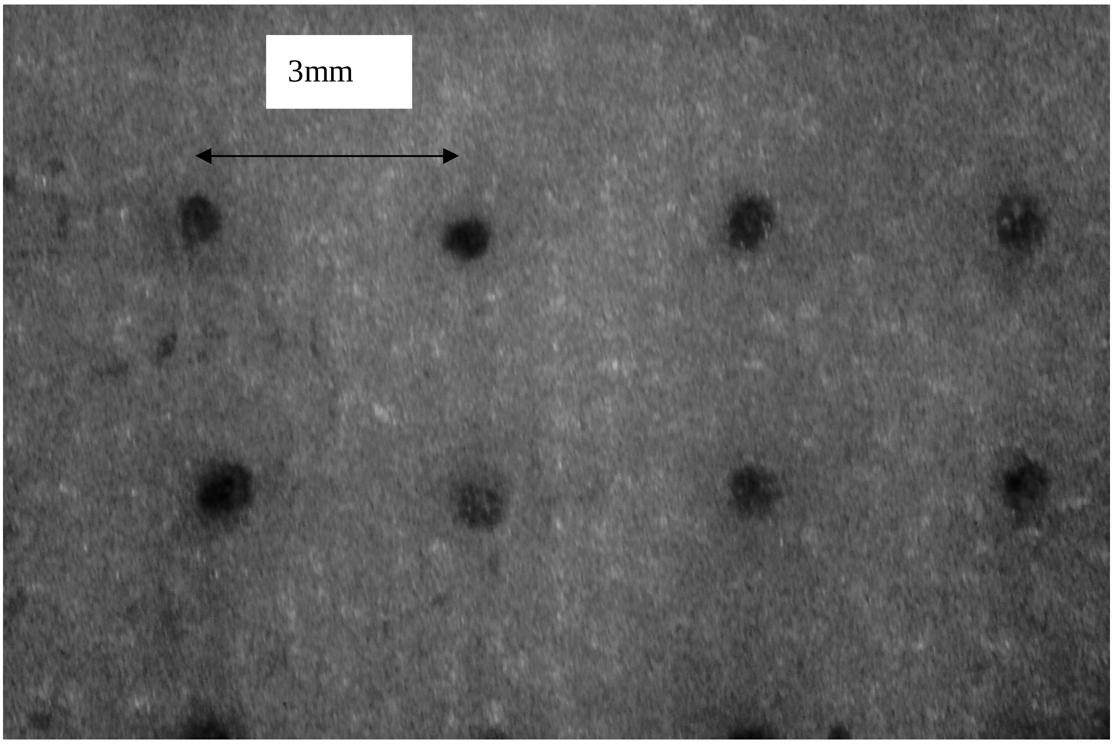

Figure 2.25: Speckle Pattern in 2% Z-pin Composites

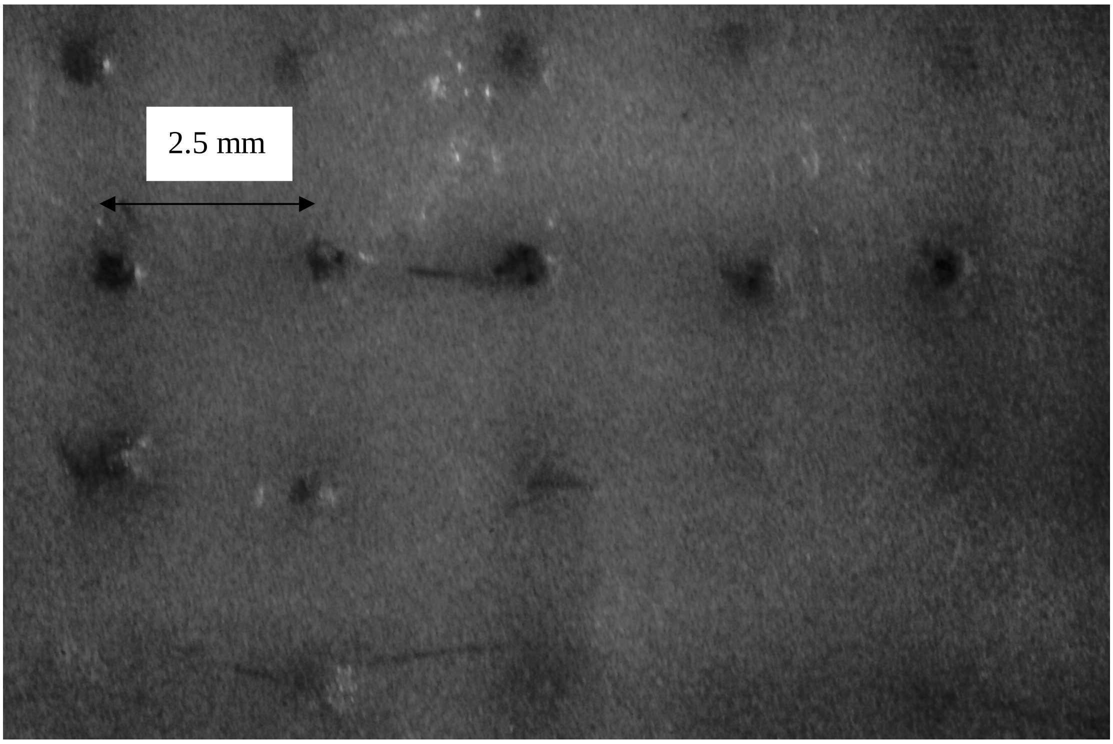

Figure 2.26: Speckle Pattern in 3% Z-pin Composites

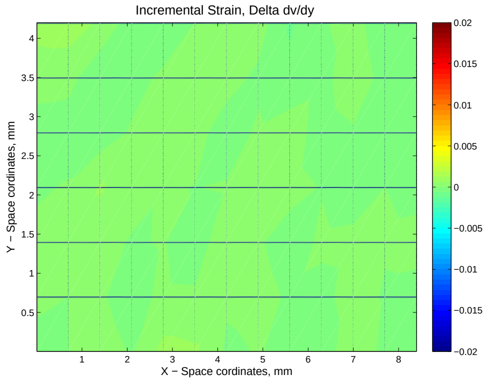

Figure 2.27: ε_{yy} when Load=1824.58N

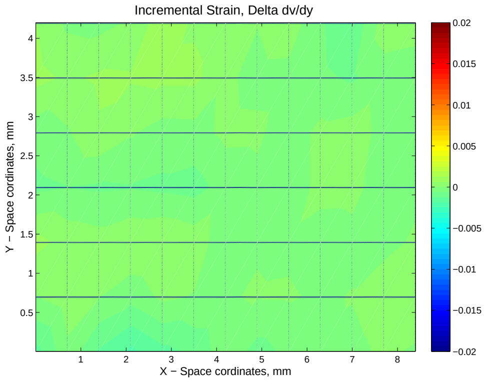

Figure 2.28: ε_{yy} when Load=1576.17N

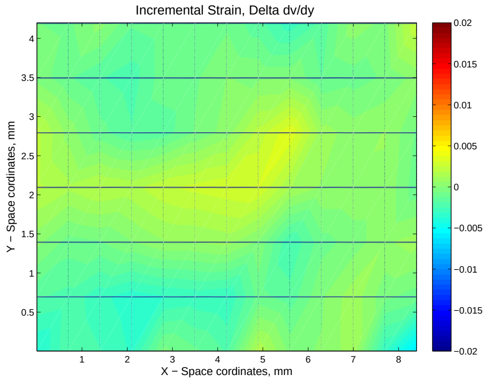

Figure 2.29: ε_{yy} when Load=3897.60N

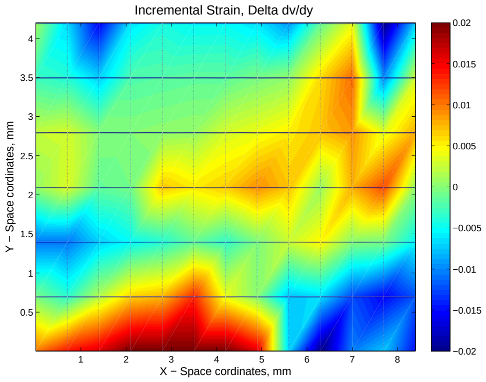

Figure 2.30: ε_{yy} when Load=3400.75N

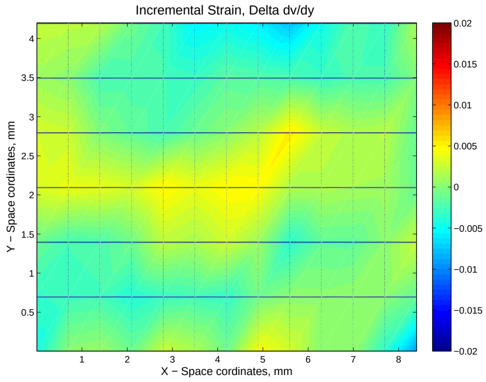

Figure 2.31: ε_{yy} when Load=5988.04N

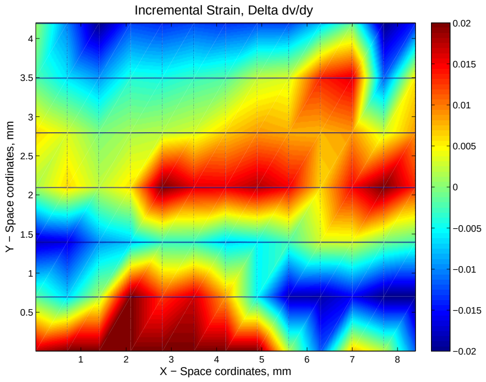

Figure 2.32: ε_{yy} when Load=5105.36N

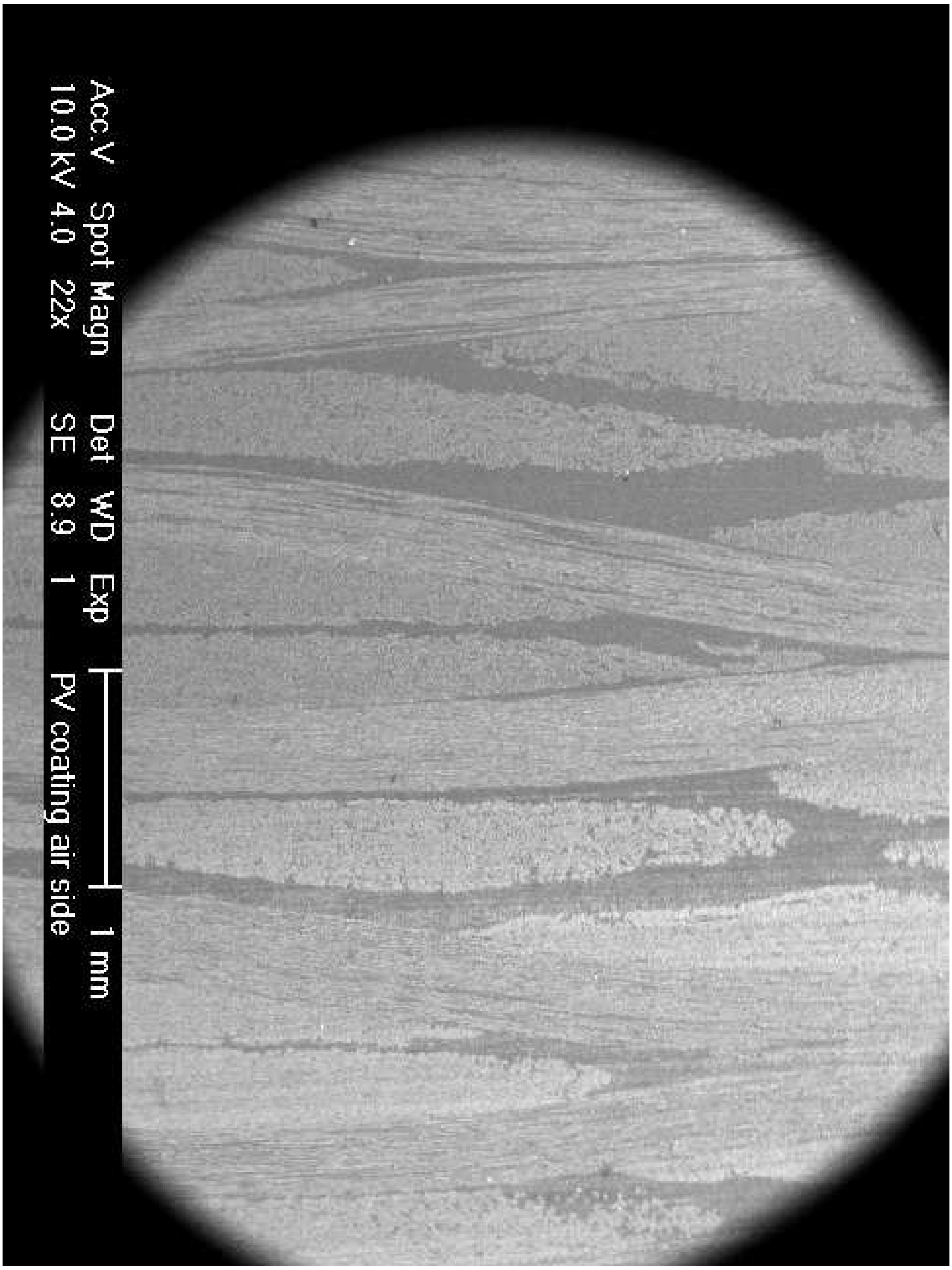

Figure 2.33: SEM Image of the Composites

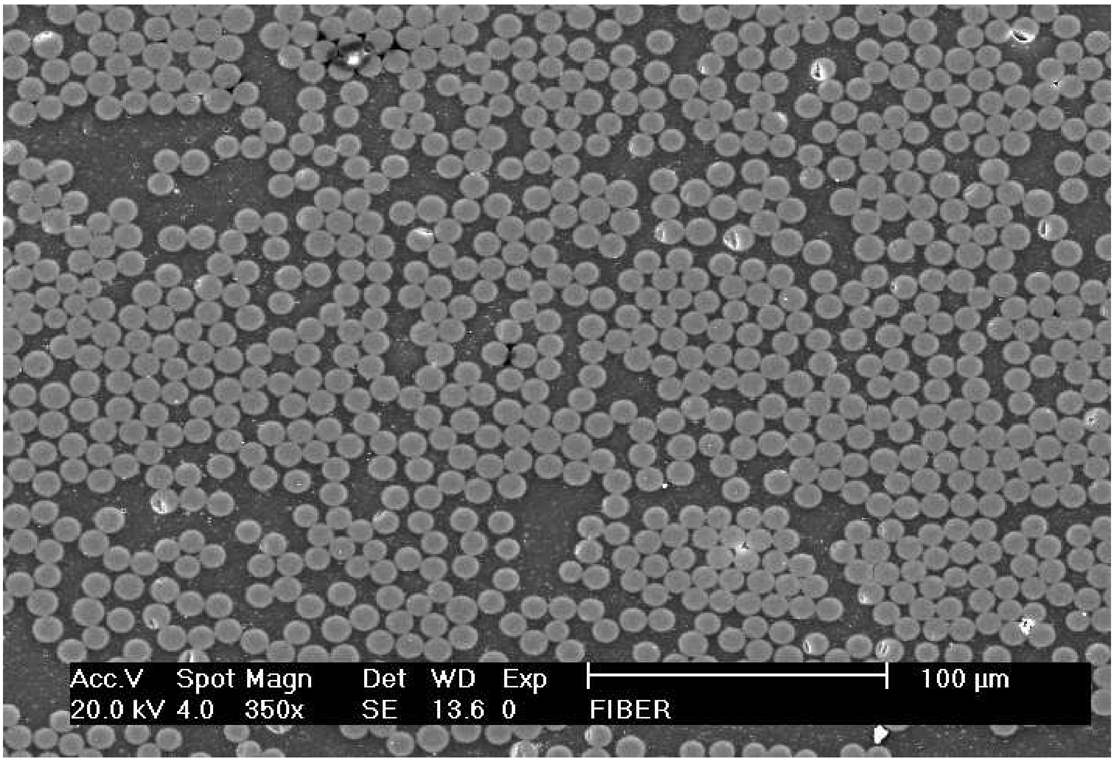

Figure 2.34: SEM Image of Fiber Tow

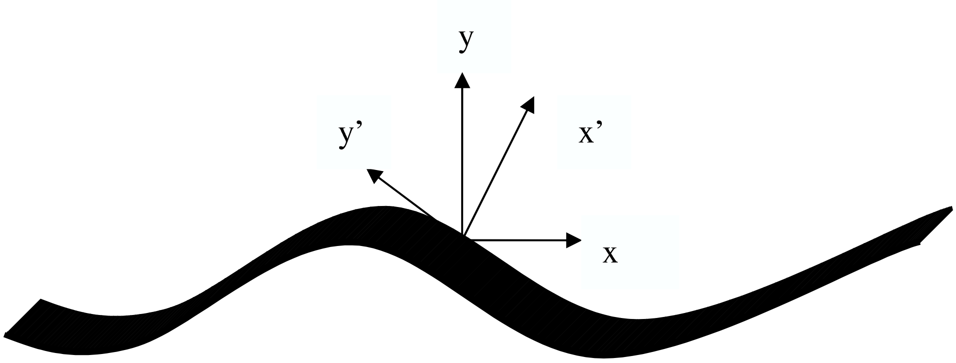

Figure 2.35: The Movement of the Monitored Window in this Algorithm

CHAPTER III

Compression Strength Limiting Mechanism in Woven Fiber Z-pinned Composites

In chapter 2, it was shown that, during the Z-pinning process, fiber distortion exists within the fiber tows and damage occurs at the boundary of the Z-pin and fiber tow. However, whether distortion of original straight fiber or damage between Z-pin and its surrounding matrix affecting the performance of Z-pin composites remains unclear. Therefore, it is the goal of this chapter to establish a finite element based model to capture the failure mechanism of an axial fiber tow when it is subjected to compression load. A 2D model is adopted for ease of computation and to clearly distinguish the parameters that influence compression strength. The 2D model shows that stress concentration starts from where distortion in the fiber tow has the maximum curvature. This region of stress concentration acts as the seed to initiate kink banding as seen in the post-experiment SEM images in chapter 2. Simulations with different Z-pin density and Z-pin diameter are also investigated. Damage at the Z-pin boundary induced from Z-pinning is regarded as imperfect bonding between Z-pin and surrounding matrix. An extreme case assuming no bonding between Z- pin and matrix is proposed to compare against the case of perfect bonding. Multiple Z-pin models are compared against a single Z-pin model to estimate the Z-pin interaction effect.

3.1. Introduction

Delamination is a common failure mode frequently encountered in traditional 2D composite structures. It has been shown that inserting Z-pins can increase the interlaminar fracture toughness and thus prevent delamination. However, many experiments, [19], [18], and [54] show that increasing the Z-pin density can decrease the in-plane properties. The finite element model in [21] shows that adding 2% of Z-pins decreases the in plain modulus by 7% to 10%. In [39], pure compression and combination of compression with shear deformation are studied. It concludes that adding the shear dramatically decreases the strength of the Z-pin composites. It is also pointed out that 4%, Z-pin composites have less strength than the 2% one. This observation is consistent with what is found in the chapter 2 and [54].

Two imperfections are induced during the Z-pinning process. The first one is distortion of the fiber tows caused by Z-pinning. The second one is imperfect bonding between Z-pin and its surrounding matrix shown in Figure 2.11. Here, the imperfect bonding is referred to as damage. These two imperfections are two concerns that can affect the performance of the entire structure. Previous studies have identified kink banding as a commonly observed mode of failure under compression of continuous fiber reinforced composites. A method is proposed in [7] to identify the initiation of the kink band. In [4], the concept proposed in [7] and Schapery's theory are used to identify the failure load under multi-axial loading. The methods proposed in [7] and [4] assume that there is misaligned fiber locally in a unidirectional composite in which most of the fibers are assumed aligned in the same direction. In the literature on textile composites, very few studies have addressed the effect of Z-pins in woven composites under compression. In this chapter, an orthotropic plastic potential for the fiber tow is derived from numerical analysis of the stress-strain curves of a representative unit cell of an axial fiber tow. This plastic potential for the fiber tow together with the plastic potential of the matrix is subsequently implemented in the finite element package ABAQUS. The matrix is modeled as a J2 isotropic hardening elastic-plastic solid. During the nonlinear compression response analysis, the arc-length method (RIKS method) in ABAQUS is used to ensure that the post failure path could be captured, including unstable equilibrium branches that occur in the post-peak regime.

3.2 Inputs to the Finite Element Models

3.2.1 In-Situ Matrix

An overview of the Z-pin composites was presented earlier in chapter 1 (see Figure 1.3). It was recognized that the layered composites consist of certain repeating units (RUCs). It is known that a single fiber is linear elastic while the matrix material used (SC-15) can be modeled as an isotropic elastic-plastic solid. However, previous studies have shown that the matrix material within the composites can display behavior that is different than the virgin resin material due to residual stresses, non-uniform curing due to fiber tows and due to non-uniform temperature field during the process of manufacturing. Thus, in this work, we will derive a method to extract the in-situ stress-strain properties as outlined below. The approach used is similar to that described in [2].

In [32], a similar approach is also adopted to characterize the in-situ matrix property. The obtained in-situ matrix effective stress-effective strain curve is subsequently used as the first trial response curve of the matrix for the numerical simulation of the [45/-45] single layer representation of the composites. The numerical model is shown in Figure 3.1, which consists of a 3×3 collection of RUCs of a single woven lamina. A single RUC of the lamina consists of fiber tows and matrix as shown in Figure 3.2 and Figure 3.4 . The fiber tows contain fibers and matrix, as was shown in Figure 1.3. The starting point in obtaining the in-situ matrix curve is the assumption that the in-situ matrix is an elastic-plastic solid obeying the J-2-isotropic hardening plastic theory with an associated flow rule. Then following the method discussed in [2], a compression test of a $[45/\text{-}45]_{8s}$ rectangular specimen was conducted with axial and transverse strain gages located as indicated in Figure 3.3. By analyzing the strain gage readings and assuming (as a first trial) that the specimen is a straight fiber $[45/\text{-}45]_{8s}$ compression specimen, a plot of $\sigma_y/2$ (σ_y is load divided by cross section area) vs $(\epsilon_y\text{-}\ \epsilon_x)/2$ provides a first estimate of the composite shear response. Next, by knowing that the fiber is elastic, the curve then provides the shear response of the in-situ matrix through the approximate formula that relates the composite shear modulus to the matrix shear modulus as shown in equation (3.1)

$$\begin{aligned} G_m &= G_{12}(\frac{1+\eta_2\nu_f}{1-\eta_2\nu_f})^{-1} \\ \eta_2 &= (\frac{G_{12f}-G_m}{G_{12f}+G_m})^{-1} \end{aligned} \tag{3.1}$$

where G_{12} is the shear modulus obtained from experiments, G_{12f} is the shear modulus of the fiber, ν_f is the volume fraction of the fiber in a unit cell, and G_m is the shear modulus for in-situ matrix. This response curve is still approximate since it was obtained analytically and by assuming that the tows are straight. Next, we use this first trial curve as the input to a finite element simulation of a [45/-45] textile lamina under compression. The FE model is shown in Figure 3.1. It consists of transversely isotropic elastic-plastic fiber tows and elastic-plastic matrix. In both these entities, the unknown that is sought is the elastic-plastic response of the in-situ matrix that will provide a match between the experiment and the simulation. Thus, prior to performing the simulation of the [45/-45] composites, it is first necessary to obtain the elastic-plastic response of the tows.

3.2.2 Elastic-Plastic Response of the Tows

The experimental result from the $[45/\text{-}45]_{8s}$ composite provides the first "trial" of the assumed elastic-plastic response curve of the in-situ matrix. It was shown earlier that the fiber tow consists of matrix and fiber as shown in Figure 1.4. Therefore, the matrix will influence the constitutive model of the fiber tow. From several SEM images, it was found that in a fiber tow, the average fiber volume fraction is $V_f = 52\%$ ($V_m = 48\%$). Using this information, a hexagonal RUC of the fiber tow was meshed as shown in Figure 3.7. It is pointed out in [26], that a hexagonal representative unit cell is the correct representative unit cell to produce transverse isotropy. In the following, the finite element analysis is performed to obtain the orthotropic plastic potential for the fiber tow. The matrix is assumed to be represented as an elastic-plastic solid obeying J2 flow theory of plasticity with an isotropic hardening law.

For the fiber tow, a simplified orthotropic plastic potential proposed in [13] is used

$$f = \frac{1}{2}\left[(\sigma_{22} - \sigma_{33})^2 + 2a_{44}\sigma_{23}^2 + 2a_{55}\sigma_{21}^2 + 2a_{66}\sigma_{31}^2\right] \tag{3.2}$$

As shown in Figure 3.7, the direction 1 is the longitudinal direction of the fiber tow. Direction 2 and direction 3 are the transverse directions of the fiber tow. Note that equation (3.2) assumes that there is no plastic deformation in the longitudinal fiber tow. This is because the ‘1’ direction response is dominated by the fibers which remain elastic up to failure In equation (3.2), only three parameters a_{44}, a_{55}, and a_{66} need to be identified.

The constants in the yield potential in equation (3.2) can be obtained from performing a transverse compressive simulation in direction 2 (or direction 3). From these simulations, the yield stress σ_{22} or σ_{33} can be identified. The plastic potential corresponding to yielding for a transverse compression in the ‘2’ direction can be obtained by identifying the yield stress

$$f_{yield} = \frac{1}{2}\left(\sigma_{22}\right)^2 \tag{3.3}$$

Subsequently, a shear simulation in the 1-2 plane is performed. From the stress-strain curve, the yield stress σ_{21} can be identified. Then, the coefficient a_{55} can be obtained by use of the fact that the equation (3.3) and equation (3.4) should be equivalent.

$$f_{yield} = a_{55}\sigma_{21}^2 \tag{3.4}$$

Due to symmetry of the representative unit cell, parameter a_{66} is equal to a_{55}. Similar to the transverse compression simulation, parameter a_{44} can be extracted by performing a shear test in the 2-3 plane.

After the coefficients a_{44}, a_{55}, and a_{66} are obtained, the plastic potential for the fiber tow is subsequently implemented in ABAQUS for futher simulation. The implementation in ABAQUS is through the use of the options of *PLASTIC and *POTENTIAL. The RIKS option is an arc-length method used in the non-linear finite element analysis to ensure that the post failure path can be captured, including unstable equilibrium paths as will be discussed later.

3.2.3 Obtaining the In-Situ Matrix Stress-Strain Curve

Using the fiber tow plastic potential, a full simulation of the [45/-45] composite test was performed using the commercial package ABAQUS. The FE mesh used (only the twos are shown for clarity) is shown in Figure 3.1. As in the experiments, compressive displacement control load was used to obtain the stress-strain response, the applied stress was defined as the reaction load in the '1' direction divided by the cross-sectional area. The average strain was defined as the overall shortening in the direction of load divided by the length in the '1' direction. This provides the "first trial" of the composite axial stress-strain response. This is then compared against the experimental results. Then, by "trial and error", the matrix stress-strain response is changed so that a near perfect match between the experiment and the simulation for the entire composite is obtained. The final trial obtained axial stress-axial strain response for the in-situ matrix is shown in Figure 3.5

3.3 2D Finite Element Model for Tow Kinking

3.3.1 2D Finite Element Model in 1-3 Plane

A 2D model of a Z-pin composite based on Figure 3.9 consisting of fiber tows, a Z-pin and the matrix surrounding it is shown in Figure 3.10. Direction X is the longitudinal direction where the compression is imposed, direction Z is the through-the-thickness direction, and direction Y is the transverse direction. It can be seen that the Z-pin is surrounded by the matrix and fiber tows. The matrix is simulated as an isotropic material for which the stress-strain curve is taken as the in-situ curve obtained in the previous section. The fiber tow is simulated as an orthotropic composite material whose material properties are obtained from imposing plane strain condition on the 3D elastic-plastic constitutive law. Therefore, parameters,

E_{11} , E_{33}, ν_{13}, and G_{13}, are used to represent elastic properties of the orthotropic fiber tow as shown in equation (3.5).

$$\begin{bmatrix} \varepsilon_{11} \\ \varepsilon_{33} \\ \gamma_{13} \end{bmatrix} = \begin{bmatrix} \frac{1}{E_1} & \frac{-\upsilon_{13}}{E_1} & 0 \\ \frac{-\upsilon_{13}}{E_1} & \frac{1}{E_3} & 0 \\ 0 & 0 & \frac{1}{G_{13}} \end{bmatrix} \tag{3.5}$$

The 2D plastic potential is obtained from simplifying equation (3.2) by retaining terms that are independent of direction 2. That is,

$$f = \frac{1}{2}\left[(\sigma_{33})^2 + 2a_{66}\sigma_{31}^2\right] \tag{3.6}$$

Although a Z-pin is transversely isotropic, the longitudinal direction of Z-pin is parallel to the through-thickness direction of the composite. Therefore, the Z-pin is isotropic in the loading plane, and was assumed so.

In this 2D model, the Z-pins are assumed to be inserted and distributed uniformly within the composite. The size of the representative unit cell shown in Figure 3.10 can thus be determined provided that the density of the Z-pins is assigned. The dimensions of the model are based upon the SEM images shown in Figure 3.9. This 2D model is also similar to the model used in [21]. The size of the representative unit cell is L= 4.5mm for a Z-pin diameter of 0.508 mm (0.02 in) and 1% Z-pin density. For the same diameter and 1% , L= 3.18mm. For a diameter of 2.80 mm (0.011 in), L is 2.25mm for 1% density.

With reference to Figure 3.10, the boundary AB is fixed along global X direction. The center point K of boundary AB is fixed along global Y direction. Boundary CD is used to impose uniform displacement along the X-direction during the simulation.

Boundary CD is free to move in the Y-direction during the compression loading. For the FE studies, the CPE4 element is used in the commercial package ABAQUS. Each CPE4 element has four nodes and each node has 2 displacement degrees of freedom, in the x and y directions, respectively.

3.3.2 Study of Imperfection on the Strength of the Composites

A linear buckling analysis is performed first with the same boundary condition to be used later. From this analysis, a buckling mode is selected as an initial geometric shape imperfection to be used subsequently in a response analysis. Figure 3.11 is the buckling mode that is used as an imperfection in the nonlinear analysis (magnified). The ratio, $\frac{h}{L}$, expressed as a percentage can be used to express the magnitude of the initial geometric imperfection. The results obtained from a simulation of the 1% Z-pin composite with a Z-pin diameter of 0.508 mm (0.02 in) is discussed first. A series of simulations for different amounts of initial imperfection was conducted by varying the amplitude of the initial imperfection. The results obtained are shown in Figure 3.12. A typical response curve is explained as follows, as shown in Figure 3.23. Initially, the response is linear. As the loading proceeds, the area where there is fiber misalignment (such as around the Z-pin) undergo shear deformation. As the shear deformation increases, because the matrix is a nonlinear softening solid, the stiffness continuously decreases. As a result, the area within the composite subjected to softening will increase in shear response, while other will do so with less magnitude. At some point in the loading history (Figure 3.23, marked as C), the propensity for rotation is greater than the ability for restoration (due to the softening shear response of the tow) leading to a limit load point. Immediately after this, the deformation starts to localize into a band (kink band) and in the unstable "snap back" portion of the curve (CD in Figure 3.23), the band starts to develop and takes on the final shape shown at E in Figure 3.23. The result, Figure 3.12, shows that from the case of no initial imperfection to 10% of imperfection magnitude (the imperfection magnitude is specified in terms of percentage. Here 1% correspond to $\frac{h}{L}$=0.01), the maximum compression strength decreases. Note that beyond the maximum load, there is a "snap-back". That is, both the macroscopic stress and macroscopic strain decrease, signifying an unstable equilibrium path. These path cannot be computed with standard non-linear procedures that either use displacement control or load control. For unstable equilibrium path, one has to use an arc-length solution method. In this thesis, all unstable equilibrium path are studied by using the Riks arc length solver, developed by Riks, [45]. The solver is available in ABAQUS and was used in conjunction with the non-linear geometry option to complete the stress-strain response repeated throughout the thesis

The decrease is plotted in Figure 3.13 and shows the effect of geometric imperfection on compression strength. Just as a global buckling mode in Figure 3.11 can be used as an initial imperfection, a local buckling mode shape can also be used as an imperfect shape. Such a local buckling mode shape is shown in Figure 3.14. Using this as the initial imperfection resulted in very similar response results as compared to the case presented in Figure 3.13. A comparison of the results for a 2% global and local initial imperfection is shown in Figure 3.15. The initial stiffness, the maximum strength, and plateau strength are all unaffected by the type of imperfection. The final deformed shape in these simulations are also similar with kind band observed.

3.3.3 Comparison of Different Diameter and Different Density on Strength of Composites

Figure 3.22 shows a comparison of the response for different diameters of the composites for the case of 1% density of Z-pins. It is seen that the d=0.508 mm (0.02 in) composites have lower compression strength than the d=0.2794 mm (0.011 in) Z-pin composites. Figure 3.21 shows a comparison of different density(1% and 2%) of d=0.508 mm (0.02 in) Z-pins. From this figure, it is seen that the 2% composites have lower strength than 1% composites. The composites behave linearly until the fiber tows localize due to the plasticity in the transverse direction. In the discussion related Figure 3.23 earlier, it must be added that initially, the stress contour display a symmetric pattern, and this symmetry disappears, due to kink band formation which leads to deformation localization and a break up of symmetry.

So far, the 2D model used is based upon no damage between the Z-pin and surrounding matrix. However, it was mentioned in chapter 2, that such damage can exist due to the insertion of Z-pins. When damage occurs as shown in Figure 3.9, it is not realistic to assume that perfect bonding exists between the matrix and Z-pins. Here, one extreme example is considered. This extreme case assumes no bonding between the matrix and Z-pin fiber. That is, the Z-pin fiber is replaced by a hole in the finite element analysis as shown in Figure 3.16. Figure 3.17 shows a comparison of the stress-strain response for the damaged case and the no damage case for a Z-pin composite with a Z-pin diameter of d=0.508 mm (0.02 in) and density of 1%. The strength for both cases are almost the same. However, the load after failure in the damage case drops to a much lower value. The result of Figure 3.17 tells that the damage at the Z-pin and surrounding matrix has a minimal effect on the strength of the composite but has an approximate effect on the plateau stress. Furthermore, it is seen that the insertion of the Z-pin which causes the fibers within the tow to have local curvature is the predominant effect that leads to the mechanism of kink banding which spreads the damage.

3.3.4 The Strength of Composites in Multi Cells

So far, the simulations have been based upon one unit cell. It is of interest to compare the results from multi cell simulations with those of single cell simulation to understand interaction between Z-pins. The finite element meshes corresponding to the 9 unit cell and 16 cell representations of the 2D geometries are as shown in Figure 3.18 . Again, as before, for the one unit cell simulations, the boundary AB is held fixed in the x-direction, but free to move in the y-direction, while boundary CD, which is free to move in the y-direction is subjected to an increasing displacement control loading in the negative x-direction. The point K in AB is fixed in both x and y direction

Figure 3.19 and Figure 3.20 show the comparison of stress-strain responses of one unit cell with 9 unit cells and 16 unit cells. For this comparison, the meshes used didn't contain any initial geometric imperfection. As can be seen in Figure 3.19, the strength of 1 unit cell model and the strength of 9 unit cell model are very similar. Note that between the maximum load (A) and unstable unloading path (B), the kink band formation can be observed. At point C, the kind band has formed completely. Figure 3.19 is the comparison of the strength between the 1 unit cell model and the 16 unit cell model. Between the highest strength (point A) and the end of the unstable path (point B), the kind band started to form, which is similar to the results in Figure 3.19. It is also noted that the strength of 1 unit cell model and the strength of 16 unit cell model are almost the same. This establishes that the onset of the kink band which is the strength limiting mechanism observed in experiments have been captured quite adequately by 1,9, and 16 RUC models presented in this chapter

3.3.5 The Strength of Composites in Multi Cells

In previous simulations, Z-pins are assumed to be encompassed in the matrix. From the results of section 3.3.3, the shape of the matrix is regarded as the dominant factor influencing the response of Z-pin textile tile composites. In fact, the shape of the matrix is also the shape of the fiber distortion. Therefore, it is concluded that the fiber distortion is the dominant factor influencing the response of the composites. However, some of the Z-pins in the composites directly contact with the fiber tows as shown in Figure 3.25. Here, in this subsection, models of Z-pins directly contacting with fiber tows are established. Firstly, models of 1% Z-pin composites (d=0.0508 cm or 0.02 in) with 9 Z-pins and models of 1% Z-pin composites (d=0.0279 cm or 0.011 in) with 36 Z-pins are established, as shown in Figure 3.26 and Figure 3.27, respectively, in order to study the interactions between different Z-pins when Z-pins are directly contacting with fiber tows. The comparison of the simulations is shown in Figure 3.28. Note that one larger diameter Z-pin (d=0.02 in) is almost equivalent four small diameter Z-pin (d=0.011). That is why 9 Z-pins are in composites of d=0.02 in and 36 Z-pins are in composites of d=0.011 in. The result in Figure 3.28 shows that the interactions between the Z-pins have influences on the response of the composites. As stated in section 3.3.3, the fiber distortion is the dominant factor in influencing the compressive response of the composites. Theoretically, the large diameter composites might have lower strength because of the large curvature of the fiber distortion due to Z-pinning. However, as we can remember, one large Z-pin can be divided into four small Z-pins. Because of this, when the Z-pin density is the same, the stress concentration starting from small Z-pin can propagate to the neighboring Z-pin shortly. This propagation of the stress concentration is so called the formation of kind band, resulting in the loss of loading capacity. The kind band during the failure state of point A and B in Figure 3.28 can be seen in Figure 3.29 and Figure 3.30.

Two models of the 1% Z-pin diameter composites with different matrix area are established and shown in Figure 3.31 and Figure 3.32, respectively. The stress versus strain response for the two models are shown in Figure 3.33. As can be seen from the results, the maximum strength of these two cases are close, indicating the shape of the matrix has no effect on the maximum strength of the composites. This is because the place where the Z-pin directly contacting to the fiber tow has the highest curvature. For both of the two numerical simulations, the curvature of contact area of the Z-pin with the fiber tow is the same. It is seen that curvature of the contact area of the Z-pin with the fiber tow is the dominant factor for the determination of the strength. The area where the matrix connects the fiber tows has smaller curvature than the contact area of the Z-pin with the fiber tows. Therefore, although the curvature of the contact area of matrix and fiber tow for two cases is not the same, the maximum strength is the same.

3.4 Conclusion

In this chapter, a 2D (1-3 loading plane) model is presented to investigate the effect of local imperfection near the Z-pin within a woven composite. It is observed that damage around the Z-pin doesn't influence the local strength of the composites but affect the post response after failure. The higher density of Z-pin composites have less strength and stiffness provided that the diameter is the same. The small diameter of the Z-pin composites have less strength and stiffness when the density is the same. The distortion of the fibers within a fiber tow induced due to Z-pinning is responsible for initiating kink banding. This kink band subsequently propagates until loss of compressive load carry capacity. On the other hand, the imperfect bonding between the Z-pin and matrix has little effect on the strength of the composites near the Z-pin. The computed results are independent of the number of RUC's used in the 2D simulations. The 1, 9, and 16 RUC, 2D representations of this problem reveal very similar values for the compressive strength. Furthermore, the numerical models have shown that small Z-pin diameter composites have a lesser compression strength than the corresponding larger Z-pin diameter composites for the same Z-pin density. The finding reinforces the experimental trend repeated in chapter 2.

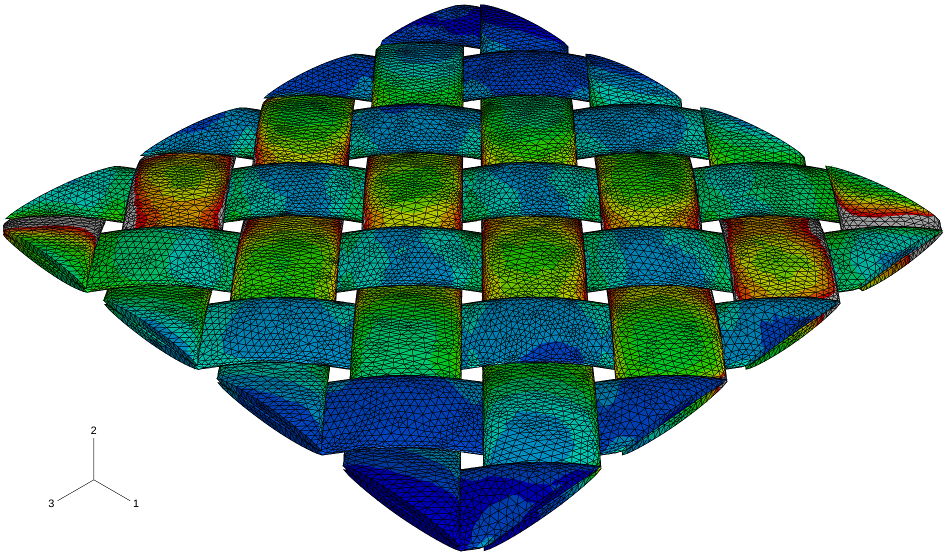

Figure 3.1: Model of a [45/-45] Lamina

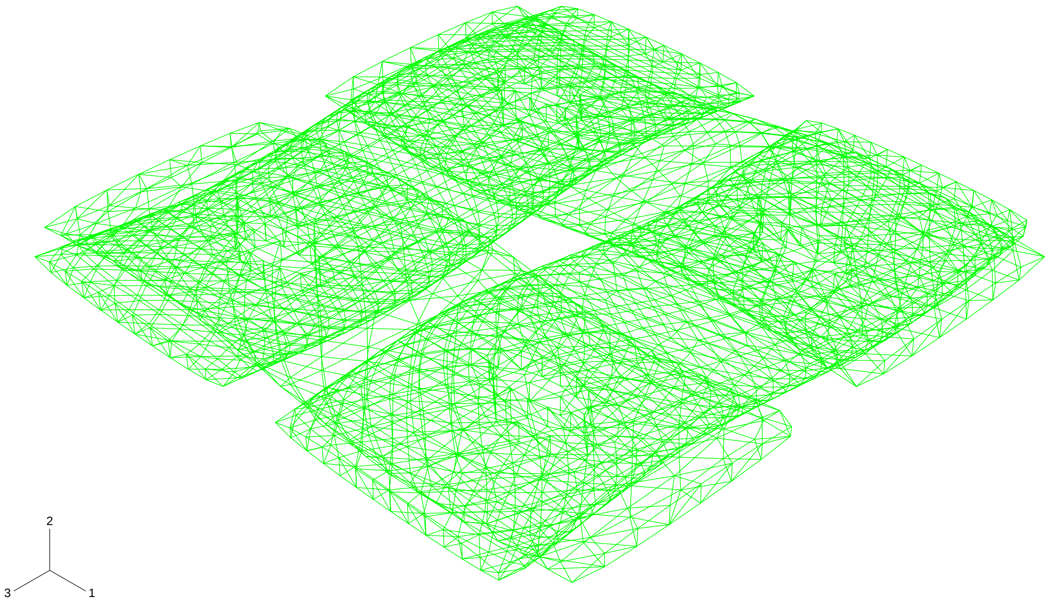

Figure 3.2: Longitudinal and Transverse Fiber Tows

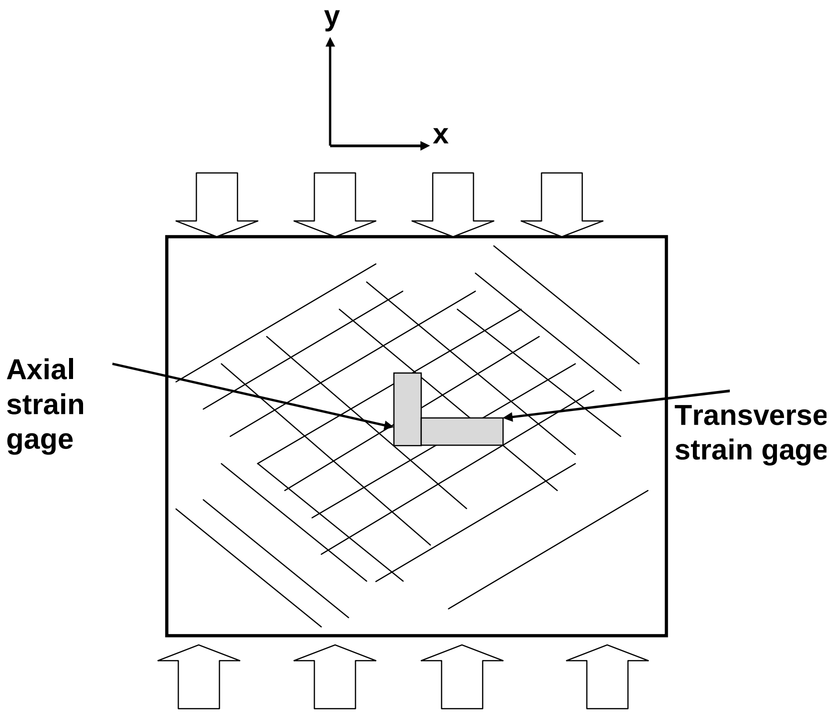

Figure 3.3: Schematics of Compression Test of [± 45] Composite Specimen

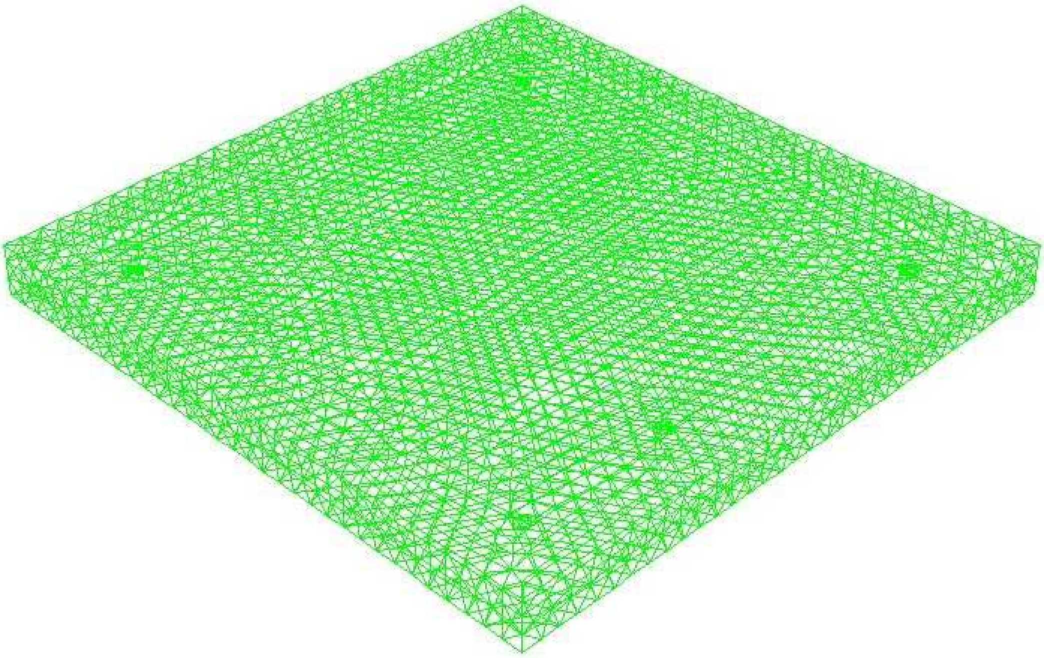

Figure 3.4: Matrix Mesh (FE)

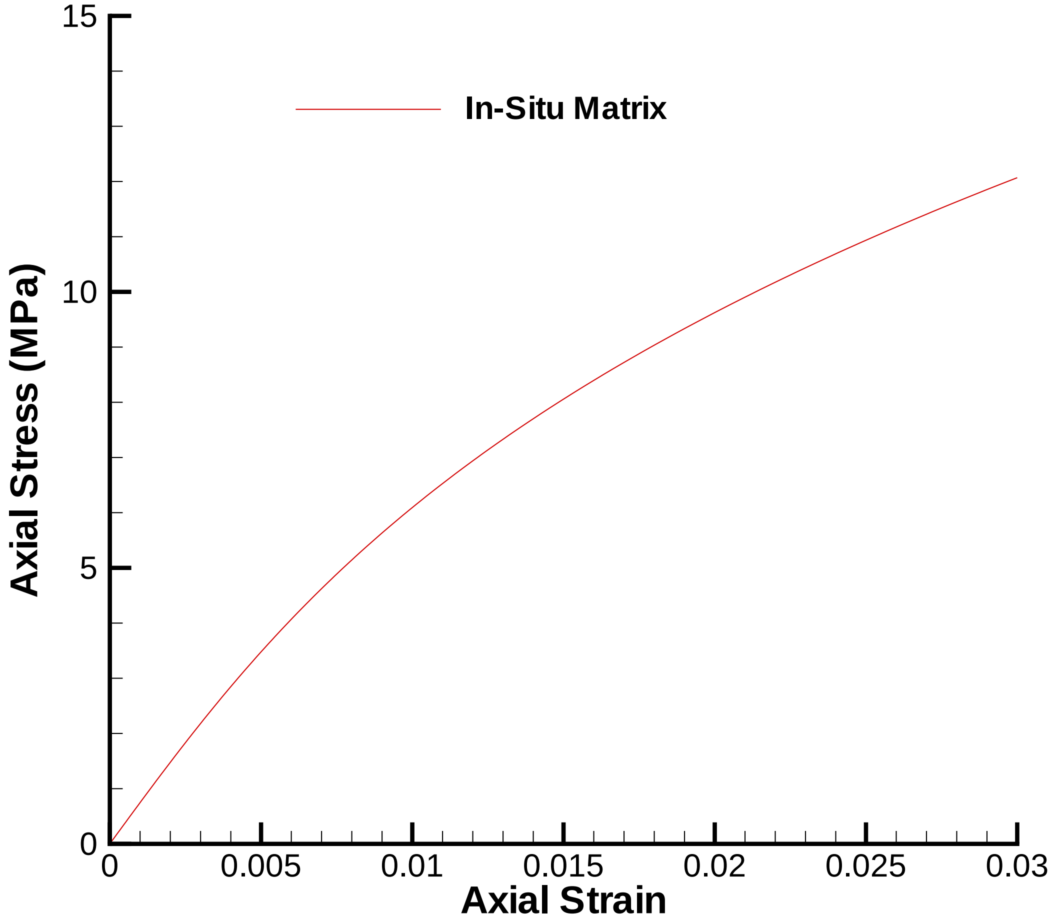

Figure 3.5: Final Axial Stress-Axial Strain Response Curve of In-Situ Matrix

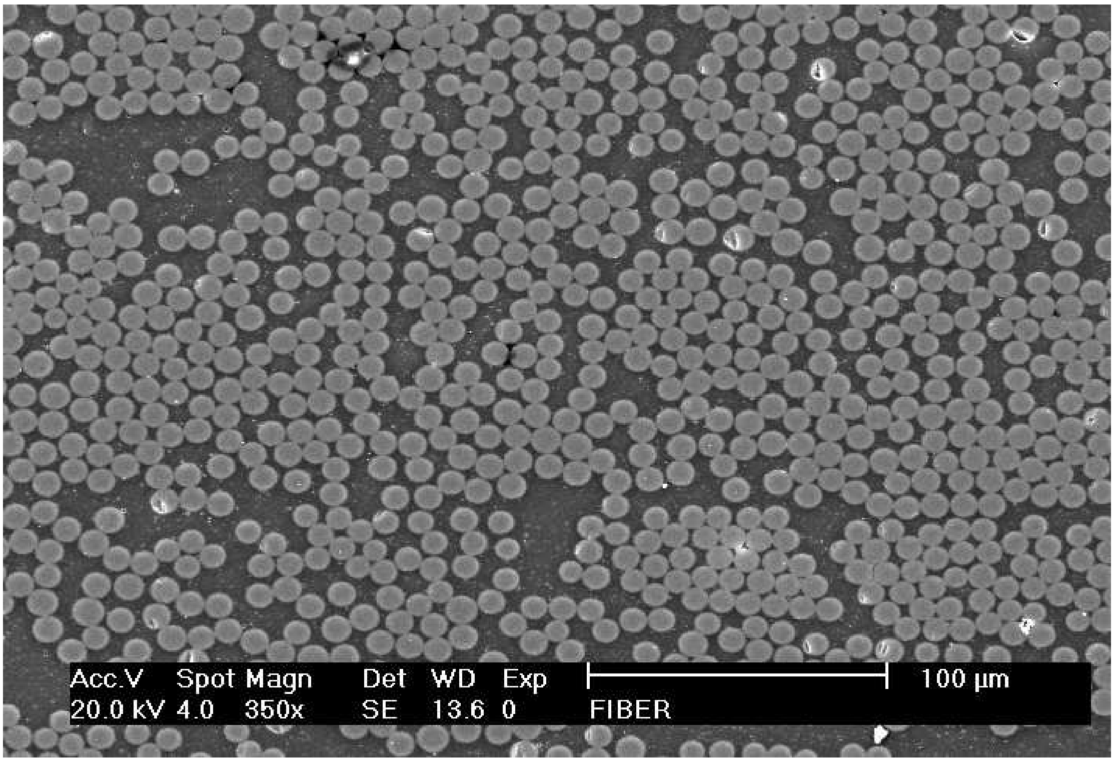

Figure 3.6: SEM Image of a Typical Fiber Tow

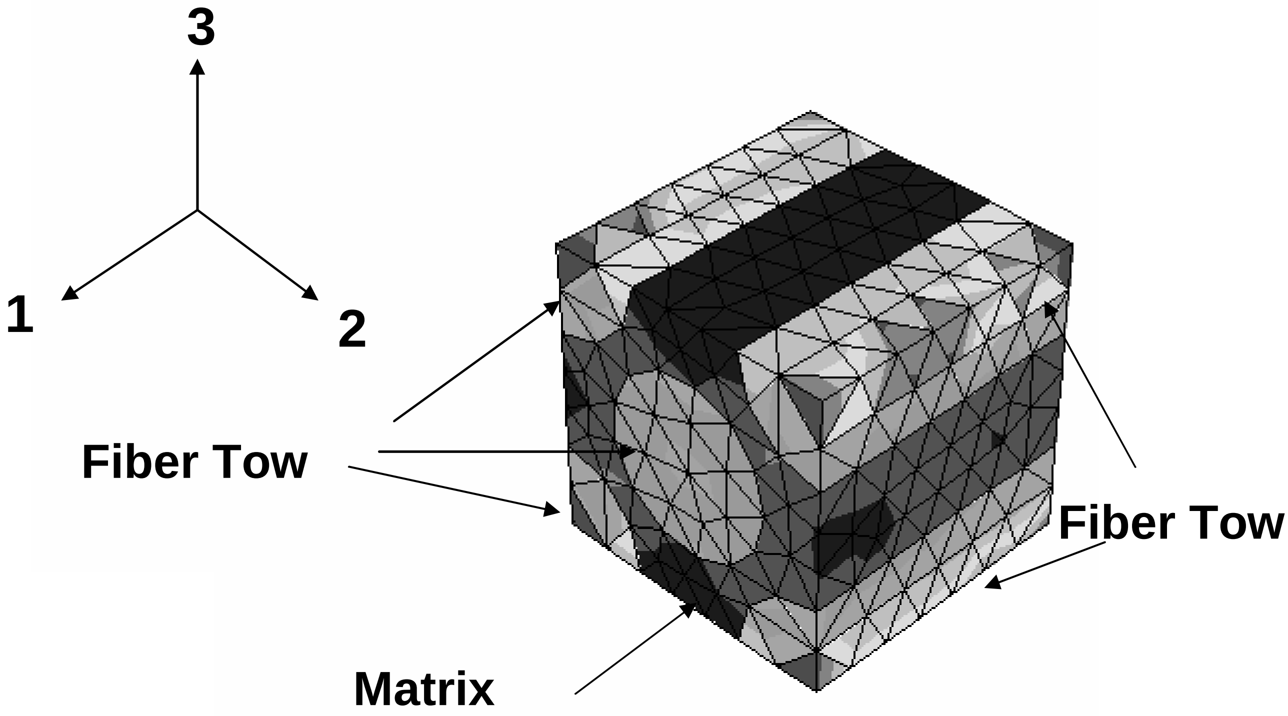

Figure 3.7: Illustration of the Representative Unit Cell of a Fiber Tow

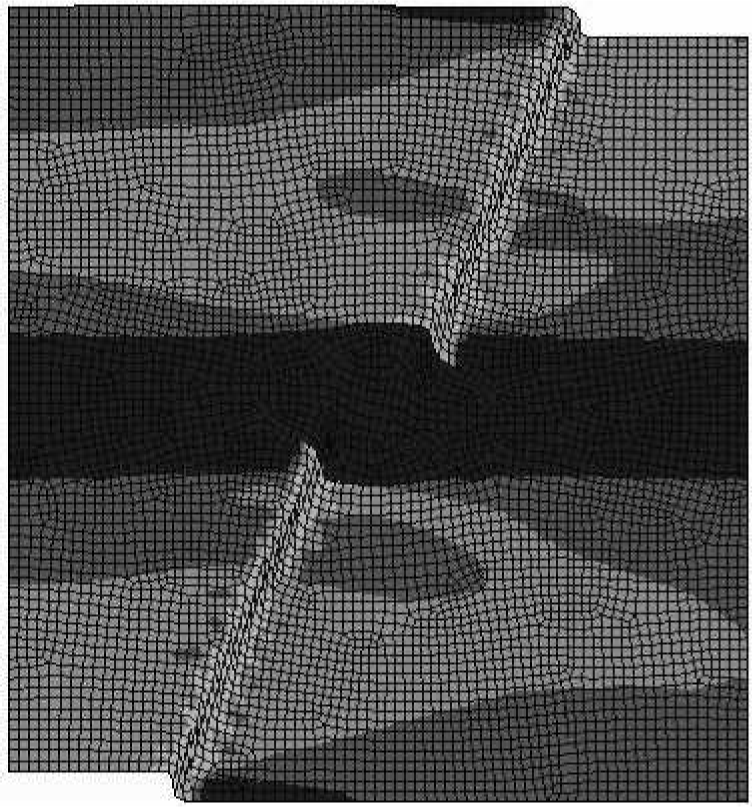

Figure 3.8: Failure Pattern of 1 RUC

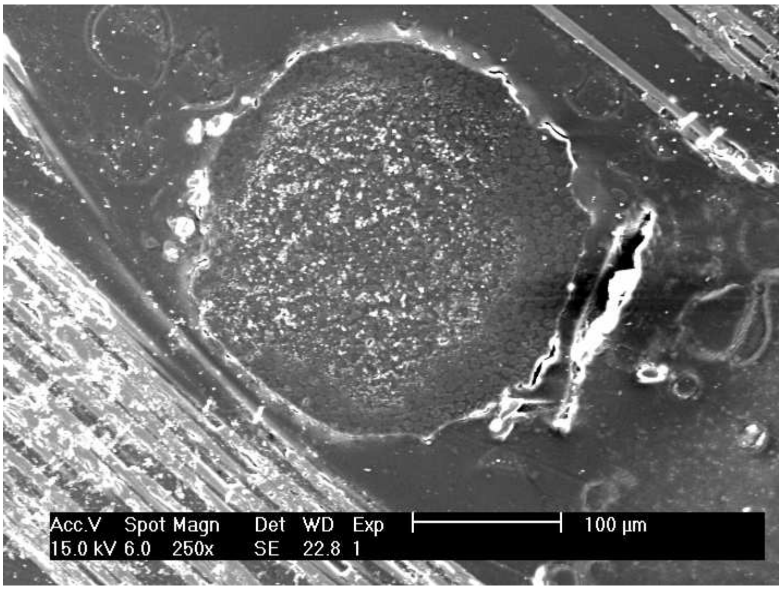

Figure 3.9: Damage Zone near the Z-pin

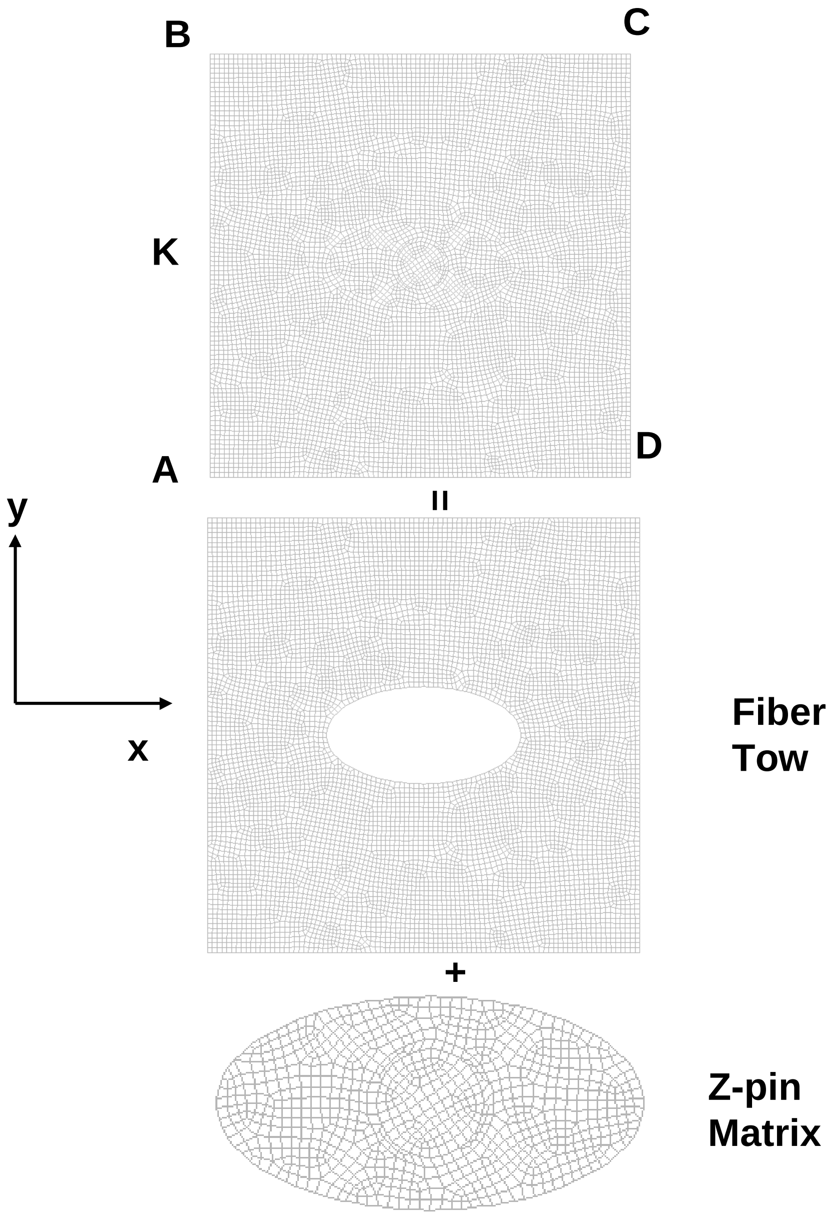

Figure 3.10: Illustration of 2D Model Unit Cell Constituents

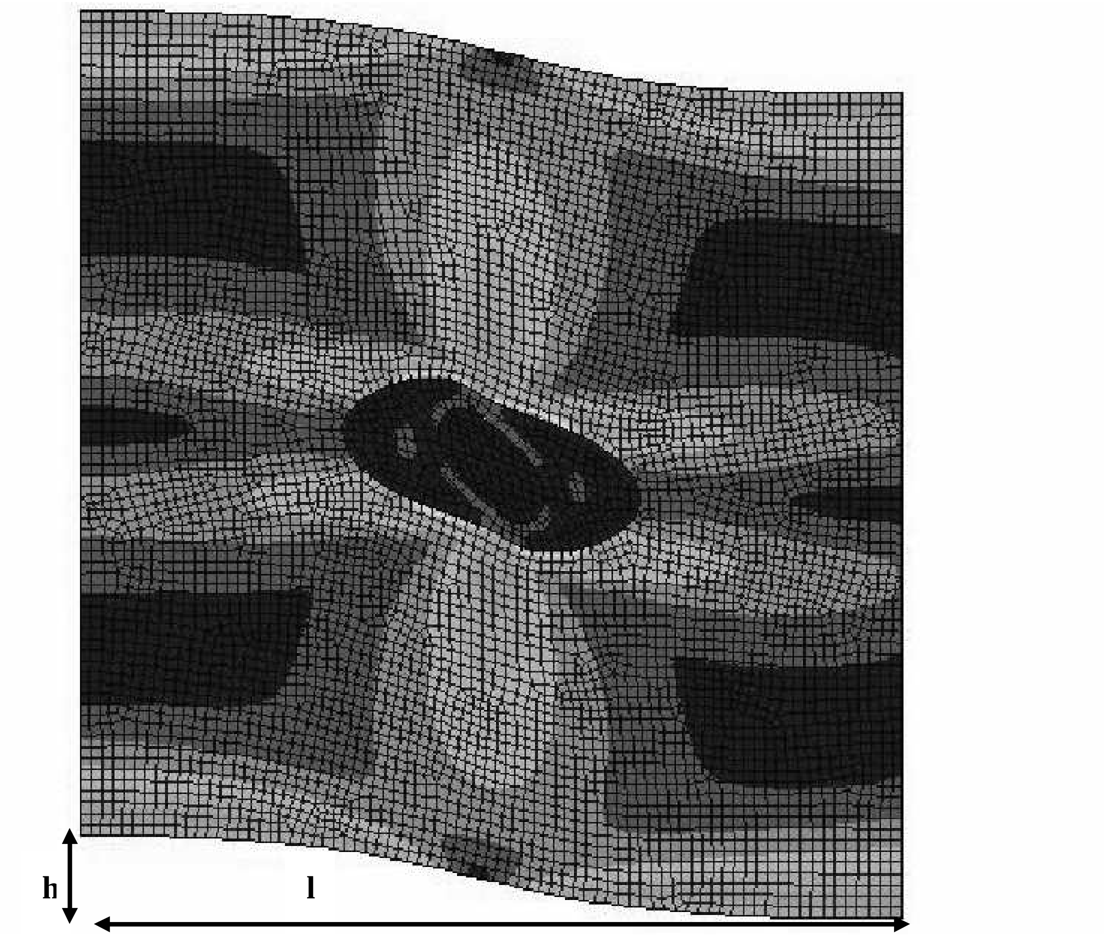

Figure 3.11: 2D Buckling Mode Used as the Initial Geometric Imperfection

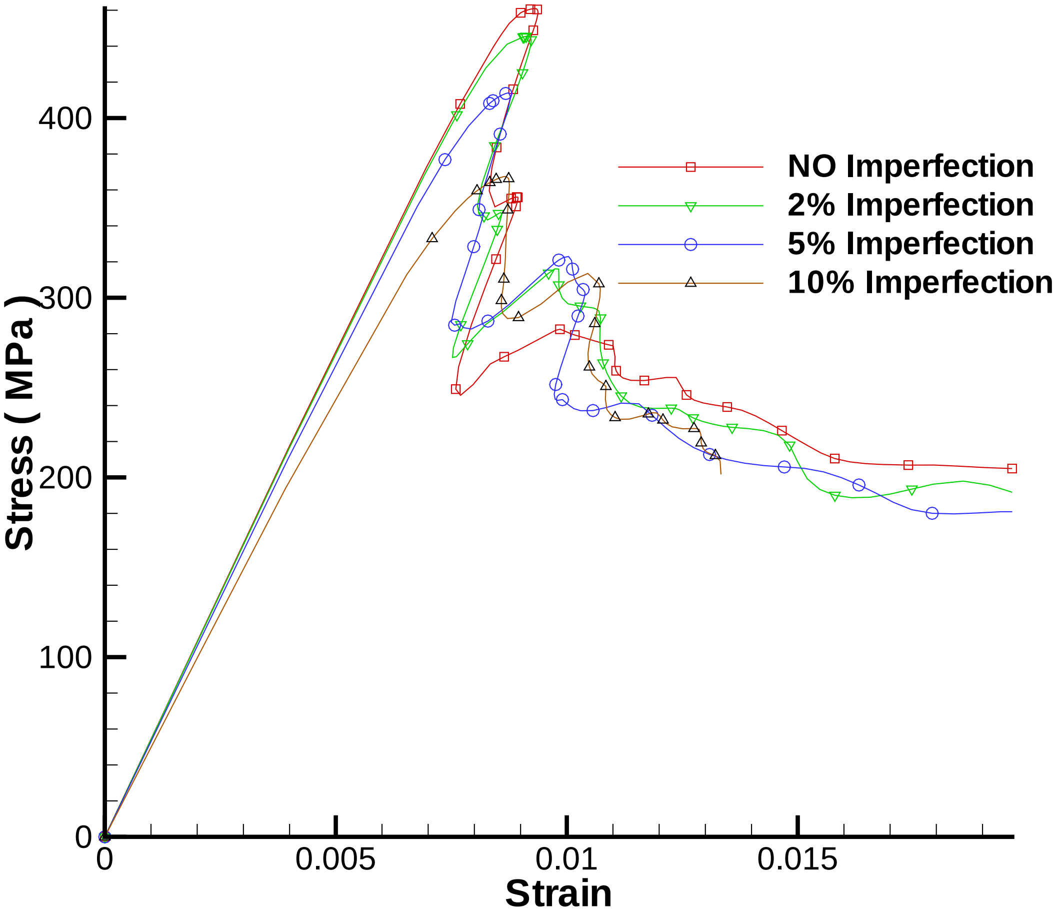

Figure 3.12: Results of Different Imperfection

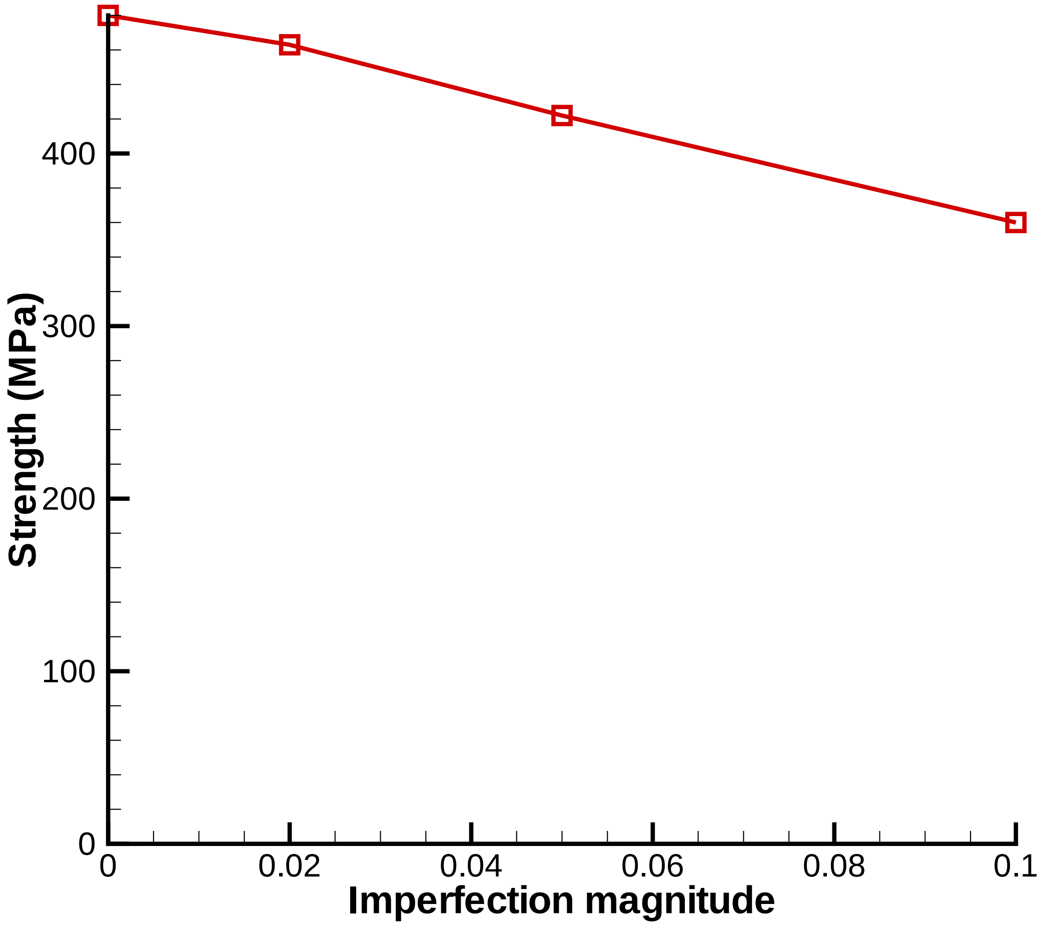

Figure 3.13: Effect of Imperfection on Compression Strength of Z-pin Composite (Z-pin Diameter=0.508 mm (0.02 in), 1% Density), and Global Initial Imperfection

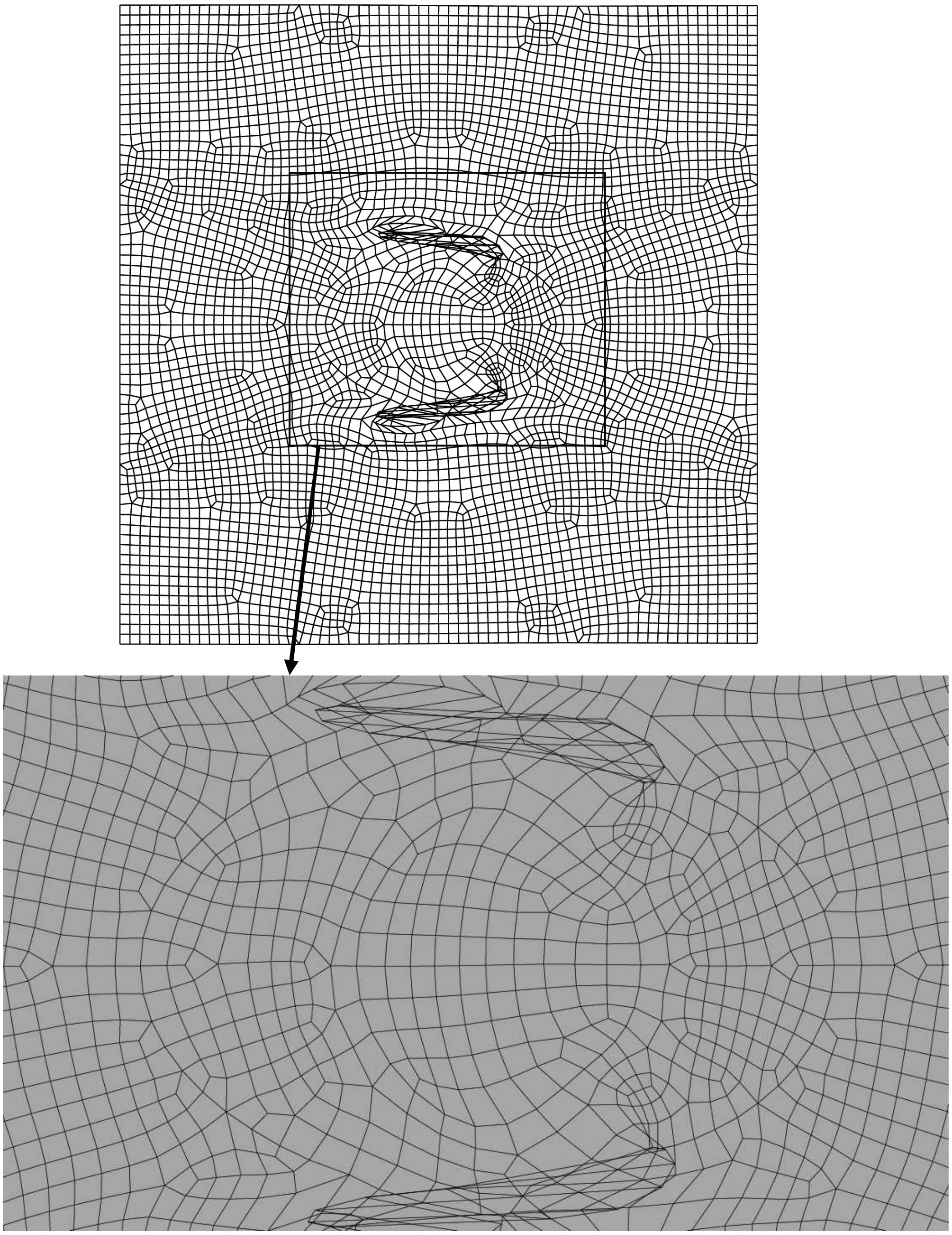

Figure 3.14: Local Buckling Mode

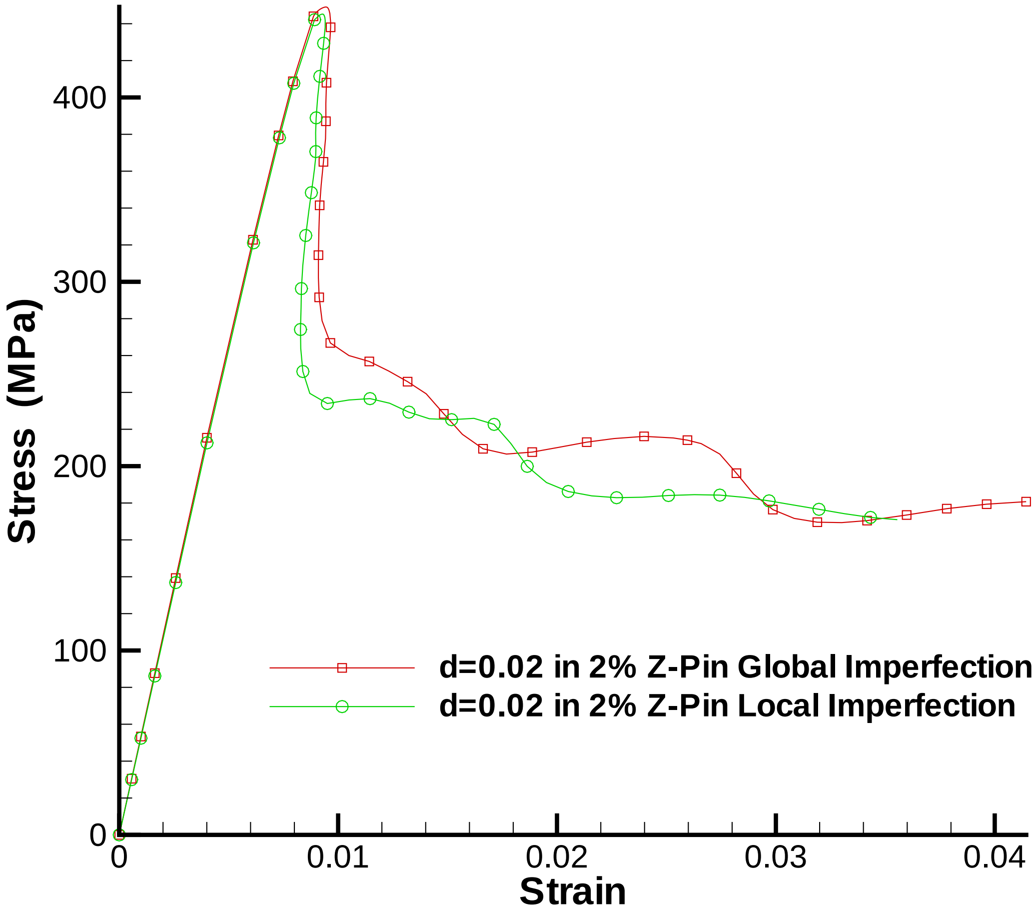

Figure 3.15: Comparison of Stress-Strain Curves for Global and Local Imperfection

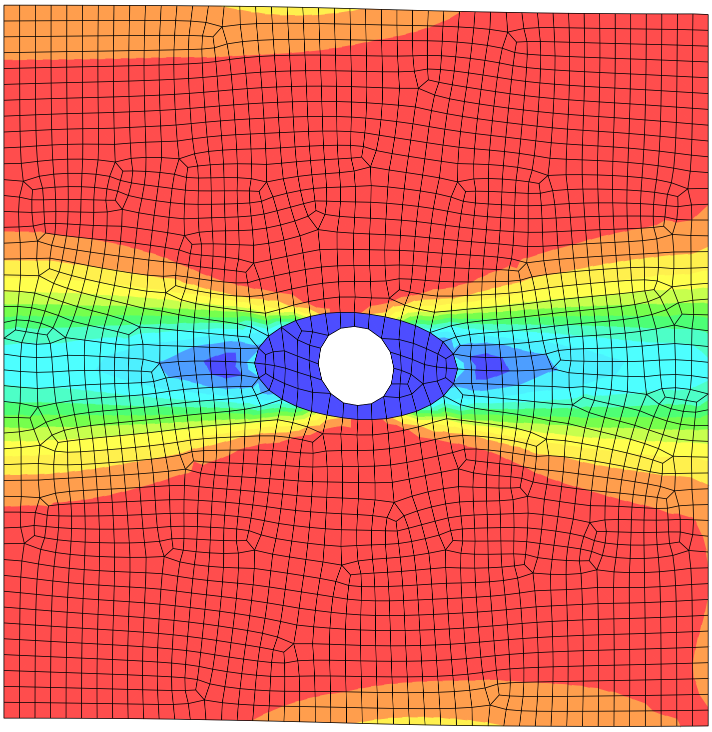

Figure 3.16: Finite Element Model of a Damaged Composite, where the Z-pin is Replaced by a Hole

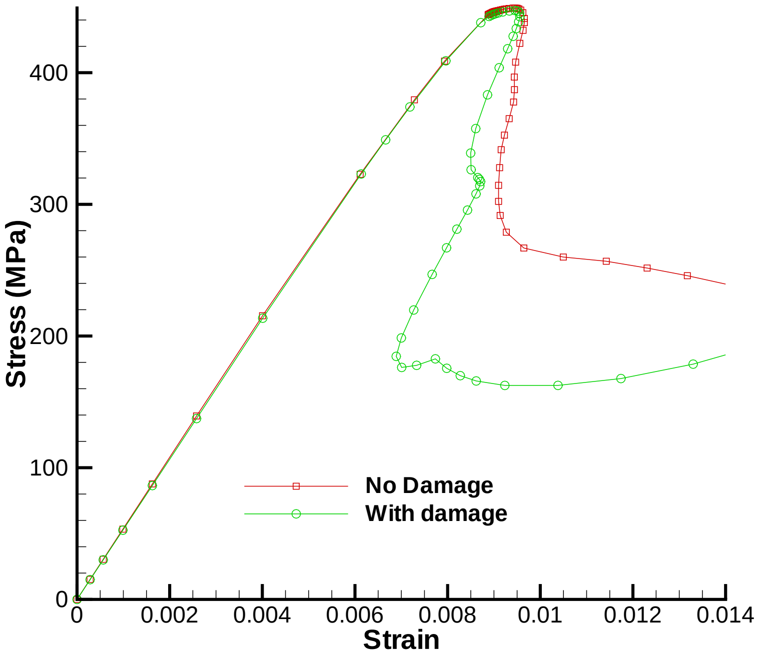

Figure 3.17: 2D Response Curve for Damage and no Damage Curve of a Composite with Z-pin Diameter of d=0.508 mm (0.02 in) and 1% Density

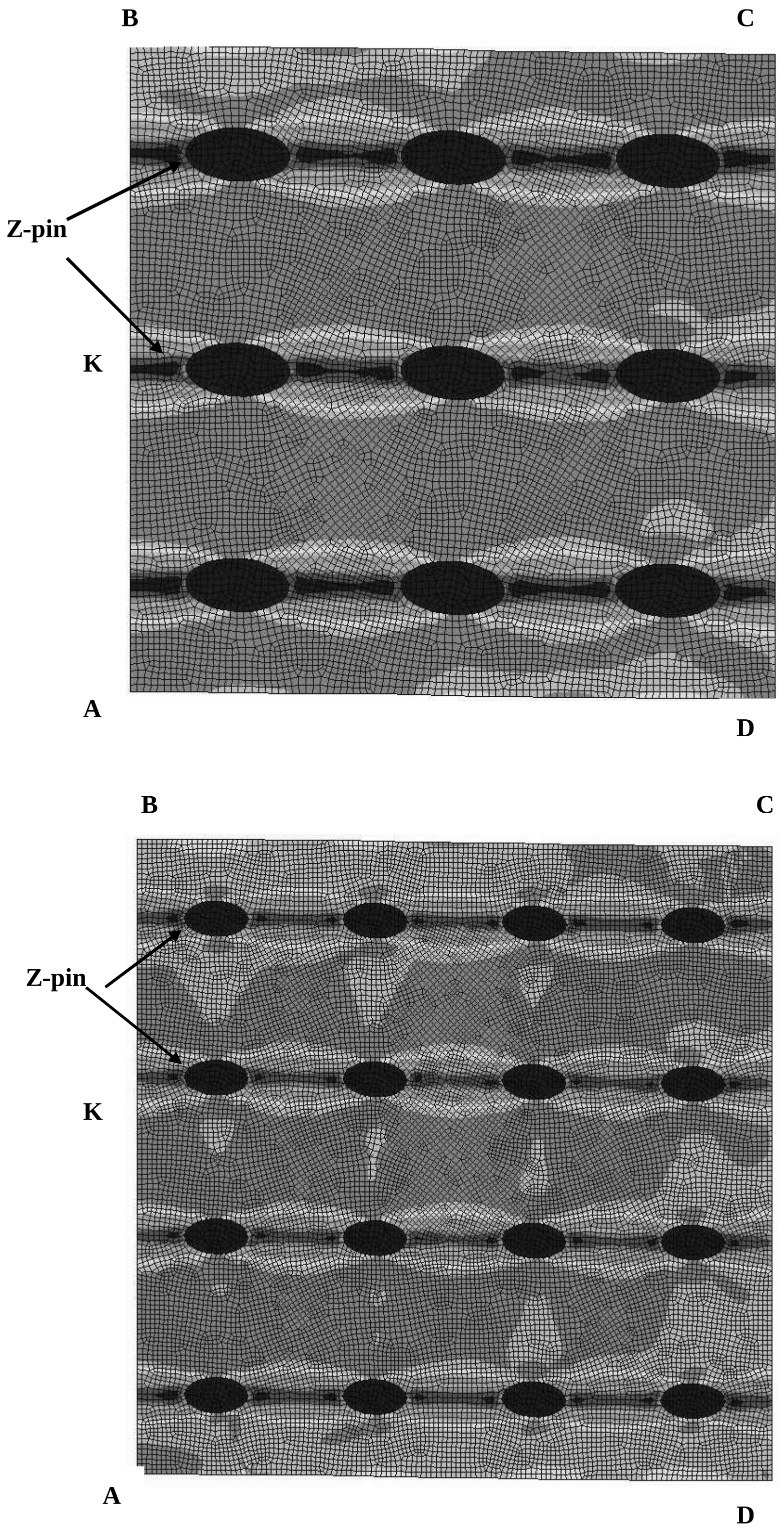

Figure 3.18: Finite Element Models of the 9 Unit Cell and 16 Unit Cell Representation of the 2D Problem Studied

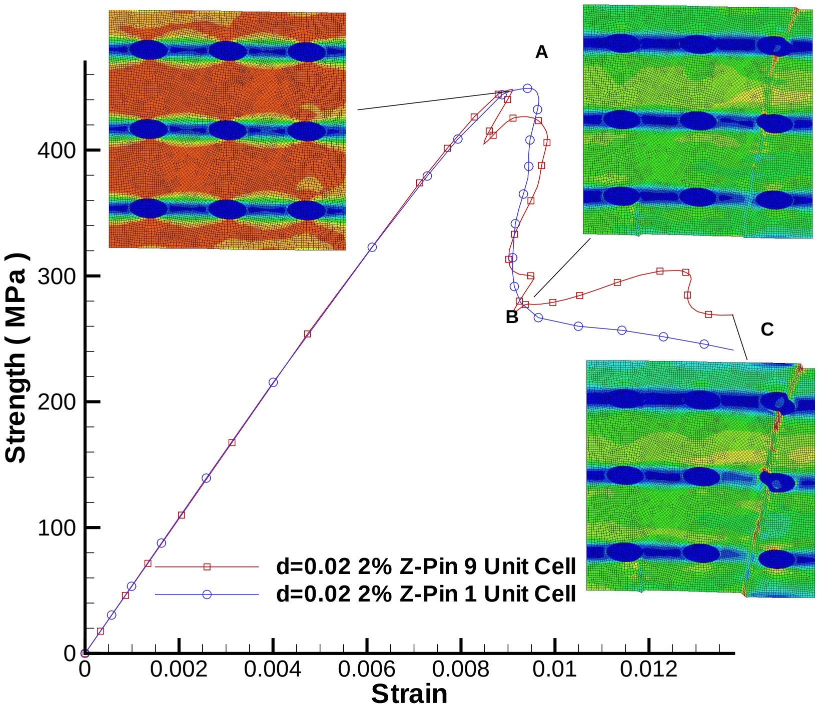

Figure 3.19: Stress-Strain Response of 9 Unit Cell Simulation. Note the Breaking of Symmetry at the Onset of Kink Banding

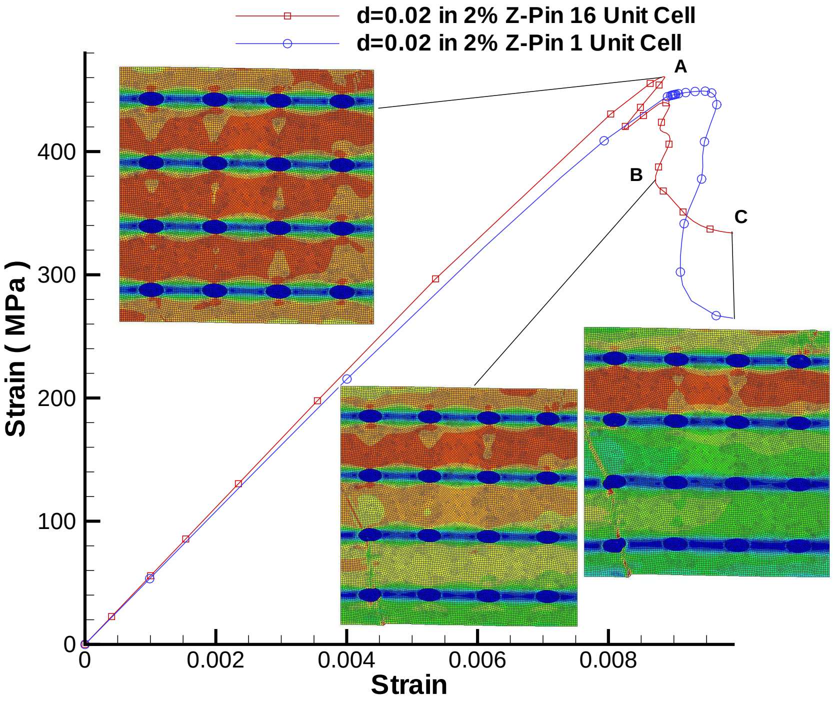

Figure 3.20: Stress-Strain Response of a 16 Unit Cell Simulation

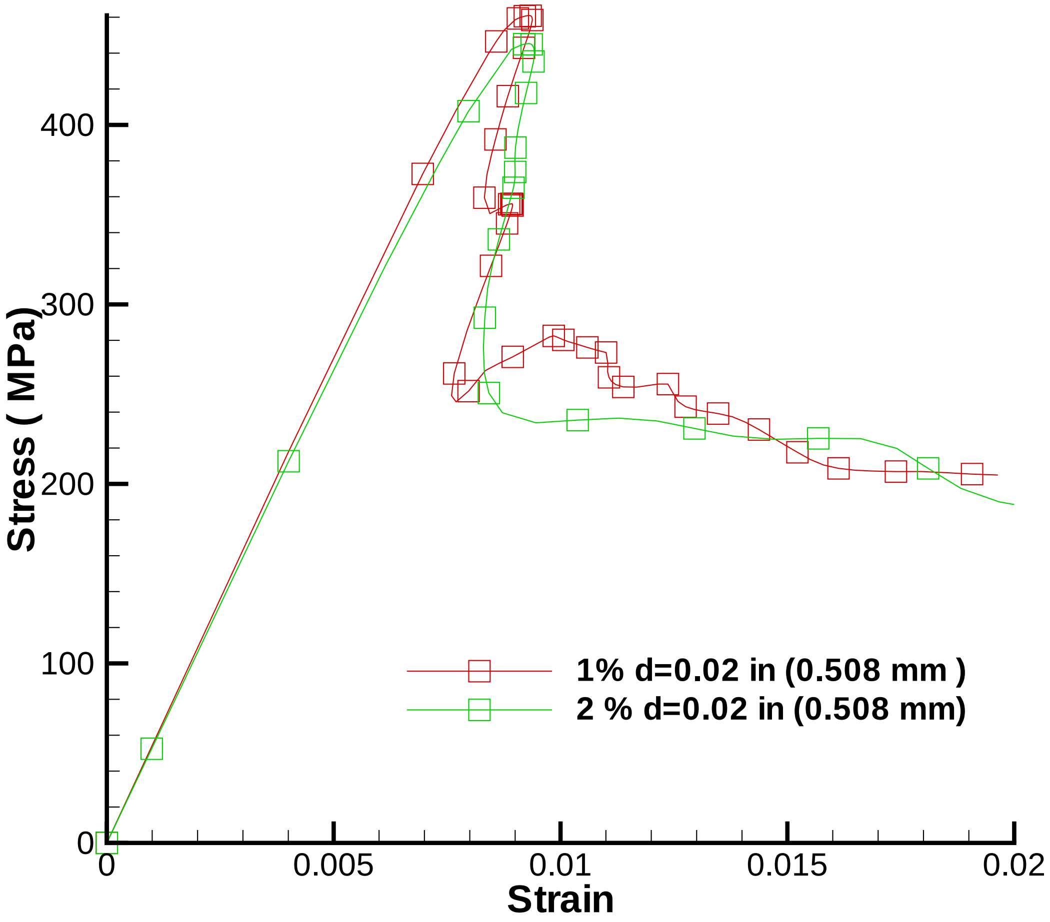

Figure 3.21: Comparison of Stress-Strain Curve for Different Density

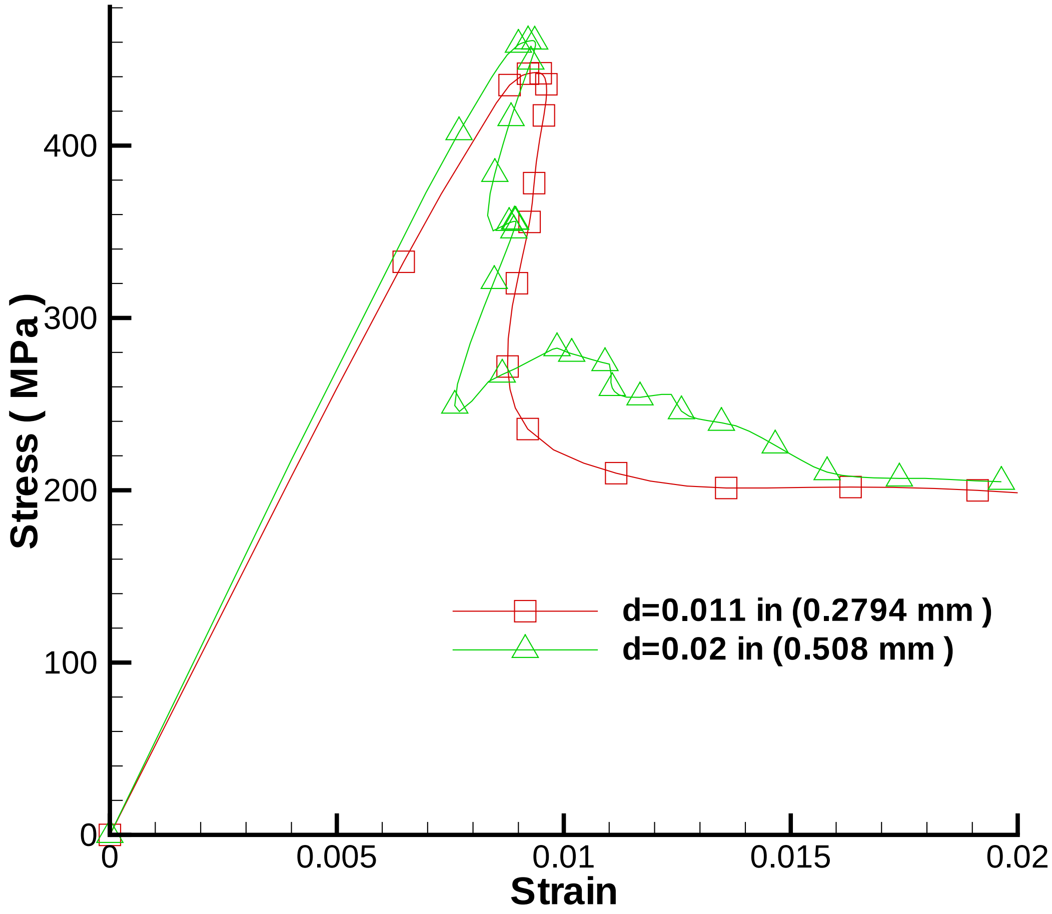

Figure 3.22: Comparison of Stress-Strain Curve for Different Diameter

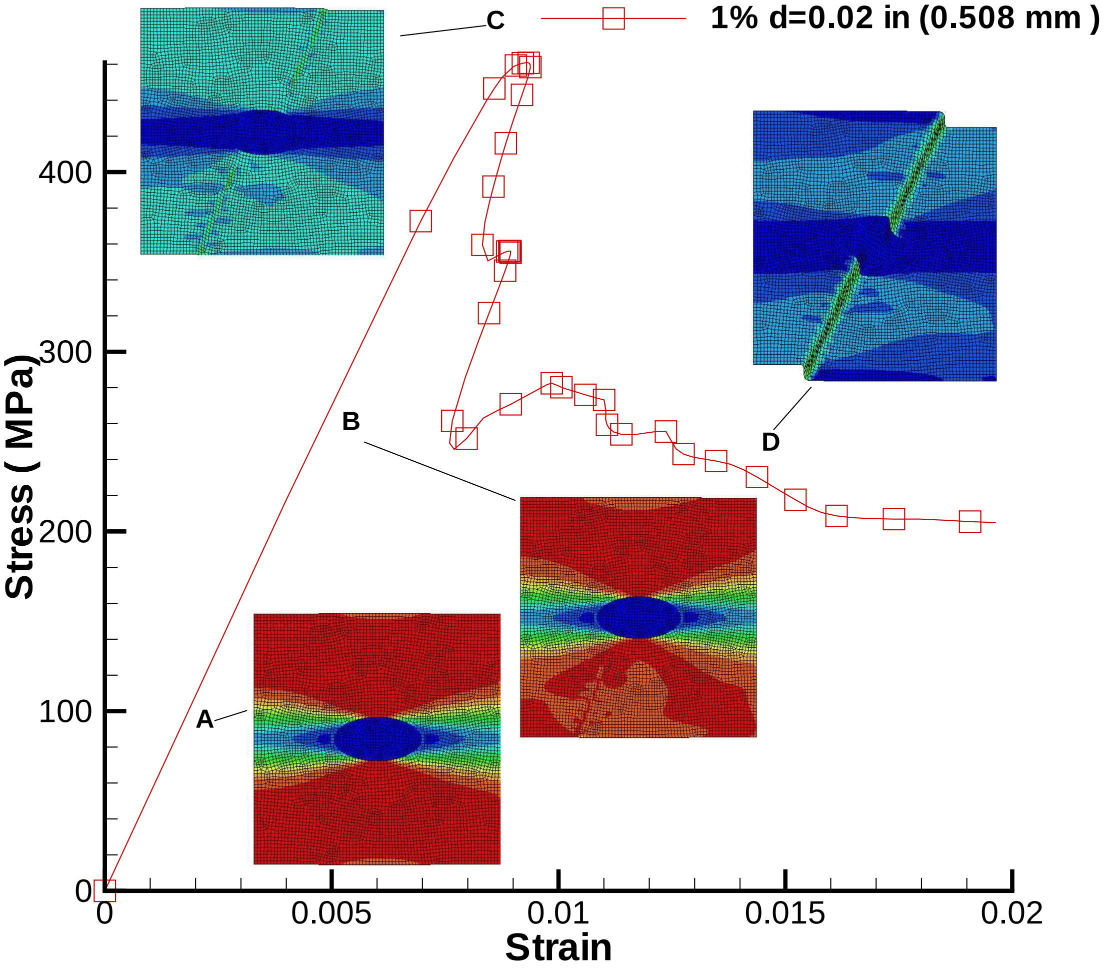

Figure 3.23: Kind Band in a Two Dimensional Model

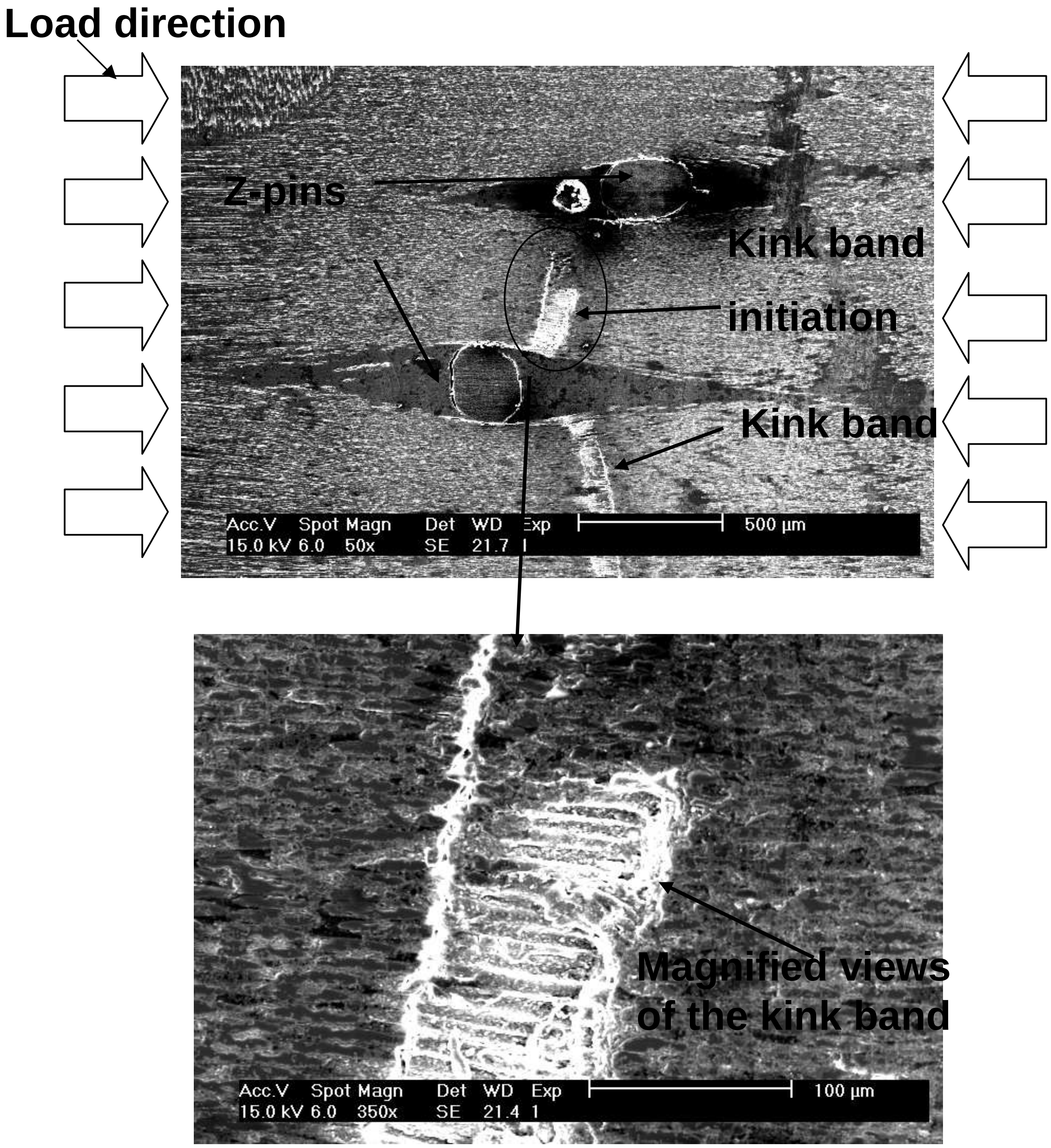

Figure 3.24: Kink Band in a SEM Image. Arrow Indicates Global Loading Direction

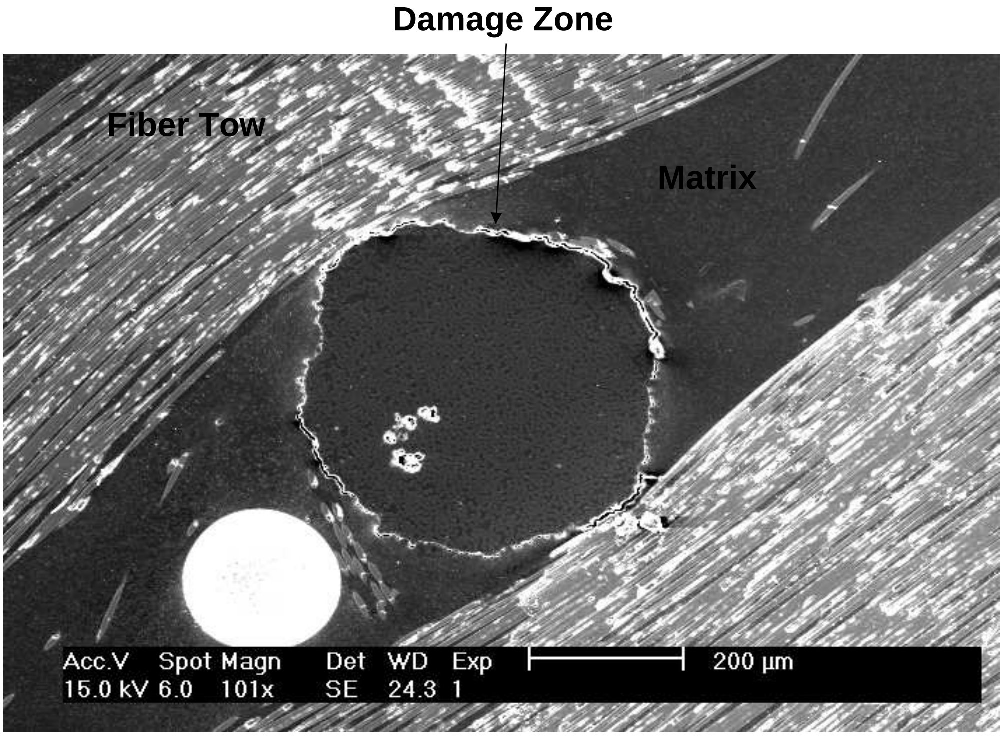

Figure 3.25: Z-pin Touches Fiber Tow Directly

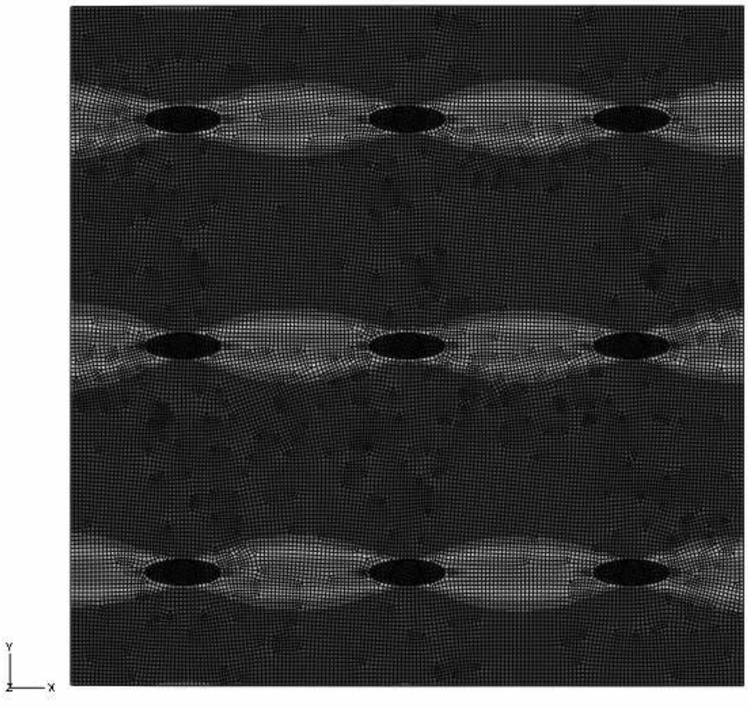

Figure 3.26: Models of Composites with d=0.0508 cm (0.02 in), 9 Z-pins, , and 1% Density

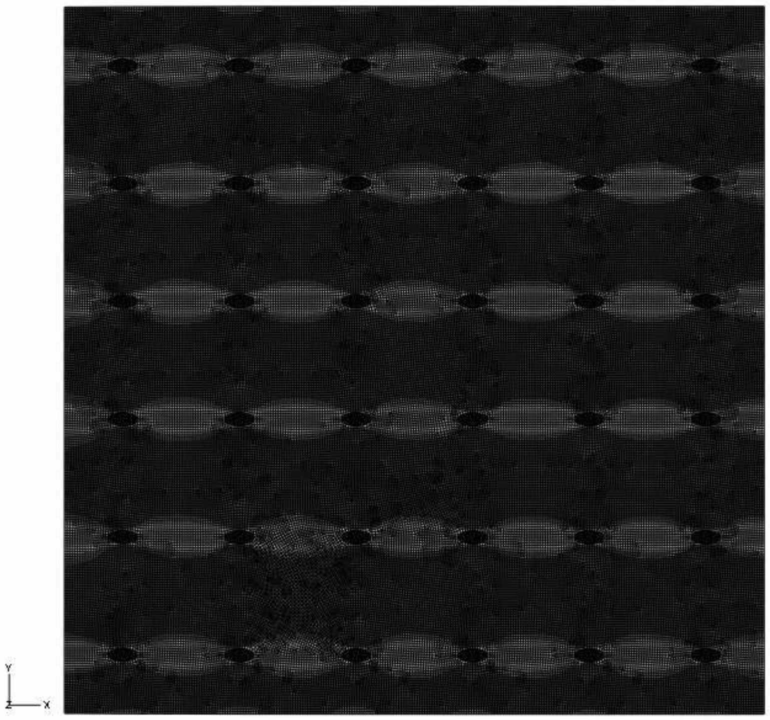

Figure 3.27: Models of Composites with d=0.0279 cm (0.011 in), 36 Z-pins, and 1% Density

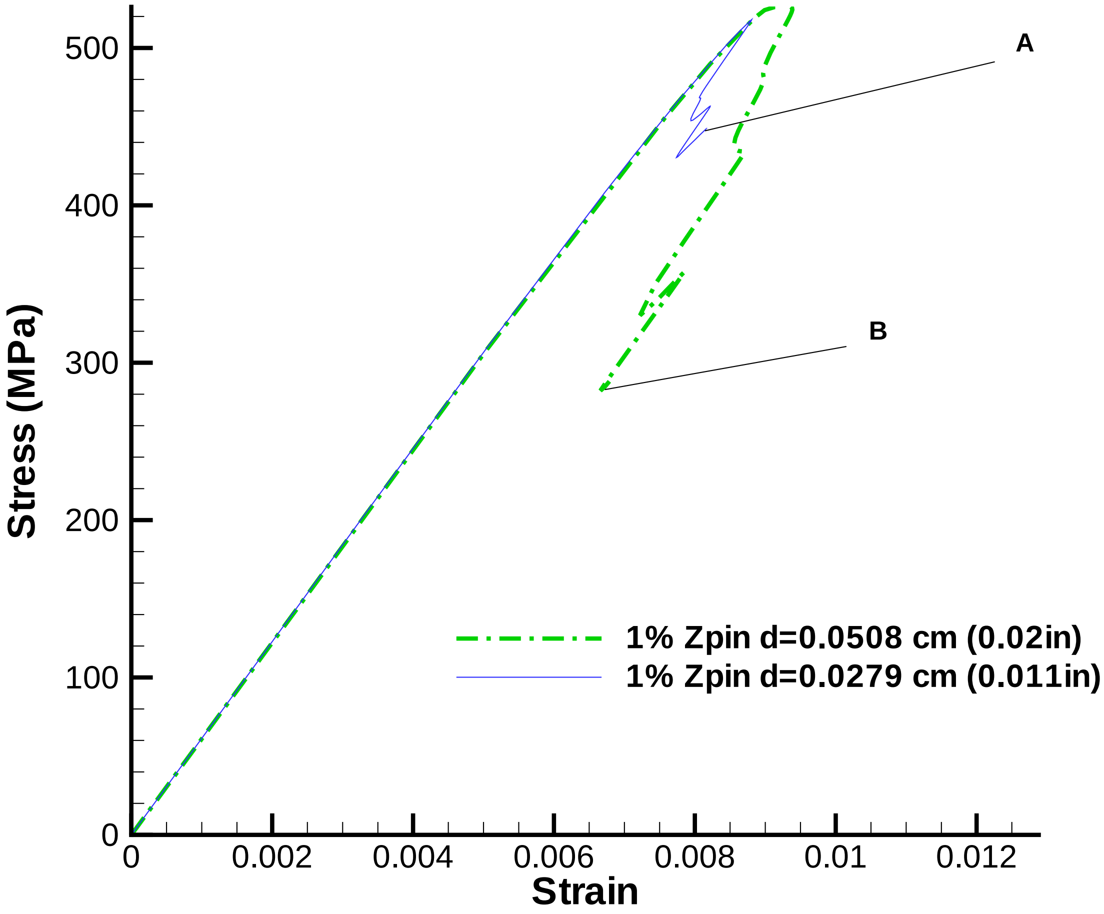

Figure 3.28: Comparison of the Composite with d=0.0508 cm (0.02 in) Z-pin Diameter and the Composite with d=0.0279 cm (0.011 in) Z-pin Diameter

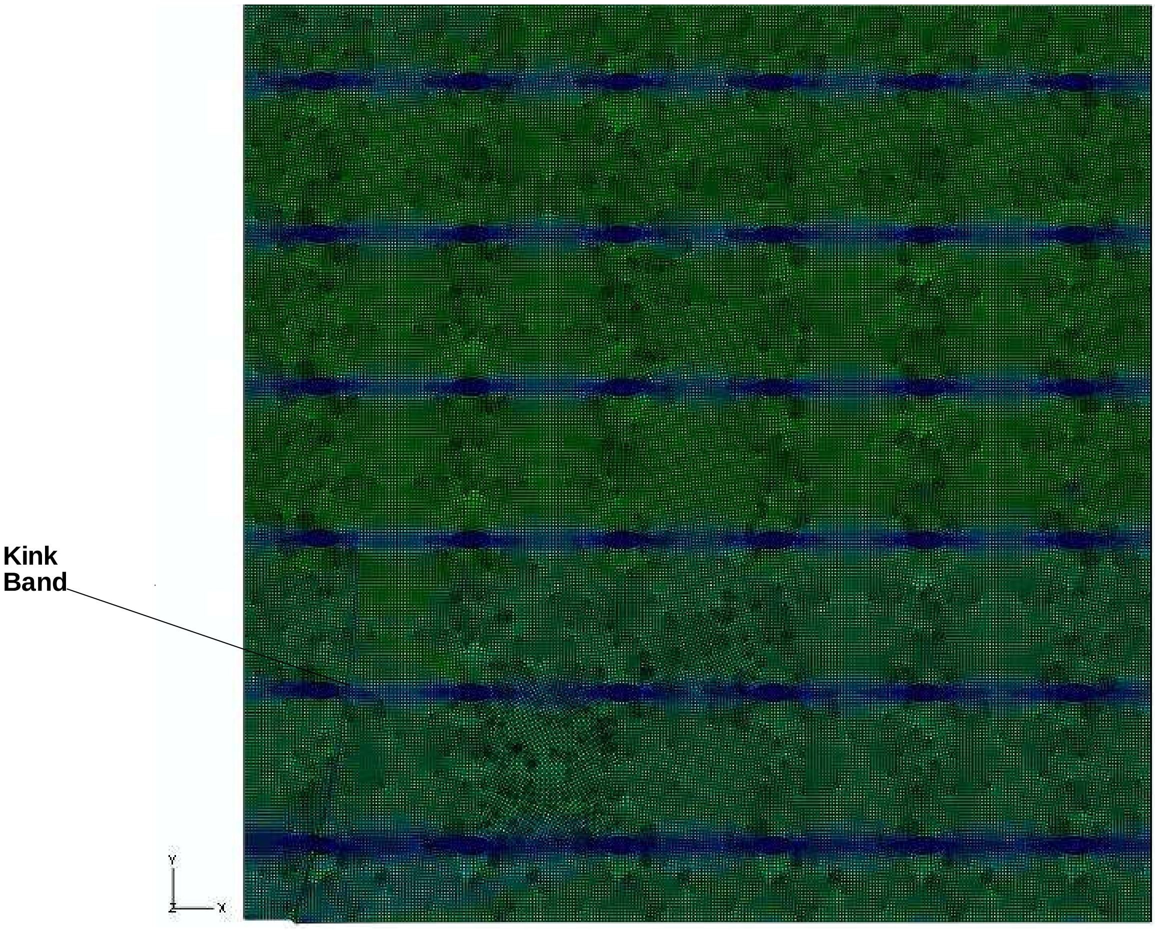

Figure 3.29: Kink Band of the Composite with d=0.0279 cm (0.011 in) Corresponding to point A

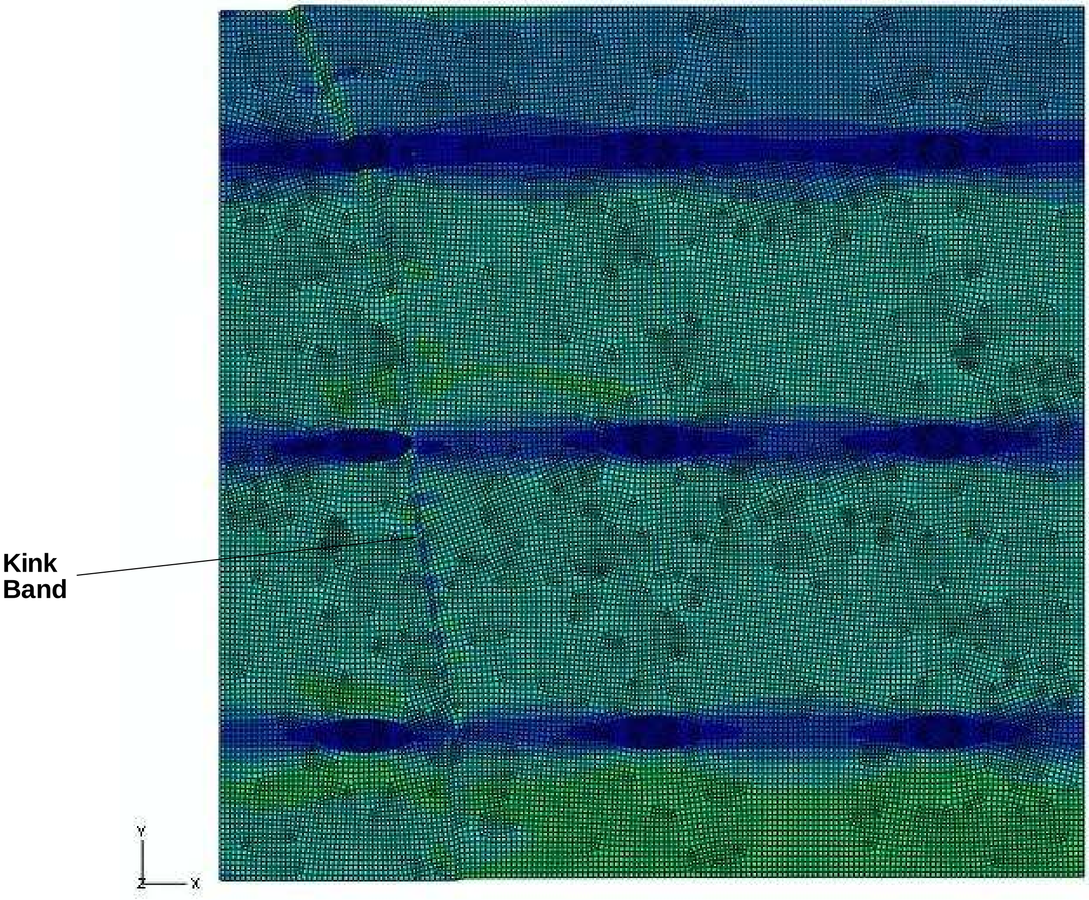

Figure 3.30: Kink Band of the Composite with d=0.0508 cm (0.02 in)corresponding to point B

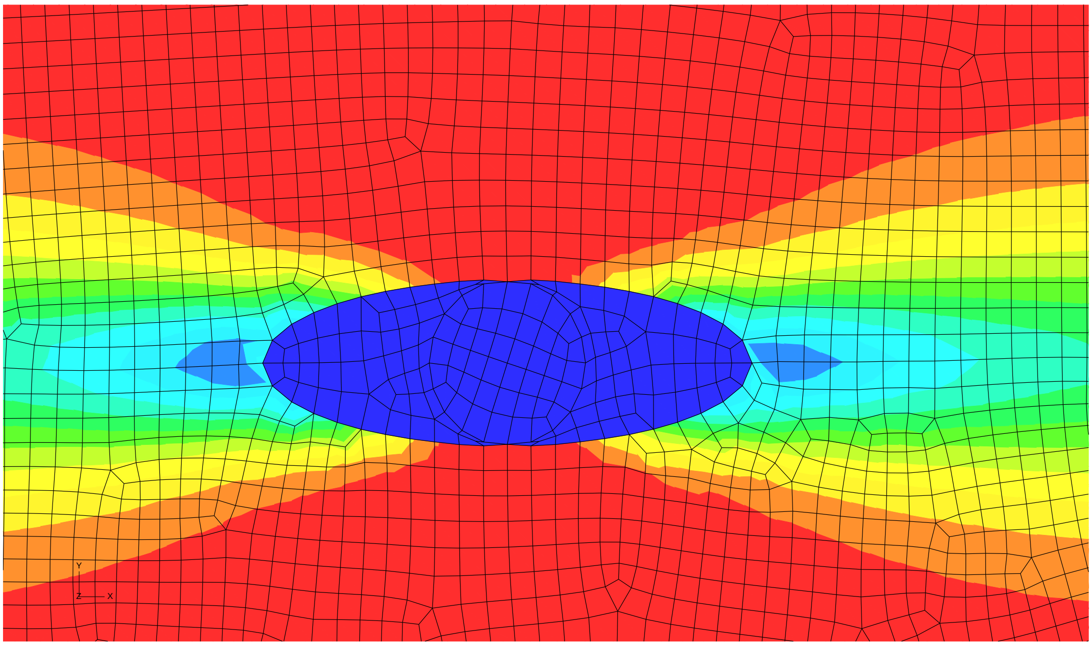

Figure 3.31: 1% Z-pin Composite with d=0.0508 cm (0.02 in) with Larger Matrix Surrounding Matrix. Note the Z-pin is Touching the Fiber Tow

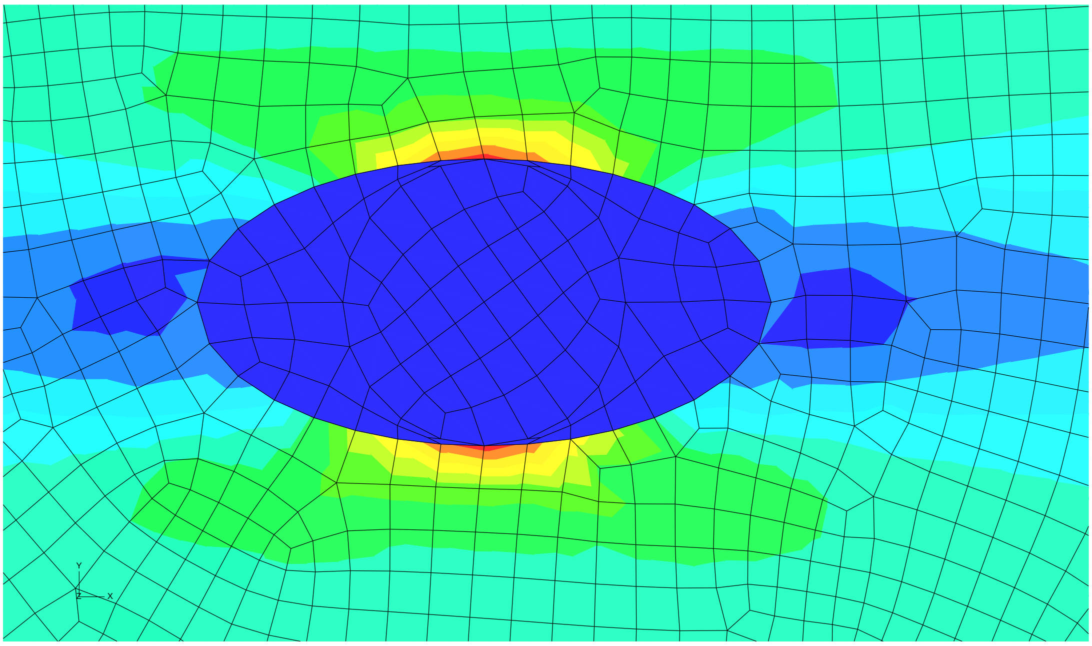

Figure 3.32: 1% Z-pin Composite with d=0.0508 cm (0.02 in) with Small Matrix Surrounding Matrix. Note the Z-pin is touching the Fiber Tow

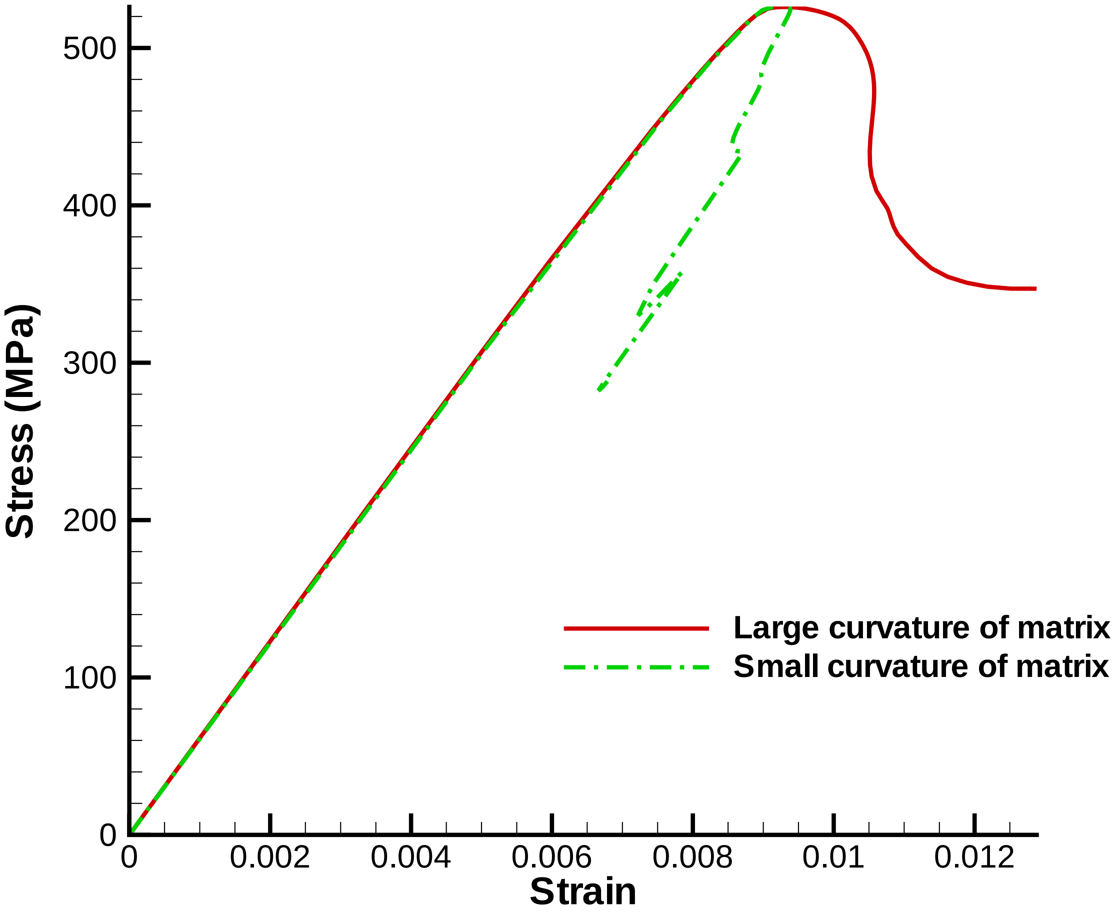

Figure 3.33: Comparison of Axial Stress and Axial Strain Curve for two 1% Z-pin Composites with Different Matrix Area

CHAPTER IV

Prediction of Compressive Strength in Multilayered Woven Z-pin Textile Composites

In chapter 2, experimental results for the compressive response and failure mechanisms of Z-pinned composites were presented. One unifying observation of the results was a similar failure mode sustained by *all* the specimens. Even though each type of the specimens (the different types and categories are listed in Table 1.1), has a different lay-up, different Z-pin diameter, or different Z-pin density, all of them failed by a local buckling instability that propagated across the specimens, in the process confining the failure to a narrow band. The planar view of a failed specimen and the side view of a failed specimen are schematically shown in Figure 4.2, while Figure 4.3 is the actual image of a failed specimen. In view of this observation, it is prudent to examine an approach in which the multi-layered aspect of the composite microstructure can be captured and at the same time providing a means to model all 16 layers of the laminate and the phase shifts associated with the stacking process. Since the failure occurs rather abruptly and spans the entire width of the specimens, in this chapter, a plane strain (2D) model of a 16 layer laminate will be developed as a means to predict the compressive strength of the laminates that have been examined experimentally.

4.1. Introduction

Many studies in the literature have assumed periodicity to choose a single RUC model of a textile composite for analyzing the stiffness of such structures ([42] and [20]).

In order to obtain the stiffness of the composites, the microstructural geometry has to be identified first. Analytical methods and finite element methods are quite successfully used to extract the stiffness and thermal properties of textile composites [44] and [31]. However, during the fabrication of a layered textile composite laminate, each ply of a laminate is not placed exactly on top of each other. Because of this, and because the dry textile fabric materials are infused with resin during the manufacturing, the layers of a cured solid laminate show a phase shift. The effect of phase shift on the compression stiffness and strength of a textile composite has not been studied before. In view of the experimental observations in chapter 2, a 2D plane-strain finite element (FE) model of a Z-pinned textile composite is developed in this chapter, using the plastic potential developed for the fiber tows in chapter 3, and using the in-situ matrix response that has also been presented in Figure 3.5 in chapter 3.

4.2. 2D Finite Element Model

4.2.1 2D Finite Element Model in 1-2 Plane

In this subsection, a 2D finite element model is proposed for the reasons described earlier, namely, that the failure mode is approximately invariant in the “width” direction of the laminate (the width direction is the ‘3’ direction). Consequently, as a first step, we can assume plane strain condition in the 1-2 plane. Furthermore, a 2D model is less expensive than the more detailed 3D models that will be described in chapter 5, which are computationally more intensive.

In the literature, one layer based numerical models are widely used to predict the strength of textile composites. The shortcoming of this one layer based model is that the effect of phase difference between different layers are not taken into consideration. In 3D FE simulations, parameters, E_{11} , E_{22}, ν_{12}, G_{12}, and G_{23} are used to represent the elastic properties of a 3D transversely isotropic fiber tow. In a 2D setting, only four of these, E_{11} , E_{22}, ν_{12}, and G_{12}, are needed. The two dimensional plastic potential is obtained from simplifying equation (3.1) to the 2D case by retaining terms that are independent of the '3' direction. That is,

$$f \quad = \quad [(\sigma_{22})^2 + 2a_{55}\sigma_{21}^2] \tag{4.1}$$

In this subsection, three 2D models are first built first in order to explain how to properly establish the 2D model from a 3D model. Subsequently, two of these models are used to study the influence of phase difference on the compressive response of the woven composites.

The fiber tow architecture in a 3D model (cross-ply composite) is shown Figure 4.4. Note that numerical models built and based upon the cross-ply composites are used to perform simulations in this chapter. When a 3D model is replaced by a 2D, 1-2 plane model, different microstructures in the 1 -2 plane are obtained depending upon which cross sections are chosen in the simulations. For example, the 1-2 plane cross sections cut from plane AA and plane BB in Figure 4.4 are different. The difference between the models from cutting plane AA and cutting plane BB is the following: The 2D model cut from plane AA in Figure 4.5 contains only matrix and fiber tows undulating in the unloading direction. However, the 2D model cut from plane BB in Figure 4.9 contains matrix, fiber tows undulating in the unloading direction, and fiber tows in the loading direction. The addition of the axial (longitudinal) fiber tows makes a significant difference as will be evident shortly.

4.2.2 Details of the Models and Finite Element Implementation

The model AA, as was explained earlier, has no axial fiber tows, while the model BB contains 16 axial fiber tows. However, an examination of the cross-section of an actual specimen in Figure 4.1 shows that there are only 13 axial fiber tows in a cross section. This is because not every layer of a laminate is stacked exactly with the same phase as each other. During the molding and consolidation process, there is movement of lamina, resulting in a phase difference among the stacked layers. To account for this, a third model, similar to the model BB, but with 13 axial fiber tows was meshed and is referred to as model CC as shown in Figure 4.6. The CPE4 Plane strain element was used in the ABAQUS simulations. These plane strain, isoparametric finite elements, have 2 displacement degrees of freedom at each node and linear interpolation shape functions are used as described in [5]

4.3 Results and Discussion

4.3.1 Influence of Phase Difference on the Strength of the Woven Composites

Displacement control loading in conjunction with the Riks arc-length solver option available in ABAQUS was used to subject models AA, BB, and CC to uniaxial compression in the x-direction. As shown in Figure 4.7, the boundaries PQ and SR are left free, while the boundary QR is free to move in the y-direction and is constrained in the x-direction. The boundary PS is subject to a uniform compression (displacement control) in the x-direction, while being free to move in the y-direction. Initially, all these models display a linear response between macroscopic applied stress (the resultant total reaction force in the boundary QR, in the x-direction, divided by the cross section area of the loading face ; the thickness in the z-direction is uniform and assumed to be one unit in dimension), and the macroscopic average strain (total specimen shortening divided by the length of the specimen in the x-direction), as indicated in Figure 4.8.

The linear stiffness obtained from the model AA is relatively small compared to that from the model BB and the model CC. This is as expected because the model AA doesn't contain any axial fiber tows. These tows are the most important part in sustaining compression in the axial direction. The Young's modulus of the model BB is slightly higher than that obtained from experiments. This is because the model BB contains 16 axial fiber tows, thus having a higher Young's modulus than that from experiments. The Young's modulus of the model CC matches the experiments very closely because the model CC is established based upon the observation of 13 axial fiber tows in Figure 4.1.

From the discussion above, it is concluded that cross sections such as the one shown in Figure 4.1 should be used in order to establish the 1-2 plane model proposed in this chapter. Otherwise, the results of the simulation will not be meaningful, when compared against the experimental observation.

Two other "ideal" models are established from cutting plane BB. The first model has no phase difference among its 16 layers of laminae as shown in Figure 4.9. In the second model, shown in Figure 4.10, the phase difference between two neighboring laminae is $\frac{\pi}{2}$. Note that the fiber tow assumes a sinusoidal shape in the x-direction. Therefore, the same phase of laminae can be seen after a depth of 4 layers. That is, the first lamina and the fifth lamina have the same phase while being packed as a laminate in this model. The results of the compression response simulations for these two models are shown in Figure 4.11. It can be seen that the model with phase difference has a higher strength than the model that has no phase difference. For the model with no phase difference, each layer tends to have similar deformed shape. Therefore, the deformed shape of the entire laminate in different laminae looks uniform. For the model with phase difference, different layers of the laminate tend to have different deformed shape. The combination of different deformation in different laminae result in uniform deformation for the whole laminate. The kink band angles as defined in Figure 2.18 for the model with phase difference and the model with no phase difference are approximately 21° degrees and 24° degrees. Since the models are established from cross-ply composites without Z-pins, these two kink band angles are compared with the kind band angles of group F from experiments as shown in Table 2.4. The kink band angles from simulations are smaller than the kink band angels from experiments. This is because, in the experiments, the fiber tows are broken at the kink band boundary, thus releasing additional energy and settling at larger angle.

4.3.2 Influence of Z-pin on the Strength of the Woven Composites

In this subsection, two models are established based upon the cross section of a real cross-ply laminate. One model contains Z-pins and another model contains no Z-pins. The 1-2 plane 2D model shown in Figure 4.12 is based on the packing as shown in Figure 4.1. Another model includes the through-the-thickness Z-pin as shown in Figure 4.13.

Figure 4.14 shows the macroscopic stress-strain curves of the composites with no Z-pin and 1% Z-pin composites with diameter of 0.02 in. It can be seen that the result of the simulation is close to the observed experimental results. The composite with Z-pins has less strength than the composites with no Z-pins. The deformed shape of d=0.02 in composites at different deformed stages “A”, “B”, and “C” are shown in Figure 4.15 , Figure 4.16, and Figure 4.17. Figure 4.15 is the deformed shape at the highest strength A. At point B, it is observed that there is slight kink band in the structure. At the same time, the load decreases and the strain increases gradually. The fully developed kind band in the deformed shape can be seen in Figure 4.17. The kink band angle (in Figure 4.17) as defined in Figure 2.18, is 32° degrees. This kink band angle is within the range of kink band angles (between 30 to 45 degree) from Table 2.3 and Table 2.4.

4.4. Conclusion

In this chapter, a plane strain 2D model condensed from a 3D model is presented for predicting and capturing the local compressive failure mode observed in experiments. This 2D model is presented in order to simulate multi layer composites. The cross section used in this 2D model can’t be chosen arbitrarily. The “correct” cross section should include axial fiber tows such as the real model shown in Figure 4.1. The results indicate that it might not be a good design if each lamina in a laminate has the same phase. It is found that composites with phase difference has higher strength than composites with no phase difference. “In-plane” composites promote kink banding failure at a lower peak compression strength compared against laminates that have have no uniformity in the phase of stacking.

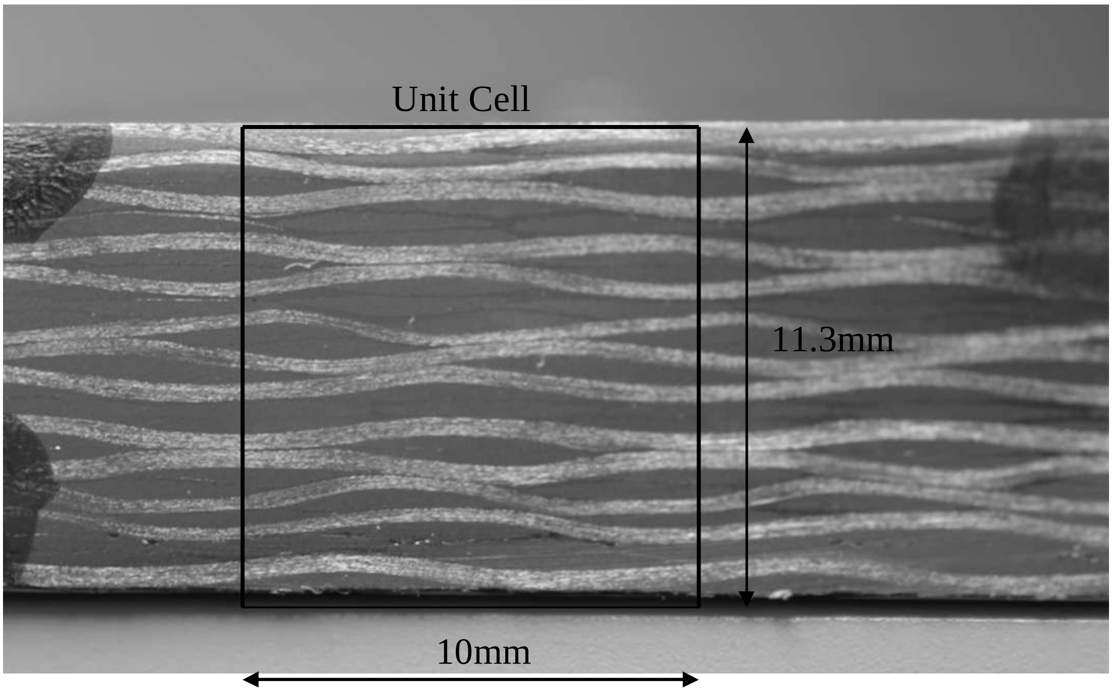

Figure 4.1: Side Image of a Cross Section. Notice that Phase Shifts between Axial Tows (Lighter Shade) of Different Laminae

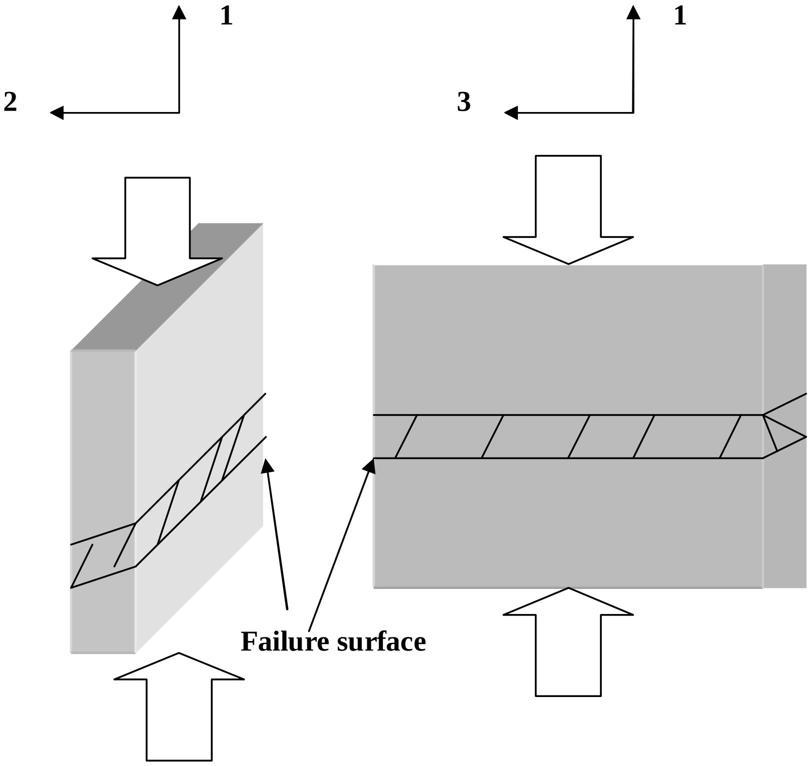

Figure 4.2: Schematic of a Failed Specimen Viewed in the 1-2 Plane and the 1-3 Plane (Commonly Observed for All Types of Specimens Studied in this Thesis)

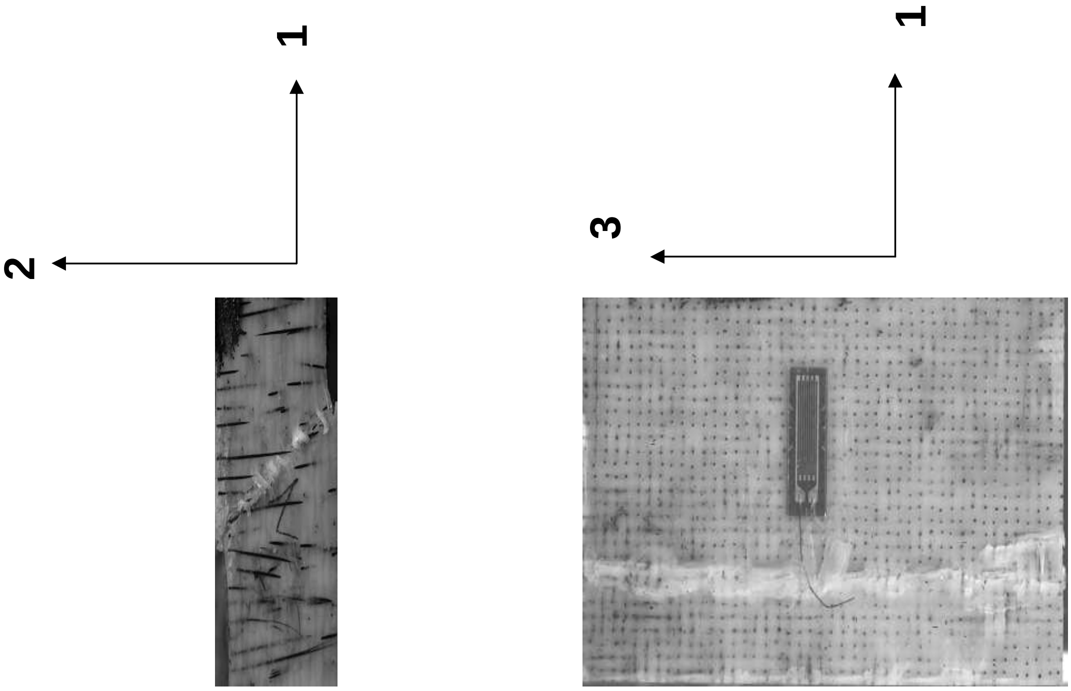

Figure 4.3: Images of a Failed Z-pin Specimen ($[45/-45/0/90]_{2s}$, 1% Z-pin) under Uniaxial Compression in the "1" Direction

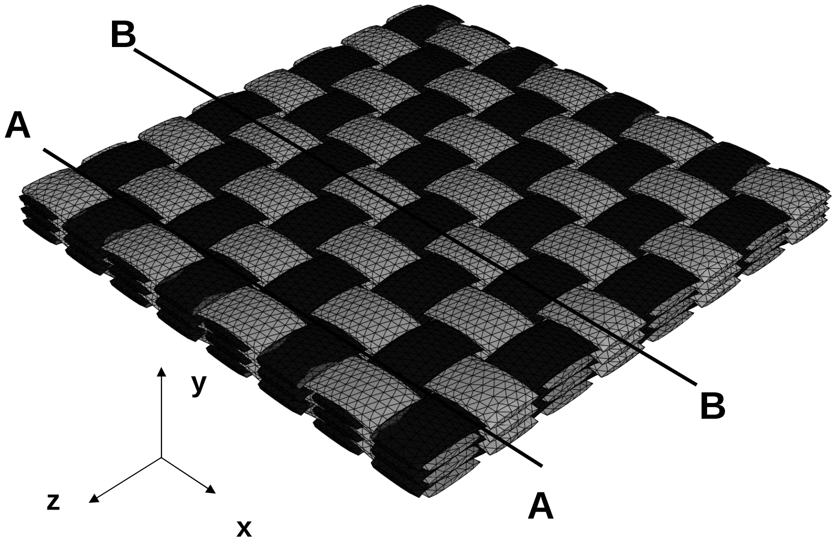

Figure 4.4: 3D Model with 9 Unit Cells in One Lamina

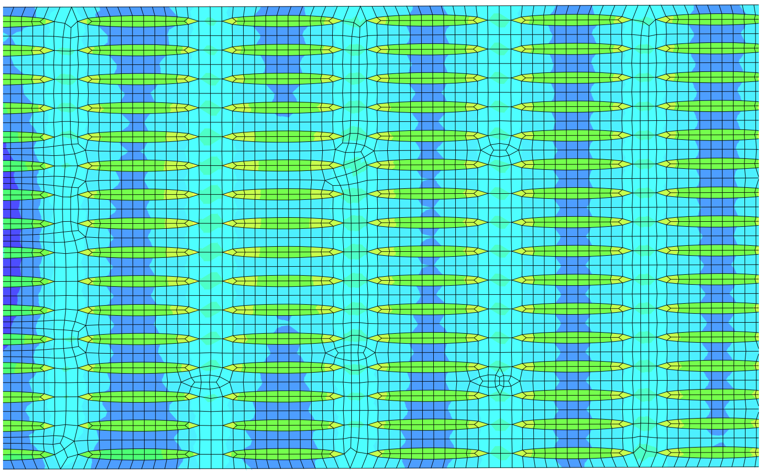

Figure 4.5: Model without Axial Fiber Tows, Cross-Section AA in Figure 4.4

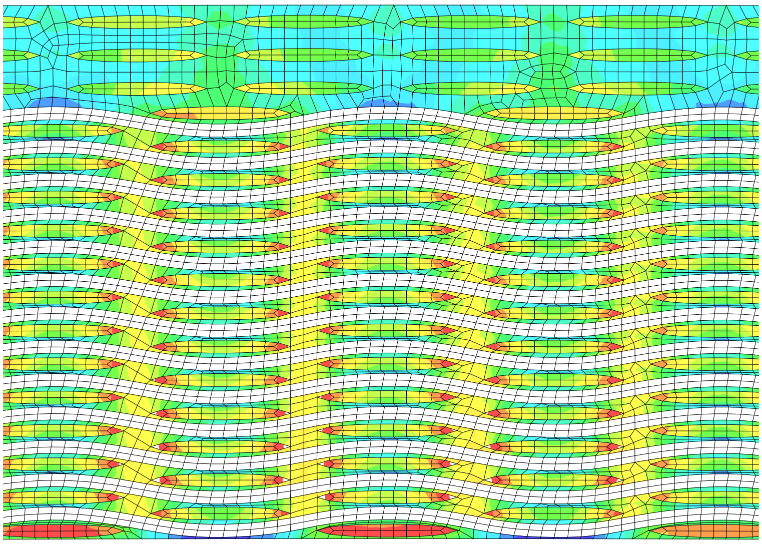

Figure 4.6: Idealized Model with 13 Axial Fiber Tows

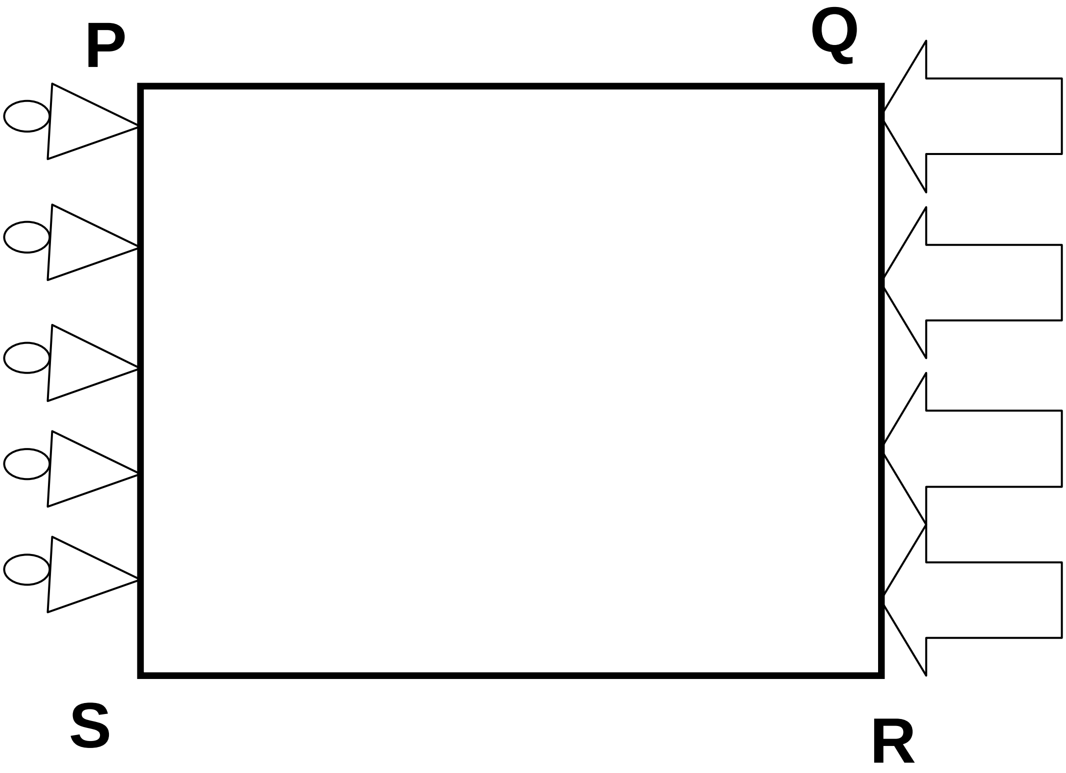

Figure 4.7: Schematic of Boundary Condition

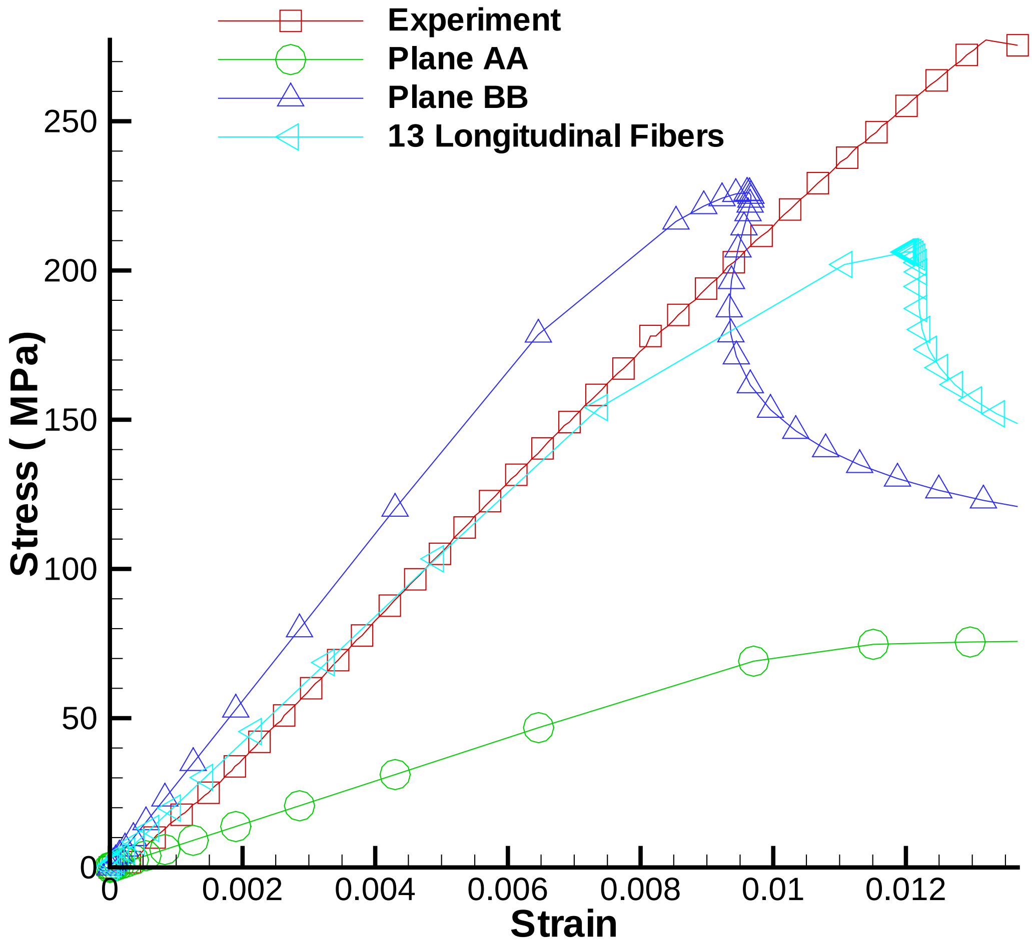

Figure 4.8: Comparison of Model AA, Model BB, and Model CC against the Experimental Results

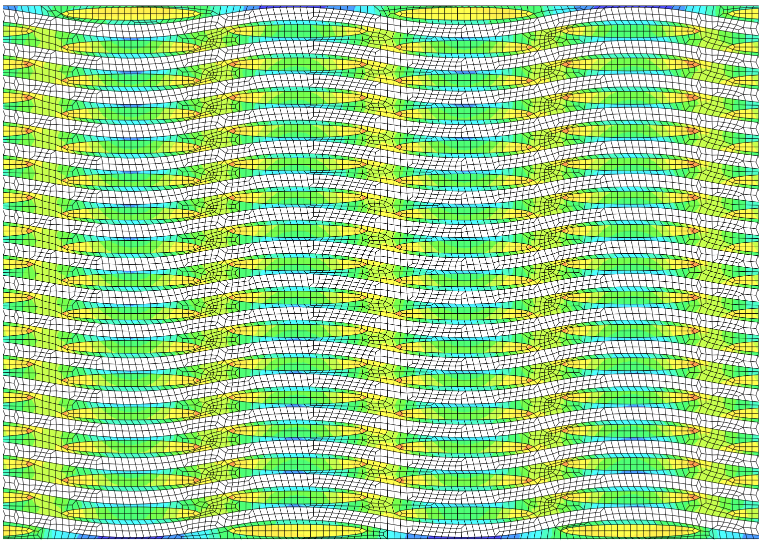

Figure 4.9: Idealized Model with No Phase Difference

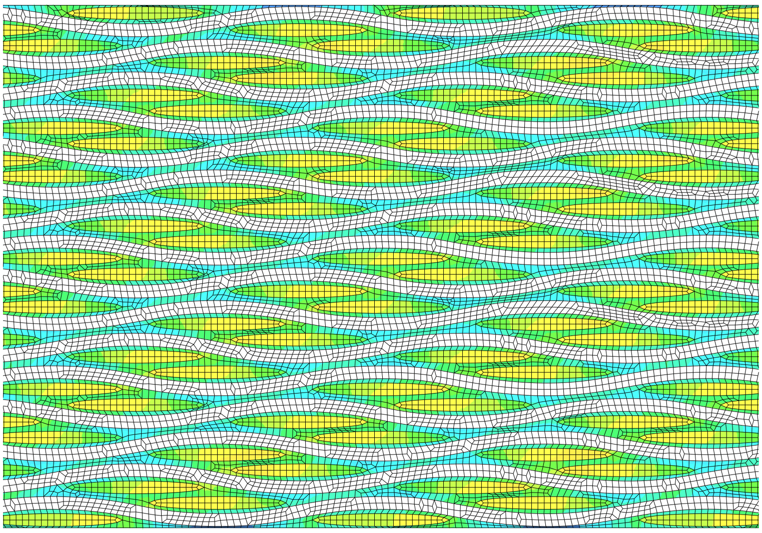

Figure 4.10: Idealized Model with Phase Difference $\frac{\pi}{2}$ between Neighboring Laminae

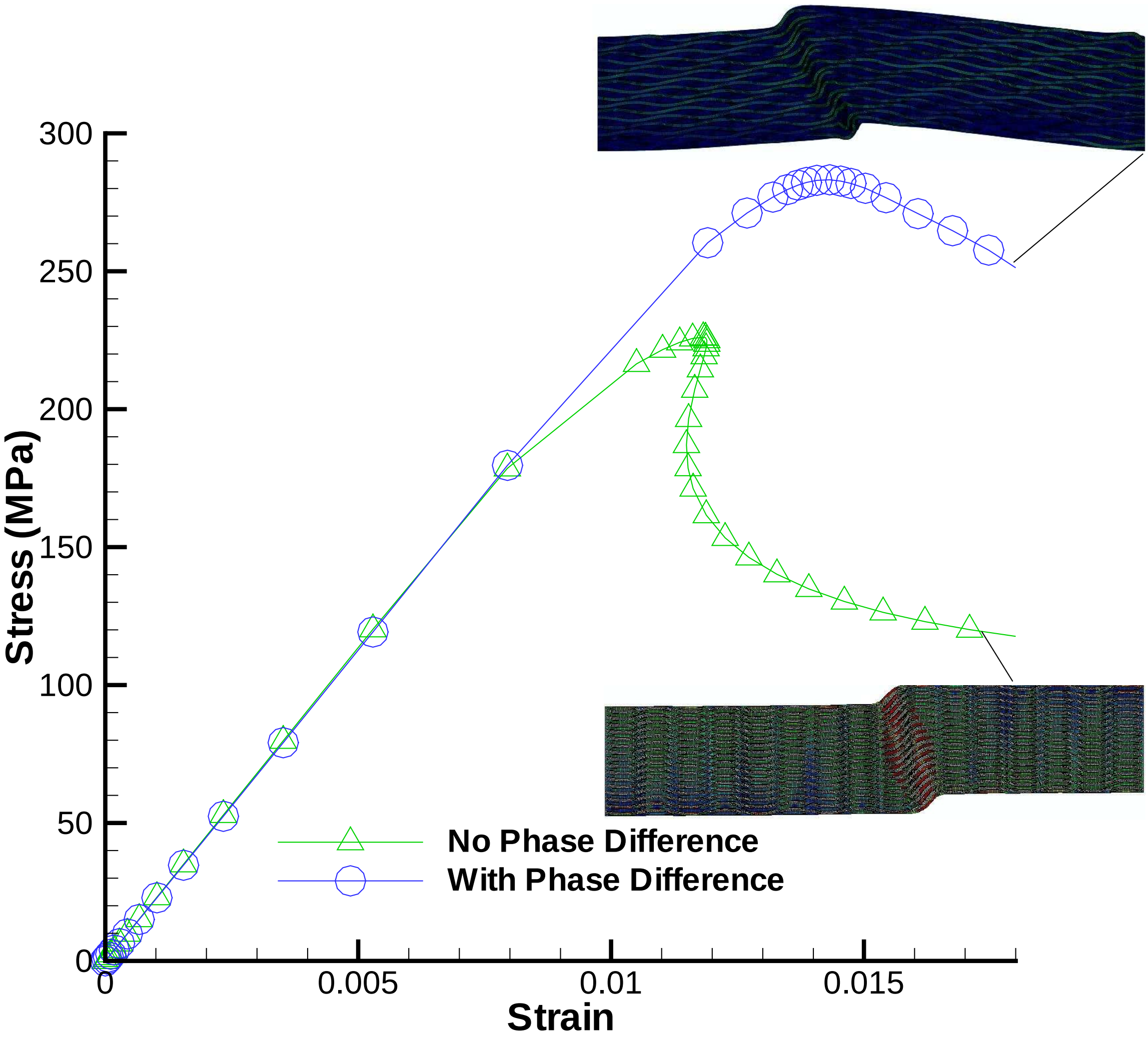

Figure 4.11: Axial Stress- Axial Strain Response with Phase Difference and without Phase Difference

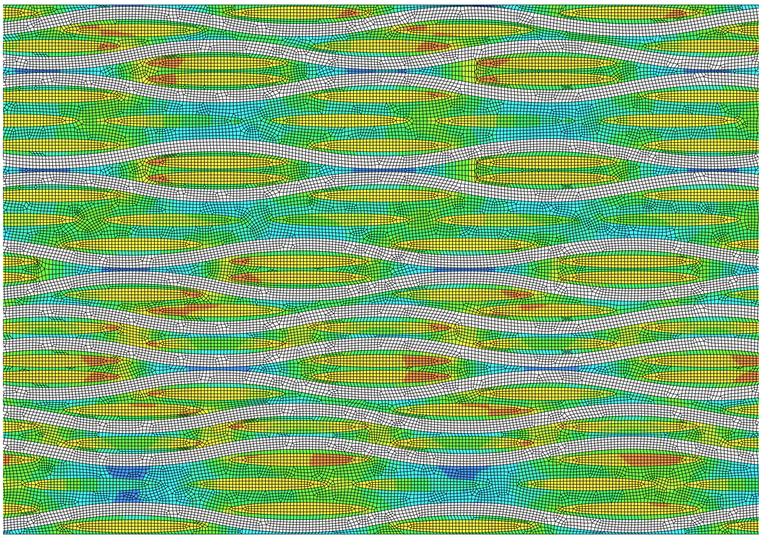

Figure 4.12: Model without Z-Pins

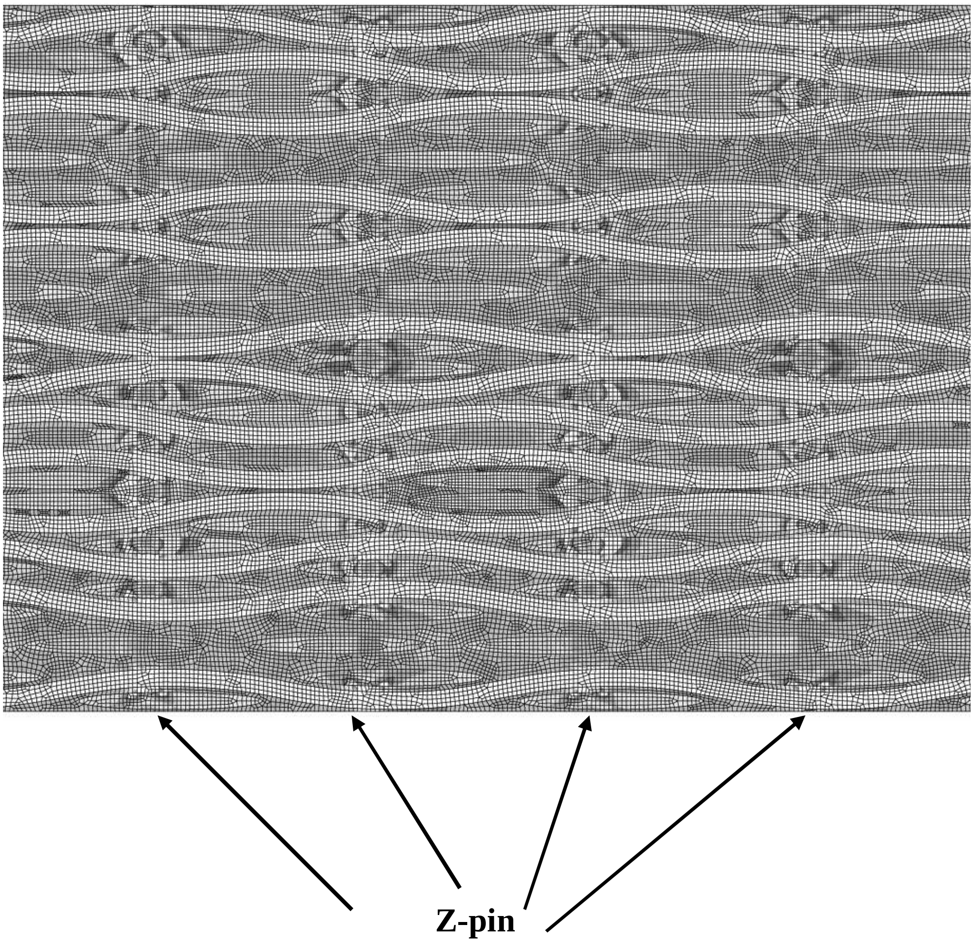

Figure 4.13: Model with Z-Pins

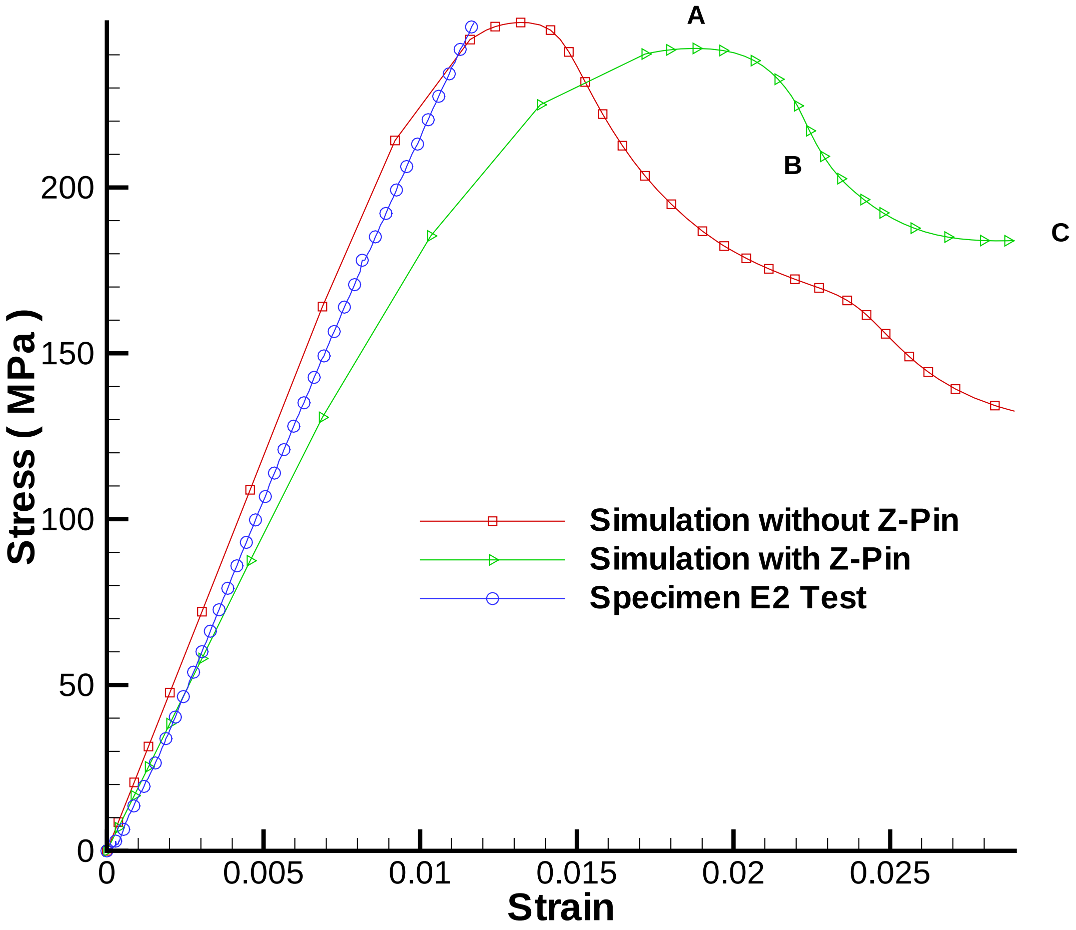

Figure 4.14: Comparison of Simulations of Z-pin Composites and no Z-pin Composites against Experiment

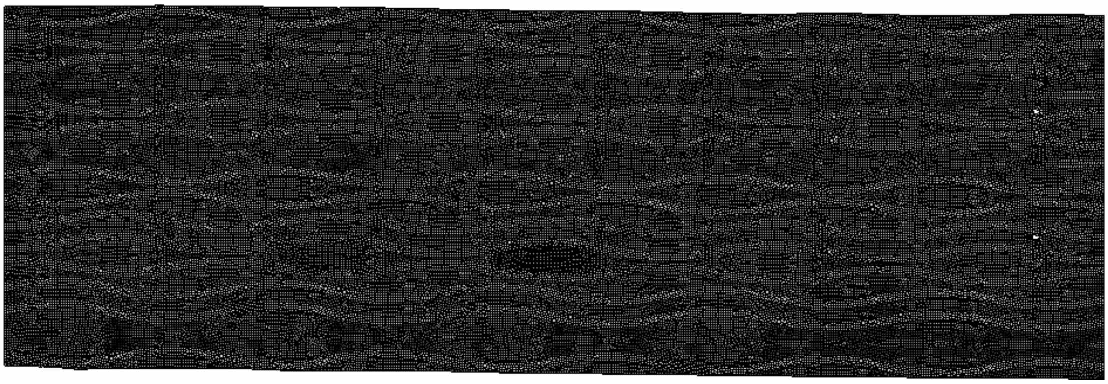

Figure 4.15: Deformed Shape Corresponding to Point A, Marked in Figure 4.14 for the 1% Z-pin Composite

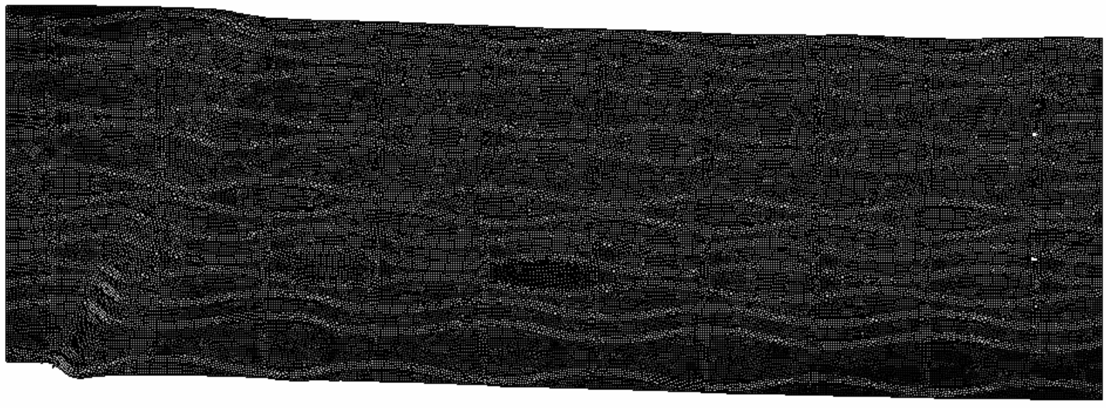

Figure 4.16: Deformed Shape Corresponding to Point B, Marked in Figure 4.14 for the 1% Z-pin Composite

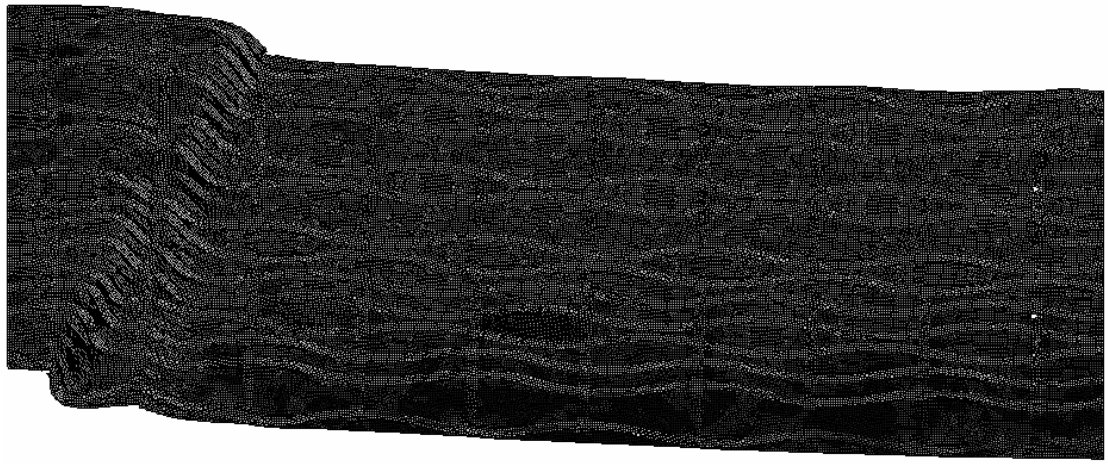

Figure 4.17: Deformed Shape Corresponding to Point C, Marked in Figure 4.14 for the 1% Z-pin Composite

CHAPTER V

Compressive Response and Failure of Z-Pin Textile Composites: 3D Numerical Simulation

In this chapter, 3D multi-layer and multi-RUC models are presented in order to accurately capture the failure mechanisms of textile composites. Simulations of 1, 9, 16, and 25-RUC models are compared first. Then, simulations of multi-layer models are compared. From the results of these simulations, the 3-layer and 16-RUC model is chosen as the best representation of the 3D multi-layer and multi-RUC model. Simulations of models with phase difference and no phase difference are also presented to show the influences on these laminates.

5.1 Introduction

A single RUC model is used extensively in the literature to simulate the response of textile composites, [42] and [20] . In order to obtain the linear stiffness of the composites, the microstructural geometry is identified first. Analytical methods and finite element methods are quite successfully used to extract the stiffness and thermal properties of different types of textile composites as shown in [44] and [31]. However, during the fabrication of the composites, each ply of the lamina in a laminate doesn't end up being stacked exactly as intended. This leads to a phase difference between laminae as was discussed in chapter 4.

In this chapter, an orthotropic plastic potential for the fiber tow that was derived from numerical analysis of the stress-strain response of a representative unit cell as discussed in chapter 3 is used together with the in-situ stress-strain response of the matrix to examine the compression response of the Z-pin multi-cell 3D model in conjunction with the finite element method. The commercial software ABAQUS is used for the simulations presented here. The matrix is modeled as a J2 isotropic hardening elastic plastic solids. During the nonlinear response analyses, the arc-length method (RIKS method) in ABAQUS is used to ensure that the post failure path, including unstable response could be captured accurately.

5.2 Creation of finite element (FE) models

In order to build 3D FE models to perform analyses, the microstructural geometry has to be identified first. Textile composites in this research are composed of the fiber tows and matrix as shown in Figure 5.1. For the Z-pin textile composites, Z-pins are inserted through the thickness in the composites. As shown in Figure 5.2, a fiber tow is a space undulating solid that closely approximates a sinusoidal shape. Therefore, the sinusoidal shape of the fiber tow is used in this 3D model. The cross section of the fiber tow is assumed to be the elliptic shape. This was motivated by SEM images of the tow cross-section. The geometry of the sinusoidal tow and the cross section of the tow used in the simulation are evaluated by taking 40 images similar to Figure 5.3 under a SEM and then the average geometrical properties are obtained. The average amplitude of the sinusoidal tow, the major axis, and minor axis are shown in Figure 5.4. The standard deviation for major axis is 0.214 mm and the standard deviation for minor axis is 0.0135 mm (based on 40 SEM images).

In one representative unit cell (RUC), two longitudinal and two transverse sinusoidal fiber tows are established as shown in Figure 5.5. Two fiber tows in each direction (longitudinal or transverse) have the same geometry but have different phase angles. In real models, these longitudinal and transverse fiber tows are embedded in the matrix as shown in Figure 5.6. The Z-pin fibers are also embedded in the matrix and fiber tows, in the case of Z-pin laminates.

After the geometry is identified, the constitutive law (response curve) of each constituent (fiber tow and matrix) is needed to implement into the finite element model to perform the nonlinear analysis. This aspect was addressed in chapter 3, as discussed earlier.

During the non-linear analysis of the RUCs, global direction 1 is the longitudinal direction, direction 3 is the transverse direction, and direction 2 is the through-the-thickness direction as shown in Figure 5.7. The face EFGH in direction 1 is fixed during the simulation and the face ABCD in direction 1 is imposed a controlled displacement. The degree of freedom in direction 2 on face ABEF and CDGH is fixed in order to simulate anti-buckling guides that are used in the experiment to prevent global buckling. As will be discussed later, this stipulation approaches the conditions in the laboratory, especially for the 16 RUC 3D model which is of the same size as the specimens discussed in chapter 2.

5.3 3D finite element model

5.3.1 Simulation of Multi RUC

In the literature, one RUC with periodic boundary condition is often used to represent and simulate the mechanical behavior of a laminate, under compression or tension loading [42] and [20]. However, for strength prediction, if one RUC is used, then the failure mechanism of one RUC as shown in Figure 5.8 is assumed to be found repeatedly in all other unit cells of specimens because of the assumption of periodicity. Of course, the failure pattern in one cell as shown in Figure 5.8 cannot represent the failure mode observed in real experiments because the failure occurs only locally within a handful of cells of the tested specimen instead of occurring periodically in each RUC. Therefore, the number of RUCs needed to model the actual specimen more realistically for strength prediction is investigated in the following. Here, the finite element representations of 1 RUC, 9 RUCs, 16 RUCs, 25 RUCs as shown in Figure 5.9, Figure 5.10, Figure 5.11,and Figure 5.12, respectively, are used in this study. The macroscopic stress-strain responses of the compressive simulations for different RUCs are shown in Figure 5.13. As before (chapter 4), initially, a linear response OA, $OA^{'}$, and $OA^{''}$ is obtained, until a limit load is reached at which stage, the deformation starts to localize in a few cells, which results in a drop in the load and eventually plateau off (B, $B^{'}$, and $B^{''}$) as shown in Figure 5.13. The localized deformation shapes, corresponding to B, $B^{'}$, $B^{''}$ are shown in Figure 5.14, Figure 5.15, and Figure 5.16 . The maximum stress, which corresponds to the compressive strength, decreases dramatically when 1 RUC is replaced by 9 RUCs. However, the trend of this decrease is not so much between the 9 RUC and 16 RUC prediction. When the model of 25 RUCs is used, the compressive strength is almost the same as that predicted with 16 RUCs. This implies that using 16 RUCs is sufficient for predicting the compressive strength. Note that the size of the tested specimen is 62.5 mm by 55.9 mm. After the grips and anti-buckling guides are imposed, the size of the specimen that is exposed is 55 mm by 45 mm. Given that one RUC is 10 mm by 10 mm, there are approximately 25 RUCs in the tested specimen. That shows that, by using 16 RUCs, the size of simulation model is close to the exposed area of the real specimen.

5.3.2 Simulation by Use of Multi Layers

In the literature, a single lamina model is frequently used. The experimental results reported in chapter 2 corresponded to multi-layered laminates. The assumption based on using only a single layer to represent the laminate needs verification. Furthermore, a single lamina model is not effective to investigate the effect of phase difference observed in the multi-layered laminates. In the following, the simulations with multi-layer representations of the composites will be discussed. Figure 5.17 shows the comparison of the compressive simulations among models with different numbers of laminae. In each case, only one RUC is used. It is found that 3-layer laminae have a higher compressive strength than a single layer lamina model. However, the strength of a 4-layer model is close to that of a 3-layer model. From these results, it is concluded that a 3-layer representation of the laminate is sufficient to simulate the compressive response. Note that the results shown in Figure 5.17 are from the models in which phase difference is not considered (there are no phase difference between the 3-layer model and 4-layer model). However, when the composites are molded, a phase difference between different layers of the laminate usually is introduced due to consolidation effects. Therefore, a model with phase difference is a more realistic representation of the laminate. Figure 5.18 shows the comparison of the macroscopic stress-strain response between models with phase difference and models without phase difference. The predicted strength for the model with phase difference is higher than that for the model without phase difference. Figure 5.19 and Figure 5.20 show the failure modes for the composites without a phase difference and with a phase difference. Note that the strength and failure mode, both change when phase difference is introduced.

5.3.3 Simulation by Use of Multi-layer and Multi-RUC Composites

Based upon the findings of the previous sections, a 3-layer model with 16 RUCs is established to simulate the experiments that were presented in the compressive tests.

Figure 5.21 and Figure 5.22 show the 3-layer 16 RUC models with phase difference and with no phase difference. Note that no Z-pins are inserted in both models shown in Figure 5.21 and Figure 5.22. The comparison of the simulation of these two models and the results obtained from experiments are shown in Figure 5.23. The deformed shapes of the simulation of the composites without a phase difference at different stages A, B, and C are shown in Figure 5.24, Figure 5.25, and Figure 5.26. After point A, kinking is initiated and can be observed near the center of the specimen as shown in Figure 5.25. At point C (Figure 5.26), the kinking is well formed and contained in a band. Figure 5.27 shows the kind band viewed from the x-y plane at deformed state C in Figure 5.26 and from kink band of the specimen. Figure 5.28 shows the comparison among the simulation of 1% cross-ply Z-pin (d=0.02 in) composites, the simulation of a cross-ply non-Z-pin composite and results of cross-ply non Z-pin experiments. It shows that Z-pin composites have lower strength than the composites without Z-pins. It is seen that the predicted results compare well with the experimental results.

5.4 Conclusions

In this chapter, a 3-layer and 3D numerical model with each layer containing 16 representative unit cells is presented. The results from experiments and predictions of the 3D model agree well . The effect of phase difference can be simulated if a multi layer model is used. It is concluded that the strength of the composites would change if the position of lamina in each layer is changed. The results show that the higher density Z-pin composites have less strength, as also seen in the experimental results of chapter 2.

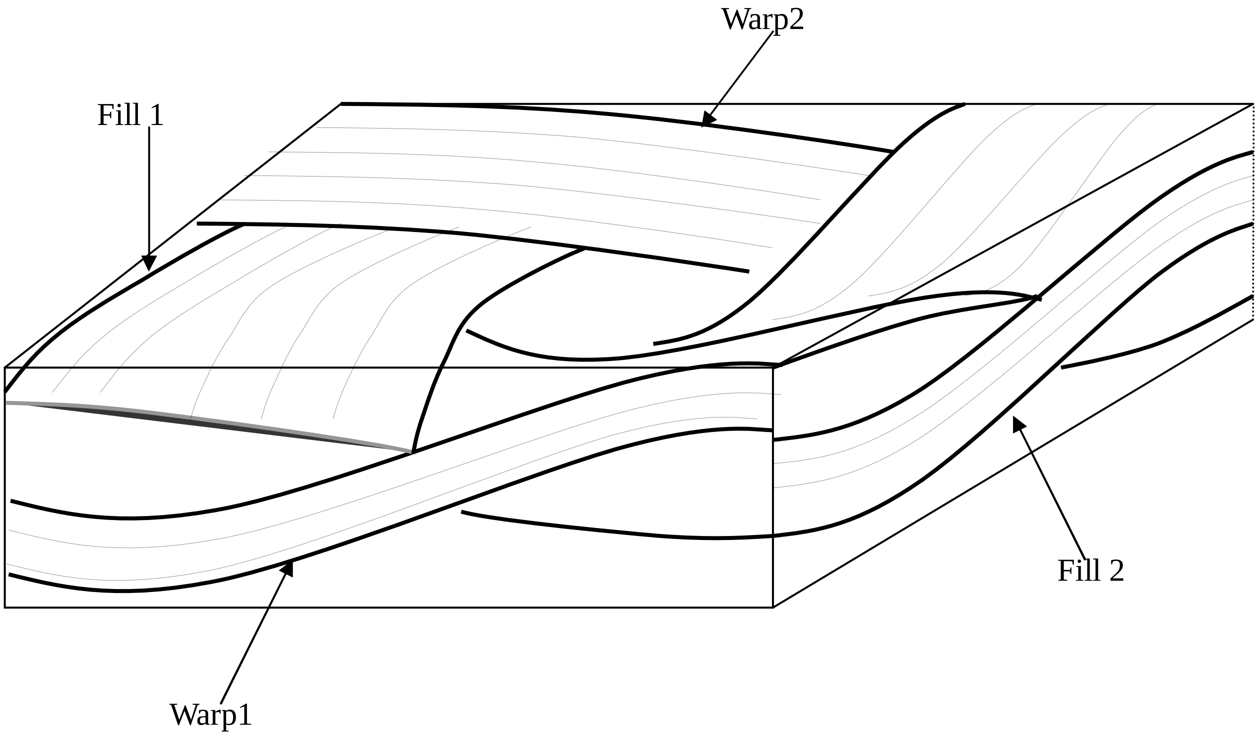

Figure 5.1: Schematics of Fiber Tow and Matrix

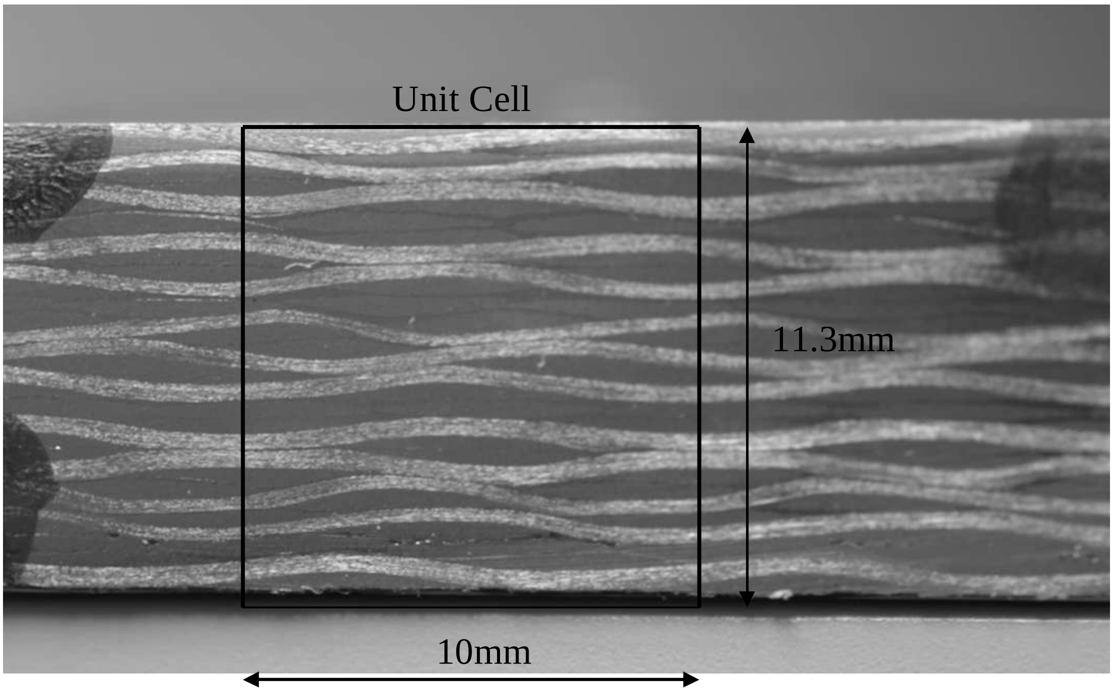

Figure 5.2: Image of Cross Section

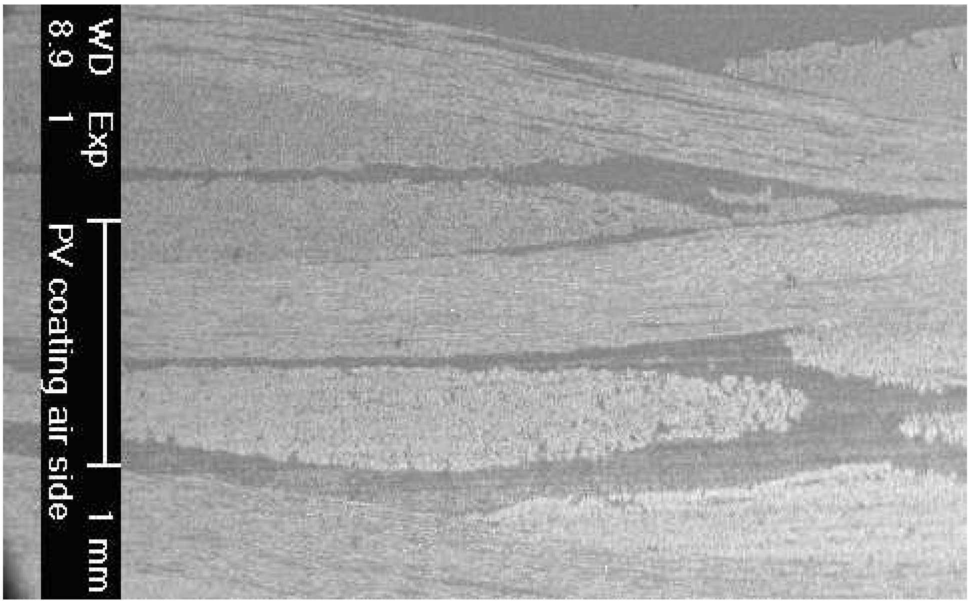

Figure 5.3: SEM Image of Fiber Tow and Matrix

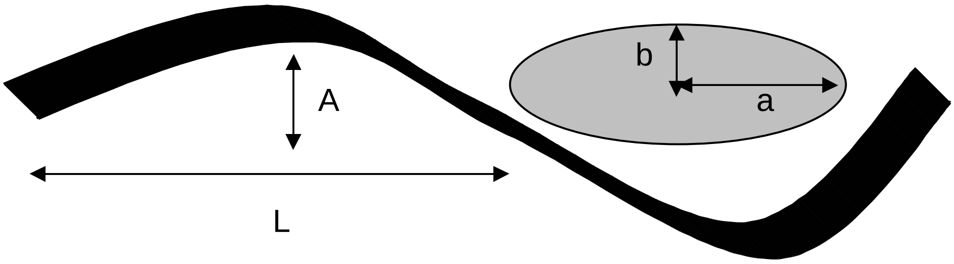

L	A	a	b
5 mm	0.26 mm	2.2 mm	0.2 mm

Figure 5.4: Fiber Parameters for RUC

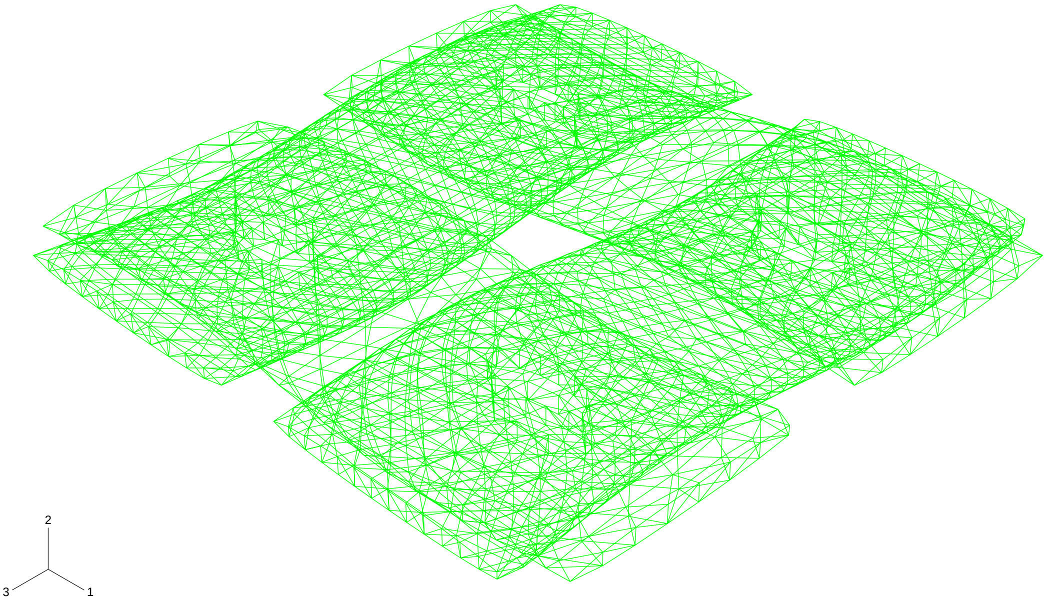

Figure 5.5: Longitudinal and Transverse Fiber Tows

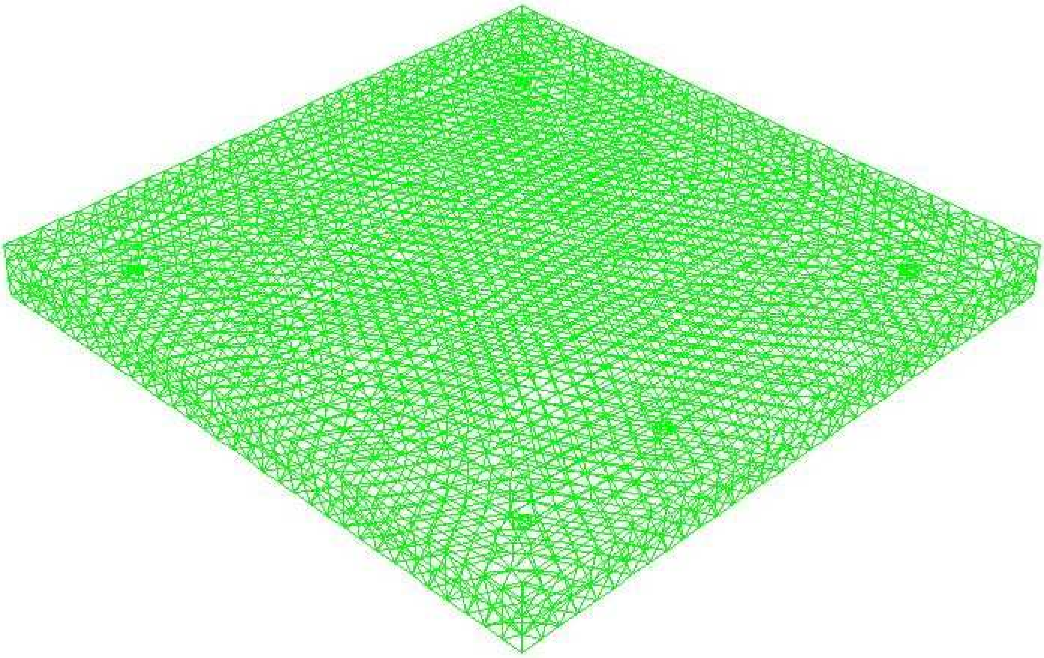

Figure 5.6: Matrix

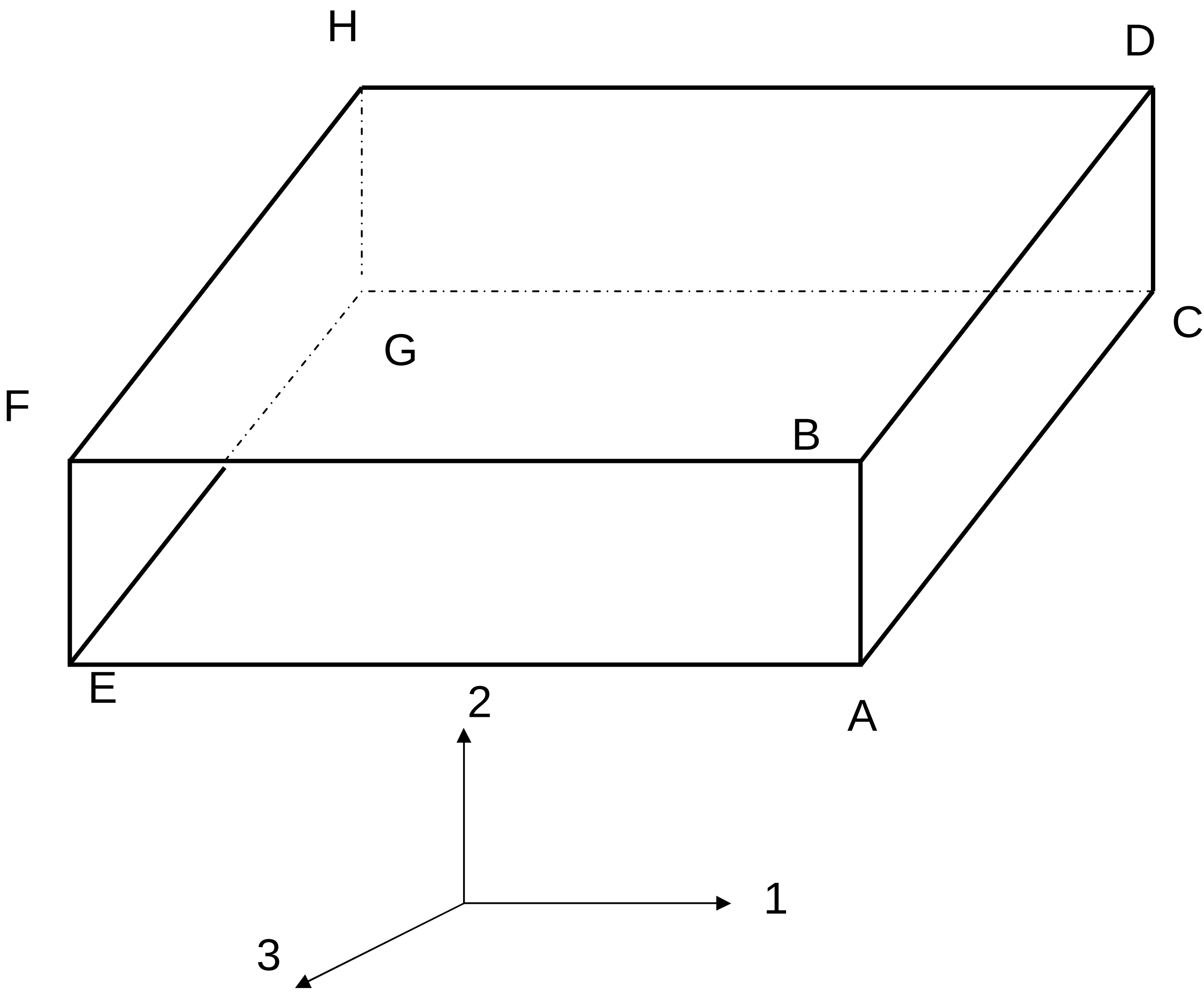

Figure 5.7: Schematic of RUC that is Used to Explain the Boundary Condition

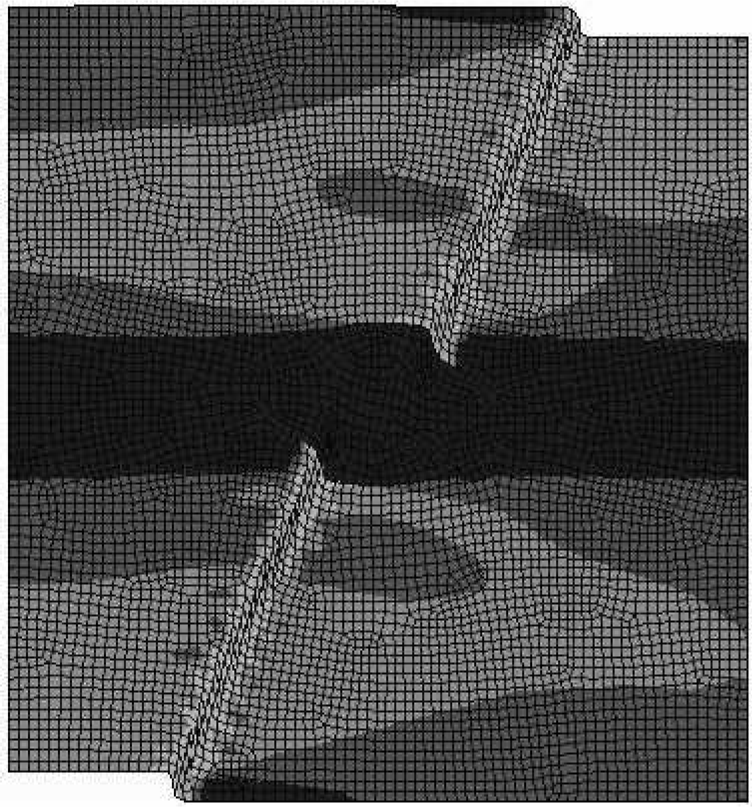

Figure 5.8: Failure Pattern of 1 RUC

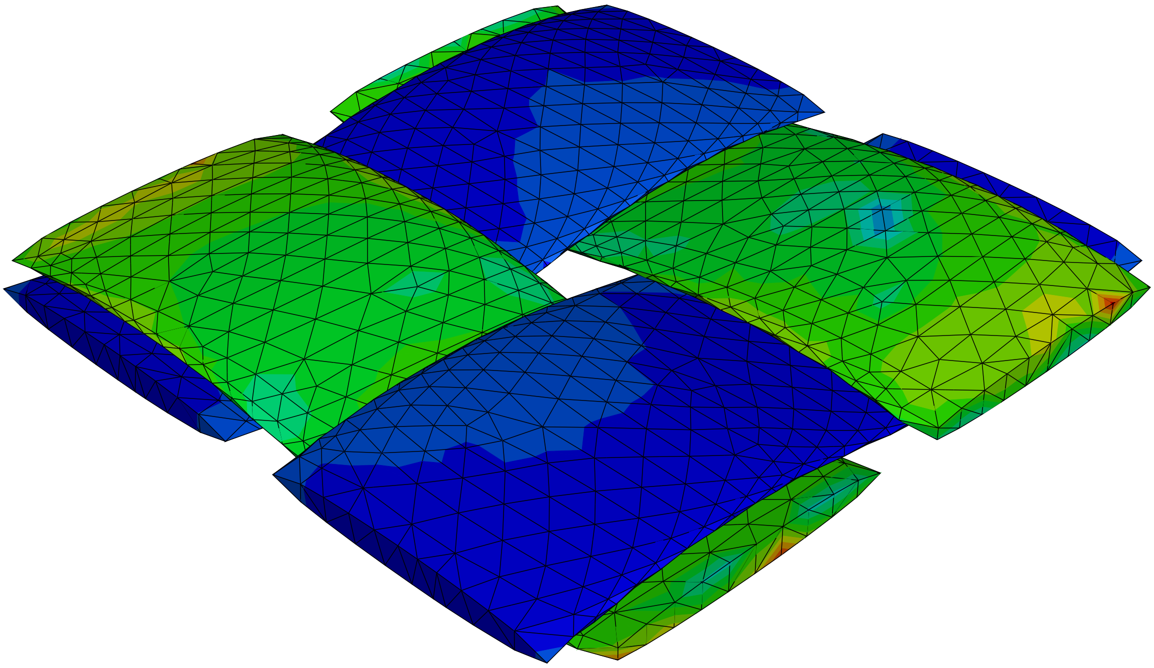

Figure 5.9: Numerical Model of 1 RUC

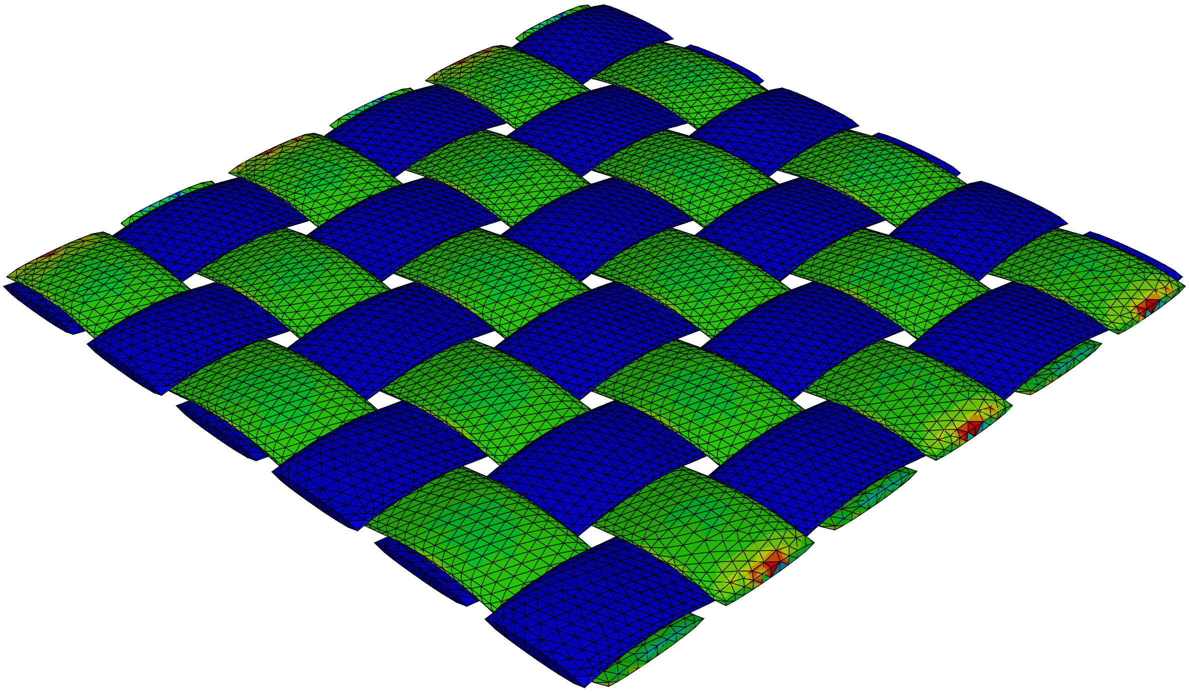

Figure 5.10: Numerical Model of 9 RUCs

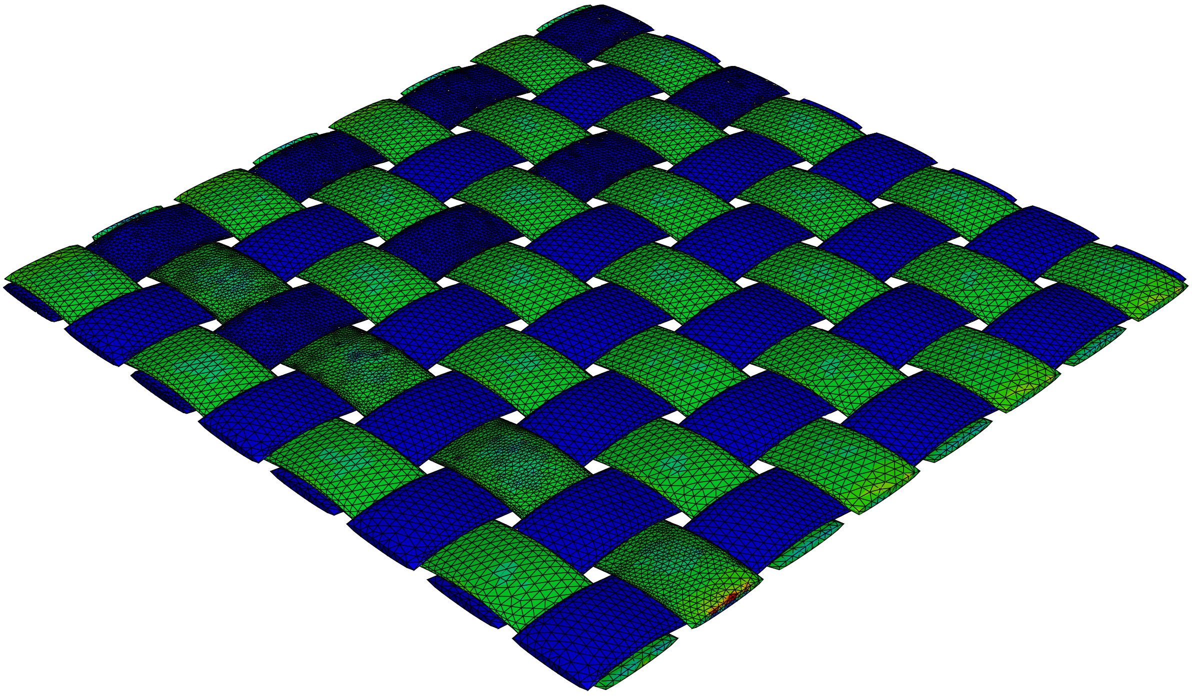

Figure 5.11: Numerical Model of 16 RUCs

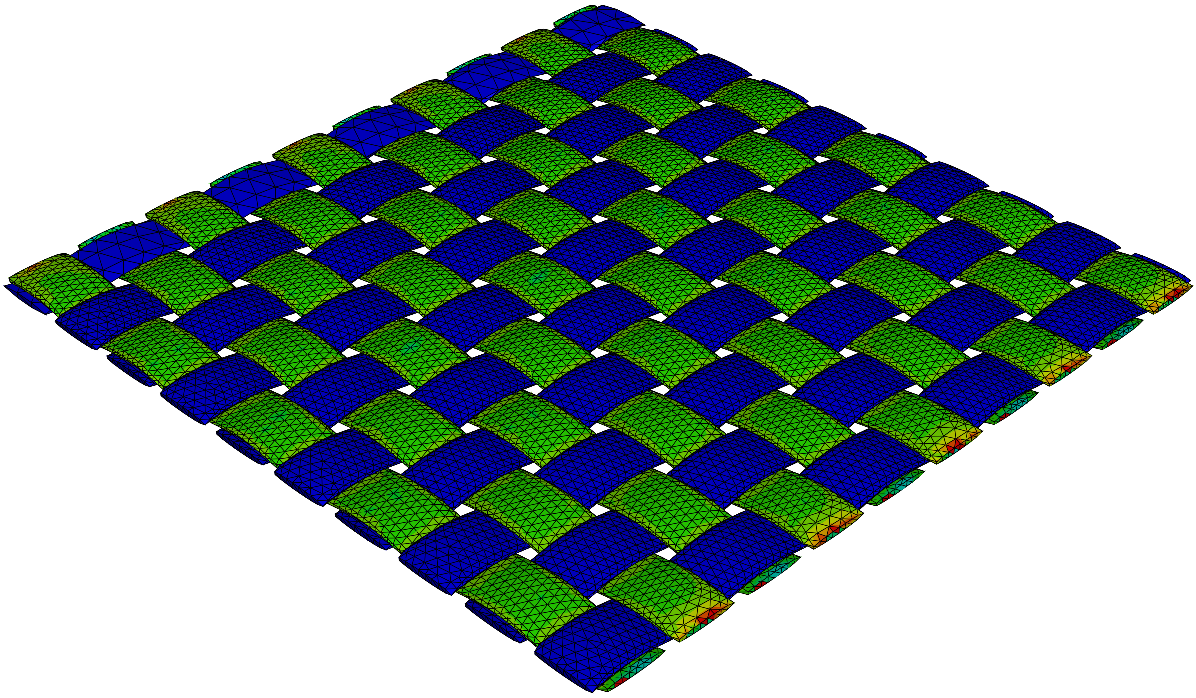

Figure 5.12: Numerical Model of 25 RUCs

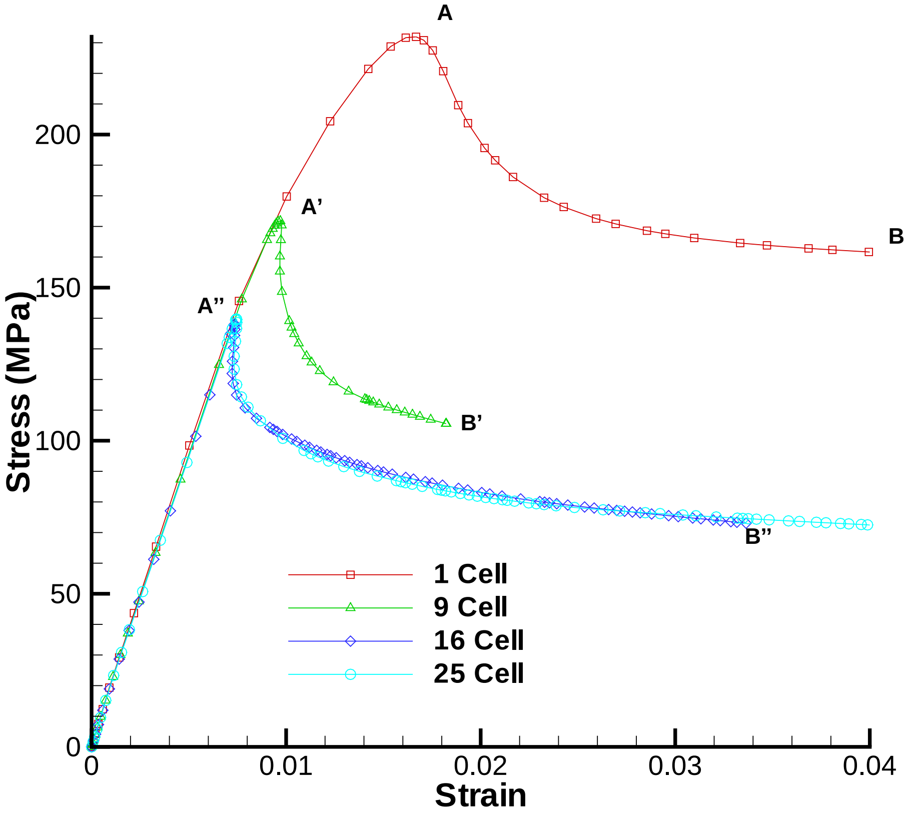

Figure 5.13: Stress-Strain Curve for Different Number of RUCs

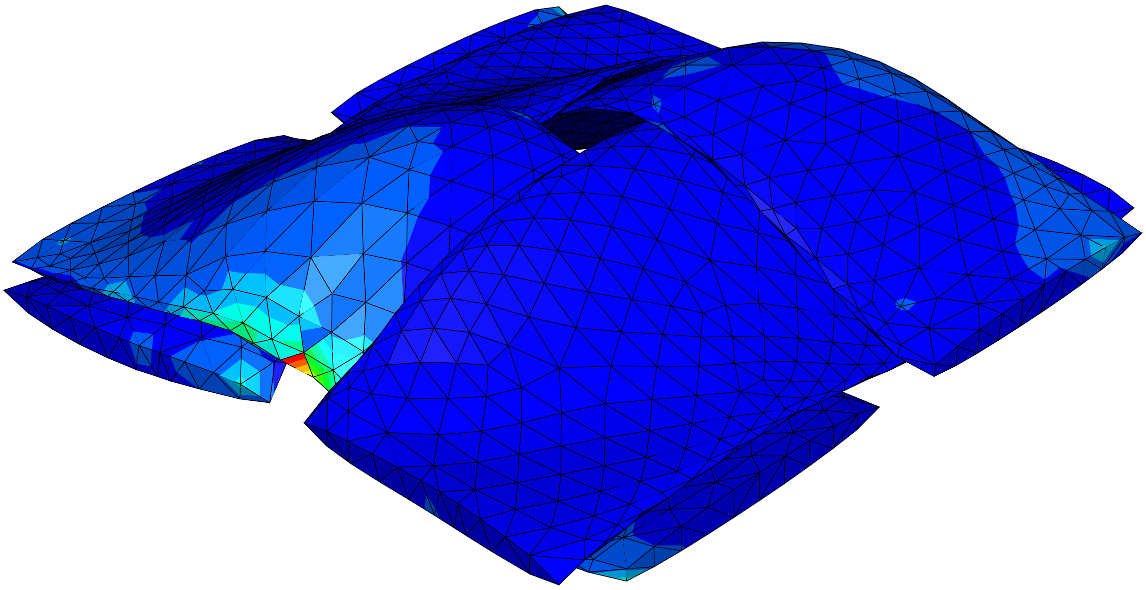

Figure 5.14: 1 RUC Model at B

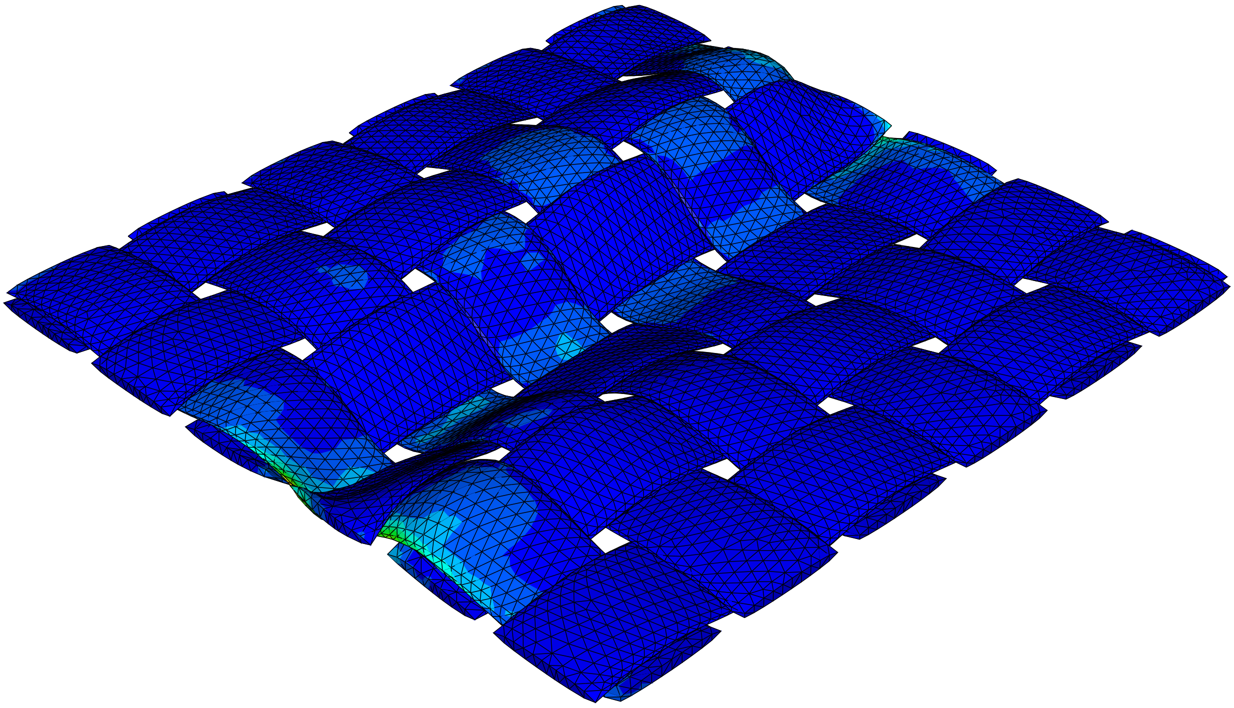

Figure 5.15: 9 RUC Model at $B^{'}$

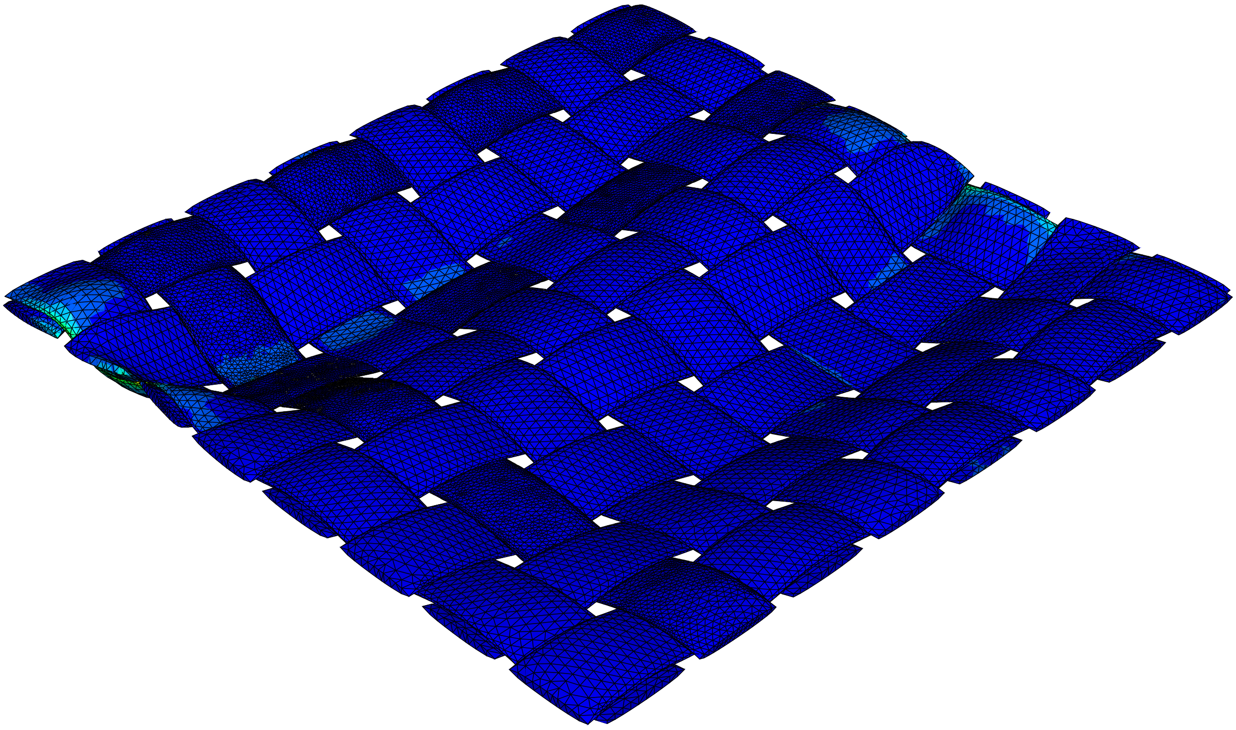

Figure 5.16: 16 RUC Model at B''

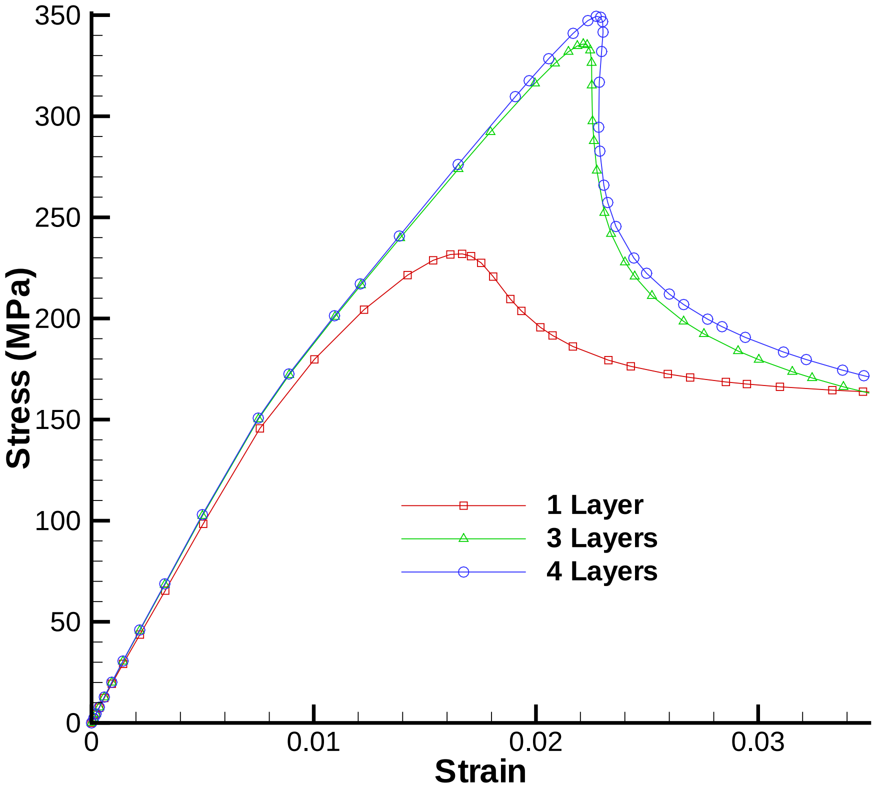

Figure 5.17: Stress-Strain Curve for Different Layers of Composites

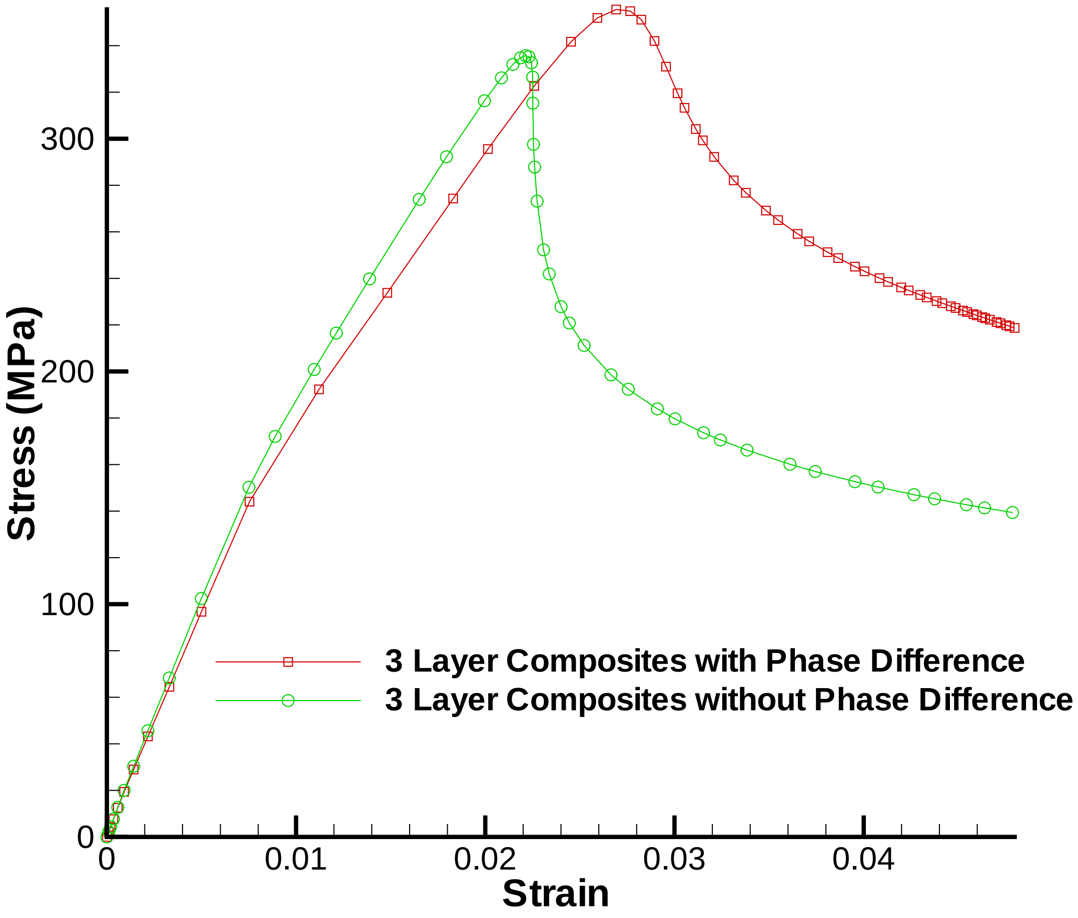

Figure 5.18: comparison of Stress-Strain Curve with and without Phase Difference

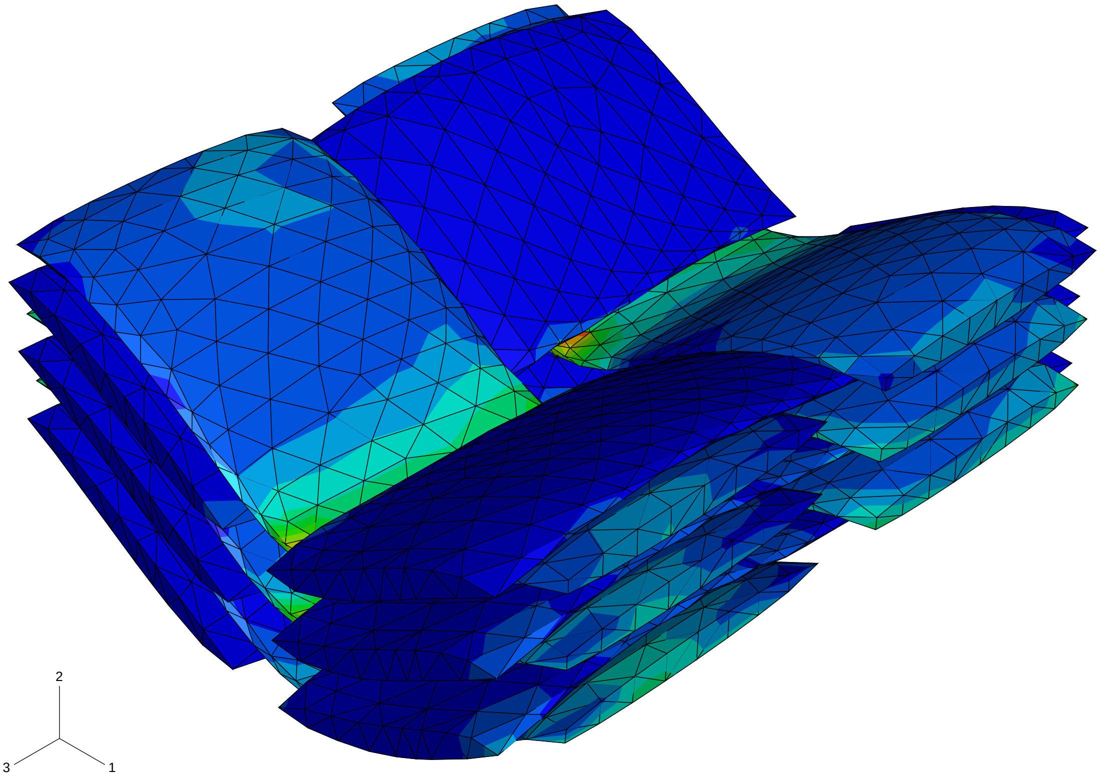

Figure 5.19: Failure Mode of Composites without Phase Difference

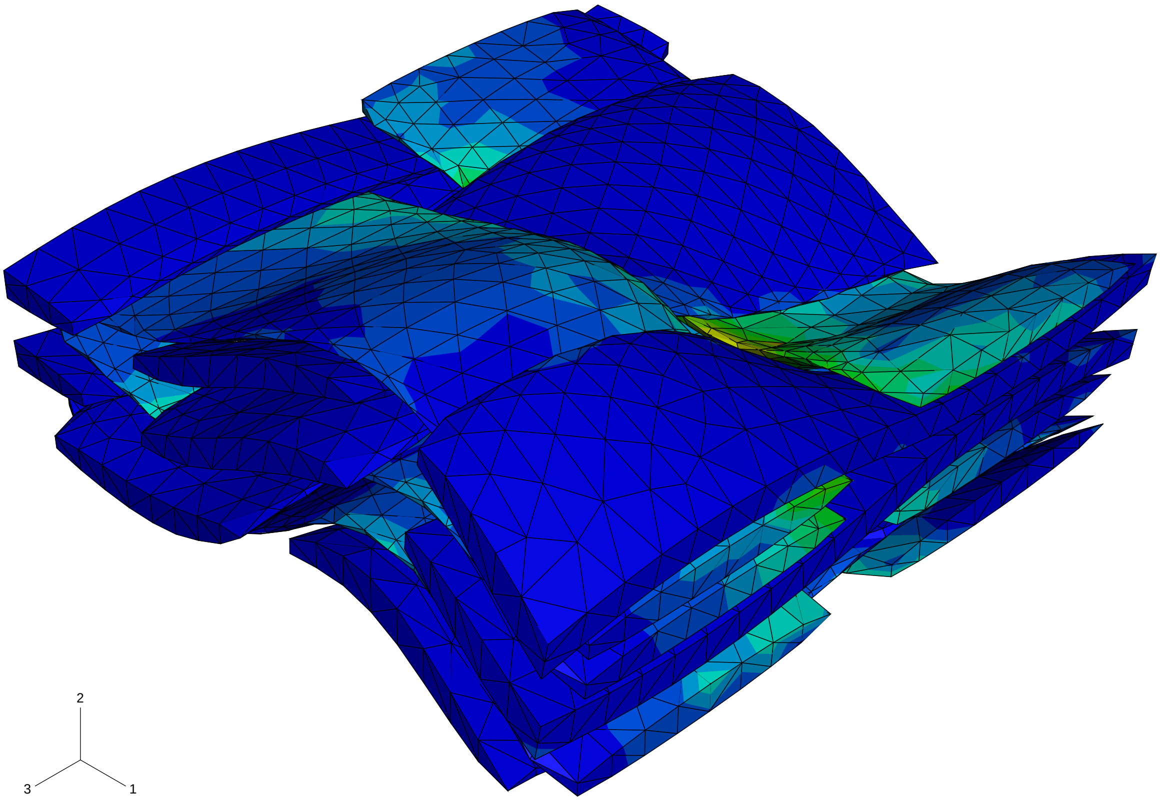

Figure 5.20: Failure Mode of Composites with Phase Difference

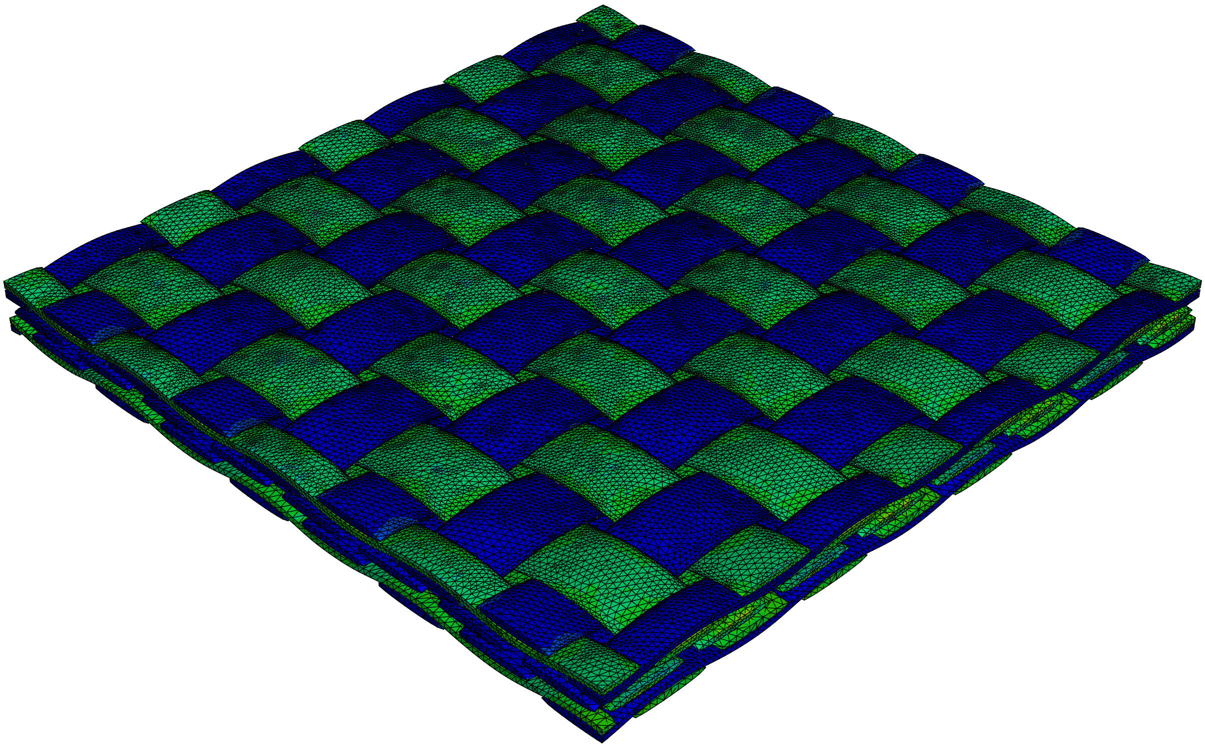

Figure 5.21: Models with Phase Difference

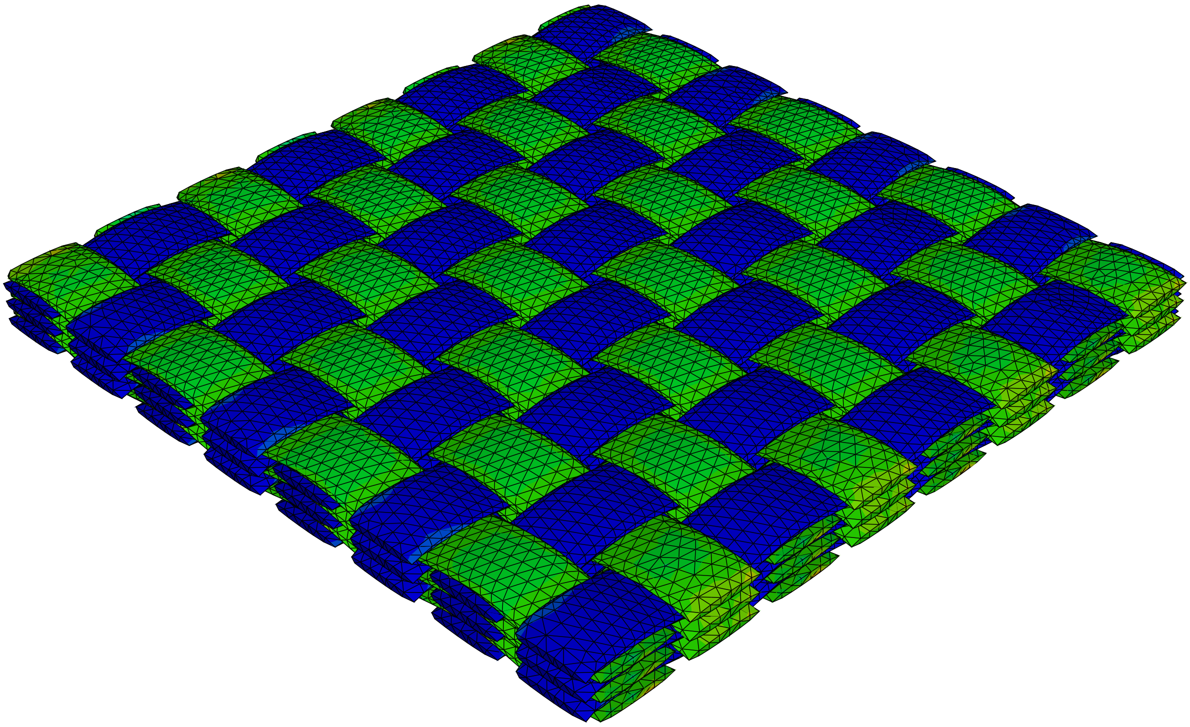

Figure 5.22: Models without Phase Difference

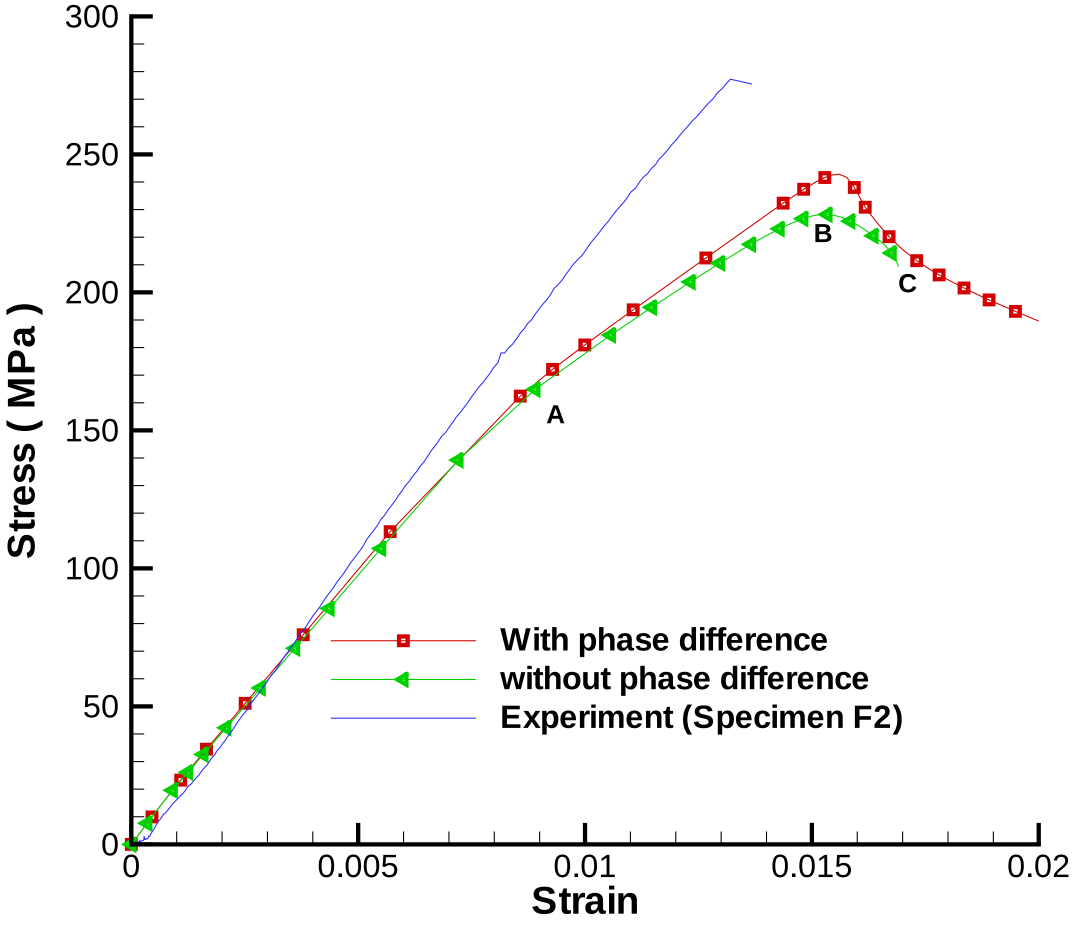

Figure 5.23: Comparison of Simulations between Models with Phase Difference and without Phase Difference

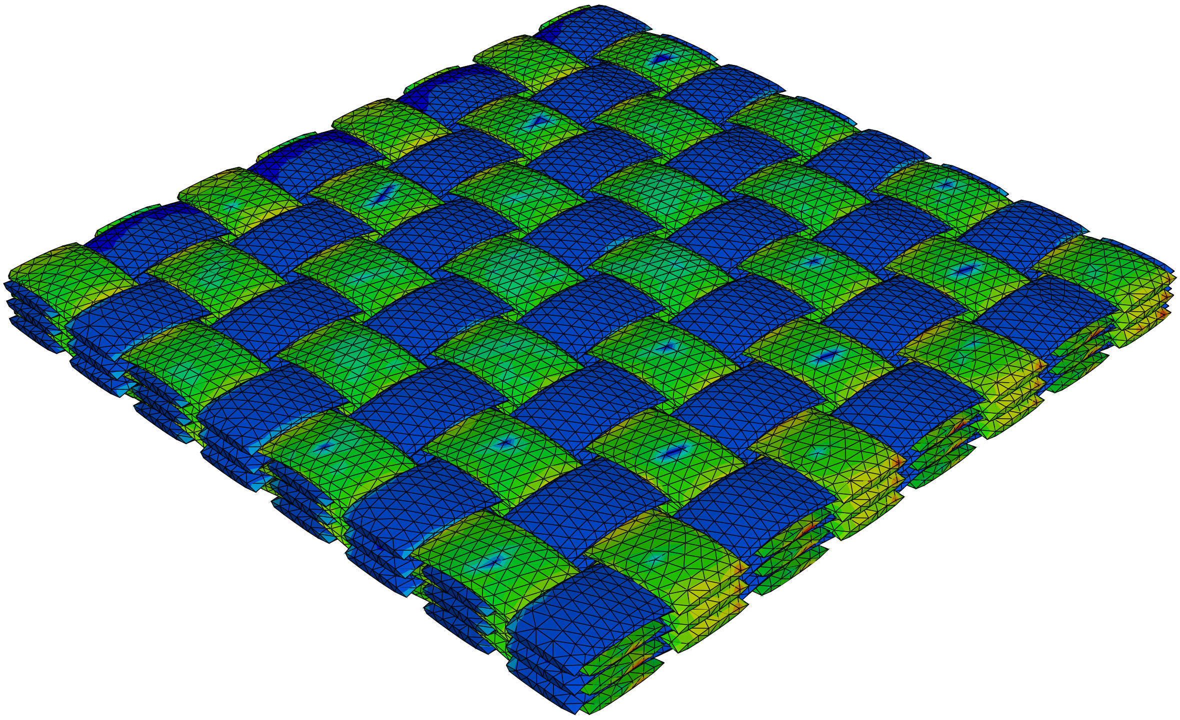

Figure 5.24: Deformed Shape at A

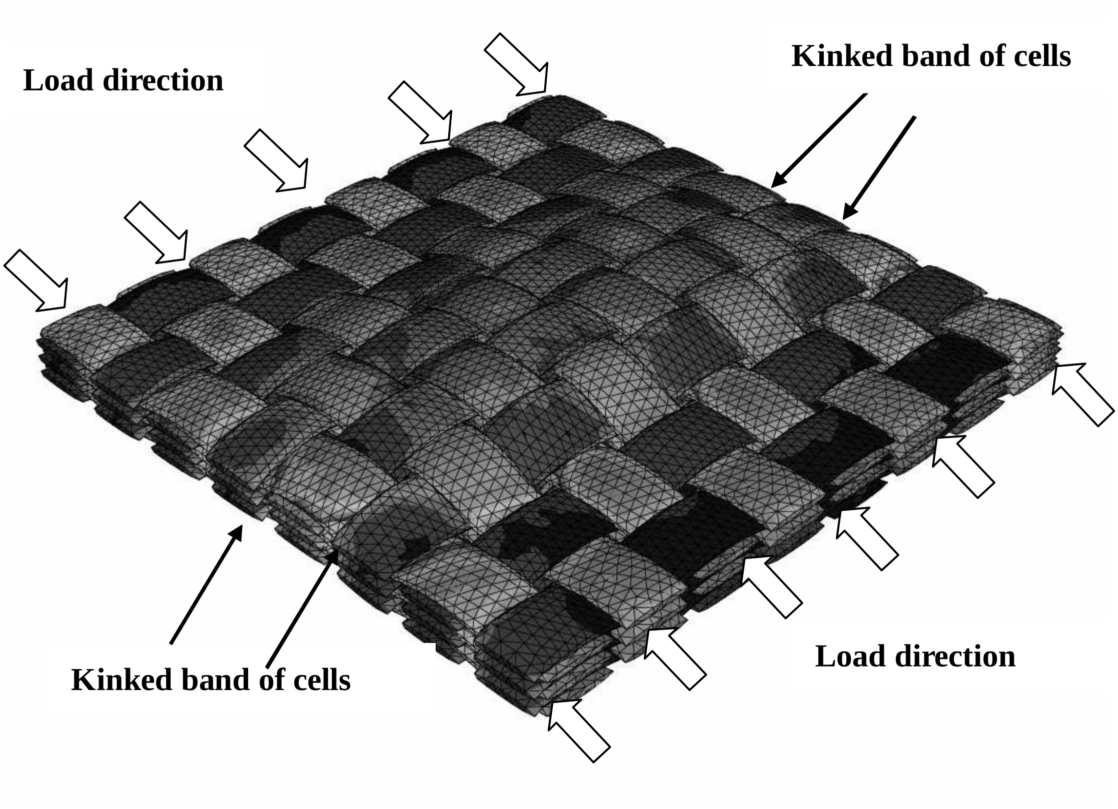

Figure 5.25: Deformed Shape at B

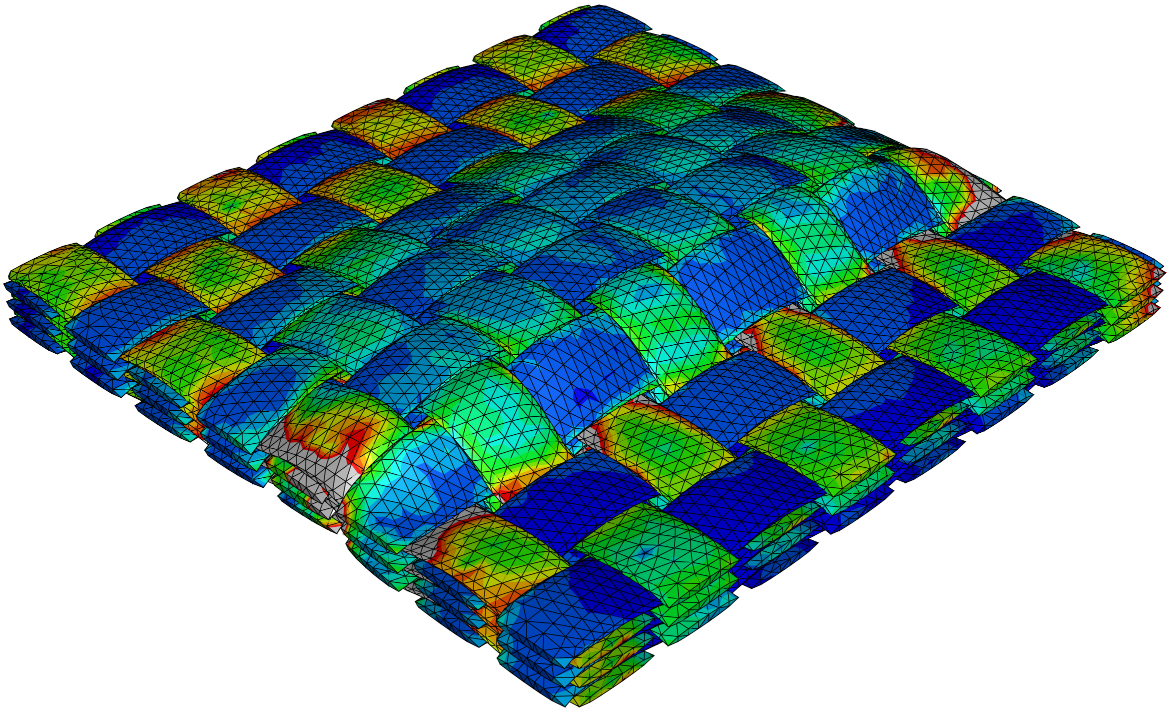

Figure 5.26: Deformed Shape at C

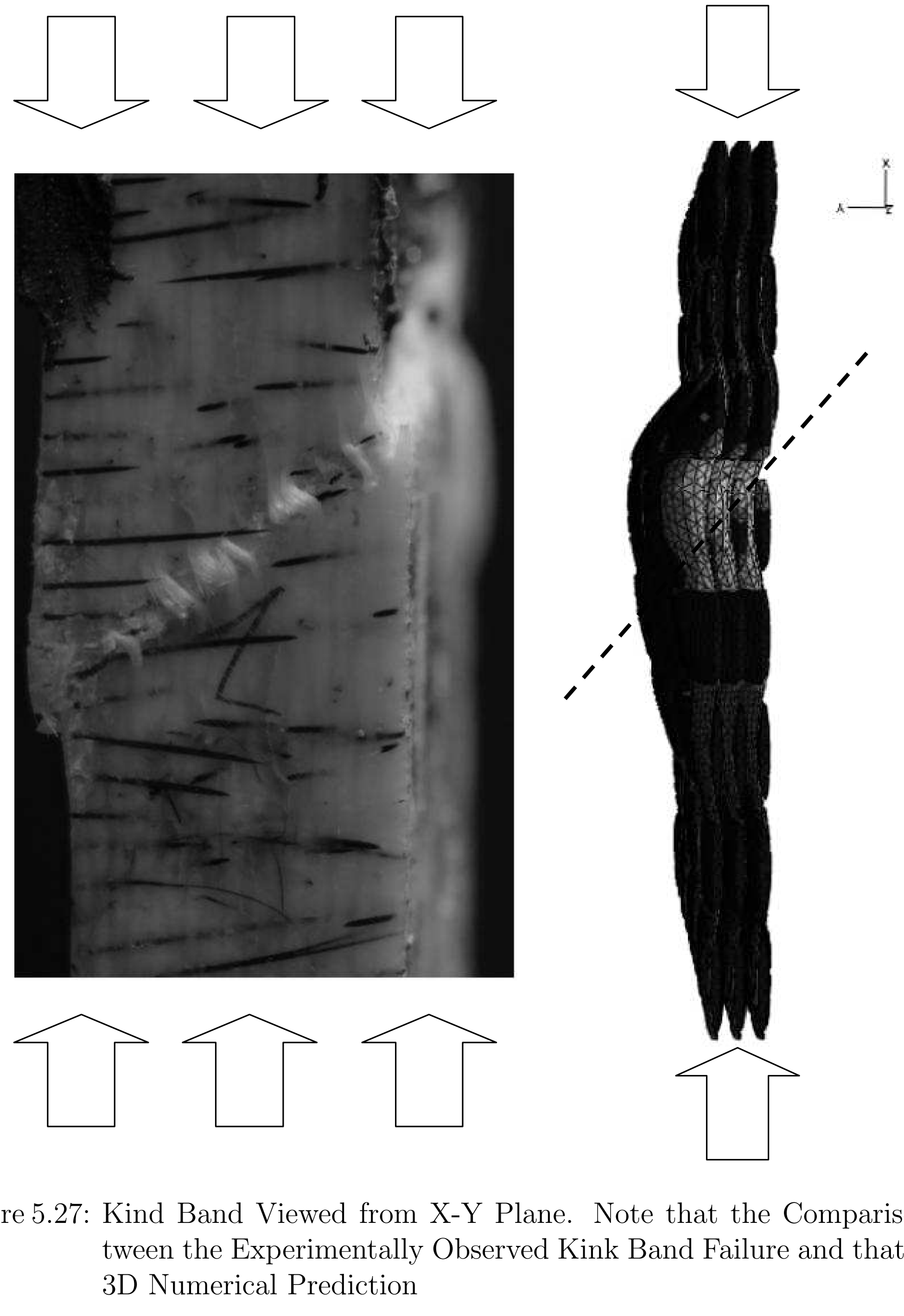

Figure 5.27: Kind Band Viewed from X-Y Plane. Note that the Comparison between the Experimentally Observed Kink Band Failure and that of the 3D Numerical Prediction

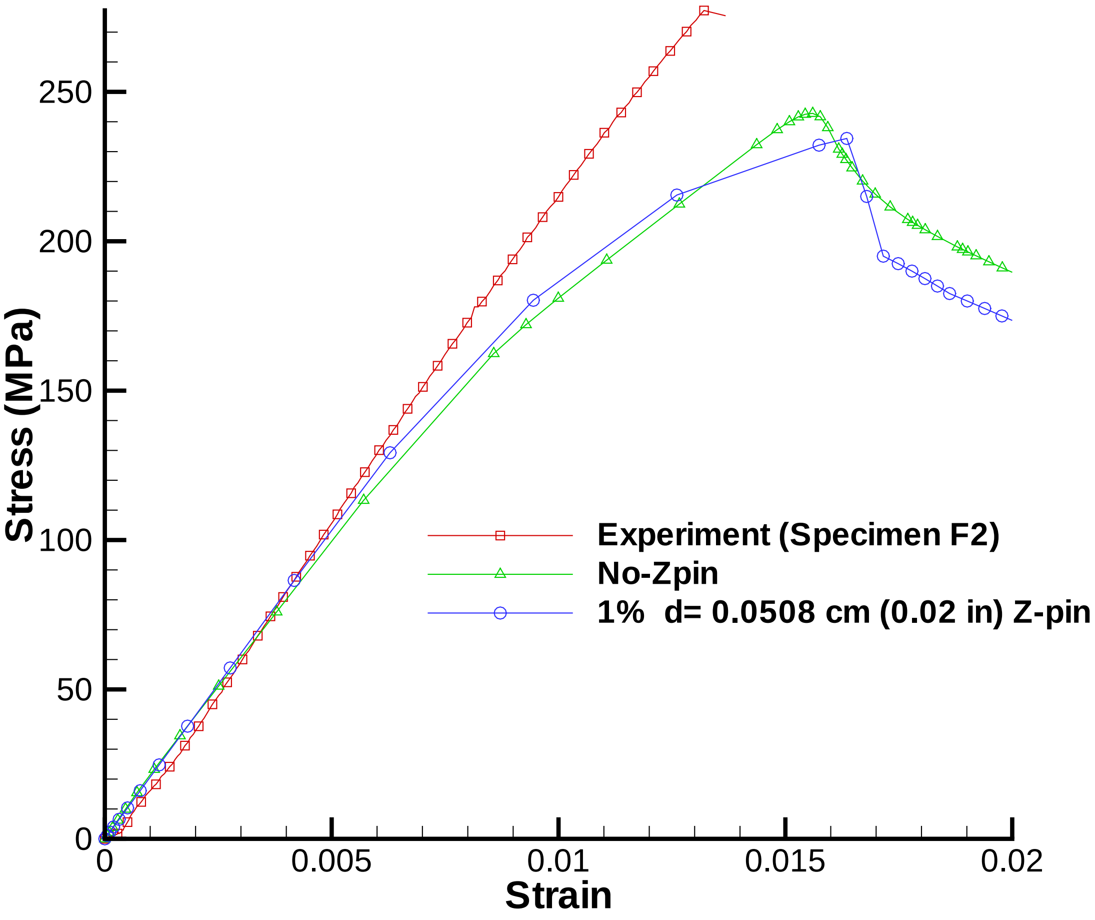

Figure 5.28: Comparison of Axial Stress-Axial Strain Response of Z-pin Composites and no Z-pin Composites

CHAPTER VI

Static and Dynamic Fracture Mode II Tests

Mode II ENF (end notch flexural) fracture tests for woven composites were performed. Influences of Z-pin density and Z-pin diameter on Mode II fracture toughness in dynamic and static loading were investigated. The experiments showed that the 2% Z-pin composite and the 3% Z-pin composite have a larger fracture toughness than the 1% Z-pin composite and composite with no Z-pin. Crack propagation changes from unstable propagation to stable propagation (crack arrest) as the Z-pin density increases. In static tests, the additional fracture toughness provided by Z-pins prevents the primary crack to further propagate, enabling the secondary crack or even tertiary crack to consume additional energy. While the primary crack is held from propagating by the friction forces provided by Z-pins, the matrix in the composite is driven into the plastic state and enables the composite to absorb more energy. For numerical simulations, a discrete cohesive zone model (DCZM) is used to perform simulations. The results of simulations agree well with results obtained from experiments. In dynamic tests, a crack advanced gage (CAG) is implemented in order to capture the initiation of the crack. “Crack arrest” can also be found in higher Z-pin density composites in dynamic tests. Similar to results in static tests, fracture toughness increases as Z-pin density increases. Also, for fixed Z-pin density, composites with smaller Z-pin diameter have higher fracture toughness than those with larger Z-pin diameter.

6.1 Introduction

The problem of delamination can be improved by inserting Z-pins into textile composites. In [22], it is indicated that inserting Z-pins increases the load capacity and leads to stable crack propagation at failure. In [46], an analytical expression to predict Mode I response of the Z-pin composites agrees well with experimental results. In [8], a 'T' joint is designed where the flanges are reinforced with insertion of Z-pins. The Z-pins increased the load at which the entire joint failed. In [64], a finite element for predicting Z-pin composite is proposed. The Z-pin pullout process is simulated by use of nonlinear springs. In [16], experiments are used to deduce pull-out law of Z-pins. Most of the literature about Z-pin composites investigates Mode I fracture toughness. There is few literature studying mode II fracture toughness of Z-pin composites. In those limited studies, different Z-pin diameter has not been discussed with respect to mode II fracture. Consequently, the primary goal of this chapter is to investigate the effect of Z-pin density and Z-pin diameter on the mode II fracture response of woven textile laminates.

6.2 Mode II Static Tests

6.2.1 Specimens and Experimental Set-up

Experimental results related to static mode II fracture response are presented in this section. Specimens are categorized into 6 groups. Group A, C, and E are $[45/-45/0/90]_{2s}$ lay-ups, with Z-pin diameters of 0.5080 mm (0.02 in), 0.2794 mm (0.011 in), and no Z-pin, respectively. Group C is Group B, D, and F are $[0]_{16}$

lay-ups composites with Z-pin diameter of 0.5080 mm (0.02 in), 0.2794 mm (0.011 in), and no Z-pin, respectively. It is to be noted that group A, group C, and group E are quasi-isotropic composites while group B, group D, and group F are cross-ply composites. From group A to group D, each group is further sub-divided into three subgroups based on the Z-pin density (1%, 2%, or 3%). Detailed descriptions of these 6 groups were summarized in Table 1.1. For each subgroup in A, B, C, D, E, and F, two tests were conducted.

A three point bending configuration is used to perform Mode II fracture tests on a servo-hydraulic MTS machine. Spacers were placed near the crack tip of the specimen (as shown in Figure 6.1) to prevent friction that might be induced when the top and bottom parts of the crack mouth touch. A higher resolution of digital cameras was placed on one side of the MTS machine in order to detect the propagation of the crack. The setup is shown in Figure 6.2.

A schematic of a tested specimen is shown in Figure 6.3. The length and width of the tested specimen is 160 mm and 25.4 mm, respectively. The height of specimens in each subgroup varies from 11 mm to 13 mm. A crack of length 40 mm and height 1 mm is initially machined as shown in Figure 6.3. In order to assist in crack initiation, a pre-crack was imposed by a sharp razor blade. At the center of the upper face and at the support points, steel pads were placed to prevent local damage to the composite. Images of the crack propagation event were recorded at 0.5 Hz, while the axial cross-head movement rate imposed on the specimen was 0.010 mm/sec (rate at which the transverse displacement control loading was imposed).

6.2.2 Experimental Results

The results of load-deflection curves for group A, group B, group C, and group D are shown from Figure 6.4 to Figure 6.7, respectively. Only one test for each subgroup is presented for clarity. The x-axis is the imposed deflection of mid-point and the y-axis is the reaction load at the mid-point. From these four figures, the maximum load for the 2% and 3% Z-pin composites increases greatly compared to the 1% Z-pin composites and no Z-pin composites.

The experimental results show that the 1% Z-pin composites don't increase the resistance for delamination compared to no Z-pin composites. As shown in Figure 6.4 and Figure 6.5, when the Z-pin density is the same, the maximum load for different laminates of quasi-isotropic family $[45/-45/0/90]_{2s}$ and of the orthotropic family $[0]_{16}$ is very similar. It is concluded that failure starts from the interface between laminae since the maximum load for both laminate groups is similar. In Figure 6.4 and Figure 6.6, when Z-pin density is fixed, the maximum load indicated in Figure 6.6 is higher than the maximum load shown in Figure 6.4. That is, a small diameter Z-pin composite has a higher fracture resistance than a large diameter Z-pin composite. This trend can also be found when the maximum loads in Figure 6.5 and Figure 6.7 are compared. This conclusion is counter to the conclusion arrived in chapter 2, which indicated that small diameter Z-pin composite has slightly lower "strength" and "stiffness" compared to larger diameter Z-pin composite. The higher fracture resistance in the small diameter Z-pin composites is due to more contact area between the Z-pin and fiber tows, thus providing more friction for pull-out resistance to prevent delamination and a higher resistance to crack propagation. From Figure 6.4 to Figure 6.7, it is also noted that additional fracture resistance provided by the Z-pin drives the composite into the plastic state (the matrix is driven to dissipate energy through matrix microcracking which is effectively "plastic like behavior"). The plastic phenomenon becomes obvious as the Z-pin density increases. Figure 6.8 is one of the tested specimens after the experiments corresponding to the 1% Z-pin composite in group C. Only the primary crack can be seen near the center of the specimen and the shape of the tested specimen doesn't change much after unloading, indicating substantial elastic energy recovery. This explains that energy being dissipated is only used for the propagation of the crack. As the Z-pin density increases, the additional fracture toughness for resisting delamination provided by the Z-pin enables the matrix in fiber tows , and between the tows in the composite to go into a plastic state before failure. Plastic deformation can be found in the 2% and 3% Z-pin composites after unloading as shown in Figure 6.9 and Figure 6.10. The plastic deformation is obvious in the 3% Z-pin composites, since the residual deformation is large.

The onset of crack propagation and subsequent crack propagation of each specimen were investigated by identifying the formation of crack in the images taken during the tests. For specimens in group E and group F , the crack propagates fast once the critical fracture toughness is reached (unstable propagation). For composites with Z-pin, crack propagation becomes more stable, meaning that there is "crack arrest" between the onset of crack propagation and the point at which the composite loses its loading capacity completely. This "crack arrest" period becomes longer as the Z-pin density increases. The images shown in Figure 6.11 was taken when load point deflection is 3.27 mm for the tested specimen F in Figure 6.7. At that instant, no crack was found. After 4 seconds when load point deflection is 3.31 mm as shown in Figure 6.12, unstable crack growth resulted in a crack that ran all the way to the mid point of the specimen. For the specimen D3 shown in Figure 6.7, when the load point deflection is 4.14 mm, the primary crack has already formed as shown in Figure 6.13. The primary crack propagated slowly (stable) unlike the (unstable) crack found in the non Z-pin composites. When the load point deflection is 5.12 mm, not only did the primary crack propagate, but another visible secondary crack could be found as shown in Figure 6.14. This shows that other energy dissipation events (secondary cracks) occurred while the primary crack is held from propagation due to the Z-pins.

Figure 6.15 and Figure 6.16 show load point deflection versus crack length for group B and group D. It is noted that, for Z-pin density less than 2%, an additional small load imposed on the specimens at the peak load results in that crack propagation after critical fracture toughness has been reached. For 3% Z-pin composites, the crack growth is more stable. It is also observed that crack propagation switches from unstable to stable as the Z-pin density increases.

6.2.3 Numerical Simulations

Cohesive zone elements have been used extensively and successfully to simulate crack propagation problems [62]. The introduction of different types of cohesive models are described in [63]. The cohesive zone element used in this paper belongs to the category of Discrete Cohesive Zone Element (DCZE). The DCZE consists of 4 nodes as shown in Figure 6.17 and the traction-separation laws are directly applied on opposing node pairs of the crack face. Details of the discrete cohesive zone method (DCZM) methodology and its implementation are described in [63]. A mixed mode fracture criterion as shown in equation (6.1) is adopted to determine crack propagation.

$$\frac{G_I}{G_{Ic}} + \frac{G_{II}}{G_{IIc}} \geq 1 \tag{6.1}$$

where, the definition of critical fracture toughness, G_{Ic} and G_{IIc}, for a triangular cohesive law, is as follows (see Figure 6.18):

$$G_{Ic} = \frac{1}{2}\sigma_c\delta_m \tag{6.2}$$

$$G_{IIc} = \frac{1}{2}\tau_c\gamma_m \tag{6.3}$$

A sensitivity study of the parameters for the end notch flexure simulations in [23] shows that mode II is dominant in ENF tests. Consequently, G_{IIc}, τ_c, and γ_m are the required parameters to implement a triangular cohesive law for the ENF test. Since a camera is placed on one side of the specimen, the timing at which the crack starts to propagate is known. Then, the corresponding load imposed on the specimen can be identified. The critical shear stress, τ_c, near the crack tip can be computed by simply using the formula in strength of materials. That is,

$$\tau_c = \frac{VQ}{I_z} \tag{6.4}$$

where $I_z = \int\int z^2 dA$ is the moment of inertia about the z-axis , $Q = \int\int z dA$, V is the shear force of the cross section at the crack tip, and A is the cross section. Triangular shape and trapezoidal shape traction-separation laws shown in Figure 6.18 are used to simulate the no Z-pin composite and Z-pin composite. For the triangular shape law, the maximum cohesive stress τ_c, initial slope K_x, and critical fracture toughness G_{IIc} are used as input. The critical displacement, γ_c, can be obtained by use of initial slope K_x and the maximum cohesive stress τ_c since the area under the traction-separation law is the critical fracture energy, G_{IIc} . The maximum γ_m is obtained by use of the expression $G_{IIc}{=}\frac{1}{2}\tau_c\ \gamma_m$. For the trapezoidal cohesive law, the maximum cohesive stress τ_c, initial slope K_x, the displacement that stress starts to drop γ_{c2}, and critical fracture toughness, G_{IIc}, are specified. The corresponding γ_{c1} and γ_m can be computed, accordingly. It was found that the triangular shape cohesive law is good for simulating unstable crack propagation (such as, propagation in composites without Z-pins). The trapezoidal shape cohesive law simulates the behavior of composites with Z-pins well.

The composite is assumed to be an orthotropic material and follows an orthotropic hardening plastic potential. The detailed derivation of the plastic potential can be found in chapter 3. With respect to Figure 6.3, the elastic properties of the specimens are as follows: E_{11}=21.7GPa, E_{33}=9.8GPa, ν_{13}=0.38, and G_{13}=5.9GPa. The plastic potential used here is derived from chapter 3.

The fracture toughness and cohesive strength were extracted as described in the following. As mentioned earlier, the approximate τ_c can be computed by use of equation (6.4) when a crack starts to propagate. The initial guess of G_{IIc} =2 N/mm is a reasonable guess of mode II fracture toughness for glass fiber composites from the existing published literature [61]. The converged value of G_{IIc} for a test is obtained when the load-deflection response from that test and the corresponding response from simulations match as shown in Figure 6.20

The model used for the numerical simulation is shown in Figure 6.19. The CPS4 element is used to simulate Z-pin composites and the user defined UEL subroutine is implemented in ABAQUS to simulate cohesive zone elements.

Figure 6.20 shows the comparison of numerical simulations with experimental results (Figure 6.7). The computed critical fracture toughness for $[45/-45/0/90]_{2s}$ composite and $[0]_{16}$ composites are shown in Figure 6.21 and Figure 6.22 . It is noted that the fracture toughness increases greatly when the Z-pin density is 2% or 3%. In each figure, (Figure 6.21 and Figure 6.22), when density is the same, the fracture toughness of d=0.02in Z-pin composites is lower than the fracture toughness of d=0.011in Z-pin composites. Although the volume fraction of Z-pins in the d=0.011in composites and the d=0.02in composites is the same (provided density is fixed), the contact area between a Z-pin and fiber tow for d=0.011in composite is almost twice that of the contact area for d=0.02in composite. It is believed that the friction forces provided by the additional contact area are the reason for the the increase of fracture toughness, which provides additional resistance to delamination. A detailed micromechanics based model for the Z-pin based traction law can be attempted by considering "pull-out" mechanics as described in [34]. In [34], a triangular law can also be used (instead of the trapezoidal law used here) for simulating Z-pin resistance as density increases.

6.3 Dynamic Mode II Test

In a static mode II test, the event time (The time between when load is applied and when the crack propagates to the center of the specimen) is more than several minutes. Under such conditions, it is easy to detect the onset of crack growth and the crack propagation afterwards by use of ordinary cameras that are used in everyday life. However, in dynamic tests, the event time is on the order of 10^{-3} second. Therefore, a high speed camera able to capture 12 pictures is used. The interval (greater than 10^{-6} sec) between each picture can be specified by the user.

The other problem crucial in a dynamic test is to be able to capture the onset of the crack growth. Accurately measuring the location of the crack during the impact event is of great concern in order to extract the change of fracture toughness during crack propagation.

In static tests, images of the crack path, and crack length taken using a high resolution camera, can be conveniently related to the load and specimen deformation, without complications with respect to the frequency of data recording. In a dynamic event, where the total duration is of the order of 1 ms, there is a need to accurately establish the initiation of the crack growth event. Thus, a novel method is employed in which conductive silver paint is deposited in the form of a thin column on the side surface of the specimen and is used as a crack advance gage (CAG). The CAG, which acts as a conductor with known resistance, is connected to a Wheatstone bridge circuit in series with a 120 Ω strain gage. The output voltage from this arrangement is used to trigger the camera at the initiation of crack advance, establishing the time corresponding to the origin of crack advance. The CAG is initially calibrated against a static test in order to determine the output signature as the crack severs the CAG. In the early stages of impact loading, the output from the CAG remains low due to the relatively small shear deformation. As load increases, the CAG output rises rapidly and approaches around 10 volts when the crack has completely severed the CAG. Several CAGs can be used as indicators of crack location during the impact event and also as a measure to corroborate the images that are captured through the high speed camera.

6.3.1 Setup of Experiment

Similar to the static test, a three point bending setup is used to perform dynamic mode II tests by use of an existing drop tower facility shown in Figure 6.23. Two specimens in different subgroups listed in Table 1.1 are used for the dynamic tests. Figure 6.24 shows that three crack advance gages are placed at different locations from the crack tip. The first CAG is 3 mm from the crack tip. The second CAG and the third CAG are 18 mm and 33 mm from the crack tip. In every 3 mm one line is drawn in order to observe the propagation of the crack in the images taken from the high speed camera. The oscilloscope is triggered when the crack passes the first CAG. At the same time, the pulse generator received the signal from the output voltage of the first CAG and subsequently (after 10^{-5} sec) sent a signal to trigger the high speed camera. Twelve pictures are taken at different time from the high speed camera. The exposure time for each picture is 10^{-6} sec. Therefore, a special flash light is used to provide enough intensity of light during the 10^{-6} sec in which an picture is grabbed.

6.3.2 Results

Figure 6.25 shows a typical load-time response of a mode II dynamic test. The x-axis represents the time and the y axis is the load recorded from a dynamic load cell. After the dropping weight hit the specimen, the load increases with a linear trend until the initiation of the crack. The signal of strain gage can be observed to stay around zero and jumps suddenly because of the crack passing through the silver paint and severing the connection of the first gage. This sudden jump occurs immediately before or after the occurrence of the peak load. Nearly linear load signal with slight oscillation can be observed in a typical load-time curve as shown in Figure 6.25. Further investigation shows that this oscillation is due to the load cell. Figure 6.26 shows the load versus time curve of the transient response output of the load cell (by hitting the load cell gently with a hammer). The dynamic load cell is produce by Kistler Inc with the type number of 9091A. The frequency of the oscillatory signal in Figure 6.25 and the frequency of the oscillatory signal in Figure 6.26 are close. Such oscillations in the load-time response can be found in all of the tests. Thus, a discrete Fast Fourier Transform (FFT) is used to filter the signal recorded by load cell. Figure 6.27 shows the load-time response before and after filtering using the FFT.

An analytical expression for critical mode II fracture toughness is proposed in [38], as

$$G_{II} = 9/16(P_m^2/B^2h^3E_{11})(a+\chi h)^2 \tag{6.5}$$

where

$$\chi = [(E_{11}/11E_{33})(3-2(\tau/(1+\tau))^2)]^{0.5} \tag{6.6}$$

$$\tau = 1.18\sqrt{E_{11}E_{33}}/G_{13} \tag{6.7}$$

In these expressions, P_m is the maximum transverse applied load, a is the crack length, B is the width of the specimens, h is height of the specimen, E_{11} is the longitudinal young's modulus, E_{33} is the transverse young's modulus, and G_{13} is the shear modulus in the 1-3 plane. The axes are shown in Figure 6.3. By identifying the maximum load, the fracture toughness can be computed. Figure 6.28 and Figure 6.29 show the fracture toughness for $[0]_{16}$ composites and $[45/-45/0/90]_{2s}$ composites. In $[0]_{16}$ composites shown in Figure 6.28, as Z-pin density increases, the critical fracture toughness increases. It is noted that equation (6.5) is an approximate expression for dynamic fracture toughness and is used here for purpose of comparison. One would need to perform a full dynamic simulations in order to obtain the dynamic fracture toughness.

When the Z-pin density is the same, the specimens with smaller Z-pin diameter have higher critical fracture toughness than specimens with higher Z-pin diameter. This trend can be also observed in Figure 6.29 for $[45/-45/0/90]_{2s}$ composites. The critical fracture toughness in Figure 6.28 and Figure 6.29 are smaller than that in static fracture test shown in Figure 6.21 and Figure 6.22

6.3.3 Why Use CAG Instead of High Speed Camera

Figure 6.30 shows the information of the load cell and three CAG near the time when the crack starts to propagates for a B3-1 specimen. The vertical axis is the load and the horizontal axis represents the time. From Figure 6.30, crack arrest occurs after the break of the first gage. This crack arrest lasts for around 750μ sec and then the crack propagates suddenly all the way through 2nd and 3rd CAG. Given that the distance between 2nd CAG and 3rd CAG is 15 mm and the smallest interval between neighboring data points recorded from the oscilloscope is 1 μ sec, the propagation speed is greater than 1500 m/sec in this specimen. Figure 6.31 shows the image taken before the test. Figure 6.32 is the one taken after 100 μ sec that the 1st CAG has already been broken. A microcrack already passed through the 1st CAG. However, the crack arrested and didn't continue to proceed. When time is 100 μ sec after the 1st CAG is broken, additional microcrack can be observed near the crack mouth. Figure 6.33, taken when time is 550 μ sec after breakage of the 1st CAG, shows the multicrack phenomenon as shown in Figure 6.32. Finally, the major crack can be found in Figure 6.34 which is taken at 1050 μ sec after breakage of the 1st CAG. Obviously, using CAG has more advantages than using the high speedcamera. First of all, from the sudden change of signal in the CAG, it is easy to identify the exact time when the crack starts to propagate. For the high speed camera, we could only capture the “INTERVAL” when the crack starts to propagate. Secondly, since these gages (CAGs) are lines of conductive silver paint, they are inexpensive.

In Figure 6.30, the 1st CAG is broken before the peak load. Increases in loading can be observed after the breakage of the 1st gage. Figure 6.35, another test for specimen B3-2, shows the same trend. When crack occurred, the composite didn’t lose its loading capacity immediately because of crack arrest. Figure 6.36 is the load response and three CAG curves near the peak load for the specimen B2-1. Loading starts to drop after the crack passes through the 3rd CAG. The duration between the breakage of the 1st CAG and the 3rd CAG is only 60 μ sec. However, for specimen B3-2, there is 250μ sec duration between the breakage of the 1st CAG and the 3rd CAG in Figure 6.35. This also shows 3 % Z-pin composites could absorb more energy than 2 % Z-pin composites during fracture process because the duration of “crack arrest” is longer.

Table 6.1 shows the propagation speed between different gages for different specimens. The crack arrest can be observed as Z-pin density increases. For groups E and F, crack propagates all the way to 3rd CAG. No arrest between different CAGs can be found. For composites with Z-pins, crack propagation speed decreases as Z-pin density increases. This trend is more obvious between 1st CAG and 2nd CAG. Crack propagation speed from 2nd gage to 3rd gage is faster than crack propagation speed from 1st gage to 2nd. Actually, crack propagation speed between 1st and 2nd

CAG should be regard as average propagation speed. By the help of high speed camera, it is observed the crack doesn't propagate immediately after breakage of 1st CAG. The initial crack remains arrested and then suddenly propagates all the way past the 2nd and 3rd CAGs without arrest.

6.4 Conclusion

The mode II fracture behavior of Z-pin composites was presented. Two types of composites, $[45/-45/0/90]_{2s}$ and $[0]_{16}$ lay-ups, were used in the tests. In each type of the composite, the response of three different kinds of Z-pin density and two different kinds of Z-pin diameter are investigated. The Z-pins greatly increase the fracture toughness than the unpinned composites. The Z-pins successfully prevent the primary crack from growing unstably while cracks on other weak planes are formed, thus dissipating more energy. The additional friction provided by Z-pins also lets the composites enter plastic state so more energy is dissipated. When Z-pin density is the same, the contact area between Z-pin and fiber tows in small-diameter Z-pin composites provides more fracture toughness than large-diameter Z-pin composites. The proposed cohesive zone model for the static test, appears to capture the trend observed in the experiments, and predicts the load- load point displacement response curves statistically.

Table 6.1: Crack Speed of the Composite

Type	Crack Speed m/sec (1st to 2nd)	Crack Speed m/sec (2nd to 3rd)
A1	500	375
A2	88.2	250
A3	14.6	375
B1	516	258
B2	500.2	750
B3	62.5	1500
C1	55.6	150
C2	22.7	750
C3	22.1	107
D1	214	750
D2	214	250
D3	53.6	250
E	500	750
F	750	750

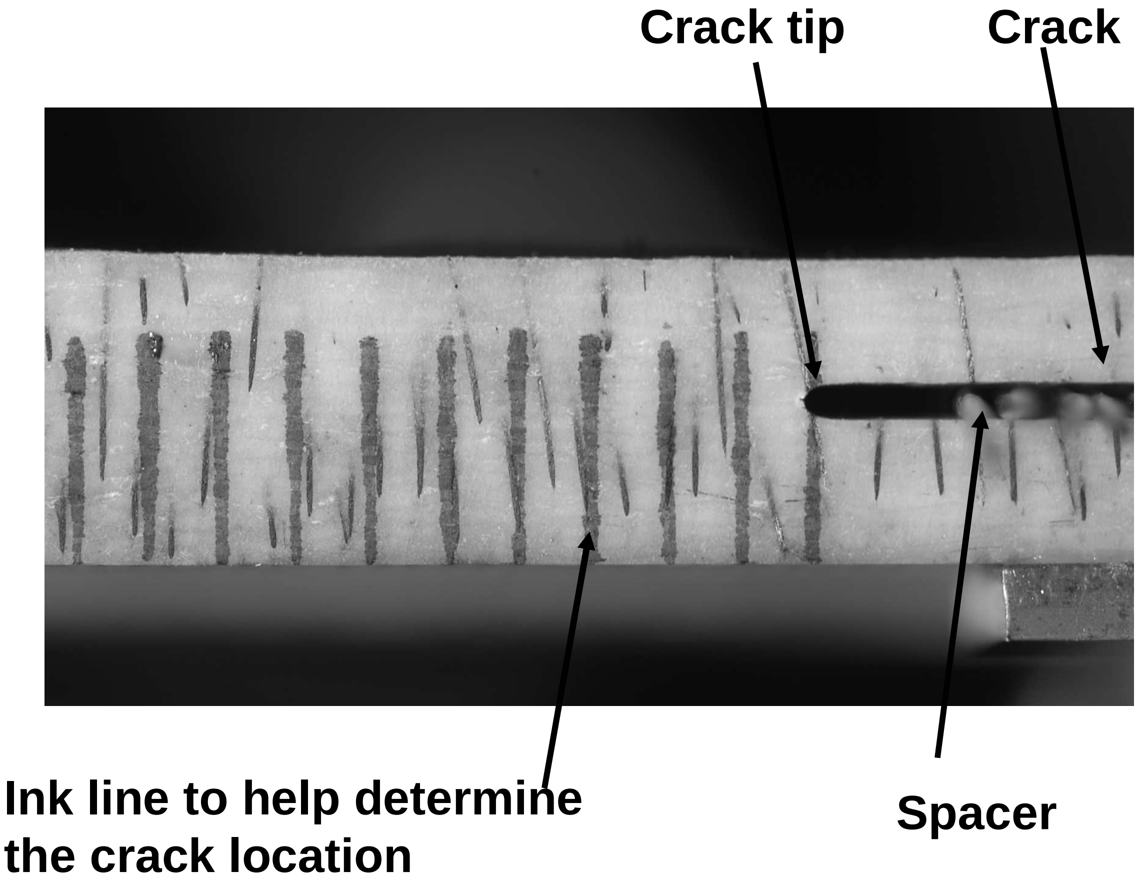

Figure 6.1: Specimen and Spacer (Only Half of the Specimen is Shown, as a Side View)

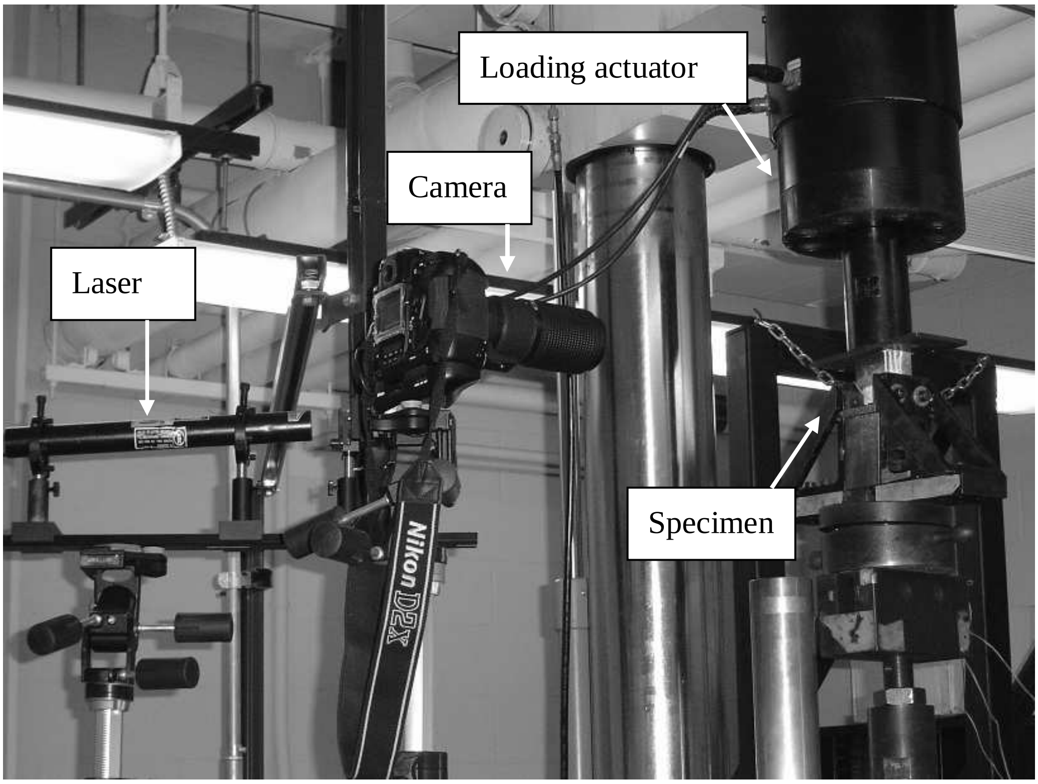

Figure 6.2: Setup of Camera

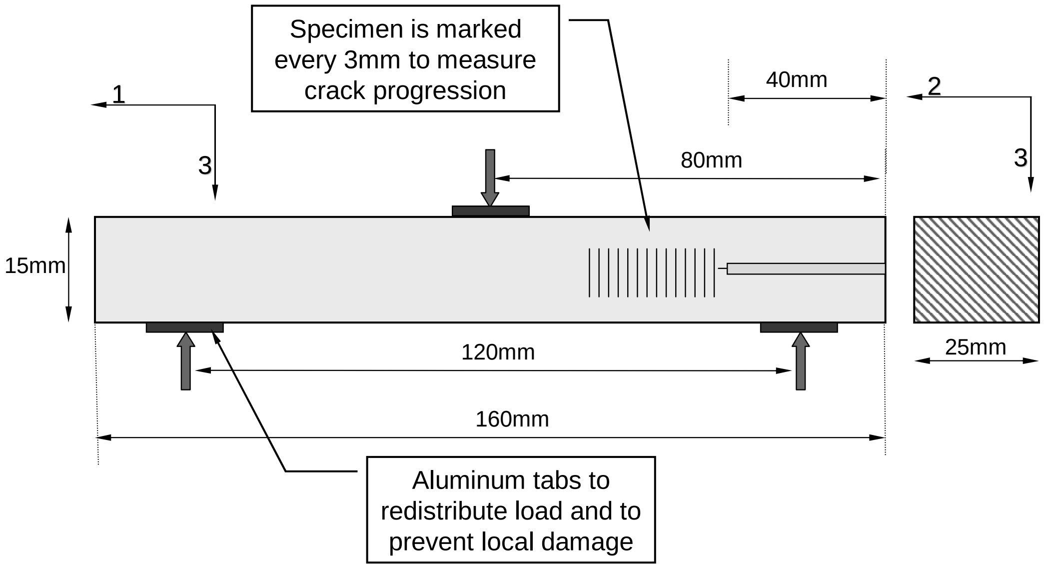

Figure 6.3: Schematic of a ENF Test Specimen

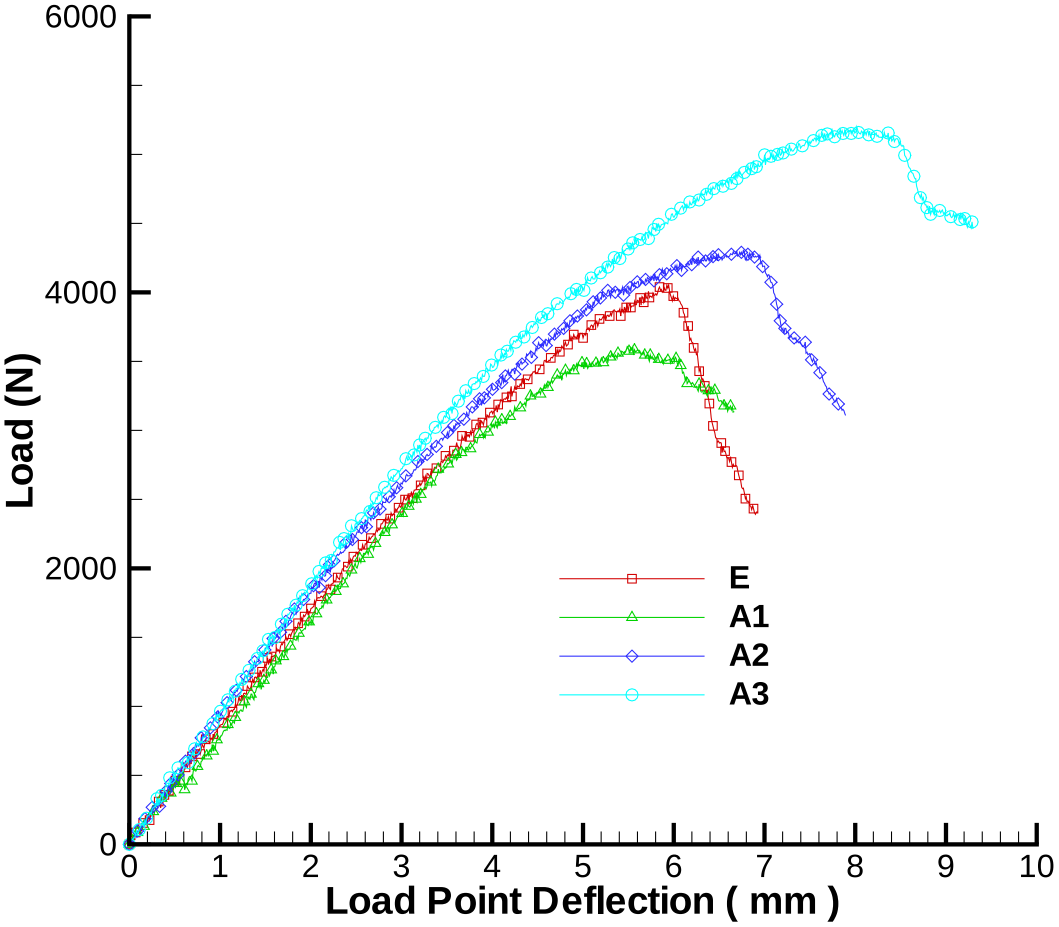

Figure 6.4: Load Deflection Plot for Group A. ‘E’ Denotes the Case with no Z-pins.

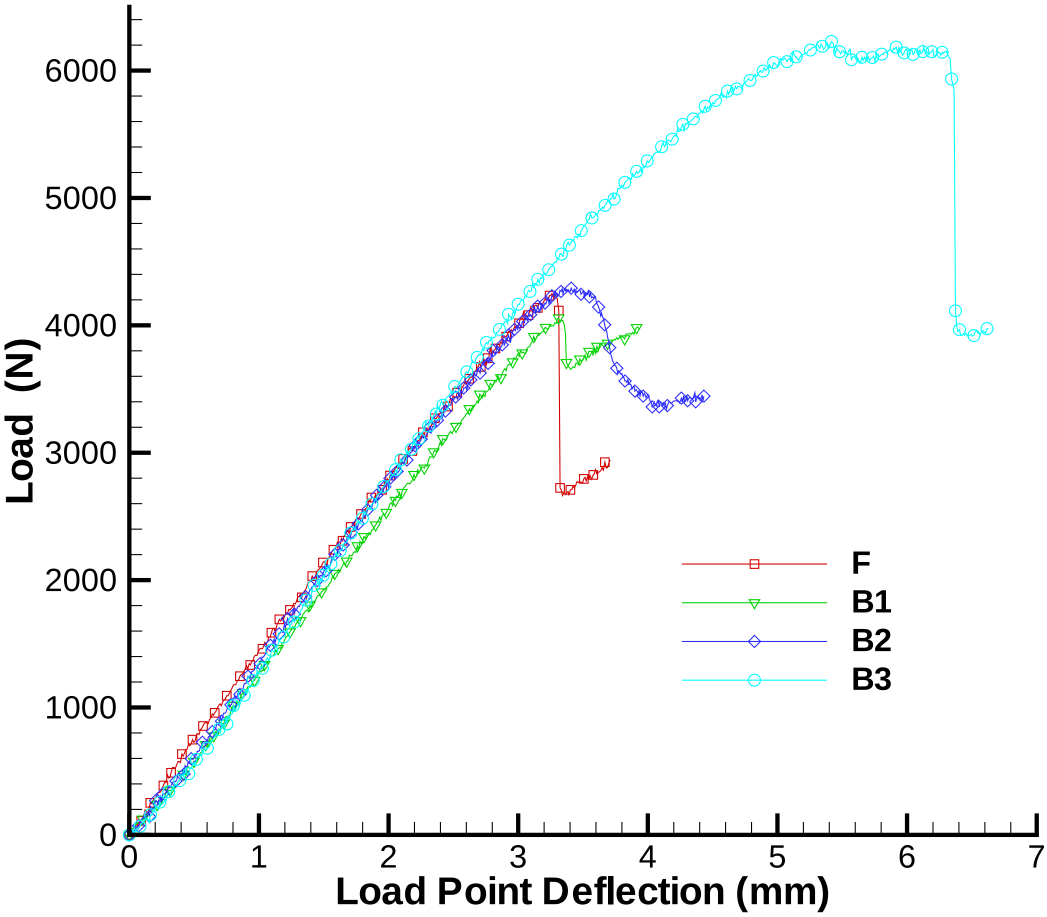

Figure 6.5: Load Deflection Plot for Group B. ‘F’ Denotes the Case with no Z-pins.

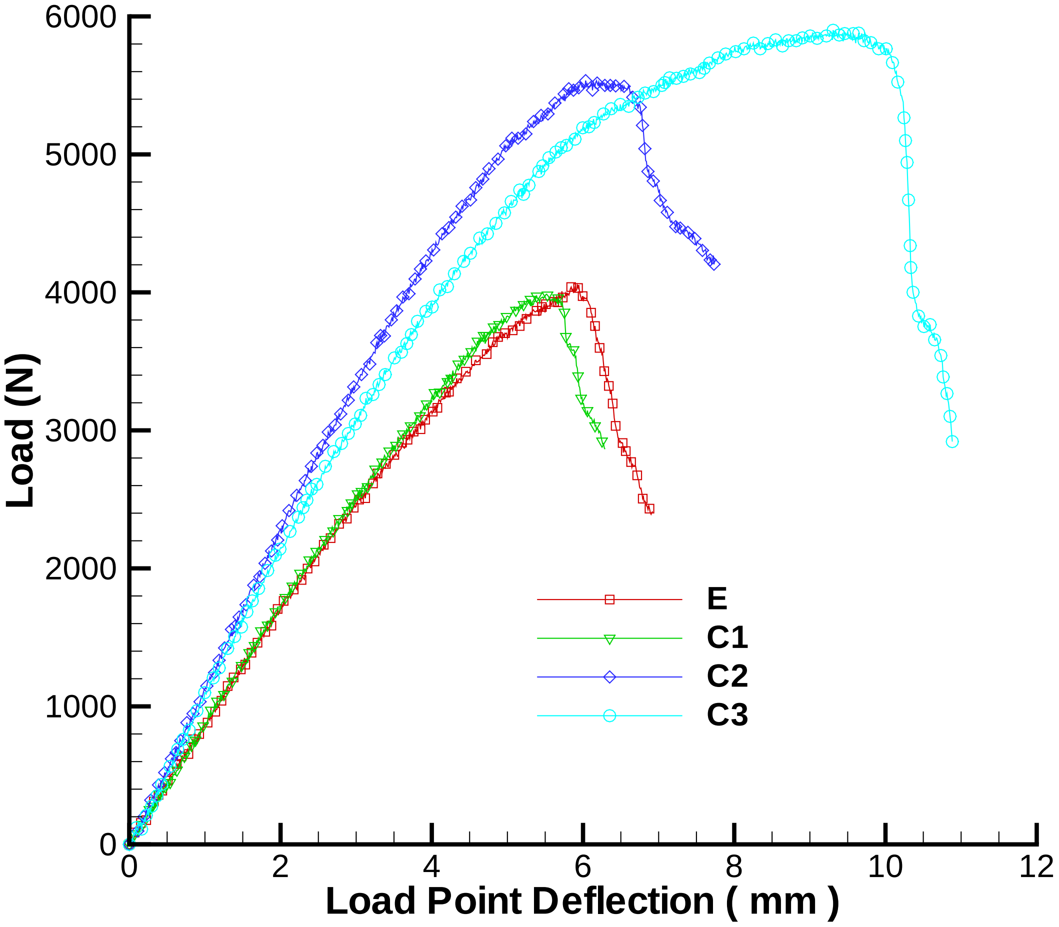

Figure 6.6: Load Deflection Plot for Group C. ‘E’ Denotes the Case with no Z-pins.

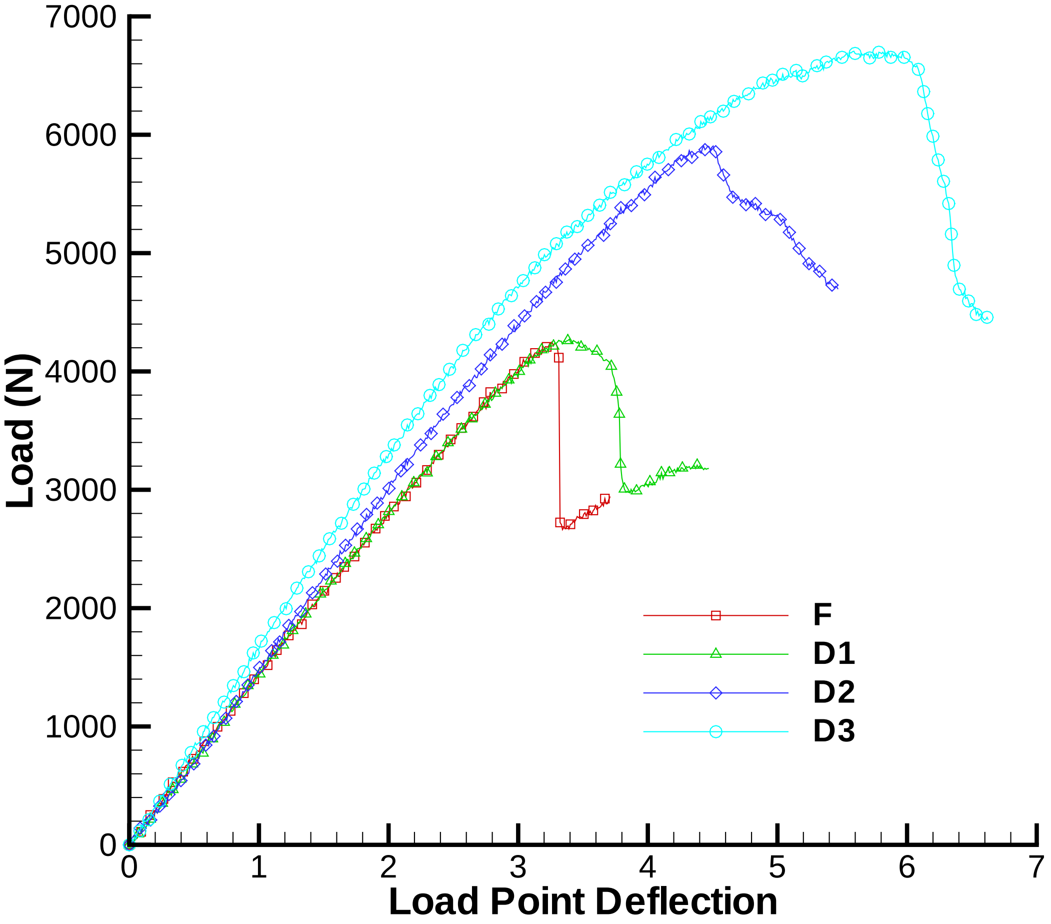

Figure 6.7: Load Deflection Plot for Group D. ‘F’ Denotes the Case with no Z-pins.

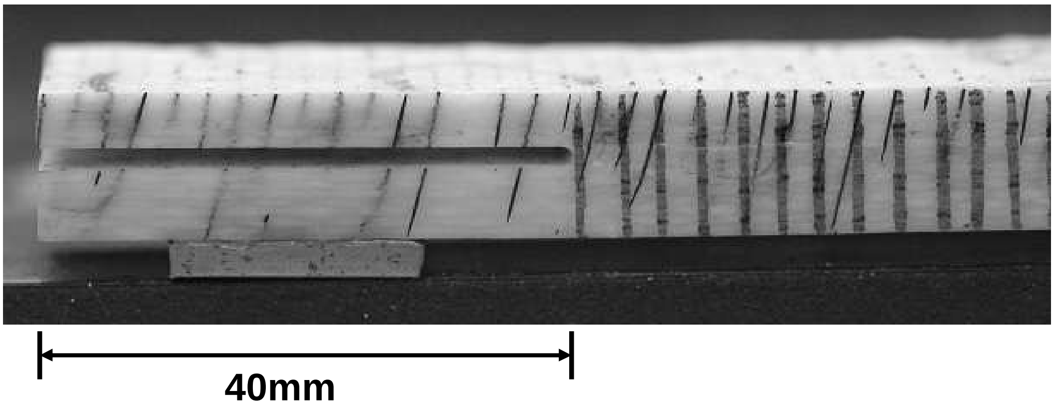

Figure 6.8: Tested Specimen of C1 after Experiments

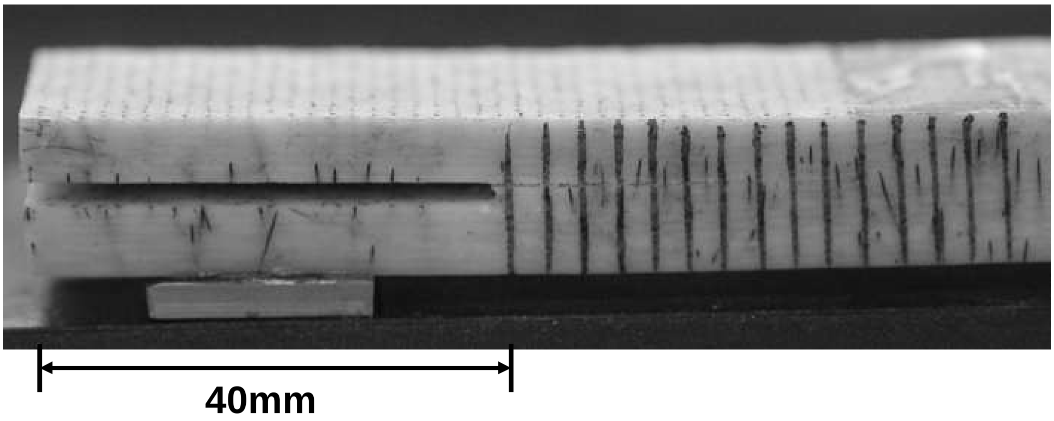

Figure 6.9: Tested Specimen of C2 after Experiments

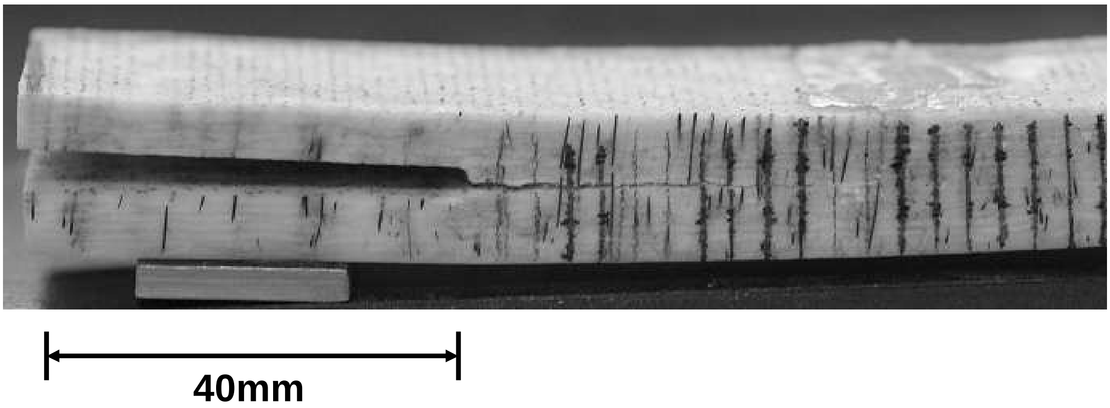

Figure 6.10: Tested Specimen of C3 after Experiments

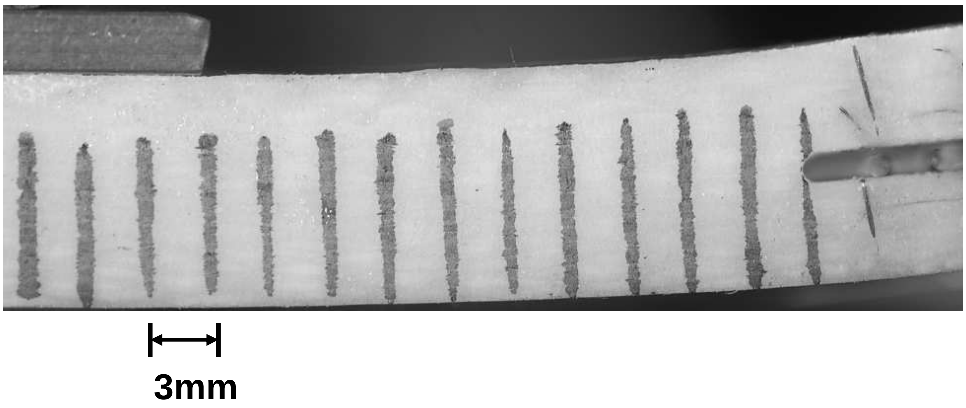

Figure 6.11: F1 Specimen Deflection=3.27 mm

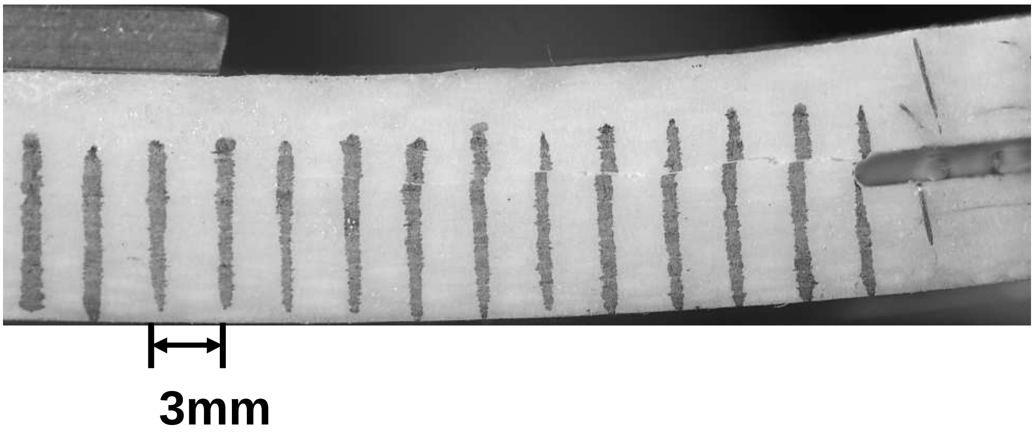

Figure 6.12: F1 Specimen Deflection =3.29 mm

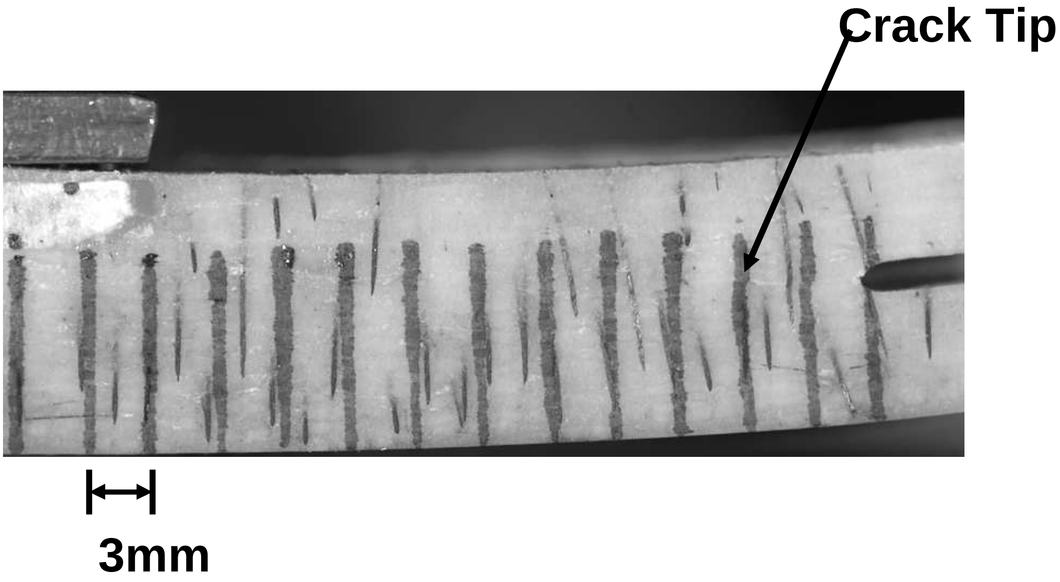

Figure 6.13: D3 Specimen Deflection=4.14 mm

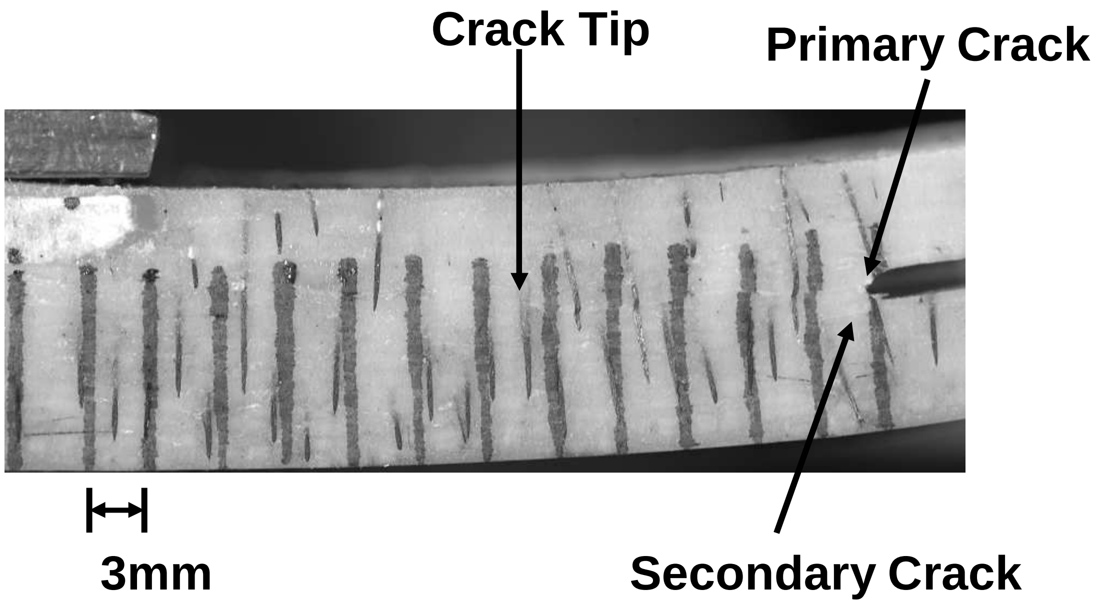

Figure 6.14: D3 Specimen Deflection=5.12 mm

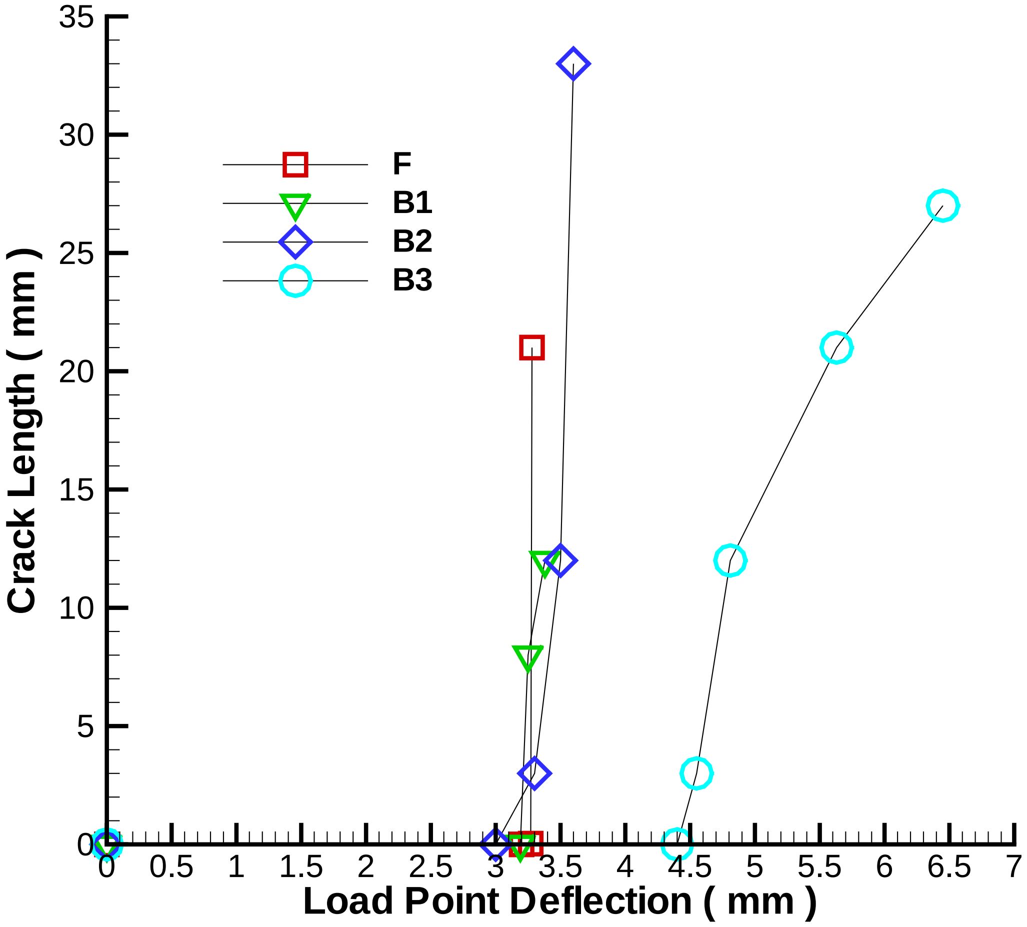

Figure 6.15: Crack Length vs Deflection for Group B

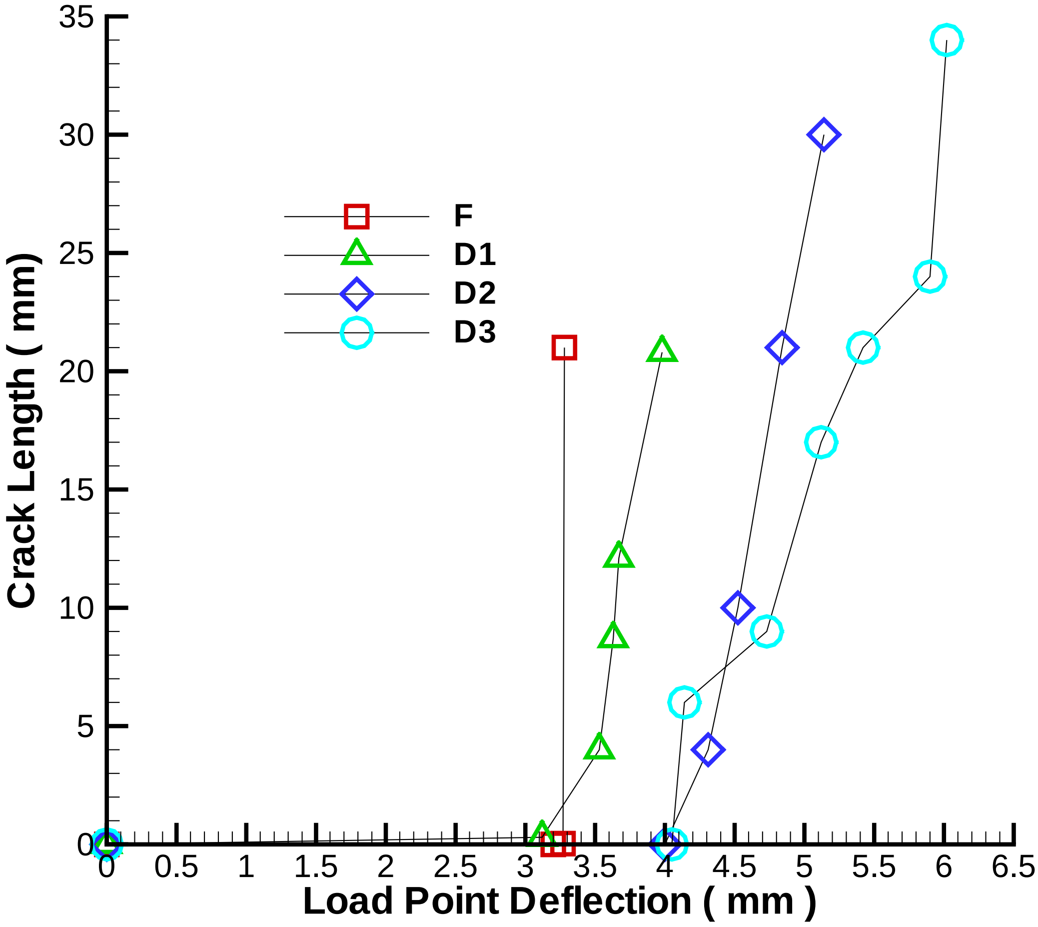

Figure 6.16: Crack Length vs Deflection for Group D

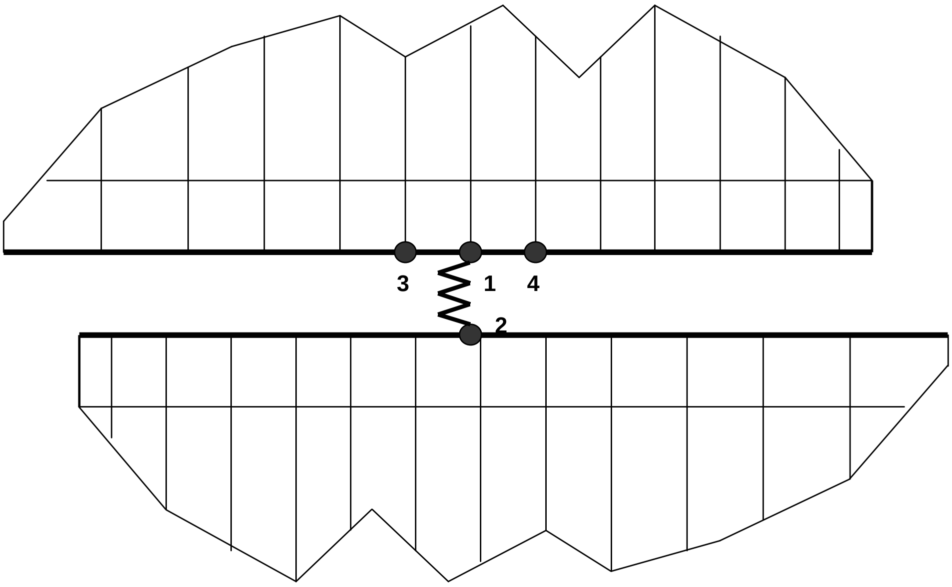

Figure 6.17: Cohesive Element

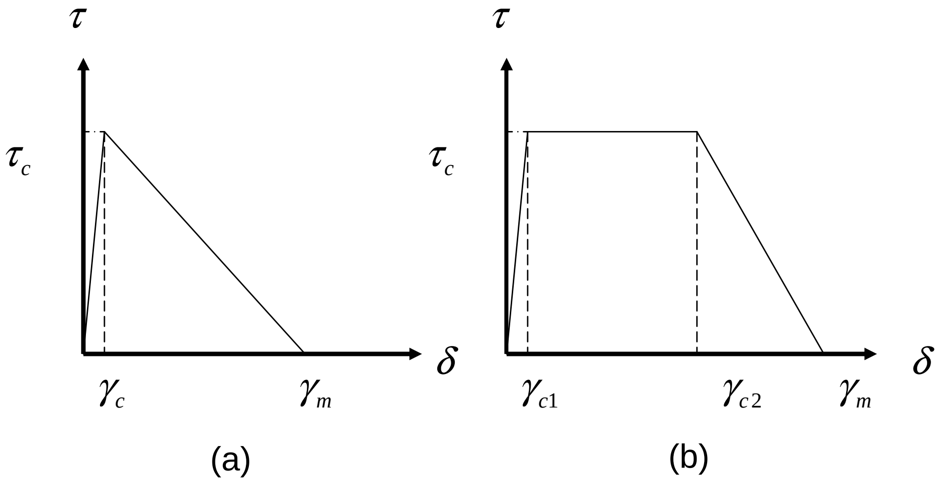

Figure 6.18: Cohesive Law

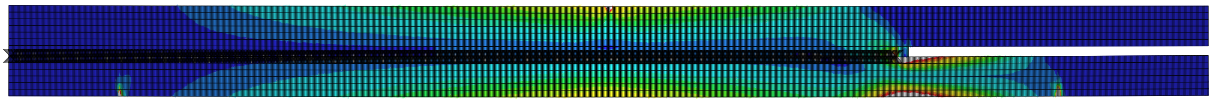

Figure 6.19: Numerical Model for Mode II Simulation

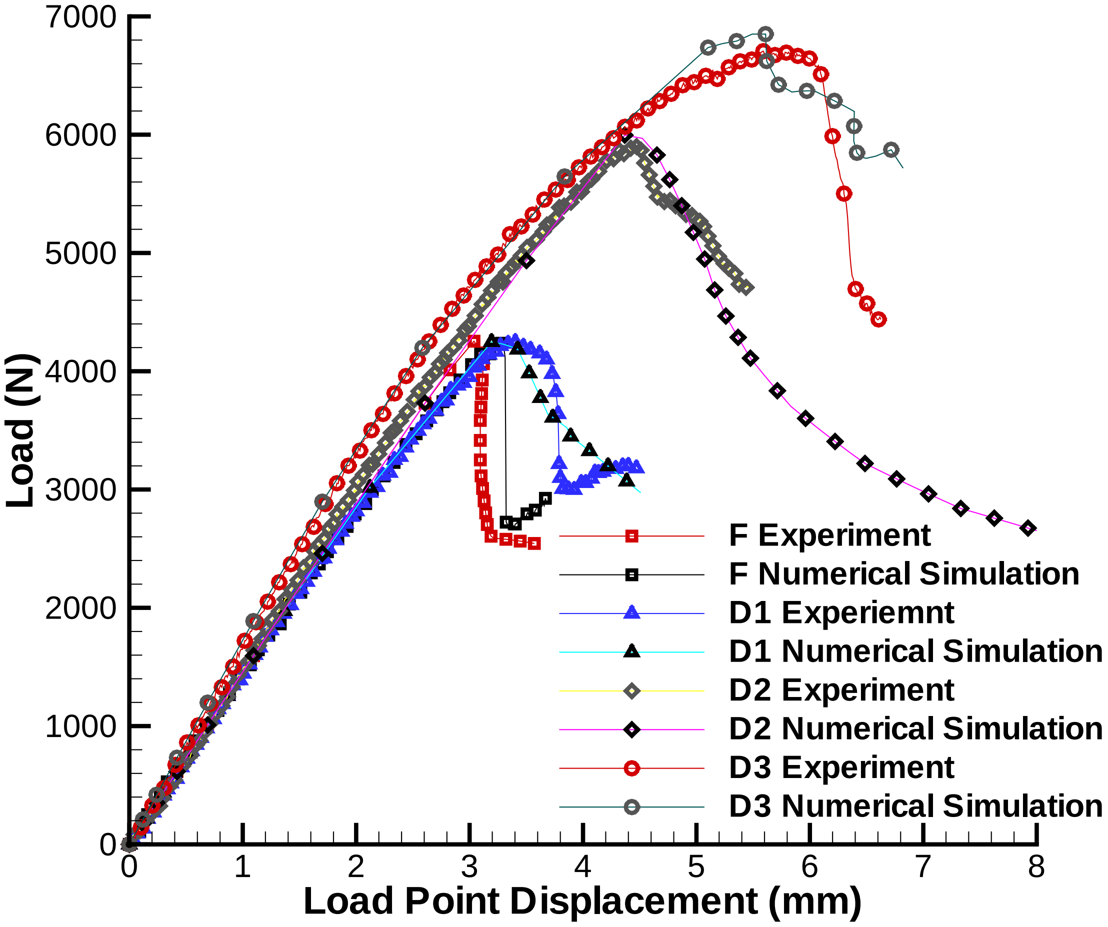

Figure 6.20: Comparison of Numerical Simulation and Experiment

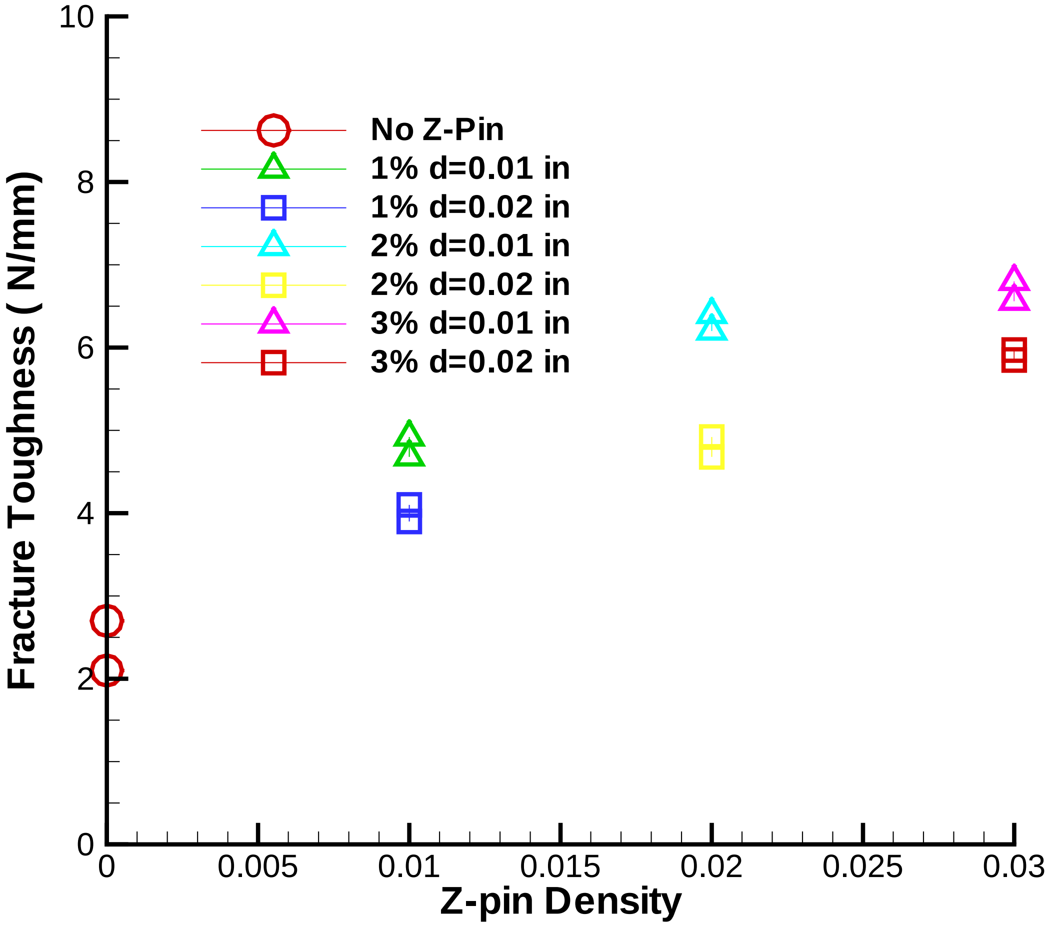

Figure 6.21: Fracture Toughness of $[45/-45/0/90]_{2s}$ Composites

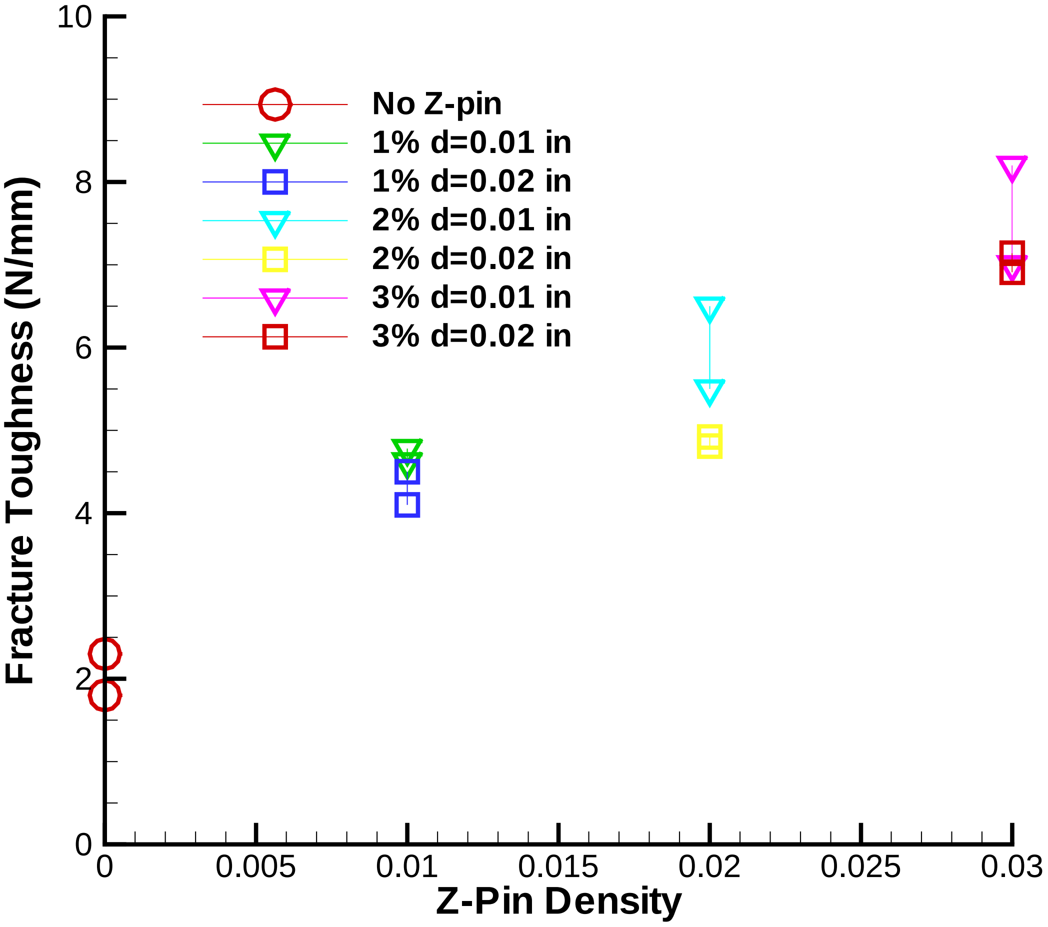

Figure 6.22: Fracture Toughness of $[0]_{16}$ Composites

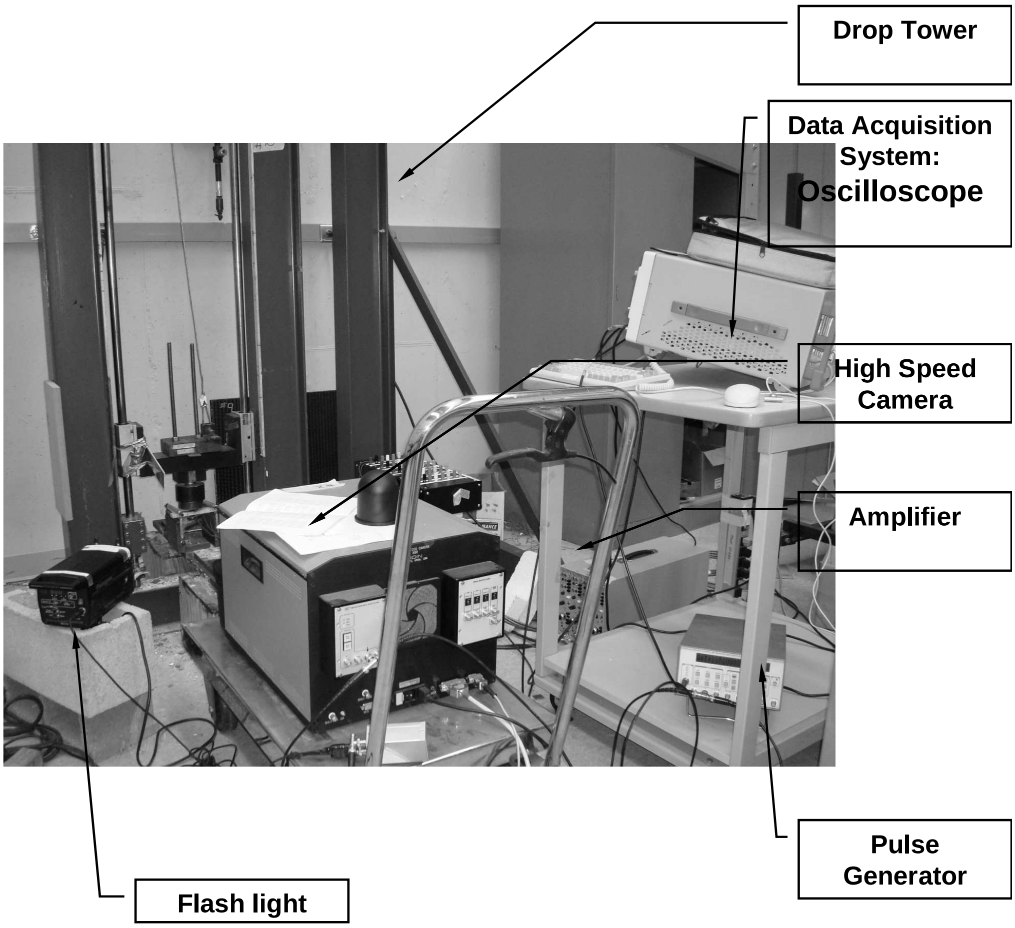

Figure 6.23: Set-up of Drop Tower

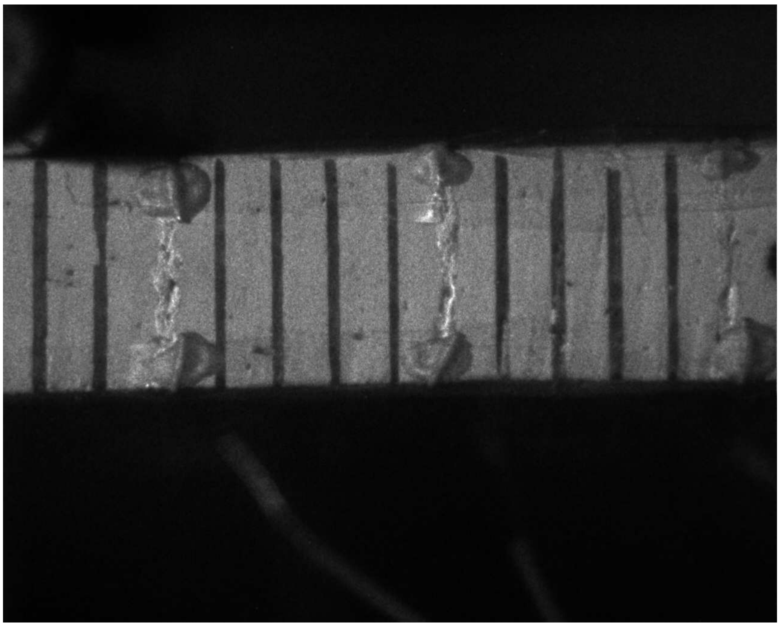

Figure 6.24: Crack Advanced Gage

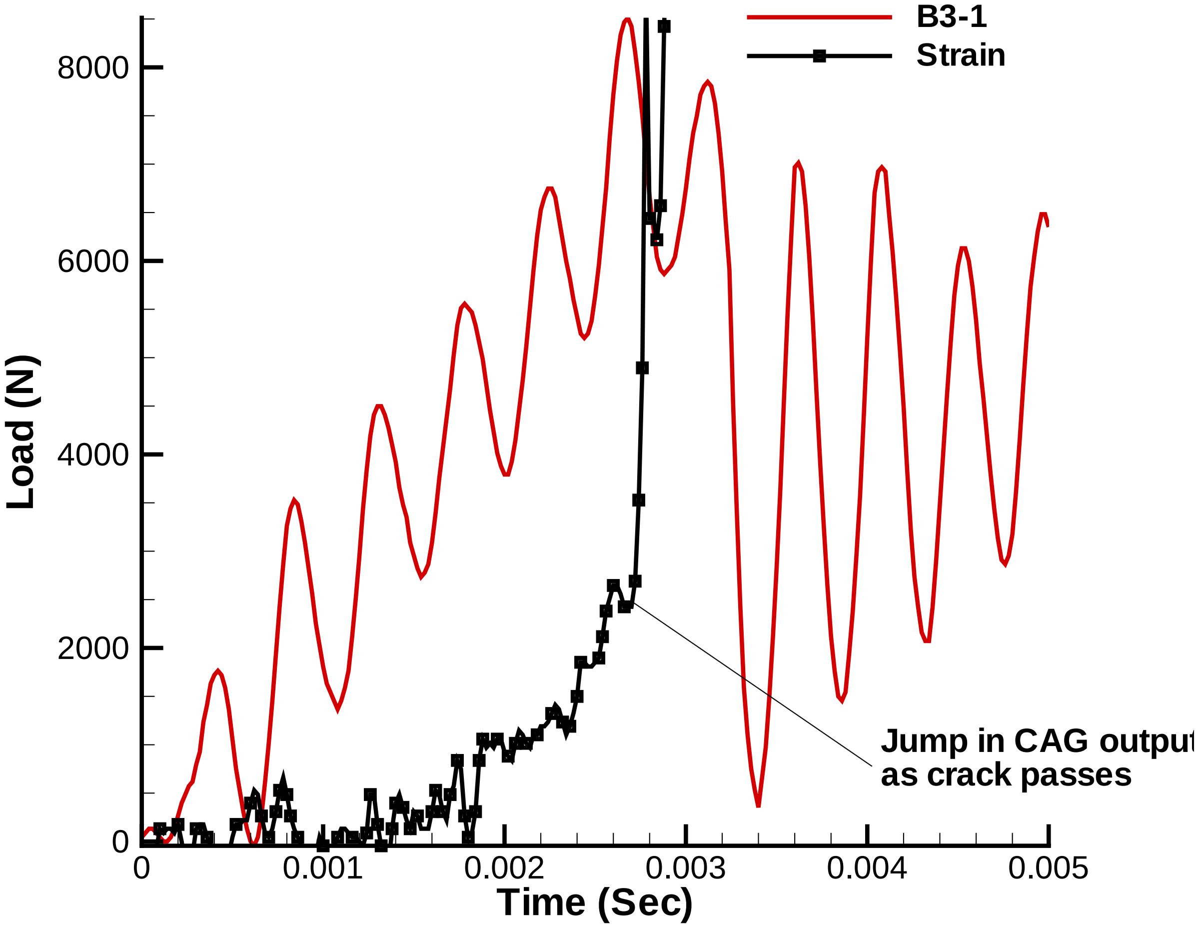

Figure 6.25: Load Versus Time of B3-1 Specimen

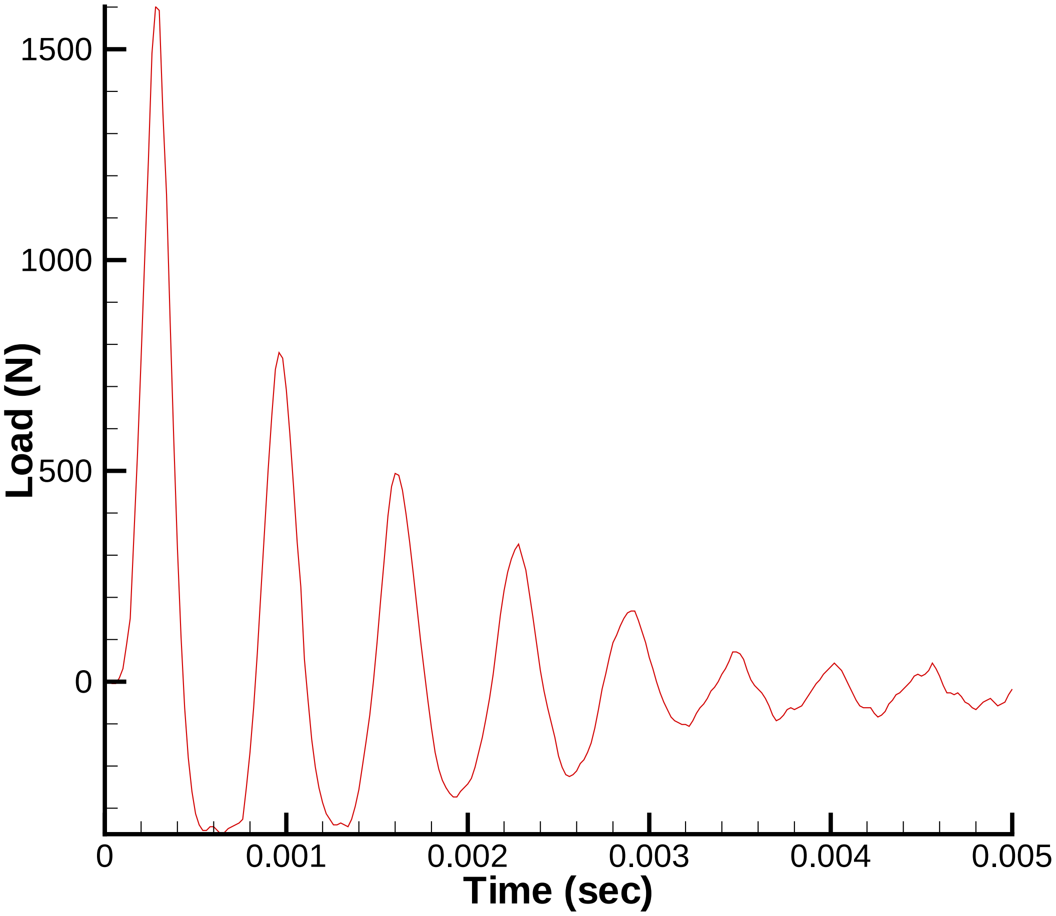

Figure 6.26: Load Versus Time of the Load Cell Transient Response, due to a "Hammer" Strike

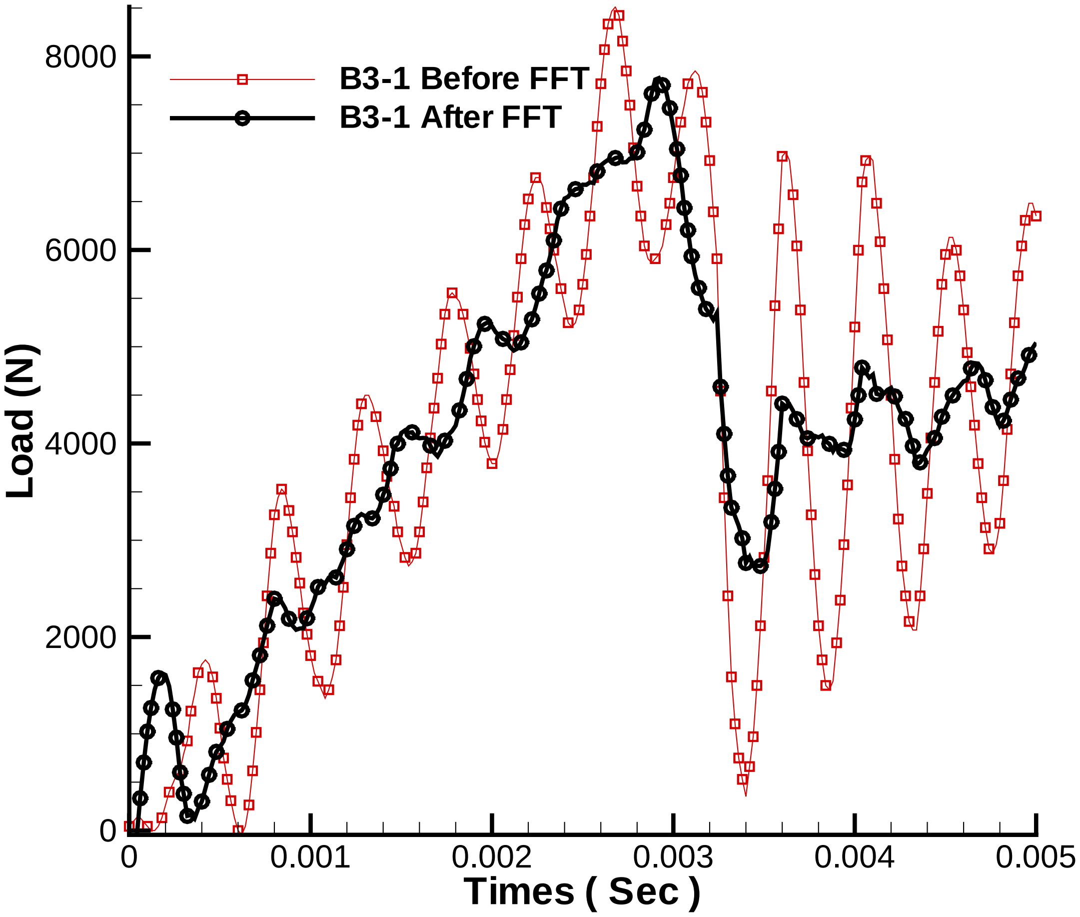

Figure 6.27: Load Versus Time of B3-1 Specimen Before and After Filtering, Using the FFT

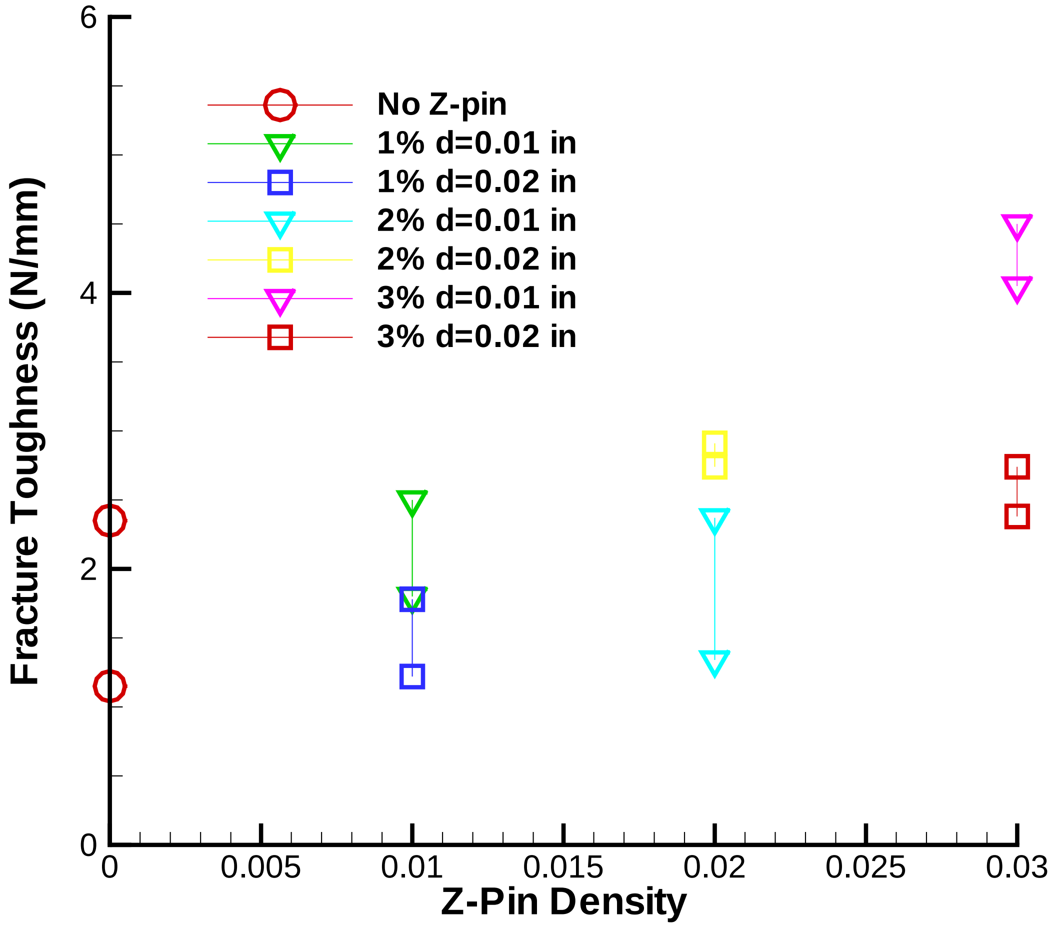

Figure 6.28: Dynamic Fracture Toughness for $[0]_{16}$ Composites

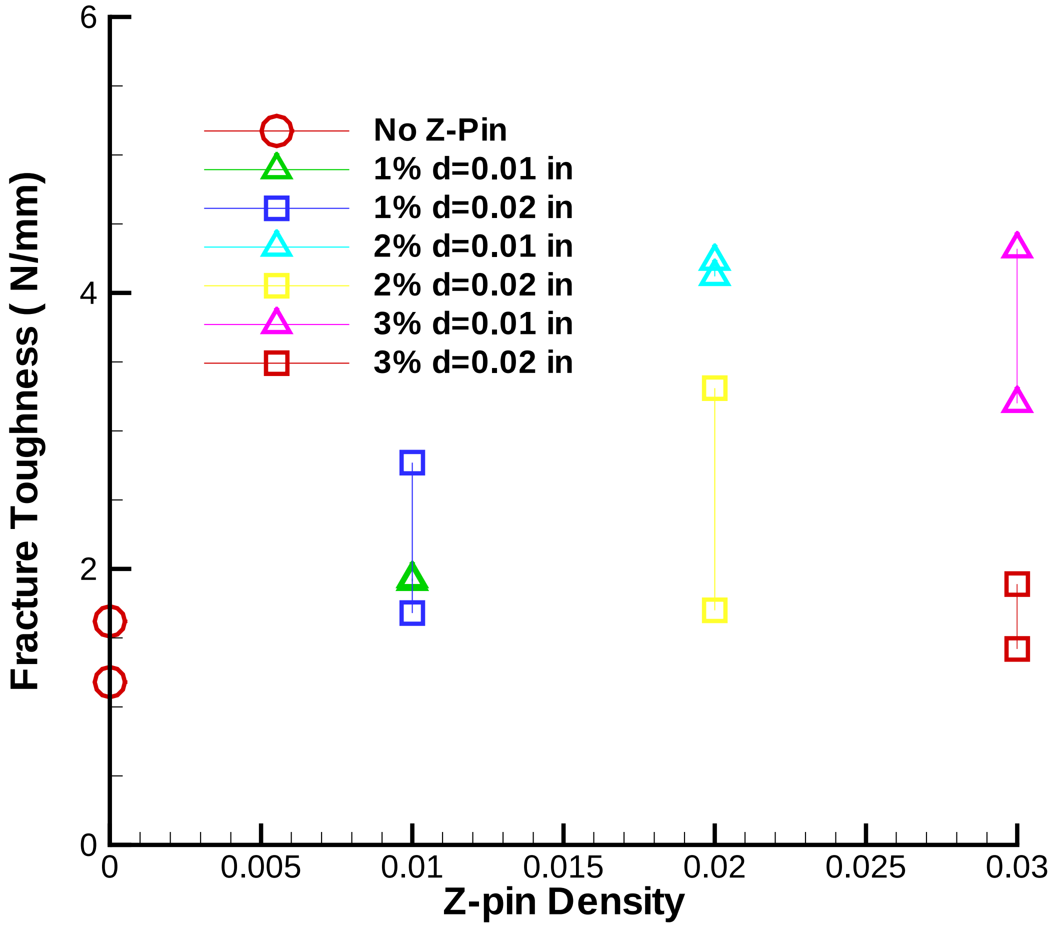

Figure 6.29: Dynamic Fracture Toughness for $[45/-45/0/90]_{2s}$ Composites

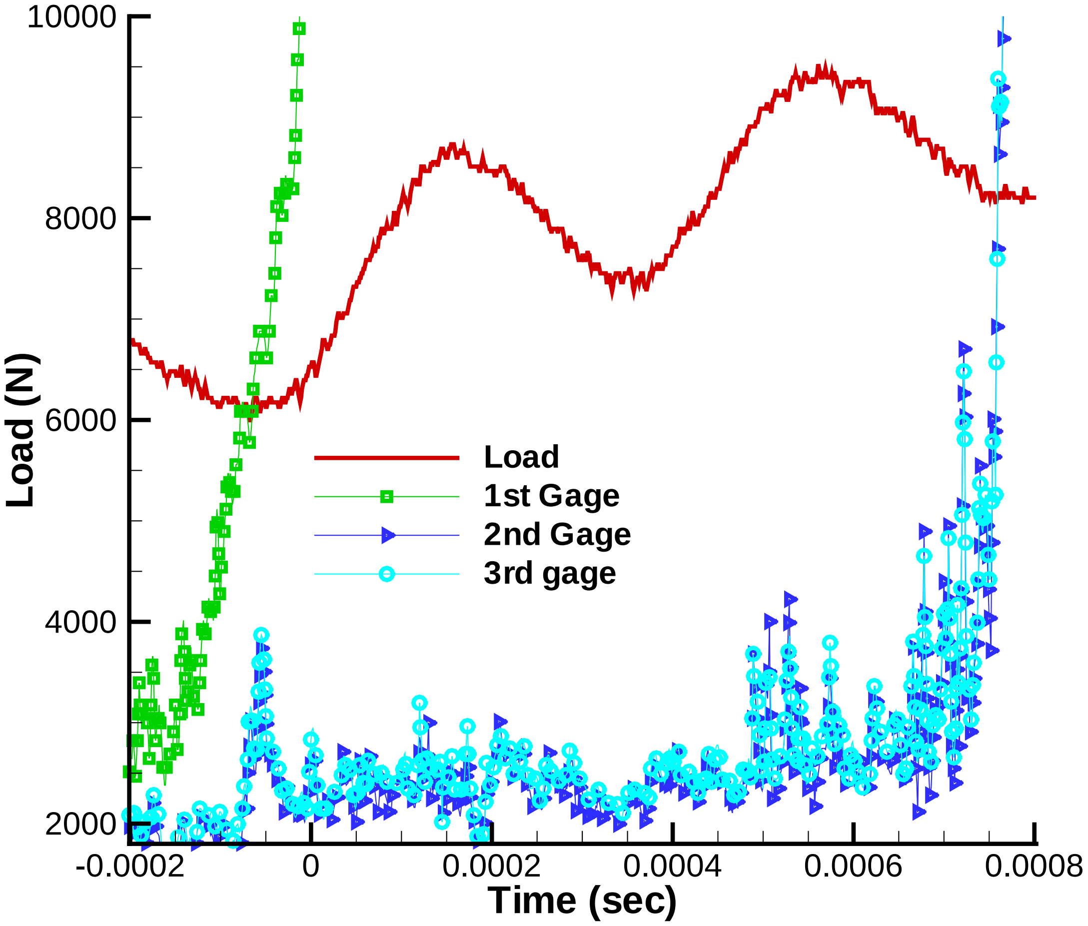

Figure 6.30: Crack Propagation Information of B3-1 Specimen

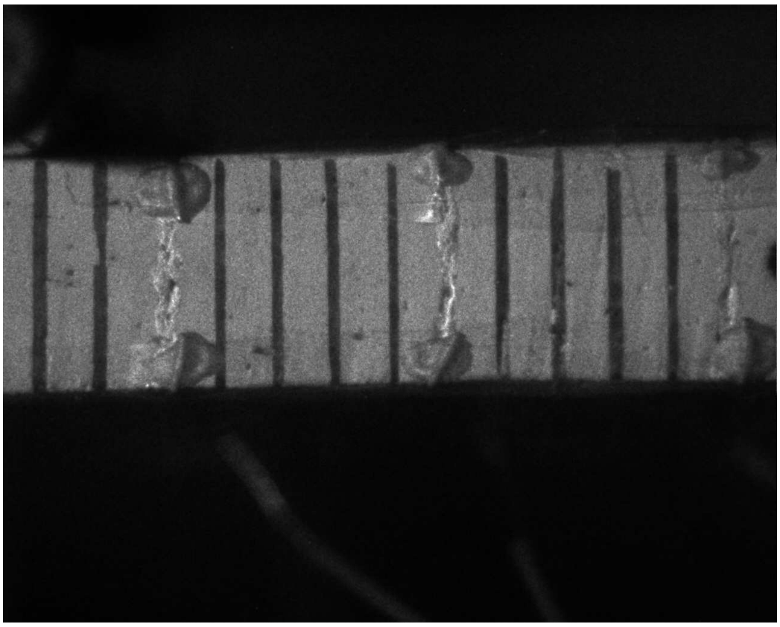

Figure 6.31: Image Taken When Time is 0 Second

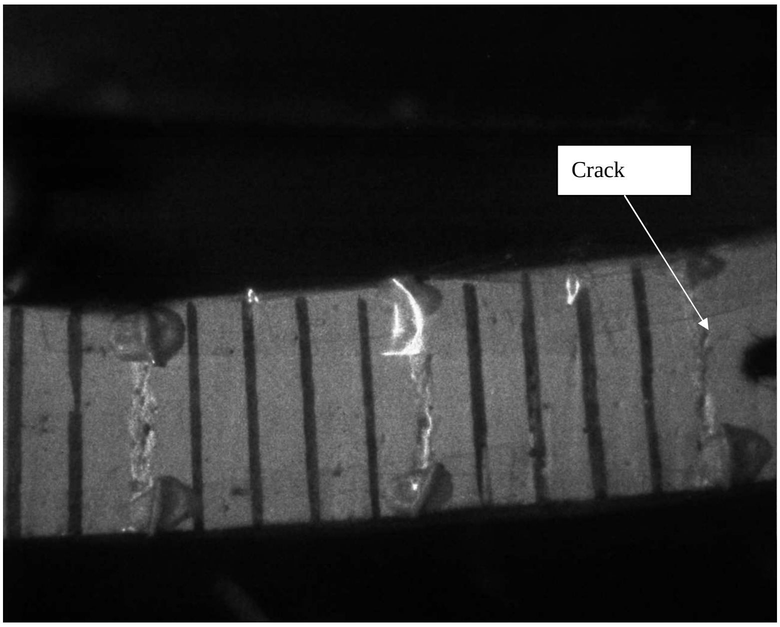

Figure 6.32: Image Taken When Time is 100 μ Second

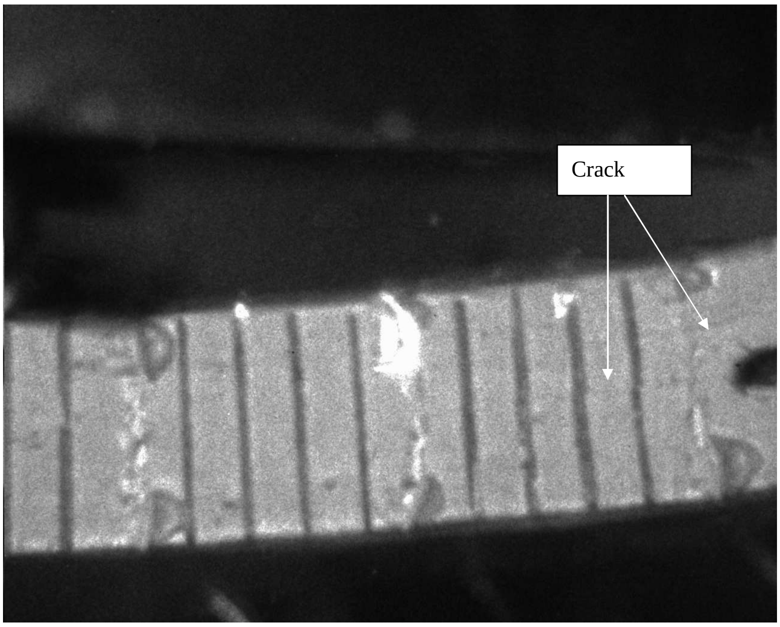

Figure 6.33: Image Taken When Time is 550 μ Second

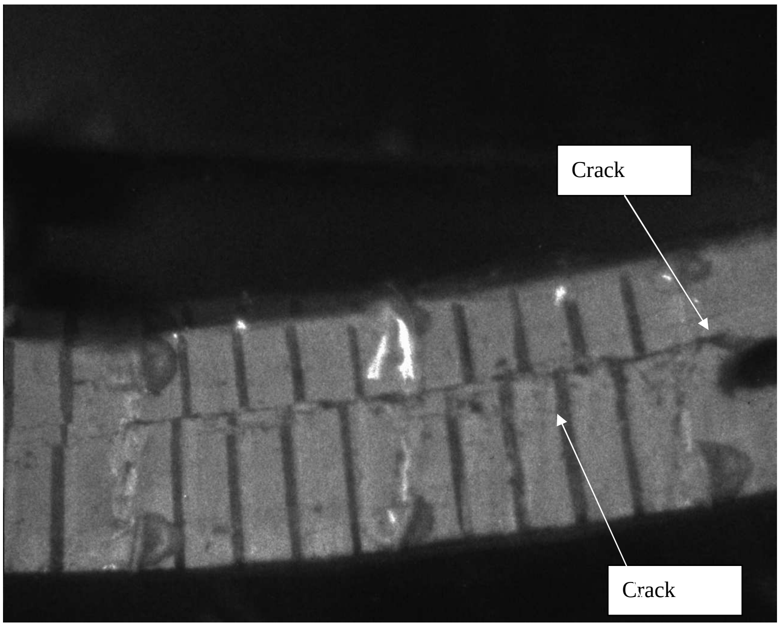

Figure 6.34: Image Taken When Time is 1050 μ Second

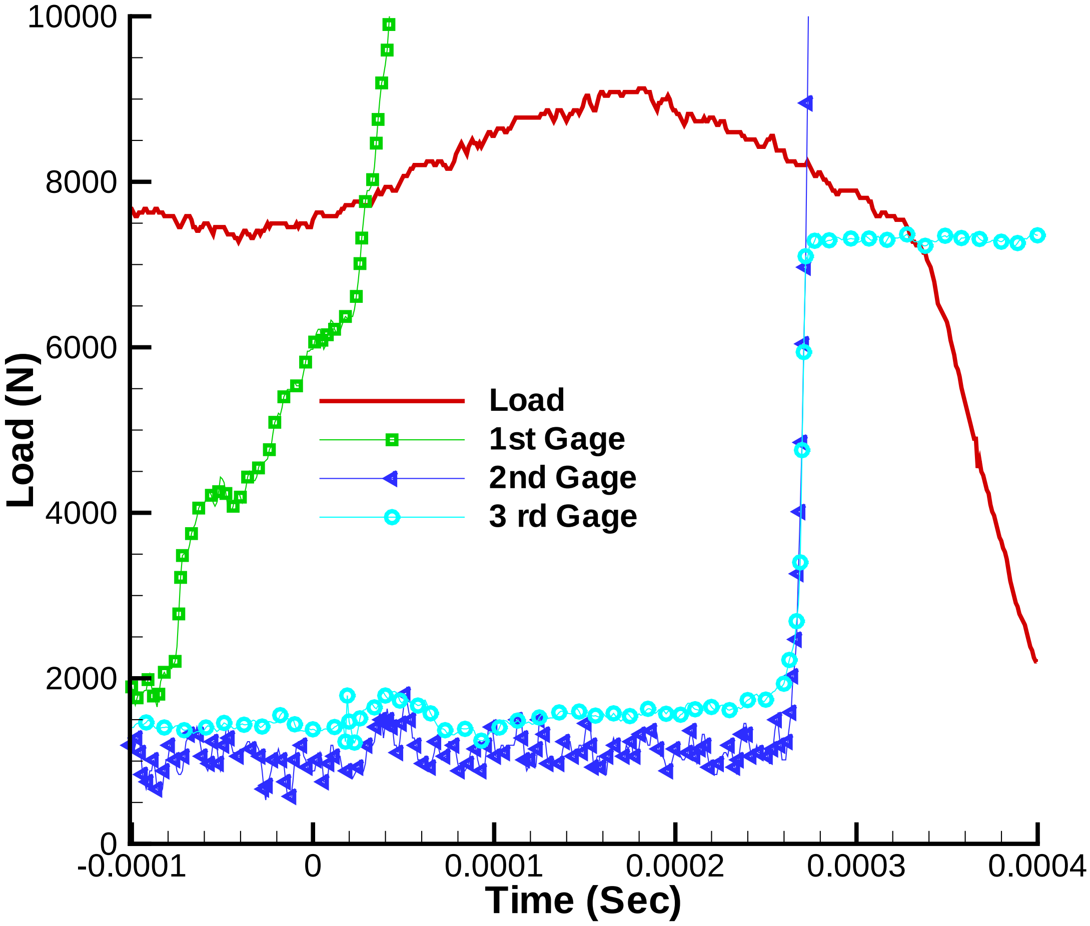

Figure 6.35: Crack Propagation Information of B3-2 Specimen

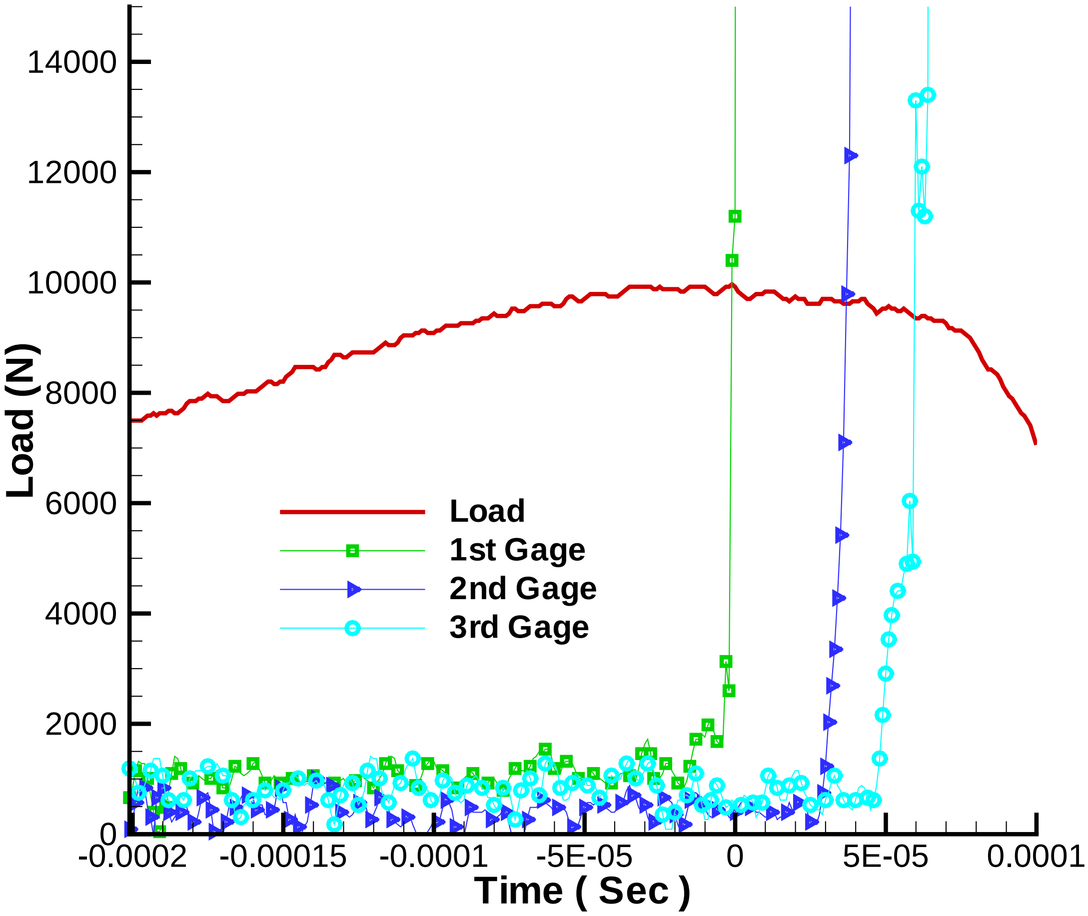

Figure 6.36: Crack Propagation Information of B2-1 Specimen

CHAPTER VII

Conclusions and Recommendations for Future Research

This thesis reports experimental results and numerical simulations of Z-pinned textile composites under in-plane compression loading. Three different numerical models were built in order to account for observation found in compression experiments. Also, experiments in static and dynamic mode II fracture were conducted to investigate the performance under transverse loads. This thesis investigated the effect of Z-pin density and Z-pin diameter on the performance of the woven composites in compression and in Mode II static and dynamic fracture. The important conclusions are summarized in the following:

7.1. Conclusions

7.1.1 Compressive Tests and Failure Mechanism of Z-pin Composites

The influence of Z-pin diameter, Z-pin density, and lay-up were all examined. Initial defects between the Z-pin and the surrounding area and unintended fiber waviness caused by Z-pin insertion have been identified as causes responsible for lowering the compression strength which is limited by fiber tow kinking leading to macroscopic kink banding. When the Z-pin diameter is set to be the same, the higher density Z-pin composites have lower strength than the lower density Z-pin composite. When the density is set to be the same, the small diameter Z-pin composites have lower strength than the larger diameter Z-pin composites. Finally, a simplified analytical method proves to be reliable in predicting the initial stiffness of the no Z-pin composite.

7.1.2 Compression Strength Prediction Using a 2D model

A 2D 1-3 plane (loading plane) model is presented to investigate the effect of local imperfection near the Z-pin within a woven composite. It is observed that damage around the Z-pin doesn't influence the local strength of the composites but does affect the post response after failure. The higher density of Z-pin composites have less strength and stiffness provided that the diameter is the same. The distortion induced due to Z-pinning is the location where the kink band starts to form. This kink band subsequently propagates until loss of load capacity. On the other hand, the imperfect bonding between the Z-pin and matrix has little effect on the strength of the composites near the Z-pin.

7.1.3 Prediction of Compressive Strength in multilayered Woven Z-pin Textile Composites- 2D Model to Account for Phase Difference

A 1-2 plane 2D model condensed from the 3D model is presented. This 2D model is presented in order to simulate multi layer composites. The cross section used in this 2D model can not be chosen arbitrarily. The ideal cross section should include longitudinal (axial) fiber tows. It is found that composites with phase difference has higher strength than composites with no phase difference.

7.1.4 Compressive Response and Failure of Z-Pin Textile Composites: 3D Numerical Simulation

A 3 layer 3D numerical model with each layer of lamina containing 16 representative unit cells is presented. The results from experiments and prediction of the 3D model agree well . The effect of phase difference can be simulated if a multi layer model is used. It is concluded that the strength of the composites would change if the position of lamina in each layer is changed. Also, the Z-pin composites will have less strength and stiffness than the unpinned composites, as predicted by the model and in agreement with experimental observations. However, the phase difference doesn't influence initial stiffness of the composite because the size of a representative unit cell in each lamina is the same.

7.1.5 Static and Dynamic Fracture Mode II Tests

The mode II fracture behavior of Z-pin composites was presented. Two types of composites, $[45/-45/0/90]_{2s}$ and $[0]_{16}$ lay-ups, were used in the tests. In each type of the composites, the response of three different kinds of Z-pin density and two different kinds of Z-pin diameter were investigated. The Z-pinning greatly increases the fracture toughness than the unpinned composites. The Z-pin successfully prevents the primary crack to propagate while cracks on the other weak places are formed, thus dissipating more energy. The additional friction provided by Z-pins also lets the composites to be loaded into plastic state, so that more energy is dissipated. When density is the same, the contact area between a Z-pin and fiber tows in small-diameter Z-pin composites provides more fracture toughness than large-diameter Z-pin composites. The proposed cohesive zone model prediction for static tests agrees well with results from experiments.

7.2 Recommendations for future research

Models to study phase difference for 2D and 3D have been proposed in this thesis. However, perfect bonding is assumed between different laminae. This is not realistic because the interface between different layers of laminae is the weakest part under impact or transverse load. Therefore, a special layer to simulate the interface is required.

Since the thickness of the interface is relatively small compared to one layer of lamina, a very fine mesh might be needed to fully simulate the response of the interface. This might be too expensive and won't be very popular for industrial use. Therefore, a multi scale method might be a feasible alternative to study the effect of the interface on the performance of the whole composite.

A comprehensive study of the combination of phase difference in the laminae of the laminated composite is recommended. In this way, the optimal permutation of phase difference can be identified and used as a design parameter. Also, it is desirable to carry out more simulations with different densities and different size of Z-pin in order to arrive at an "optimal" Z-pin density and Z-pin size for enhancing mechanical performance in compression and mode II fracture.

APPENDICES

APPENDIX A

Improved Speckle Method for Measuring In-Plane Displacement and Strain Fields

An improved method to compute the displacement field and strain field from the speckle recorded from a CCD camera is proposed. Previous studies have shown that the displacement field can be determined from two neighboring speckle images by use of the fast Fourier transform. Moreover, the accuracy of determining the displacement field in this manner relies on the ability to determine the peak position of the Fourier spectrum precisely. We present an improved method which can measure the displacements to an accuracy of 2μm is presented, provided that the distance between two pixels corresponds to 0.1 mm. The algorithm developed to obtain the displacement field uses the assumption that the displacements within each sub-element of the image are constant and evaluated at the center of the sub-element. However, instead of moving the entire sub-element in each loop in the algorithm, a fraction of the sub-element size is adopted to generate a family of overlapping sub-elements, resulting in an enhanced resolution of the resulting displacement field.

A.1. Introduction

Digital speckle methods are robust and well studied for measuring in-plane displacement and strain fields. Of these, speckle correlation photography has several advantages, including full-field and non-destructive measurement, and ease of set up to acquire data from a test specimen [12] and [48]. Typically, there are two ways to extract information regarding the displacement field from the speckle patterns recorded from CCD camera. Both methods divide the entire image into many sub-elements to perform point-wise filtering. The first way is based on calculating the cross correlation coefficient. Such a method deals with data in the spatial domain. Depending on the type of cross correlation coefficient that is chosen (the absolute difference coefficient [65], the least-square coefficient [58], the cross-correlation [6]), the displacement field and strain field can be obtained from the expression of the extreme correlation coefficient.

The second way is based on the fast Fourier transform (FFT) which treats the speckle information in the frequency domain. The accuracy of this method hinges on locating the position of the peak of the Fourier spectrum precisely and accurately [11]. Because the FFT is a discrete Fourier transform, the peak in the frequency domain does not correspond to the real peak. Here, real peak refers to the location of the analog Fourier transform. Indeed, the accuracy of the calculated displacement field depends on how accurately the peak position is determined. More comprehensive studies that deal with speckle images in the frequency domain can be found in [51], [50], and [49]

In [11], a bi-parabolic fitting is used to locate the position of the discrete peak with an assumption of axis-symmetry of the spectrum. In the present paper, a technique is presented that does not rely on assuming that the FFT spectrum is axi-symmetric. The spatial details of the spectrum is known to be dependent on the movement of the speckles in the images to be analyzed. Thus, without making any assumptions regarding the nature of the FFT spectrum, the present technique employs a higher order bi-cubic spline interpolation method to extract the position of the discrete FFT peak. In addition, a family of overlapping sub-element windows is used in analyzing the speckle images to compute the displacement field. These improvements result in an increased accuracy and resolution with which the point-wise displacement field can be obtained.

A.2. Experiment Setup

The instruments used to generate and capture the speckle image are shown in Fig A.1. The schematic drawing is shown in Fig A.2. The area in which the displacement field is to be measured is illuminated by a laser beam so that a speckle pattern is generated on the surface of the specimen. The speckle images are captured by a CCD camera and simultaneously stored in a memory card in the camera. The size of the images taken from CCD is 4288 by 2848. Each pixel can store a gray scale value ranging from 0 to 65535(16 bit). Also, the timer in the camera and the timer in the data acquisition system are synchronized so that the corresponding "load" on the specimen is also known. A series of images at pre-determined time intervals are collected during a typical experiment. Thus, a series of speckle images at known time states and corresponding to known external load states are available at the end of an experiment. Suppose an image is captured at time $t = t_1$,corresponding to a displacement field $\tilde{u}(\tilde{x}, t)$, then by comparing the image capture at $t = t_1 + \Delta t$, corresponding to $\tilde{u}(\tilde{x}, t + \Delta t) = \tilde{u}(\tilde{x}, t) + \Delta\tilde{u}(\tilde{x}, \Delta t)$, to the image captured at $t = t_1$, the incremental displacement field is computed, as described in the next section.

A.3. Theory of digital image correlation in the frequency domain

Each speckle pattern image stored in the computer is a matrix of size NxM, containing numerical entries that range from 0 to 65535. The size NxM depends on the CCD recording device used. The value of the entries is dependent on the intensity of light with 0 representing pure white and 65535 representing pure black.

Suppose that the image intensity at $t = t_1$ is defined as $h_1(\tilde{x})$ and the image intensity at $t = t_1 + \Delta t$ is defined as $h_2(\tilde{x})$ where

$$h_1(\tilde{x}) = h(x, y) \tag{A.1}$$

$$h_2(\tilde{x}) = h_1(\tilde{x} - \tilde{u}) + n(x, y) \tag{A.2}$$

where $n(x, y)$represents noise in the signal

Denote the complex Fourier transform of $h_1(\tilde{x})$ as $H_1(\omega_x, \omega_y)$, the complex Fourier transform of $h_2(\tilde{x})$ as $H_2(\omega_x, \omega_y)$ and the complex Fourier transform of $n(x, y)$ as $N(\omega_x, \omega_y)$ where, by definition

$$\begin{aligned} H_1(\omega_x, \omega_y) &= \int\int h(x, y) \exp[-j2\pi(x\omega_x + y\omega_y)] \\ &= |H(\omega_x, \omega_y)| \exp[j\phi(\omega_x, \omega_y)] \end{aligned} \tag{A.3}$$

$$\begin{aligned} H_2(\omega_x, \omega_y) &= \int\int (h(x-u, y-v) + n(x, y)) \exp[-j2\pi(x\omega_x + y\omega_y)] \\ &= |H(\omega_x, \omega_y)| \exp[j\phi(\omega_x, \omega_y) - 2\pi(u\omega_x + v\omega_y)] + N(\omega_x, \omega_y) \end{aligned} \tag{A.4}$$

The multiplication of $H_1(\omega_x, \omega_y)$ and the complex conjugate of $H_2(\omega_x, \omega_y)$ is defined as $F(\omega_x, \omega_y)$ where

$$\begin{aligned} F(\omega_x, \omega_y) &= |H(\omega_x, \omega_y)| exp[j\phi(\omega_x, \omega_y)] * |H(\omega_x, \omega_y)| exp[j\phi(\omega_x, \omega_y) - 2\pi(u\omega_x + v\omega_y)] \\ &+ N(\omega_x, \omega_y) \\ &\approx |H(\omega_x, \omega_y)|^2 exp[j2\pi(u\omega_x + v\omega_y)] \end{aligned} \tag{A.5}$$

Define the Fourier transform of $F(\omega_x, \omega_y)$ as $G(\zeta, \eta)$, then

$$\begin{aligned} G(\zeta, \eta) &= \int\int F(\omega_x, \omega_y) exp[j2\pi(\zeta\omega_x + \eta\omega_y)] d\omega_x \omega_y \\ &= \int\int |H(\omega_x, \omega_y)|^2 exp[j2\pi((\zeta - u)\omega_x + (\eta - v)\omega_y)] = \bar{G}(\zeta - u, \eta - v) \end{aligned} \tag{A.6}$$

In practice, $\bar{G}(\zeta - u, \eta - v)$ is a peak from which the displacement components u and v can be identified. That is, u and v are the distances away from the center of the frequency spectrum. Repeating the above two-step discrete FFT for each sub-element and spanning the entire image enables determining the complete displacement field. If two identical images are used in the analysis, the displacement vector u and v should be identically zero. However, in practice, two identical images can produce a shift which depends on the numerical accuracy of the procedure.

A.4. Increased sensitivity by increasing the number of data points

In the technique that has been presented here, a single image is dived into many sub-elements during the subsequent analysis. Therefore, each loop in the program is used to extract the displacement for the corresponding sub-element. This also implies that the monitored window shifts the location of the sub-element in a subsequent step. In order to increase the resolution of the computed displacement field, instead of shifting the sub-element in each subsequent loop, only a fraction (1/4 size) of the sub-element is shifted. This is schematically shown in Figure A.3. In doing so, one has over-lapping sub-elements and thus a larger number of data points are generated which can subsequently be used to describe the surface displacement field. This is somewhat analogous to the idea of mesh refinement in numerical techniques such as the finite element method in classical mechanics [5]. It is to be noted that the choice of size in shifting $1/4H_h$ or $1/4H_v$ as in Figure A.3) is entirely at the discretion of the user. In theory, one can generate a large number of points to increase the accuracy of the displacement field by changing the amount of the shift.

A.5. Increased accuracy by interpolation of the area near the peak

The accuracy of the method as presented here in the frequency domain depends upon the precision with which the location of the peak of the Fourier spectrum is identified. Since this is done numerically, the peak of the spectrum does not correspond to the real (analog) peak. Usually, there is a small distance between the real peak and the peak as extracted by a digital technique. Therefore, it is necessary to enhance the accuracy of the methods of peak extraction, so that the digital peak is computed as close as possible to the "actual" peak. One way to improve this is to use a continuous Fourier transform (CFT) [47], [40], and [35]. However, it is pointed out that this is computationally inefficient. It is recommended to obtain the Fourier spectrum using the FFT first. Then, by searching in the neighborhood of points of the pseudo- peak, the real peak can be identified by use of interpolation [30]. In, [11], it is assumed that the FFT spectrum is axi-symmetric. By use of this assumption, an algorithm to interpolate the data near the peak and extract the displacement vector from the interpolated spectrum, is derived. In this paper, the assumption of axi-symmetry is relaxed. Furthermore, bi-cubic spline functions are used to fit the data points near the peak. After this, via interpolation, an approximation to the real peak is obtained. Note that there are no assumptions regarding the shape of the spectrum near the peak because the shape is dependent on the details of the displacement field that is being interrogated. The introduction of bi-cubic spline interpolation is described in [10]. Figure A.4 and Figure A.5 show the peak of the spectrum before interpolation and after interpolation. The peak and its neighboring 24 points are extracted from the original spectrum shown in Figure A.4. After the interpolation, the interpolated spectrum used for extracting the real peak is shown in Figure A.5. Obviously, the location of the peaks in Figure A.4 and Figure A.5 are slightly different. Here, two images from a real experiment are used to show why it is necessary to interpolate the data near the peak and locate the position of the real peak. The original peak (obtained without bi-cubic interpolation) is 1 pixel away from the center, both in the vertical and the horizontal directions. That is, (u,v)=(1,1) as shown in Figure A.4. However, after the bi-cubic interpolation, the real peak can be captured with an improved accuracy. That is, (u,v)=(0.9611, 0.8833). It is worth mentioning the extent of the accuracy that the present method can incorporate. Originally, the accuracy in capturing the location of the peak in Figure A.4 is limited to integer pixel values only. After interpolation, the 5x5 matrix of points are transformed to a size of 257x257. Noting that previously 25 points (5x5) are selected to extract the real peak in the frequency domain, the present use of spline interpolation extends this ”grid” of points to 9x9, because one point is inserted between two neighboring points of the original 5x5 square. This interpolation is repeated 6 times and leading to a grid of 257 x 257. Therefore, the accuracy in determining the position of the peak is now 5/257 pixel.

A.6. Numerical Experiemnts

Example 6.1 to example 6.4 are used to demonstrate the reliability of the proposed method. Example 6.5 and Example 6.6 show analyses of actual experimental data.

A.6.1 NUMERICAL TENSILE TEST

Figure A.6 is a speckle pattern image, say IMAGE A, from an instant of time at which a composite material sample was under load. The size of this image is 400 x 400 pixels. IMAGE A is fixed in the left boundary AB and in its right boundary CD is stretched by 5 pixels by use of well-known software Photoshop [1]. The horizontal displacement field after analysis is shown in Figure A.7. The x-axis represents the position along the boundary AC and the y-axis represents the position along the boundary AB. The z-axis represents the displacement field for the corresponding position in Figure A.6. It is seen that the displacement varies linearly from the left boundary AB to the right boundary CD. Also, the horizontal displacement along boundary AB is zero and finally the horizontal displacement is calculated to be 5 pixels along the boundary CD. It is notes that, in the proposed method, the entire image is divided into many sub-elements. During the analysis, the displacement within each sub-element(assumed constant)is obtained. These discrete displacement data are centered at each subelement. When these data are used with the plotting software in Matlab to generate the 2 dimensional displacement plot as shown in Figure A.7, Matlab uses a high order polynomial to interpolate the discrete data and subsequently plot it. That is the reason why there are ”waves” in the displacement field which is strictly ”linear” to within 0.02 pixels.

A.6.2 Compressive test

In this example, image A shown in Fig A.6 is fixed along the boundary AB and is compressed 5 pixels along the boundary CD. Figure A.8 shows the horizontal displacement field of this deformation. The x-axis represents the position along the boundary AC and the y-axis represents the position along the boundary AC. The z-axis represents the displacement field for the corresponding position. Similar to the previous example, the horizontal displacement varies linearly. It also shows that the displacement is zero along AB and becomes -5 pixles along the boundary CD. The "waviness" in the figure is due to reasons explained earlier.

A.6.3 Rigid body translation test

A rigid body translation to the left of 5 pixels is imposed on the Image shown in Fig A.6. The displacement field after analysis is shown in Figure A.9. The definitions of the x-axis, y-axis, and z-axis are the same as those in example 6.1 and 6.2. As can be seen in Figure A.9, after point-wise analysis, the displacements of the speckles throughout the specimen are approximately uniform at 5 pixels.

A.6.4 Rigid body rotation

Figure A.10 and Figure A.11 represent the speckle pattern before and after rotation. All the speckles in the Figure A.10 are rotated clockwise about the center of the image. Figure 11 shows the displacement field in quiver form from Figure A.10 to Figure A.11. It is evident that the displacement is small for points located near the center of the specimen and the displacement is larger for points away from the center. In between, the displacements vary linearly as expected. These trends are captured in Figure A.12.

A.6.5 Tension test

As shown in Figure A.13, an ASTM standard D638 dog-bone tension specimen was subjected to tensile load using a MTS servo-hydraulic Machine. One side of the specimen was illuminated by a He-Ne laser and images were recorded for subsequent analysis. A strain gage was attached on the other side of the specimen. A typical speckle pattern of the monitored area is shown in Figure A.14. Different images at different times and the corresponding loads on the specimen are recorded. In each incremental analysis, the relative average displacement between line AA and line BB is computed. The average strain can thus be obtained by dividing the relative displacement by the height of the undeformed monitored area. The difference of the applied load between the initial image and final image are used to obtain the stress increment by dividing the load increment by the specimen undeformed area. Figure A.15 shows the comparison of the stress-strain curves obtained from the speckle method and strain gage, respectively.

A.6.6 Bi-axial test

An in plane bi-axial test of a 2D triaxially braided composite was performed and results are reported in [43]. During the tests, an area that is equal in size to the repeating unit cell of the composite was monitored as shown in Figure A.16. The speckle images at seven different states were recorded and saved in the data acquisition system. Here, we demonstrate the versatility of the developed method by analyzing these images. In order to obtain the strain fields, the first image is subsequently used as the reference state. By use of any two images, the strain field between these two images can be computed. Figure A.17 $\sim$ Figure A.22 shows the incremental strain field ε_{xx}. Figure A.23 $\sim$ Figure A.28 shows the incremental strain field ε_{yy}. Figure A.29 Figure A.34 shows the incremental strain field γ_{xy} . The strain concentration is observed at the left side of the monitored area. Subsequent post-experiment inspection showed that this area corresponded to large amounts of damage as reported in [43]. The evolution of the strain field in relation to the development of surface damage is also evident in the speckle strain fields. Now, when one relates these observations to the actual textile architecture of the specimen, it is immediately seen that the regions of highest strain correspond to the location of the bias-braid and the crossing of two bias-braids.

A.7. Accuracy of the current method

As shown in Figure A.35, the length of the monitored area is 2000 pixels. The size of the sub-element is assumed to be 200 pixels. Suppose that the load P is imposed so that a uniform strain of 0.0001 is enforced throughout the entire monitored area. Image 1 is taken at the start of the experiment and image 2 is taken when a strain of 0.0001 is imposed. Line DD is assumed to be the fixed end. Consequently, it is expected that sub-element ♯1 will displace 0.2 pixel and sub-element ♯2 will displace 0.18. Since the accuracy of this current method is limited to 0.02 pixel, the present technique can still provide a "good" result for analyzing these two images. However, suppose that there are intermediate images between image ♯1 and image ♯2. Then it is possible that these intermediate images when analyzed yields no information that is resolvable within the accuracy of the technique presented. The proposed method does require that two neighboring speckle images are always used to extract the displacement field, in order to ensure that the images are correlated. This will not happen if the two images correspond to displacement fields that are large (several pixels). In these instances, the peak in the FFT spectrum is not very sharp, since the images are uncorrelated. Furthermore, the technique described and the experiments reported in this paper are under in-plane deformation. Therefore, out of plane deformation is not discussed in this paper.

A.8. Conclusion

An improved method to compute the displacement field and strain field from the speckle recorded from a CCD camera has been presented. The method has been validated through the use of several examples. The proposed method can be used to measure non-homogenous surface strain fields in heterogenous materials. The proposed method can measure the displacements to an accuracy of 2μm, provided that the distance between two pixels corresponds to 0.1mm. The algorithm developed to obtain the displacement field uses the usual assumption that the displacements within each sub-element of the image are constant and evaluated at the center of the sub-element.

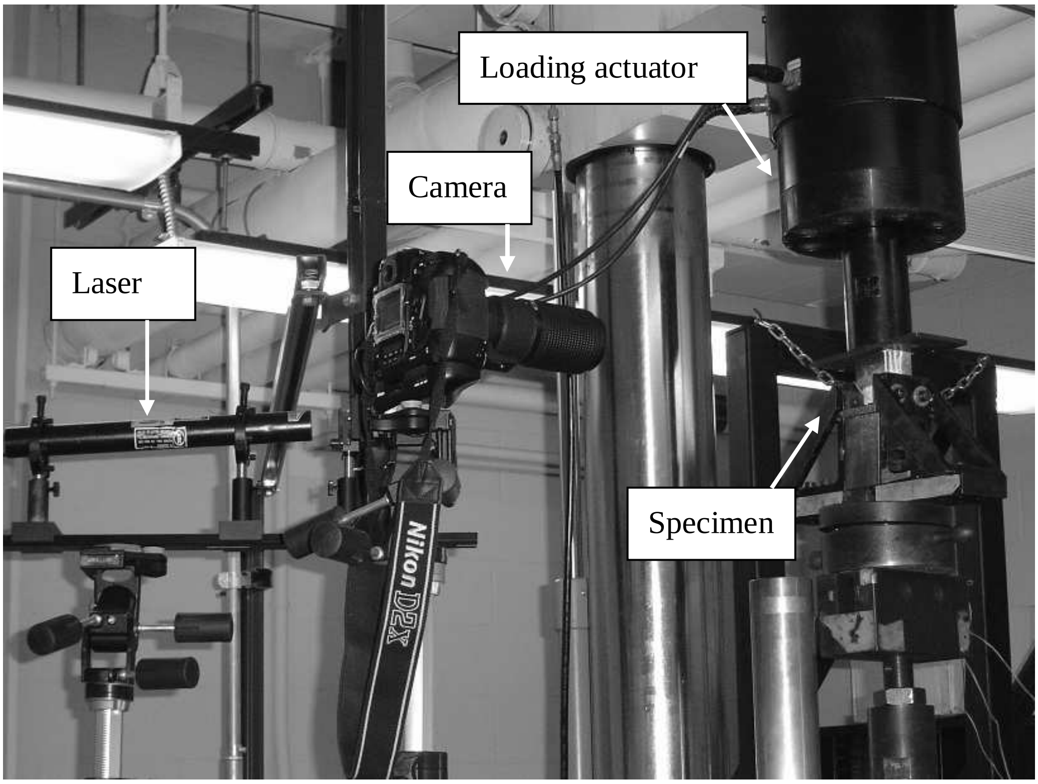

Figure A.1: Experimental Setup

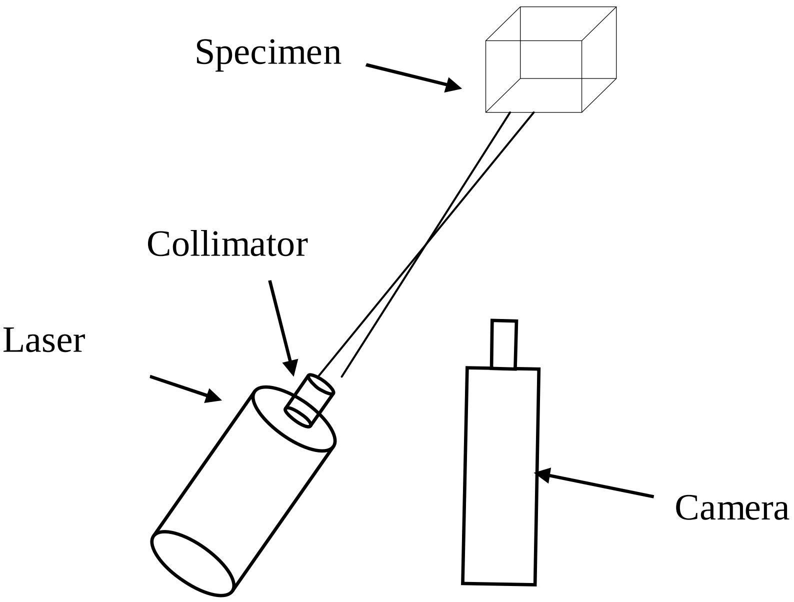

Figure A.2: Schematic Drawing of the Experimental Setup

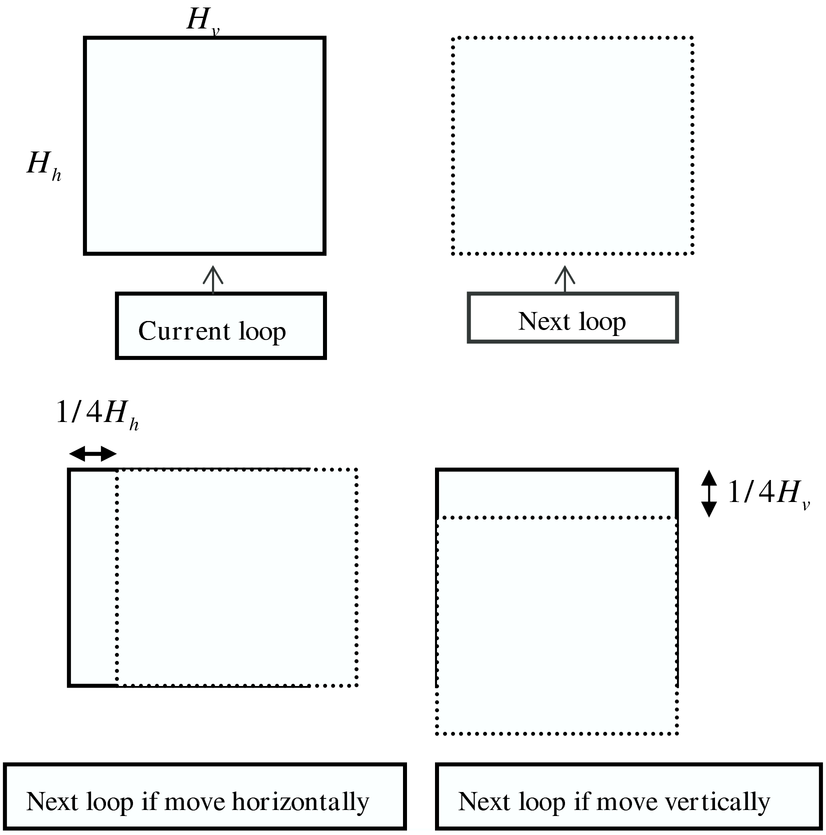

Figure A.3: The Movement of the Monitored Window in this Algorithm

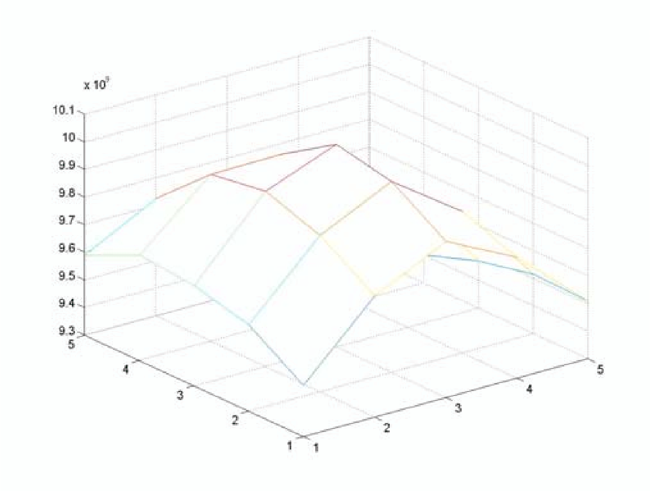

Figure A.4: Peak before Bi-Cubic Interpolation

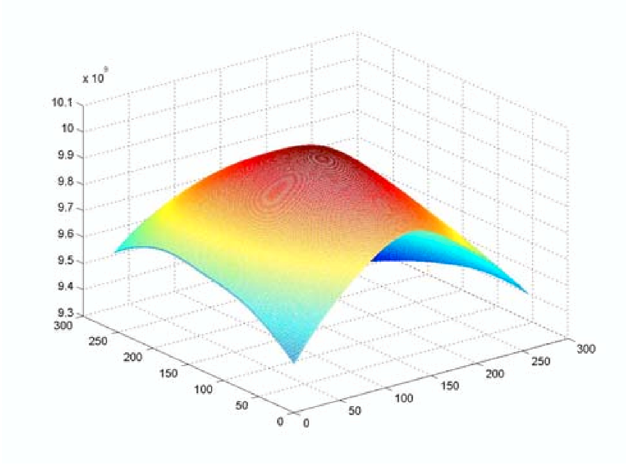

Figure A.5: Peak after Bi-Cubic Spline Interpolation

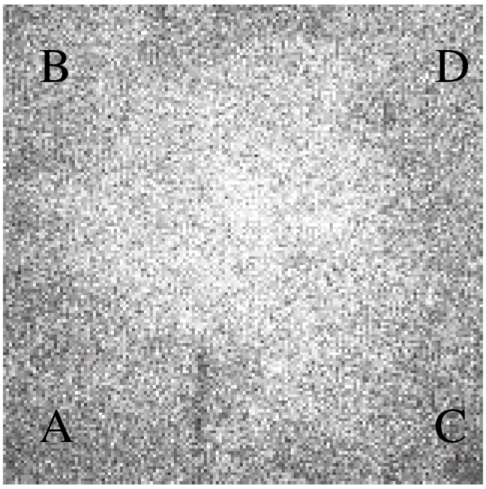

Figure A.6: Speckle Pattern

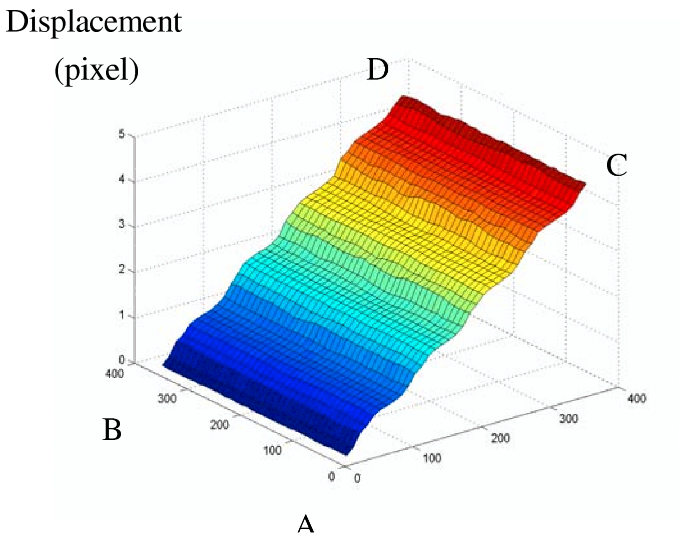

Figure A.7: Horizontal Displacement Field after Stretching

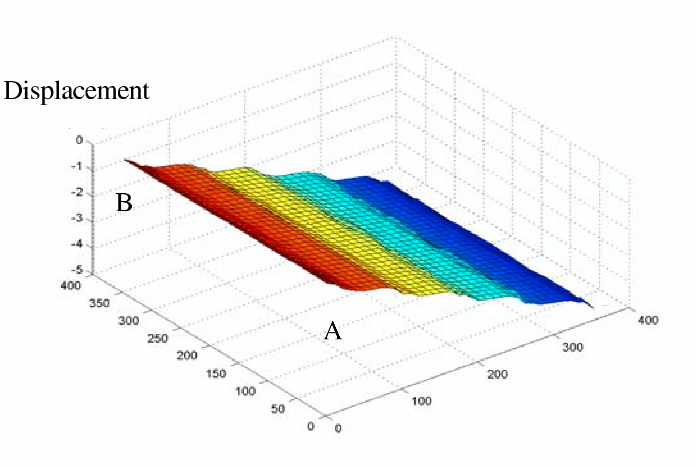

Figure A.8: Horizontal Displacement Field after Compression

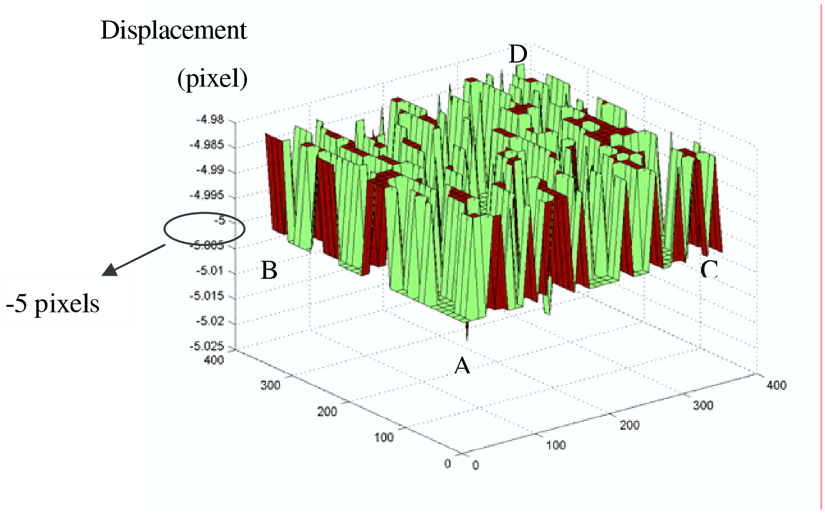

Figure A.9: Horizontal Displacement Field after Rigid Body Translation

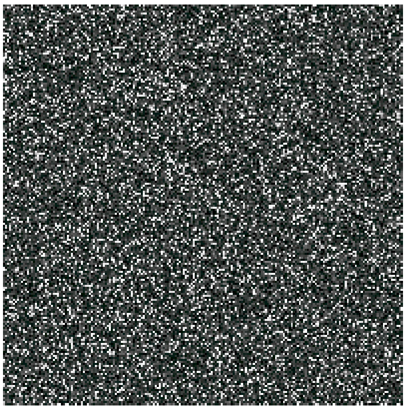

Figure A.10: Speckle before Rotation

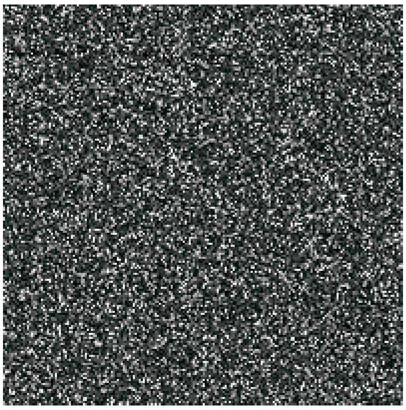

Figure A.11: Speckle after Rotation

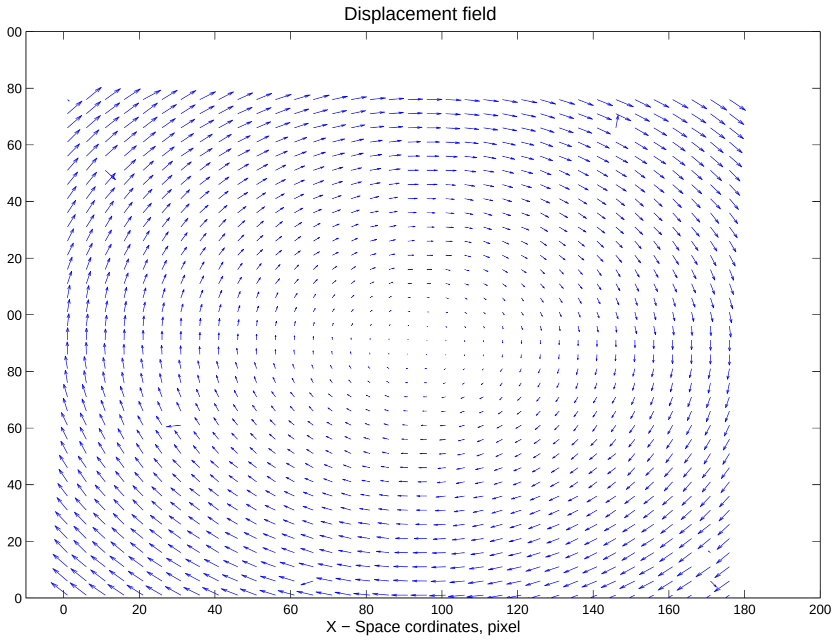

Figure A.12: Displacement Field of Rigid Body Rotation

Figure A.13: Aluminum Specimen

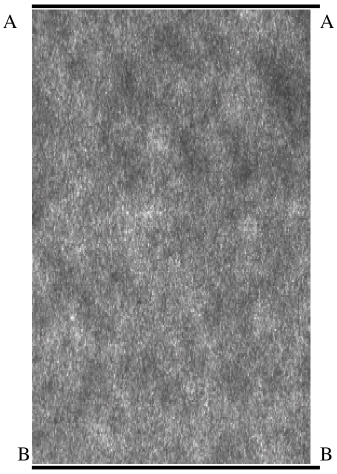

Figure A.14: Speckle Image of the Monitored Area

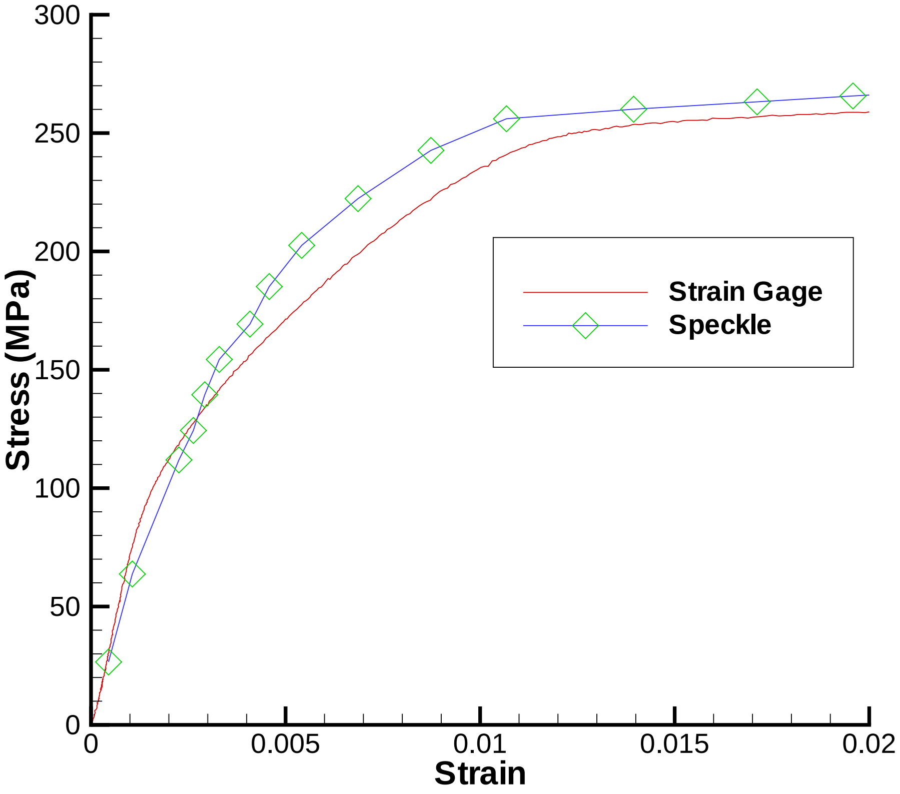

Figure A.15: Comparison of Stress-Strain Curve

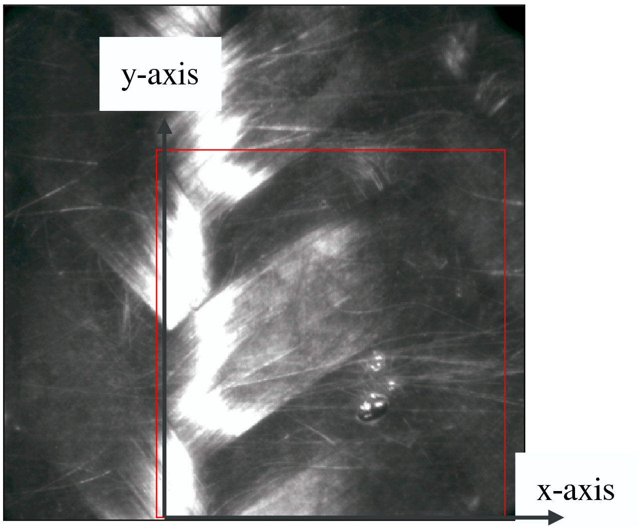

Figure A.16: Illustration of Monitored Area

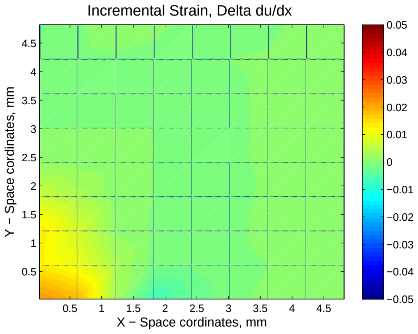

Figure A.17: ε_{xx} from State 1 to State 2

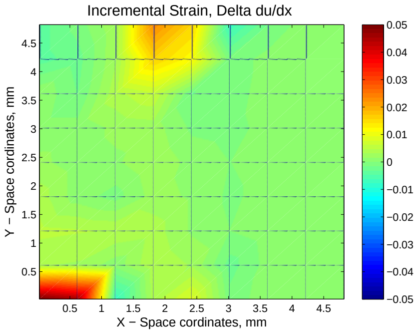

Figure A.18: ε_{xx} from State 1 to State 3

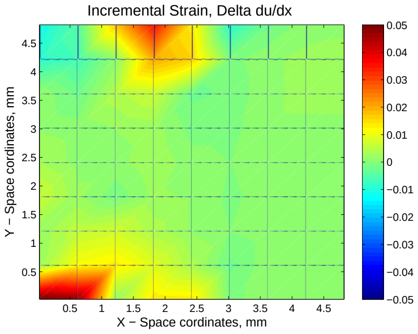

Figure A.19: $\varepsilon_{xx}$from State 1 to State 4

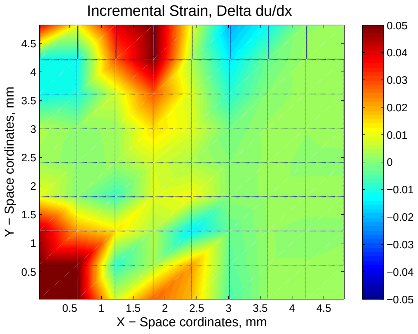

Figure A.20: $\varepsilon_{xx}$from State 1 to State 5

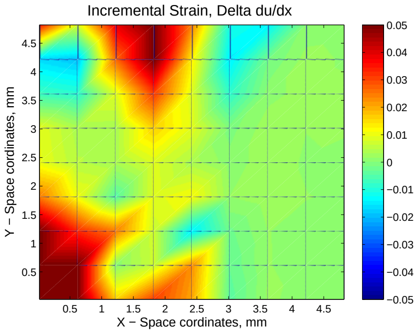

Figure A.21: ε_{xx} from State 1 to State 6

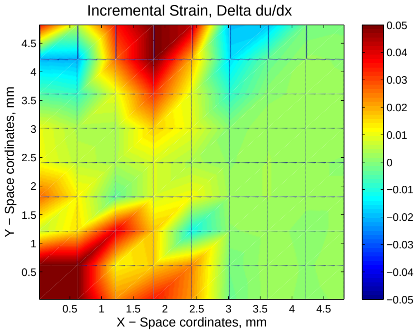

Figure A.22: ε_{xx} from State 1 to State 7

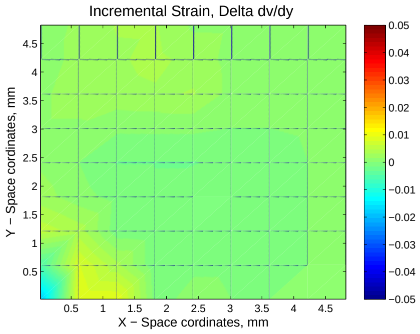

Figure A.23: ε_{yy} from State 1 to State 2

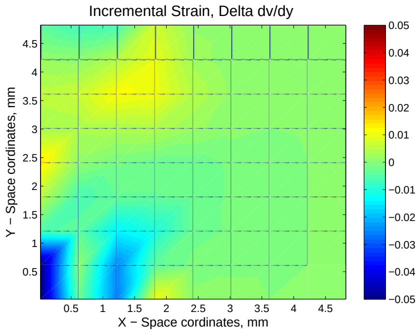

Figure A.24: ε_{yy} from State 1 to State 3

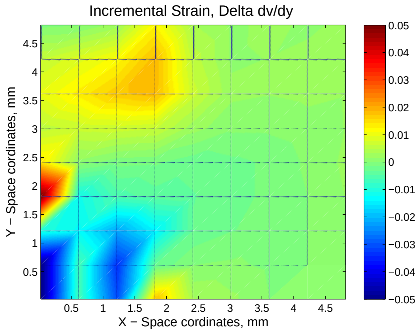

Figure A.25: ε_{yy} from State 1 to State 4

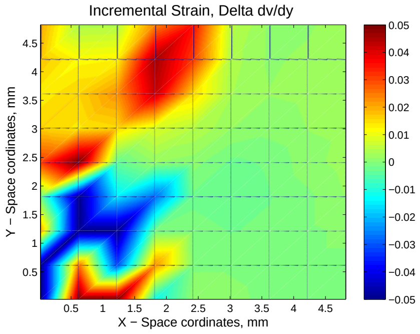

Figure A.26: ε_{yy} from State 1 to State 5

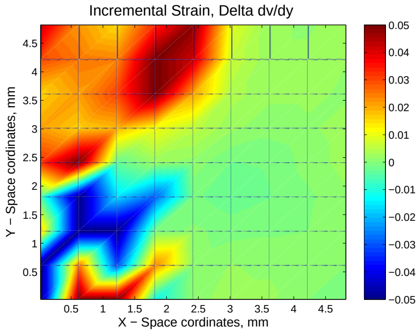

Figure A.27: ε_{yy} from State 1 to State 6

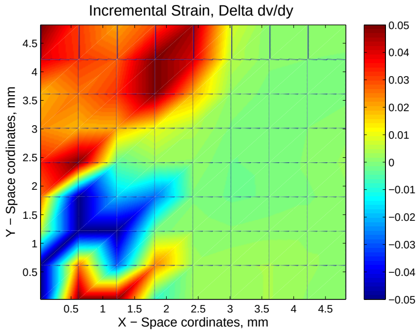

Figure A.28: ε_{yy} from State 1 to State 7

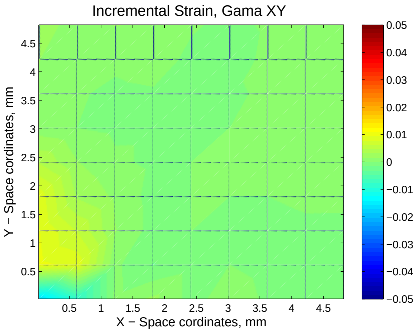

Figure A.29: γ_{xy} from State 1 to State 2

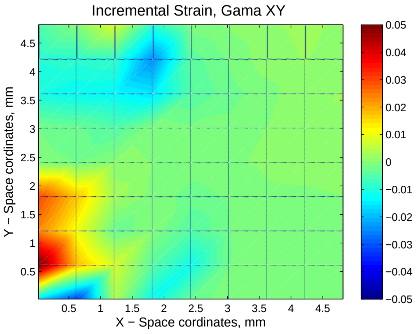

Figure A.30: γ_{xy} from State 1 to State 3

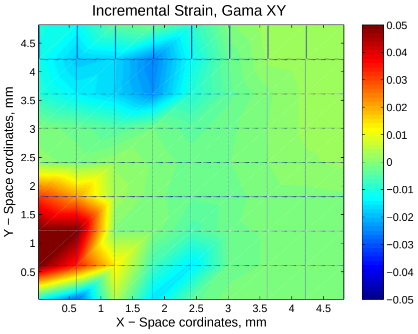

Figure A.31: γ_{xy} from State 1 to State 4

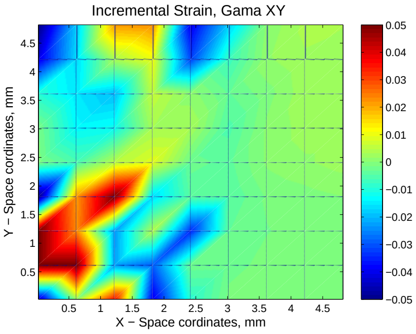

Figure A.32: γ_{xy} from State 1 to State 5

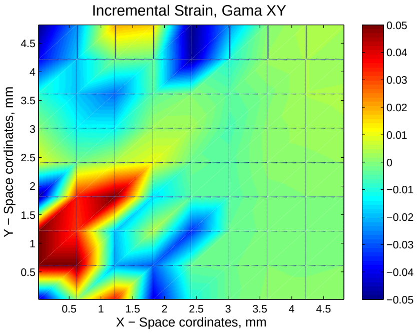

Figure A.33: γ_{xy} from State 1 to State 6

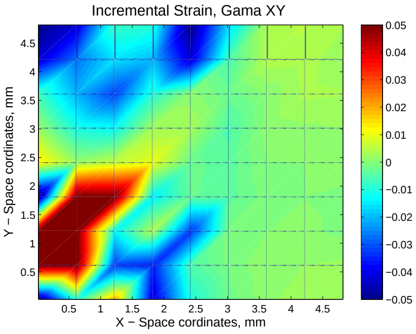

Figure A.34: γ_{xy} from state 1 to state 7

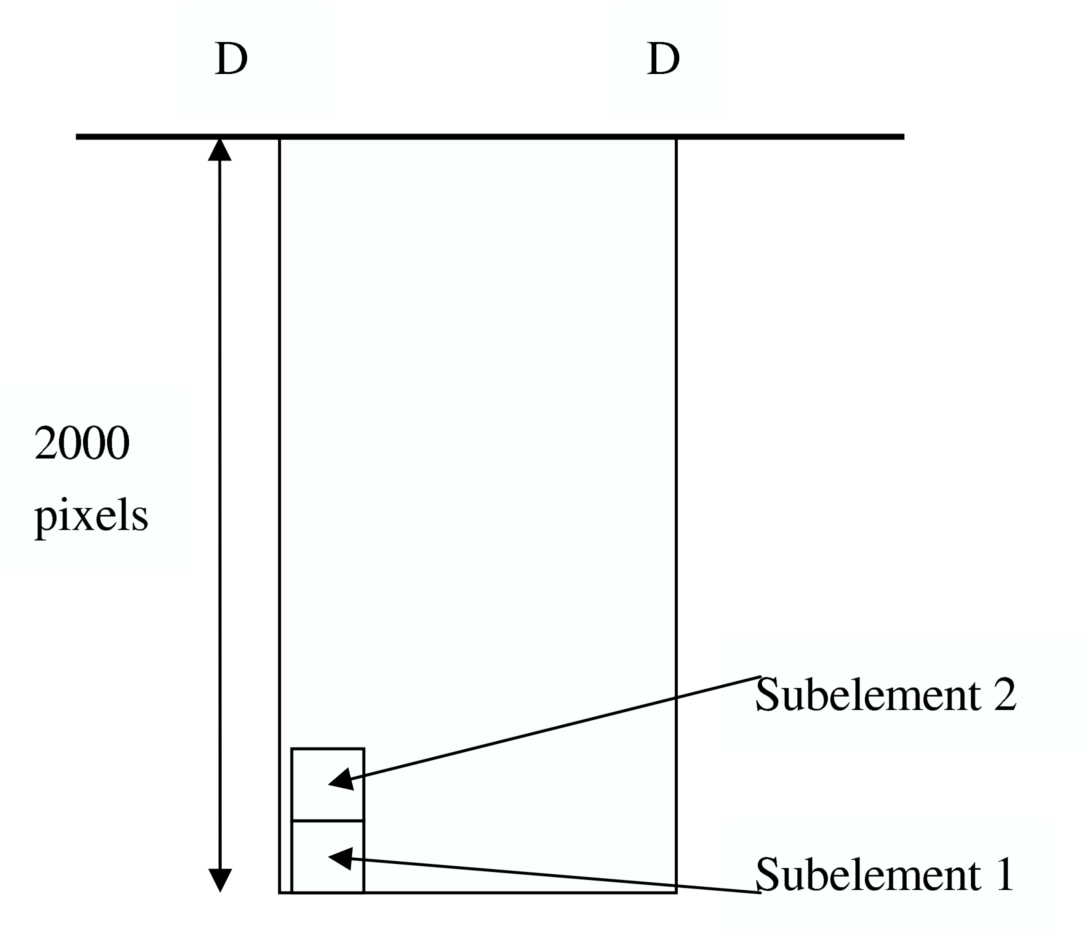

Figure A.35: Schematic Drawing of the Specimen

APPENDIX B

In-Plane Tensile Properties of Z-pin Composites

B.1. Tension Test Results

A limited number of tension tests were conducted by use of quasi-isotropic composites with Z-pin diameters of 0.5080 mm (0.02 in.), 0.2794 mm (0.011 in.), and no Z-pin, respectively. The classification of these composite laminates is given in Table 1.1. In each subgroup, two specimens cut in "dog-bone" shape were used to perform experiments. A typical specimen and its dimension is shown in FigureB.1.

Figure B.2 and Figure B.3 show the comparison of the axial stress- axial strain response in group A and group C. Only one test in each subgroup is presented for clarity. The stress-strain curve is linear initially and becomes "soft" as load increases. Nonlinearity sets in early at about 0.5% macroscopic strain.

In both of the groups, there is a trend that the strength decreases as Z-pin density increases. The difference is more obvious than the tests conducted in compression (chapter 2). The comparison of strength and stiffness in group A is summarized in Figure B.4 and Figure B.6. Similar to strength, the stiffness decreases as Z-pin density increases. Comparison of strength (Figure B.5) and stiffness (Figure

B.7) in group C has this trend. Observing the failure surface of group A specimen in Figure B.8 shows that the failure length becomes "shorter" as Z-pin density increases. That is, the region of intense damage (referred to " failure length") is influenced by Z-pin density. Similar phenomenon can be observed from the failure length of group C specimens in Figure B.9. Matrix cracking (distributed) leads to the softening behavior observed in the axial stress- axial strain response. As loading proceeds, this distributed damage accumulation increases, finally leading to poor load transfer between the tows. At a critical state of damage, the axial fiber-tow strength is exceeded loading to failure. Delamination due to matrix damage can be observed between different laminae as shown in Figure B.10 Failure surface can be observed to pass near the Z-pin as shown in Figure B.11.

B.1. Summary

Results from tension tests of quasi isotropic laminated textile composites are reported in this appendix. Degradation of the matrix leading to fiber tow rupture is the main failure mechanism by which the structure loses its load carrying capacity. Similar to the compression response (chapter 2), the failure surface intersecting the Z-pin boundary can always be observed. The fiber undulation and distortion are the "seeds" to initiate matrix cracking. When the accumulated damage reaches a critical level, catastrophic failure occurs, leading to loss of load bearing capacity

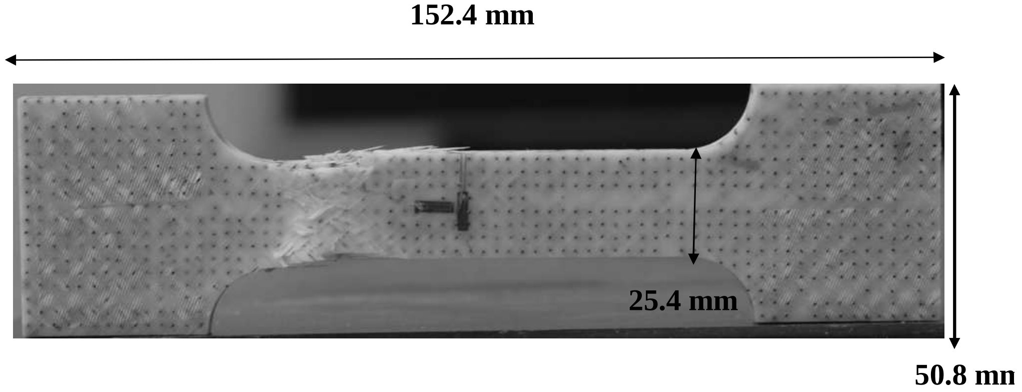

Figure B.1: “Dog Bone” Shape Specimen for Tension Test

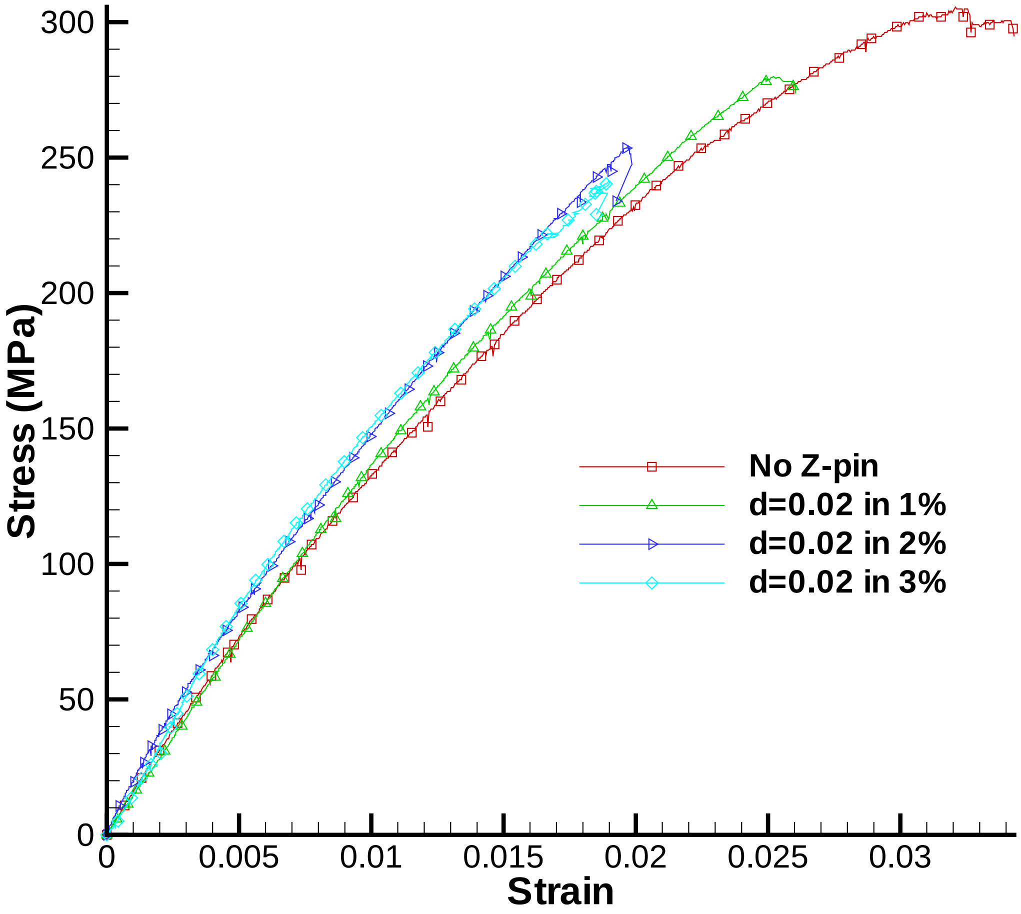

Figure B.2: Stress-Strain Response for Group A and Group E

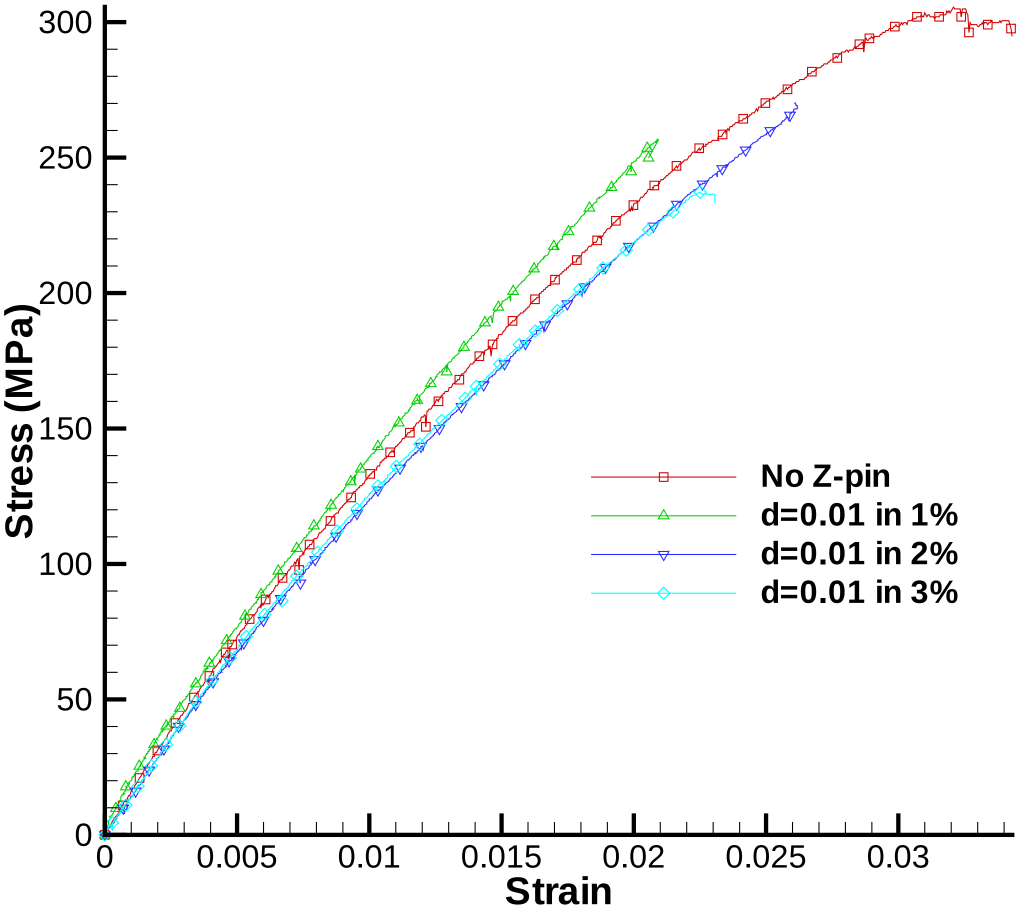

Figure B.3: Stress-Strain Response for Group C and Group E

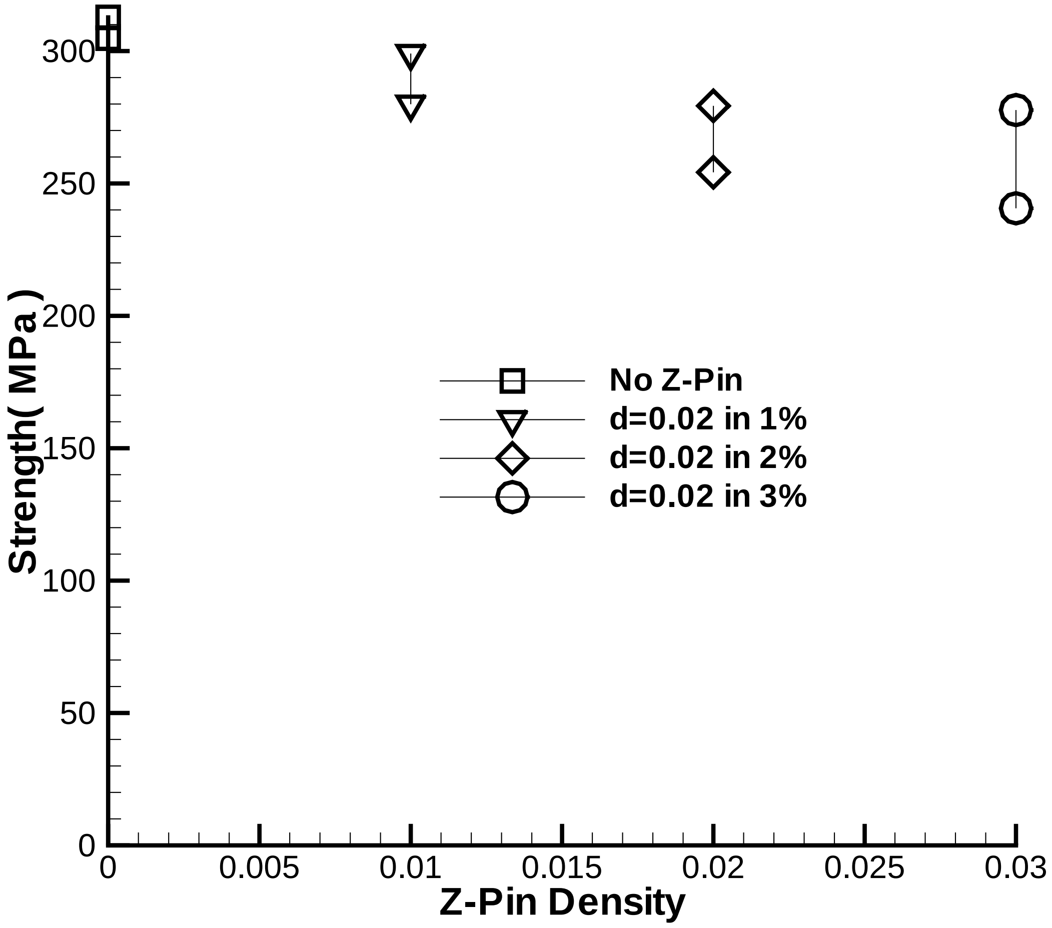

Figure B.4: Comparison of Strength between Group A and Group E

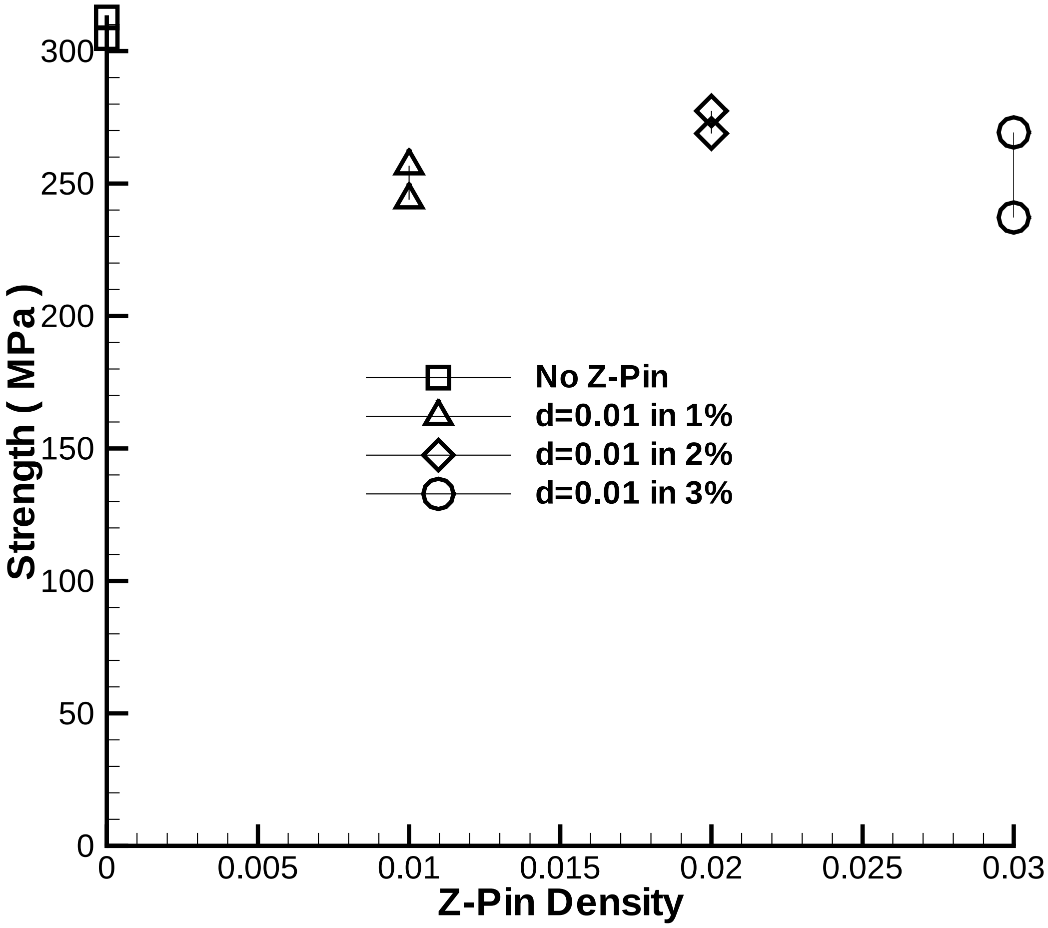

Figure B.5: Comparison of Strength between Group C and Group E

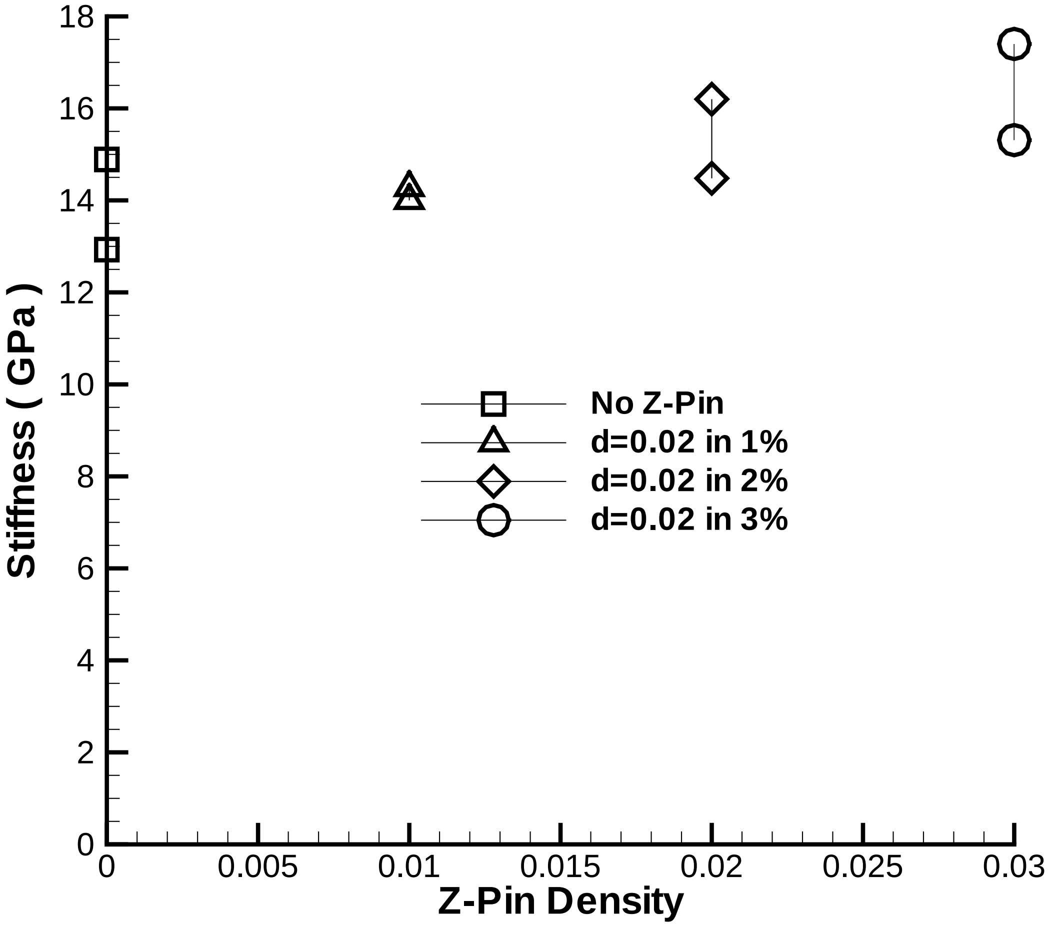

Figure B.6: Comparison of Stiffness between Group A and Group E

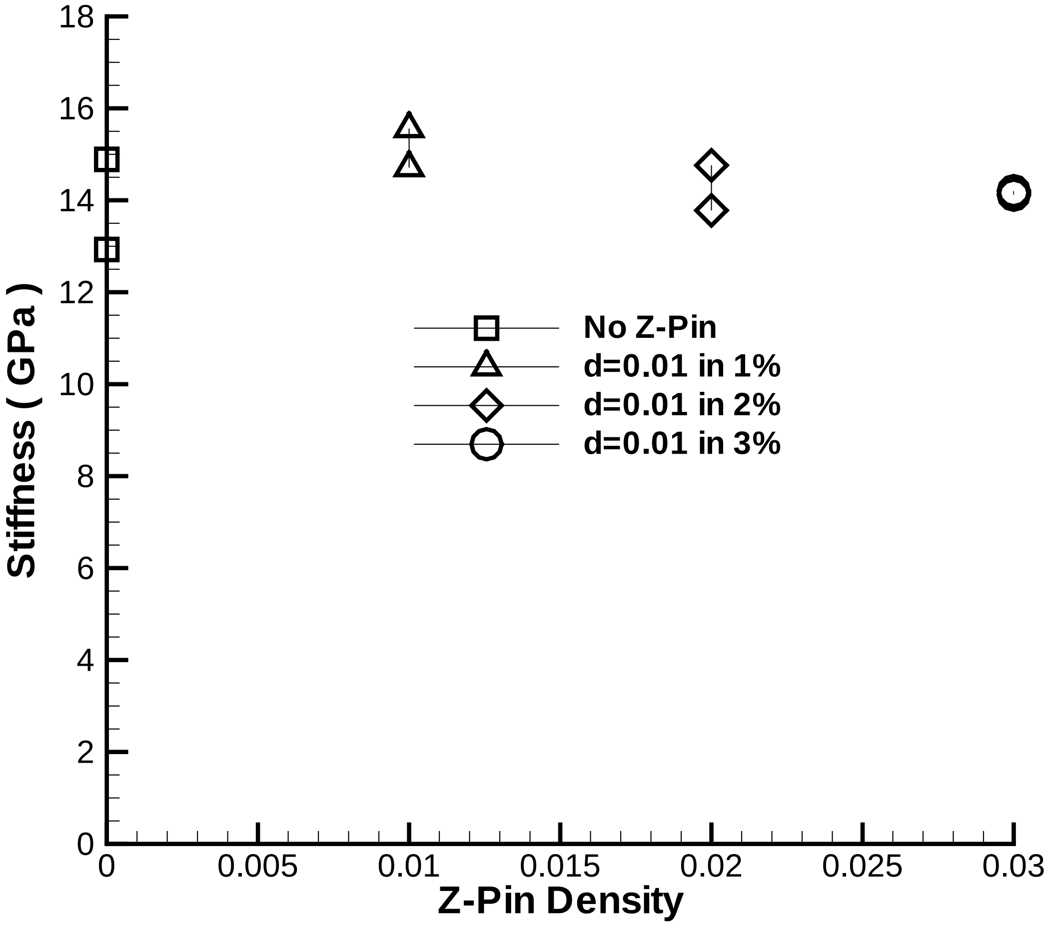

Figure B.7: Comparison of Stiffness between Group C and Group E

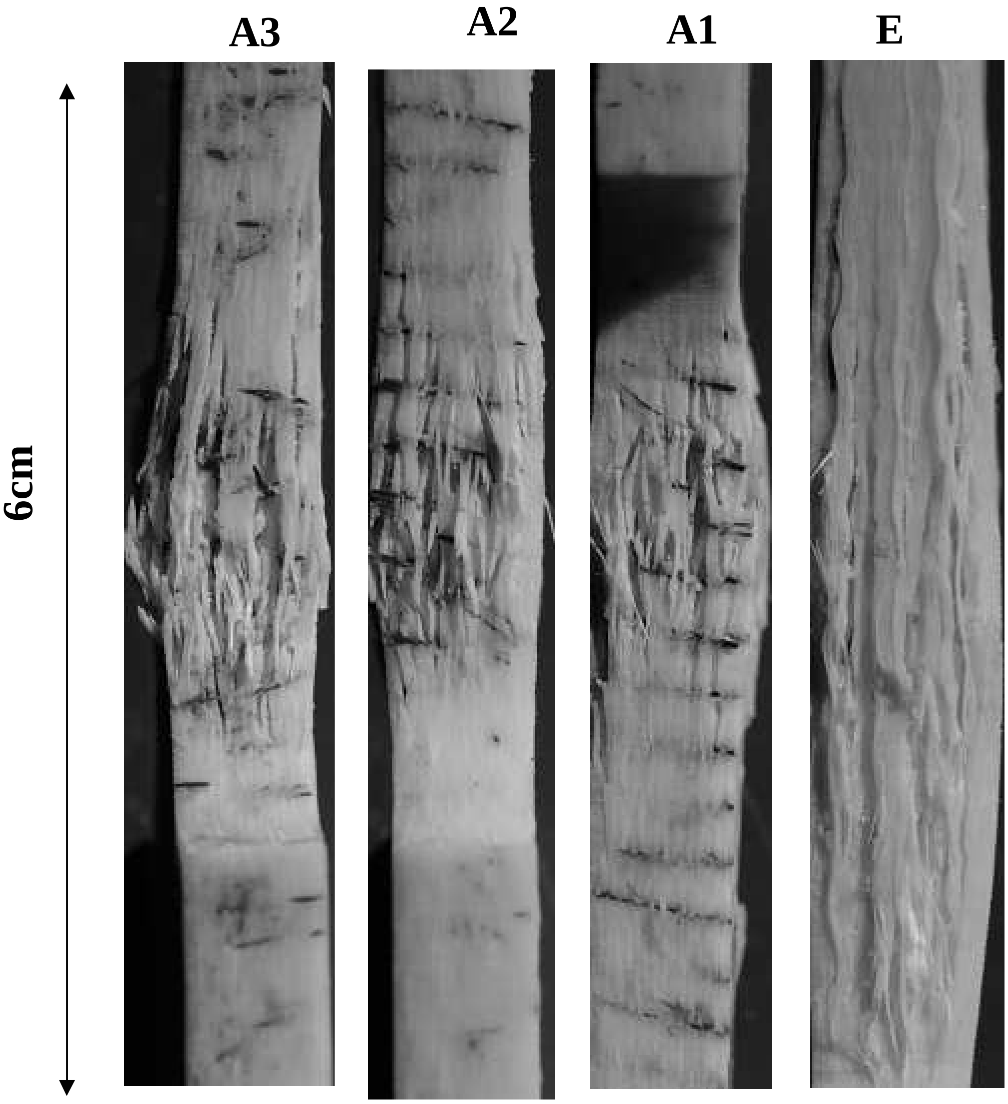

Figure B.8: Failure Pattern in Group A and Group E (A1 is 1% Z-pin Density, A2 is 2% Z-pin Density, A3 is 3% Z-pin Density). Notice How the Smaller Spacing between Z-pins (Larger Density) Leads to a Small Zone of Intense Damage

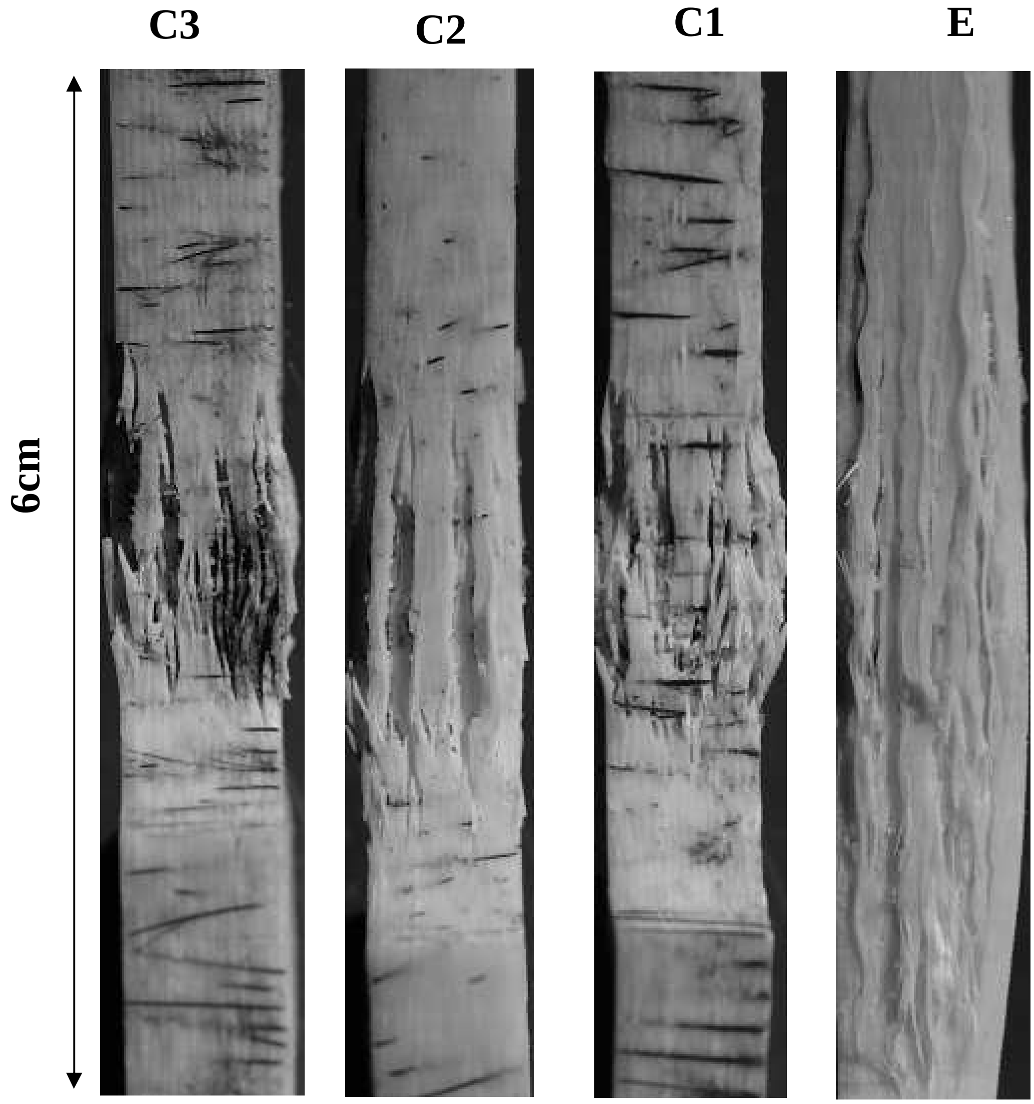

Figure B.9: Failure Pattern in Group C and Group E (C1 is 1% Z-pin Density, C2 is 2% Z-pin Density, C3 is 3% Z-pin Density). Notice How the Smaller Spacing between Z-pins (Larger Density) Leads to a Small One of Intense Damage

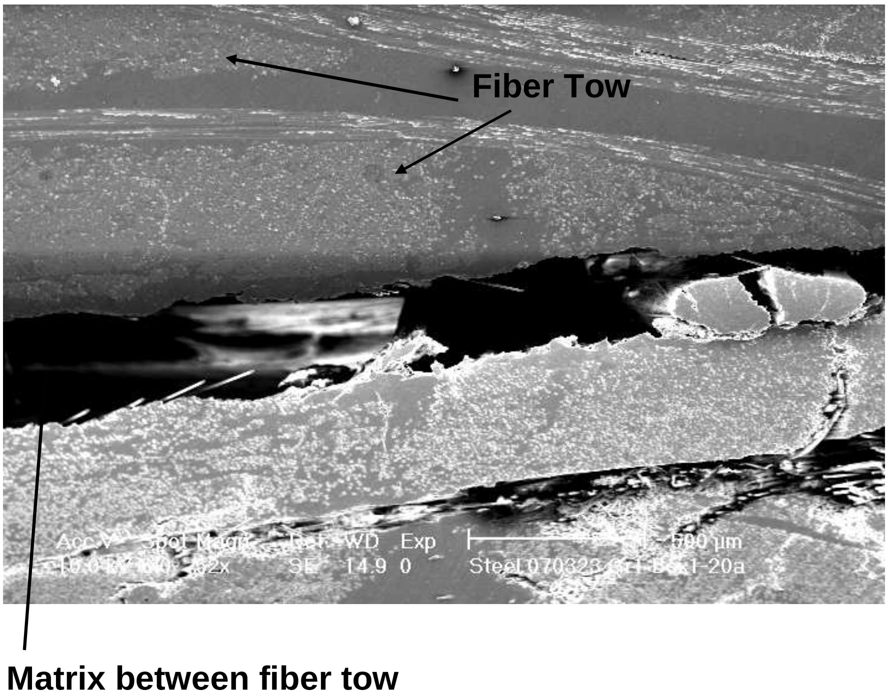

Figure B.10: Delamination between Fiber Tows,as Seen in a Failed A Specimen, after Tension Load

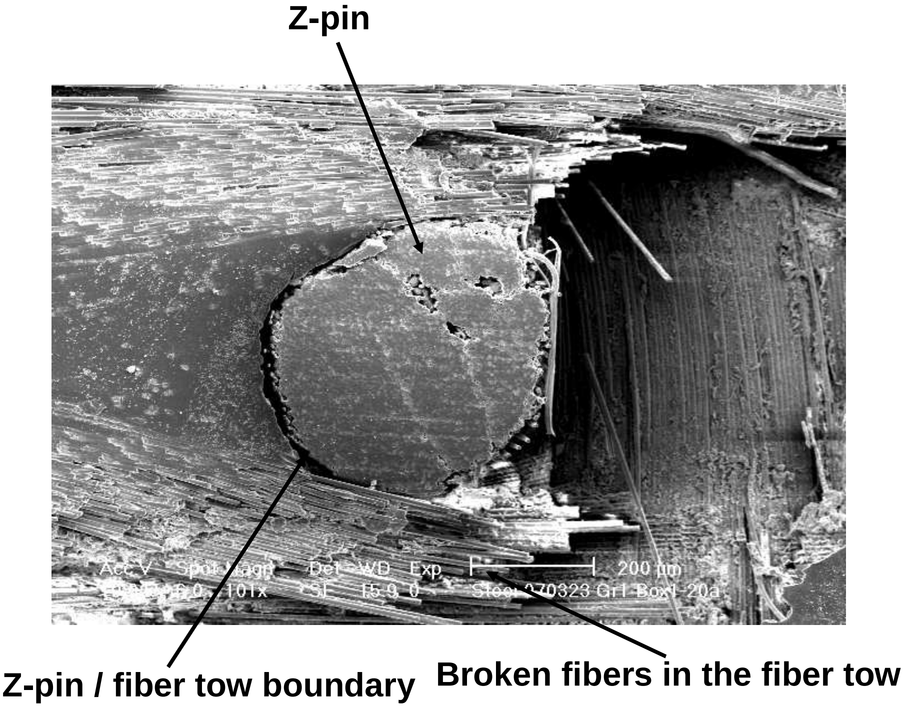

Figure B.11: Fiber Tow Breakage near Z-pin Imaged through a SEM

BIBLIOGRAPHY

BIBLIOGRAPHY

[1] *Adobe Photoshop 7.0.* San Jose, Calif., 2002.

[2] Ahn, J., H. *Failure mechanisms of notched laminated composites under compressive loading at room and elevated temperature.* PhD thesis, University of Michigan, 1999.

[3] Akisanya, A., R., Meng, C., S. Initiation of fracture at the interface corner of bi-material joints. *J. Mech. Phys. Solids 51*, 1 (2003), 27–46.

[4] Basu, S., Anthony, A., W., Ambur, D., R. Compressive failure of fiber composites under multi-axial loading. *J. Mech. Phys. Solids 54* (2006), 611–634.

[5] Bathe, K., J. *Finite Element Procedure in Engineering Analysis.* Prentice Hall, Englewood Cliffs, NJ, 1996.

[6] Bruck, H., A., McNeill, S., R., Sutton, M., A., Peters, W., H. Digital image correlation using newton-raphson method of partial differential correlation. *Exp. Mech 29*, 3 (1998), 261–267.

[7] Budiansky, B., Fleck, N., A. Compressive failure of fibre composites. *J. Mech. Phys. Solids 41*, 1 (1993), 183–211.

[8] Byrd, L., W., Birman, V. The estimate of the effect of z-pins on the strain release rate, fracture and fatigue in a composite co-cured z-pinned double cantilever beam. *Composite Structures 68* (2005), 53–63.

[9] Chang, P., Mouritz, A., P., Cox, B., N. . Flexural properties of z-pinned laminates. *Composites Part A 38*, 2 (2008), 244–251.

[10] Chapra, S., C., Canale R., P. *Numerical Methods for Engineerings.* Mcgraw-Hill, Columbus, OH, 1998.

[11] Chen, D., J., Chiang, F., P., Tan, Y., S., Don, H., S. Digital speckle-displacement measurement using a complex spectrum method. *Applied Optics 11*, 3 (1993), 1839–1849.

[12] Chen, F., Griffen, C. T., Hung, Y. Y. White light digital speckle photography for measuring rigid body motion. *Acta Optica Sinica 15*, 9 (1994), 1235–1239.

[13] Chen, J. L., Sun, C. T. A plastic pntontial function suitable for anisotropic fiber composites. *Journal of Composite Materials 27*, 14 (1993), 1379–1390.

[14] Chou, T. W. *Microstructural design of fiber composites* (1992).

[15] Cox, B., N. Constitutive model for a fiber tow bridging a delamination crack. *Mechanics of Composite Materials and Structures 6*, 2 (1999), 117–138.

[16] Dai, S., C., Yan, W., Liu, H., Y., Mai, Y., W. Experimental study on z-pin bridging law by pullout test. *Composites Science and Technology 64* (2004), 2451–2457.

[17] Freitas, G., Fusco, T., Campbell, T., Harris, J., Rosenberg, R. Z-fiber technology and products for enhancing composite design. *Proc. of the 83th Meeting of the AGARD SMP on Bolted/Bonded Joints in Polymeric Composites* (Sep 2-3 1996), 17–1–17–8.

[18] Freitas, G., Magee, C., Boyce, J., Bott, R. Service tough composite structures using z-fibers process. *Proc. 9th Dod/NASA/FAA Conf. Comp., Lake Tahoe* (Nov 1991), 2657–2665.

[19] Freitas, G., Magee, C., Dardzinski, P., Fusco, T. Fiber insertion process for improved damage tolerance in aircraft laminates. *J. Advanced Mat. 25* (1994), 36–43.

[20] Gonzaleza, A., Graciani, E., Paris, F. . Prediction of in-plane stiffness properties of non-crimp fabric laminates by means of 3d finite element analysis. *Composites Science and Technology 68*, 1 (2008), 121–131.

[21] Grassi, M., Zhang, X., Meo, M. Prediction of stiffness and stresses in z-fibre reinforced composite laminates. *Composites: Part A 33* (2002), 1653–1664.

[22] Greenhalgh, E., Lewis, A., Bowen, R., Grassi, M. Evaluation of toughening concepts at structural features in cfrp part i: Stiffener pull-off. *Composites Part A 37* (2006), 1521–1535.

[23] Gustafson, P., A. Analytical and experimental methods for adhesively bonded joints subjected to high temperatures. *PhD thesis, University of Michigan* (2008).

[24] Hahn, H., T., Pandy, R. micromechanics model for thermoelastic properties of plain weave fabric composites. *J. Eng. Material Technology 116* (1994), 517–523.

[25] Huang, H., J., Waas, M., A. An improved speckle method for measuring in-plane displacement and strain fields. *Optical Engineering 46*, 5 (2007), 0510051–05100511.

[26] Hyer, M. W., Waas, A. W. Micromechanics of linear elastic ciontinuous fiber composites. *T. W. Chou, ed., Comprehensive Composite Materials, Vol. 1, Chapter 12. Elsevier Science* (2000), 345–375.

[27] Ishikawa, T., Chou, T., W. Elastic behaviour of woven hybrid composites. *J. Material Science 16* (1982), 2–19.

[28] Ishikawa, T., Chou, T., W. Stiffness and strength behavior of woven fabric composites. *J. Material Science 17* (1982), 3211–3220.

[29] Jones, R. *Mechanics of composite materials* (1975).

[30] Kemao, Q., Asundi, A. Characterizing young's fringe's orientation and spacing by fourier transform and radan transform. *Optics and Laser technology 34* (2002), 527–532.

[31] Khare, G., Chandra, N., Silvain, J., F. Application of eshelby's tensor and rotation matrix for the evaluation of thermal transport properties of composites. *MECHANICS OF ADVANCED MATERIALS AND STRUCTURES 15* (2008), 117–129.

[32] Kyriakides, S., Arseculeratne, R., Perry, E., J., and Liechti, K., M. On the compressive failure of fiber reinforced compoistes. *International Journal of Solids and Structures 32*, 6/7 (1995), 689–738.

[33] Li, S., Wang, J., Thouless, M., D. The effects of shear on delamination in layered materials. *J. Mech. Phys. Solids 52*, 1 (2004), 193–214.

[34] Liu, H., Y., Zhou, L. M., Mai, Y., W. On fiber pull-out with a rough sruface. *Phil Mag 70*, 2 (1994), 359–372.

[35] Liu, J., Ying, H. Fft spectrum by fourier transform. *J. Vibration Eng. 8*, 2 (1995), 162–166.

[36] Naik, N., Ganesh, V., K. Prediction of the thermal expansion coefficients of plain weave fabric composites. *Comp. Structures 26* (1993), 139–154.

[37] Naik, R., A. Failure analysis of woven and braided fabric reinforced composites. *J. Composite Material 29* (1995), 2334–2363.

[38] Nwosu, S., N., Hu, D., Dutta, P., K., W. Dynamic mode ii delamination fracture of unidirectional graphite/epoxy composites. *Composites: Part B 34* (2003), 303–316.

[39] O'brien, T., K., Krurger, R. Influence of compression and shear on the strength of composite laminates with z-pinned reinforcement. *Applied Composite Materials 13* (2006), 173–189.

[40] Oppenheim, A., V. *Signals and systems.* Prentice-Hall, Englewood Cliffs, NJ, 1983.

[41] Quek, S., C., Waas, A., M. The crushing response of braided and csm glass reinforced composite tubes. *Journal of Composite Structures 52* (2001), 103–112.

[42] Quek, S., C., Waas, A., M., Shahwan, K., W., Agaram, V. . Compressive response and failure of braided textile composites: Part 2xcomputations. *International Journal of Non-Linear Mechanics 39*, 4 (2004), 649–663.

[43] Quek, S. C., Waas, A. M., Shahwan, K. W., Agaram, V. Compressive response and failure of braided textile composites: Part 1- experiments. *International Journal of Non-Linear Mechanics 39* (2004), 635–648.

[44] Quek, S., Waas, A., M., Shahwan, K., W., Agaram, V. . Analysis of 2d triaxial flat braided textile composites. *Journal of Mechanical Sciences 45* (2003), 1077–1096.

[45] Riks, E. An incremental approach to the solution of snapping and buckling problems. *International Journal of Solids and Structures 15* (1979), 529–551.

[46] Robison, P., Das, S. Mode i dcb testing of composite laminates reinforced with z-direction pins: a simple model for the investigation of data reduction strategies. *Engineering Fracture Mechanics 71* (2004), 345–364.

[47] Shapiro, V., A., Kavardjikov, S., A. Approach to automatic analysis of young's fringes in speckle photography. *Applied Optics 23* (1993), 4378–4387.

[48] Sirohi, R. S. *Speckle Metrology.* Marcel Dekker,New York, 1993.

[49] Sjodahl, M. Electronic speckle photography: Increased accuracy by nonintegral pixel shifting. *Appl. Opt. 33* (1994), 6667–6673.

[50] Sjodahl, M. Accuracy in electrical speckle photography. *Appl. Opt. 36* (1997), 2875–2885.

[51] Sjodahl, M., Benckert, L. R. Electronic speckle photography: analysis of an algorithm giving the displacement with subpixel accuracy. *Appl. Opt. 32* (1993), 2278–2284.

[52] Sridhar, N., Massabo, R., Cox, B., N.; Beyerlein, I., J. Delamination dynamics in through-thickness reinforced laminates with application to dcb specimen. *International Journal of Fracture 118*, 2 (2002), 119–144.

[53] Steeves, C., Fleck, N. *Proc. 12th international Conf. Comp. Mat.* (July 1999).

[54] Steeves, C., Fleck, N., A. Z-pinned composite laminates: knockdown in compressive strength. *Proc. DFC5, March, London* (1999), 60–68.

[55] Tada, Y., Ishikawa, T. Experimental evaluation of the effects of stitching on cfrb laminate specimens with various shapes and loading. *Key Engineering Material 37* (1989), 305–316.

[56] Tong, L., Mouritz, A.P., Bannister, M. *3D Fibre Reinforced Polymer Composites* (2002).

[57] Tvergaard, V., Hutchinson, J., W. On the toughness of ductile adhesive joints. *J. Mech. Phys. Solids 44*, 5 (May 1996), 789–800.

[58] Vendroux, G., W., Knauss, G. Submicron deformation field measurement: Part 2. improved digital image correlation. *Exp Mechanics 38*, 2 (1998), 86–92.

[59] Whitcomb, J., Kyeongsik, W. Enhanced direct stiffness method for finite element analysis of textile composites. *Comp. Structures 28* (1994), 385–390.

[60] Whiteside, J., B., Delasi, R., J., Schulte, R., L. Measurement of preferential moisture ingress in composite wing and spar joints. *Comp. Sci. and Tech 24* (1985), 123–145.

[61] Woo, S., C., Choi, N., S., Chang, Y., W. Toughness and fracture mechanisms of glass fiber/aluminum hybrid laminates under tensile loading. *Journal of Mechnaical Science and Technology 21*, 12 (2007), 1937–1947.

[62] Xie, D., Chung, J., Waas, A., M., Shahwan, K., W., Schroeder, J., A., Boeman, R., G., Kunc, V., Klett, L., B. Failure analysis of adhesively bonded structures: from coupon level data to structural level predictions and verification. *International Journal of Fracture 134* (2005), 231–250.

[63] Xie, D., Waas, A., M. Discrete cohesive zone model for mixed-mode fracture using finite element analysis. *Engineering Fracture Mechanics 73* (2006), 1783–1796.

[64] Yan, W., Liu, H., Y., Mai, Y.,W. Mode ii delamination toughness of z-pinned laminates. *Composites Science and Technology 64* (2004), 1937–1945.

[65] Zhou, P., Goodson, K., E. Subpixel displacement and deformation gradient measurement using digital speckle correlation. *Opt. Eng 40*, 8 (2001), 613–620.